Hypercrosslinked Polymers for Supercapacitor Applications

The University Of Sheffield.

Xuefeng Qi

A thesis submitted to the University of Sheffield in partial fulfilment to the requirements for the degree of Doctor of Philosophy

September 2021

Contents

Abstract

The use of fossil fuels has resulted in serious environmental problems such as pollution and global warming. Therefore, green and sustainable energy sources have been intensively researched and widely used. With the development of green energy, the demand for more effective energy storage devices to enhance energy efficiency has increased as well. Among all the energy storage devices, supercapacitors are known for high power density, long life span and fast charge/discharge rate. As a novel type of porous material, porous organic polymers (POPs) have promising potentials for supercapacitor applications because of their high porosity, tunable pore structures and functionalities, for example, covalent organic frameworks (COFs), such as conjugated microporous polymers (CMPs) have already shown good supercapacitive performance. In my work, hypercrosslinked polymer (HCP) materials are investigated for being used as supercapacitor electrode materials due to their ease of synthesis and low cost. Due to pore structures are closely related with supercapacitive performance, the pore structure controlling of HCPs is one of the main aims of this work. In chapter 3, the method for structure controlling is using monomers with different sizes and geometries. The HCPs synthesized from different monomers have BET surface areas varying from 127.1 m^2/g to 1255.6 m^2/g. The specific capacitances obtained at 2 mV/s of these HCPs vary from 2.2 F/g to 96 F/g. As heteroatom-doped activated carbons have shown increased supercapacitive performance, the monomers containing heteroatoms with different configurations are used for HCP synthesis in chapter 4 to investigate the effects of the heteroatom contents on the porous properties and supercapacitive performance of the HCPs. Compared with the non-doped HCPs, most of the heteroatom containing HCPs show a downward tendency in their BET surface areas. The oxygen-containing Diphenyl ether HCP and Dibenzofuran HCP show higher specific capacitances than other samples in this chapter, and the specific capacitances of these two samples are higher than those of their corresponding non-doped HCPs which are synthesized in chapter 3, indicating the oxygen content with some specific

configurations could enhance the supercapacitive performance of the HCPs.

In chapter 5, the method for HCP structure controlling is using different monomer to crosslinker ratios for HCP synthesis. With using different monomer to crosslinker ratios for HCPs synthesized from different monomers, the porous structures and specific capacitances of these HCPs are various. For Terphenyl HCPs, the BET surface areas of them vary from 34.5 m^2/g to 548.5 m^2/g while the specific capacitances of TPB HCPs range from 5.4 F/g to 113.8 F/g. The TPM HCP synthesized with a monomer to crosslinker ratio 1-6 has the highest BET surface area and highest specific capacitance in this work, 1783.5 m^2/g and 132.8 F/g, respectively. These results indicate that using different monomer to crosslinker ratios is an effective method for structure controlling of HCPs.

Acknowledgment

Firstly, I would like to thank my supervisor, Dr. Robert Dawson, for providing me the opportunity to undertake my PhD, and thank for his support and guidance. My supervisor is always kind and patient, working with him is a pleasant experience.

I would like to thank, Dr. Supakorn Tantisriyanurak, Dr. Alex James, Dr. Arosha Karunathilake, Shaobo Du and many past members of Dawson Group, many thanks for their help and support during my PhD. The time we work together will be unforgettable memories in my life. Special thanks for Shaobo, my good friend, for his help and accompany.

I also appreciate the support from the academic, technical and administrative staffs of the Department of Chemistry, University of Sheffield, especially the staffs of NMR service and elemental analysis for running my samples.

I am grateful for my parents and my sister who provide financial and mental support constantly. Without the firm supports from my family, I can never accomplish my PhD study.

I would like to express special thanks to my wife, who accompanies and takes good care of me. Because of her dedication, I can concentrate on my work. During the most difficult times, her accompany and encouragement motivated me to keep going.

I also need to thank my friends, Dr. Fangqi Liu, Dr. Yidong Xu, Dr. Yuhe Huang, Dr. Xiaoliang Fang, Dr. Ge Wang, Dr. Dawei Wang, Dr. Ziye Dai, Dr. Feifan Lang, Dr. Tao Cheng, Prof. Yin Ning, Prof. Di Zhou, Cheng Qian and Ziyi Li, who gave me useful advices and provided me a lot of help.

My PhD study is a rather challenging journey due to some unexpected incidents including the COVID-19 pandemic. I would like to express my gratitude again to my supervisor, to my colleagues, to the staff of the department of chemistry, to my family and to my friends. It is impossible to finish my PhD study without your support and help.

List of Abbreviations

1D One Dimensional

2D Two Dimensional

3D Three Dimensional

AC Activated carbon

ACF Activated carbon fiber

BET Brunauer-Emmett-Teller

BILPs Benzimidazole-linked polymers

CMPs Conjugated Microporous Polymers

CNTs Carbon nanotubes

COFs Covalent Organic Frameworks

CP/MAS Cross-Polarisation Magic Angle Spinning

CTFs Covalent Triazine Frameworks

CV Cyclic voltammetry

CVD Chemical vapor deposition

CPE constant phase angle element

DCE Dichloroethane

DMB Dimethoxybenzene

DMSO Dimethyl sulfoxide

DVB Divinylbenzene

EC Electrochemical capacitor

EDLC Electrical double layer capacitor

EIS Electrochemical impedance spectroscopy

FDA Formaldehyde Dimethyl Acetal

FTIR Fourier Transform Infrared

GO Graphene oxides

GCD Galvanostatic charge/discharge

HCPs Hyper-Cross-Linked Polymers

IHP Inner Helmholtz plane

IUPAC International Union of Pure and Applied Chemistry

MWCNTs multi-walled carbon nanotubes

NL-DFT Non-Local Density Functional Theory

NMR Nuclear Magnetic Resonance

OHP Outer Helmholtz plane

PAFs Porous Aromatic Frameworks

PAN Polyacrylonitrile

PANI Polyaniline

PIMs Polymers of Intrinsic Microporosity

PTFE Polytetrafluoroethylene

RGO Reduced graphene oxides

SSA specific Surface area

STP Standard temperature and pressure

SWCNTs Single-walled carbon nanotubes

TGA Thermogravimetric Analysis

TCD Thermal conductivity detector

TPB Triphenylbenzene

TPM Triphenylmethane

TPMA Triphenylmethylamine

TPMO Triphenylmethanol

TPMT Triphenylmethanethiol

TPPM two-pulse phase modulation

VBC Vinyl Benzyl Chloride

W_s Warburg element (short)

Chapter 1 Introduction and Background

1.1 Introduction to porous organic polymers

There is a wide variety of materials with permanent internal porosity, like zeolites and activated carbons.[1–4] Because of the large specific surface area, they are widely applied in gas adsorption, catalyst, water treatment and so on. In the last fifteen years, novel organic materials have been synthesized and developed, porous organic polymers (POPs). The common characteristics for this type of porous materials can be listed as (1): The molecular network is formed of rigid organic building blocks, (2): The major linkage for constructing the polymer molecule network is stable covalent bond.[5] Due to the many different types of monomers and synthesis methods, there are a wide variety of sub-classes of POPs, like porous aromatic frameworks (PAFs),[6] polymers of intrinsic microporosity (PIMs),[7] covalent triazine-based frameworks (CTFs),[8] benzimidazole-linked polymers (BILPs)[9] etc. However, the various names of these porous organic polymer sub-branches may cause confusion for the outside audience. There is a simpler classification of porous organic polymers based on structural features to cover as many materials as possible. According to this classification method, there are three main categories polymers, covalent organic frameworks (COFs), conjugated microporous polymers (CMPs) and hypercrosslinked polymers (HCPs). These three categories of materials will be introduced in this part.

1.1.1 Covalent organic frameworks

Covalent organic frameworks (COFs), are a unique sub-class of POPs because of their crystallinity. In 2005, the first COF material was published and named as COF-1.[10]

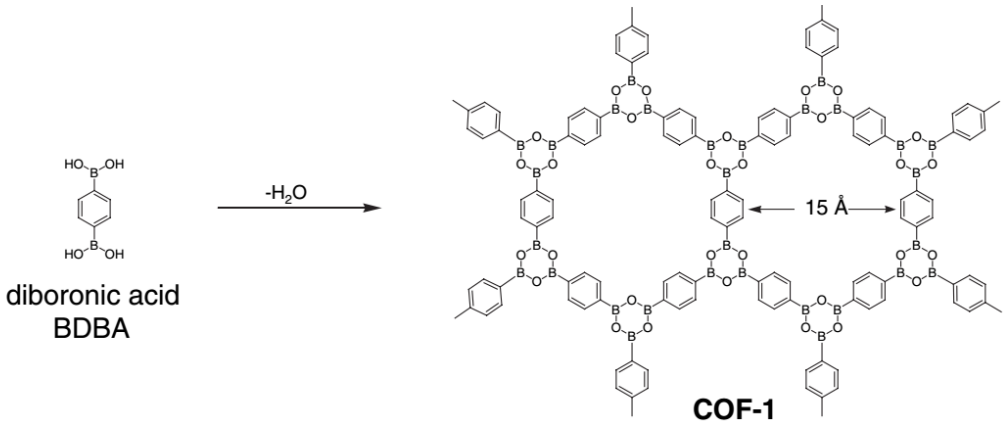

Figure 1.1.1 Schematic of synthesis and structure of COF-1[10]

In the figure 1.1.1, it can be seen that the synthesis of COF-1 is achieved by a self-condensation reaction of p-benzenediboronic acid. It is worth emphasizing that reversible nature of the condensation reactions for COFs synthesis is the key to ensure the crystallinity of COFs, as the opportunity to eliminate the defects in the frameworks by the constant formation and breaking of the B-O bonds until the thermodynamic product is obtained.[11,12] The p-benzenediboronic acid has a benzene ring structure in the molecule, providing rigidity of the framework, while the boron-oxygen heteroatomic rings (B_3O_3) formed in the condensation not only reinforce the rigidity of the network, they also have a planar structure. So, the ordered arrangement of the molecule network in COF-1 is obtained. As the first member of COF family, the self-condensation of p-benzenediboronic acid is the insptration for the designing of other COFs. The monomers with different geometries and sizes can be employed for COF synthesis, this endows the highly controlled structure of COFs.

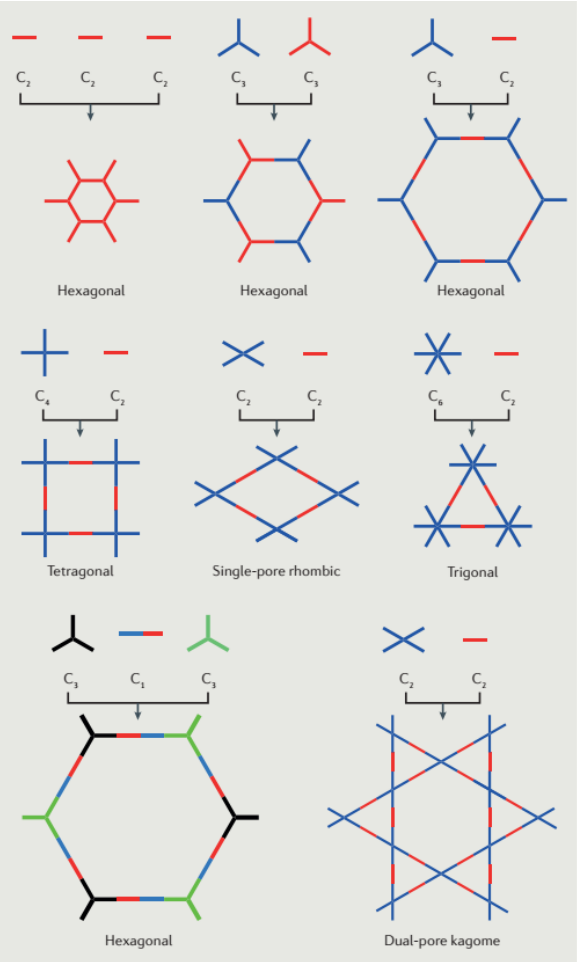

Figure 1.1.2 2D COF designing topology for building blocks with different geometries[13]

The figure 1.1.2 shows that the monomers that have different geometries could be used to construct COFs with different pore structures. The building blocks with different geometries are classified into C_2, C_3, C_4 and C_6 group.[14–18] The number refers to how many ends in different directions of a monomer could participate in the reaction of the linkage forming.

The boronate ester and imine linkages constructed by condensation reactions have planar structure which is essential for COFs.[19,20] The illustration of boronate ester and imine linkage are shown in figure 1.1.3.

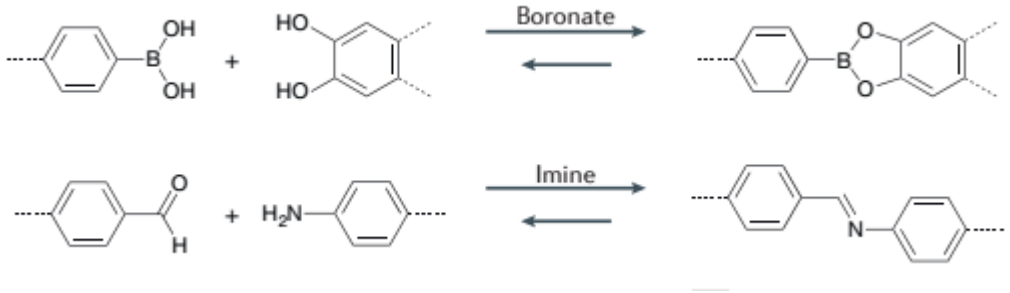

Figure 1.1.3 Schematic of boronate ester and imine structure formation in condensation reactions[13]

For COFs linked by boronate ester linkages, they usually have higher crystallinity than those linked by imine linkages, but they tend to be unstable in the presence of water, acids and alcohols, while for imine linked-COFs, the chemical stability under the condition of water, acids and alcohols is enhanced.[13,21]

Some typical boronic acid and catechol containing building blocks used for synthesis of boronate ester-linked COF are displayed in figure 1.1.4 and some typical aldehyde containing and amine containing building blocks used for synthesis of imine-linked COFs synthesis are shown in figure 1.1.5.

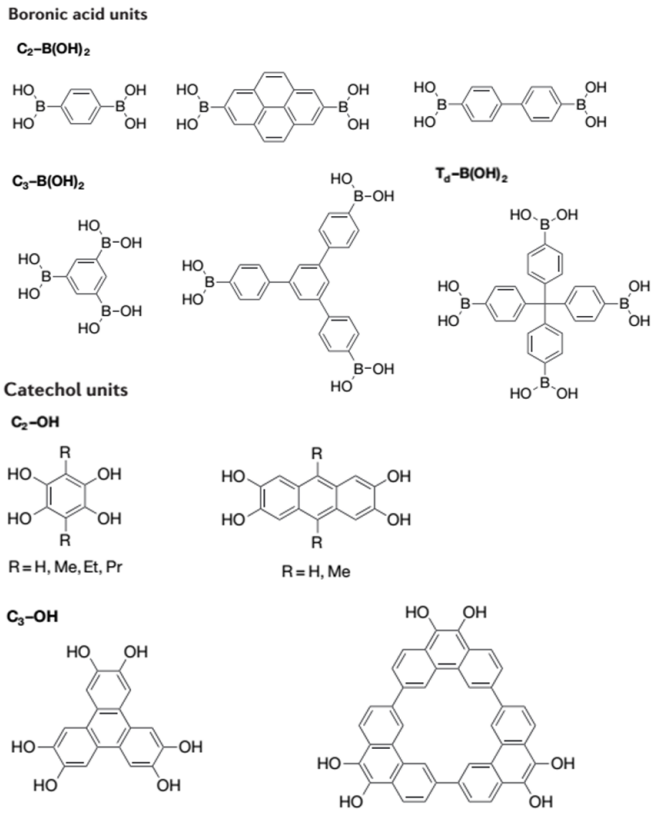

Figure 1.1.4 The boronic acid containing and catechol containing building blocks for boronate condensation[13]

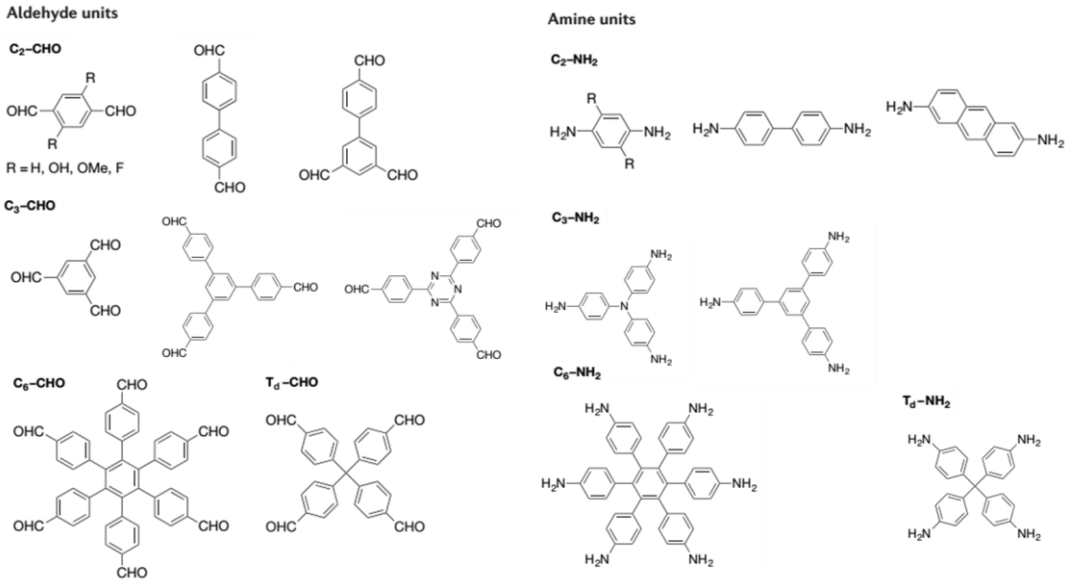

Figure 1.1.5 The aldehyde containing and amine containing building blocks for imine formation[13]

In the lists of COF building blocks, it can be seen that the monomers have a variety of sizes and geometries. By using these monomers, the opportunities for synthesizing COFs linked by boronate ester or imine linkages with diverse pore structures are provided. The idea of designing structures of COFs by using monomers with different sizes and geometries can be applied to some other porous organic polymers as well.

1.1.2 Conjugated microporous polymers

The first conjugated microporous polymer (CMP) was published in 2007.[22] The synthesis method for prototypical CMPs was Sonogashira-Hagihara cross coupling of a terminal ethynyl containing monomer and an aromatic monomer with halide end group, for example, 1,3,5-triethynylbenzene and 1,4-diiodobenzne. The illustration of CMP synthesis with Sonogashira-Hagihara cross coupling is shown in the figure 1.2.1.

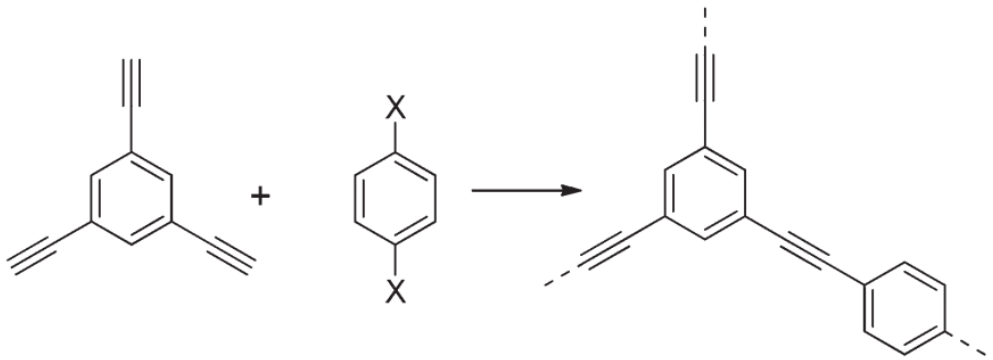

Figure 1.1.6 Schematic of Sonogashira coupling reaction for CMP synthesis (X= Br or I)[23]

The name of conjugated microporous polymer comes from its structural features. Take a CMP network obtained from Sonogashira-Hagihara cross coupling as an example, the rigid aromatic building blocks are connected by carbon-carbon triple bond linkages, therefore, the building blocks and linkages are all conjugated. Due to the high rigidity of the carbon-carbon triple bonds and the fast rate of the coupling reaction, the aromatic building blocks are trapped as the kinetic product rapidly, thus there is no chance for the CMPs to have an ordered arrangement in their molecular networks. As a result, CMPs are amorphous materials. Compared with COFs, there is a wider selection of synthesis methods for CMP synthesis, shown in the figure 1.1.7.

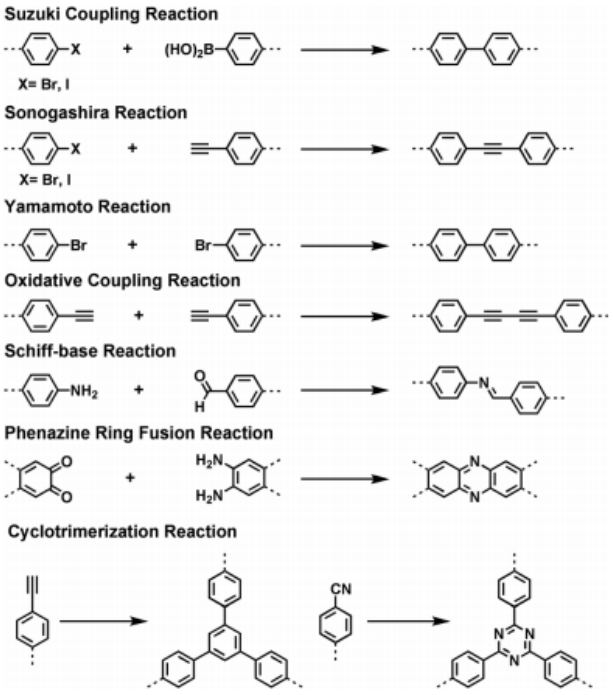

Figure 1.1.7 The synthesis methods for CMPs[24]

It can be found the synthesis methods shown above including coupling reaction,[25–28] condensation reaction[29,30] and cyclotrimerization reaction.[31] To distinguish between CMPs and other POPs, Xu et al. proposed that a CMP material should be fully conjugated, i.e., conjugation system in the framework can be extended through the linkages between building blocks, otherwise it cannot be categorized as a CMP material.[24] Due to the greater options for CMP synthesis methods, there are more monomers available for CMP synthesis. For CMPs, using building blocks with different sizes and geometries is also suitable for attaining different porous structures of CMPs. The schematic monomers with different geometries for CMP construction are listed in figure 1.1.8.

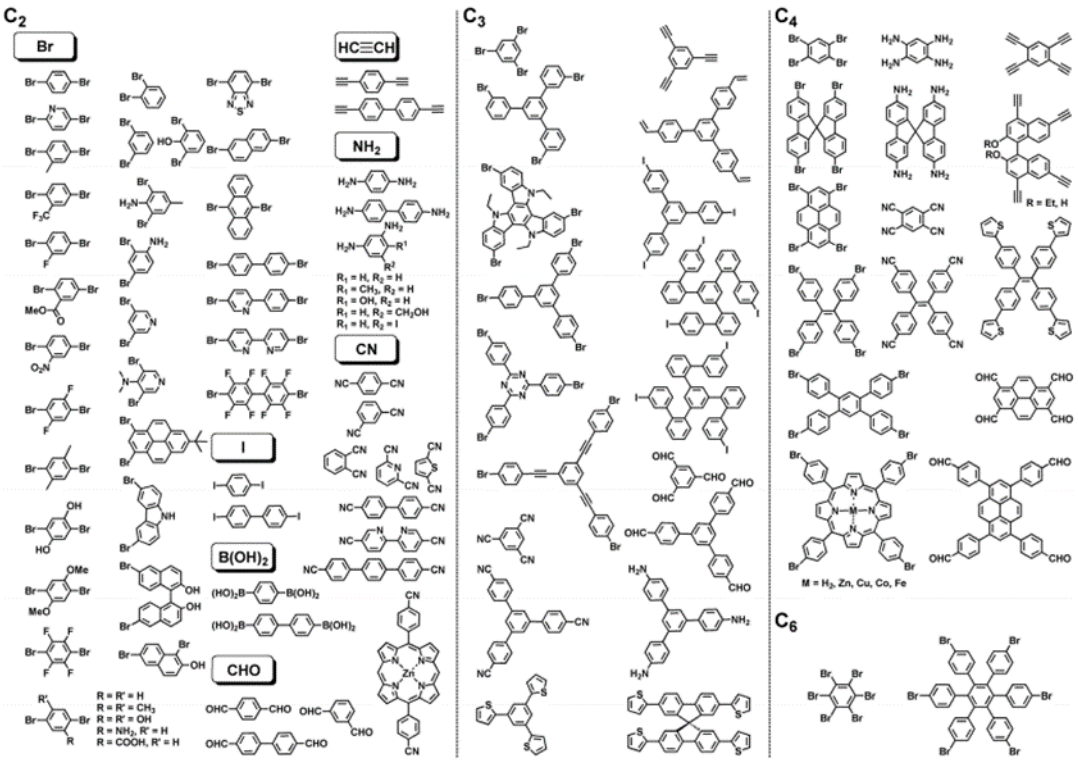

Figure 1.1.8 Schematic of building blocks of CMPs[24]

The functional groups employed in coupling reaction to build CMPs include bromine group, iodine group, boronic acid group, ethynyl group while the active groups for condensation reaction contains aldehyde group, amino group. It is similar to COFs that the classification of building blocks of CMPs can be also based on their geometries, C_2, C_3, C_4 and C_6 for obtaining CMPs with different porous structures.[32–34]

1.1.3 Hypercrosslinked polymers

Compared with COFs and CMPs, the research to HCPs has a much longer history. The first work about HCPs was published in 1970s by Davankov and Tsyurupa,[35] therefore, the first HCP sample was named Davankov resins.[36] At that time, HCPs were made from polystyrene and divinylbenzene co-polymers. Briefly speaking, there are two main steps for this kind of HCP preparation. The first step is the swelling or dissolution of the polymer precursor and the next step is to make the polymer chains crosslinked. So, this kind of preparation method is called post crosslinking.

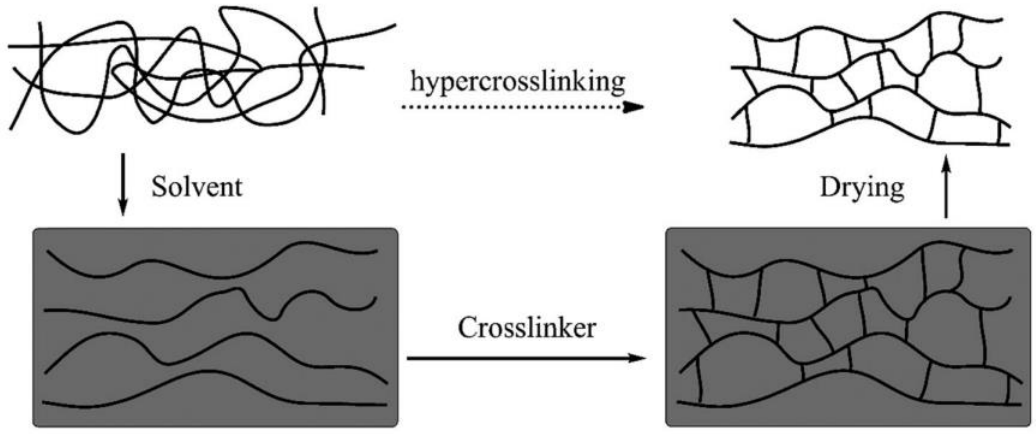

Figure 1.1.9 Schematic of HCP synthesis with post crosslinking methods[37]

Since 1970s, the post crosslinking methods had been developed for almost 50 years. The crosslinking can be achieved by using external crosslinkers, like tetrachloromethane (CCl4)[38], dichloroxylene[35], trifunctional tris-(chloromethyl)-mesitylene (TCMM)[39], etc. With external crosslinkers, the post-crosslinked HCPs can have high BET surface area. For example, the BET surface area of the hypercrosslinked polystyrene with dichloroxylene as crosslinker at high crosslinking degree is higher than 1000 m^2/g.[35] The crosslinking method can internal crosslinking as well.[40] Ahn et al. used a series of vinylbenzyl chloride–divinylbenzene copolymers (VBC-co-DVB) with different DVB content as precursors for post crosslinking.[41] The internal crosslinking of these samples was achieved by internal condensation of chloromethyl groups with catalyst $FeCl_3$. The highest BET surface area of these samples can be as high as 2090 m^2/g. However, although the HCPs synthesized with post-crosslinking

method can achieve high porosity, the preparation of precursor for post crosslinking is usually a time-consuming procedure.

In 2011 a new synthesis method for HCP called knitting method was published.[42] This method can be intuitively described that the rigid aromatic building blocks are knitted by methylene linkages to form a microporous framework.

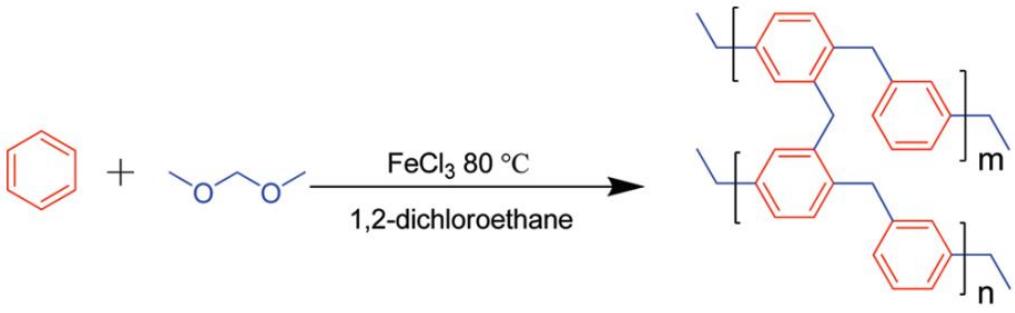

Figure 1.1.10 Schematic of the knitting method for HCP synthesis[42]

This method is based on Friedel-Crafts alkylation reaction. In the presence of Lewis acid, the electrophilic substitution will occur between the hydrogen of an aromatic rigid building blocks and external crosslinkers. Therefore, this method is classified into external crosslinking. The mechanism of knitting method is introduced in scheme 1.1.1.

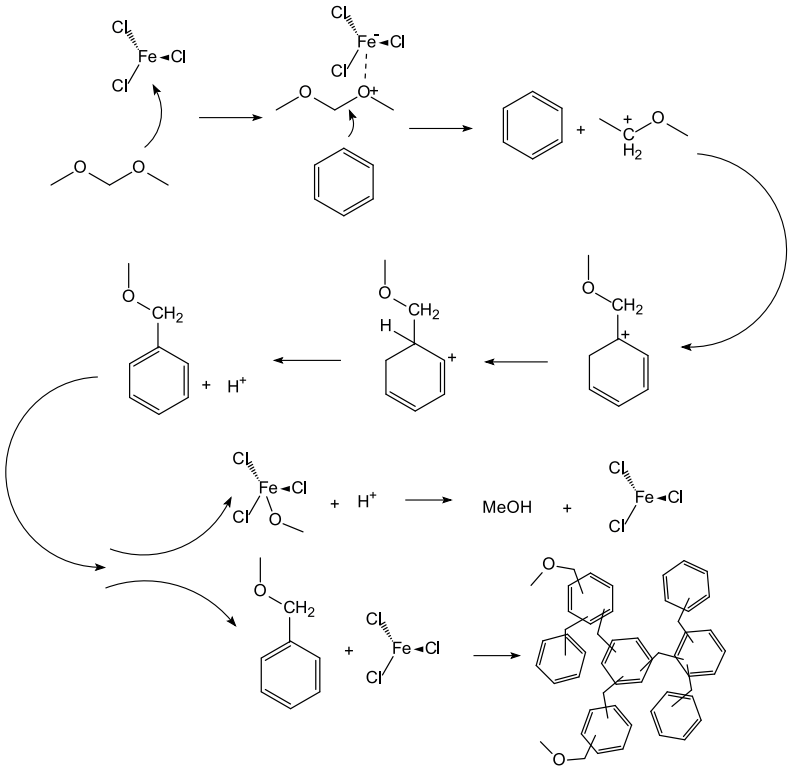

Scheme 1.1.1 Mechanism of $FeCl_3$ catalyzed Friedel-Crafts alkylation reaction for HCP synthesis

To be brief, the $FeCl_3$ catalyst complexes with crosslinkers first, reducing the binding energy between the methoxyl group and the central carbon atom. Then, intermediate carbocations are produced and they react with aromatic rings by adding methoxymethyl groups to phenyl rings with releasing methanol molecules. If these methoxymethyl groups could react with other aromatic rings, they will be converted into methylene linkages to form a rigid HCP network, otherwise they will become incompletely reacted crosslinker residues.

For hypercrosslinked polymers obtained with knitting method, because of the rigidity of aromatic moieties, the monomers will be trapped by the crosslinkers rapidly due to the fast reaction rate of the Friedel-Crafts alkylation reaction, this situation is similar to the CMPs synthesized with the Sonogashira-Hagihara cross coupling, thus HCPs are amorphous as well. The advantage of knitting method is porous hypercrosslinked polymers can be synthesized rapidly with a low cost. Just like COFs and CMPs, using different monomers can be employed for obtaining HCPs with various pore structures. The illustration of monomers used for knitting methods of HCP synthesis are shown in the figure 1.1.11.

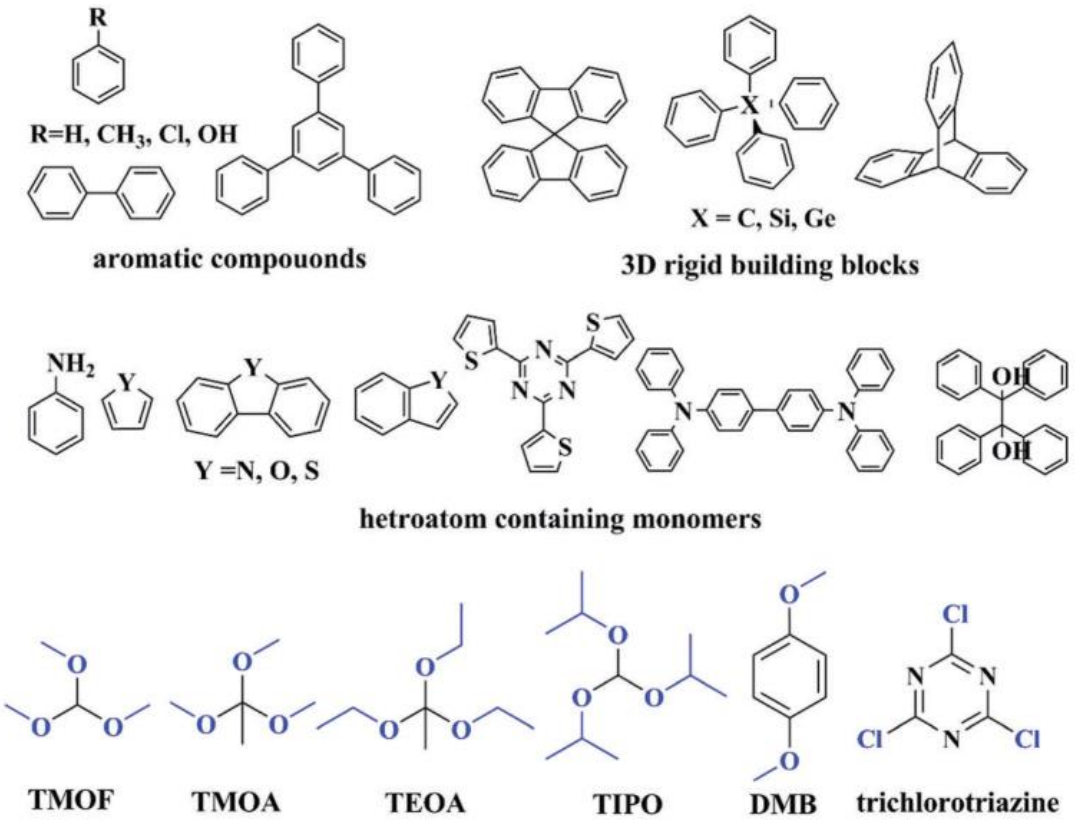

Figure 1.1.11 Schematic of HCP monomers and external crosslinkers with different structures[37]

Employing monomers with different structures has an impact on the pore structures of HCPs. Due to the reactants of Friedel-Crafts alkylation reaction involve both monomers and crosslinkers, using different external crosslinkers could result in different pore structures of HCPs as well. For instance, if dimethoxybenzene (DMB) replaces dimethoxymethane as the external crosslinker, then the linkage in the framework will be benzene rings rather than methylene originated from dimethoxymethane.[43] The different ratio of monomer to crosslinker could result in different porous structure of HCPs as well.[42] The functionality can be introduced to HCPs by using heteroatom containing monomers, e.g., Luo et al. successfully synthesized HCP with knitting method with the heteroatom containing monomers, including furan, pyrrole, and thiophene.[44]

Due to the porous structures of POPs, these polymers have a wide range of applications, for example, gas separation,[45] gas capture and storage,[46] chemosensor,[47] and wastewater treatment.[48] In addition, POPs are also used for energy storage devices like lithium-ion batteries,[49] fuel cells,[50] as well as supercapacitors.

1.2 Energy storage mechanism of supercapacitors

The overuse of fossil fuel has resulted in some serious problems such as environmental pollution and global warming.[51–54] Therefore, clean and sustainable energy sources have been intensively researched and commercialized. With the development of alternative energy like wind energy,[55,56] solar energy,[57,58] tidal energy,[59,60] geothermal energy[61,62] etc., developing more effective energy storage devices to enhance energy efficiency has been a focused research area. Energy storage devices, e.g., lithium-ion batteries,[63] sodium-ion batteries,[64,65] potassium-ion batteries,[66,67] fuel cells,[68,69] supercapacitors and so on, have grown rapidly. As a fast-developing energy storage device, supercapacitor, also called electrochemical capacitor (EC), is attractive and promising for energy revolution due to its high specific power, long cycle life and fast charge/discharge rate.

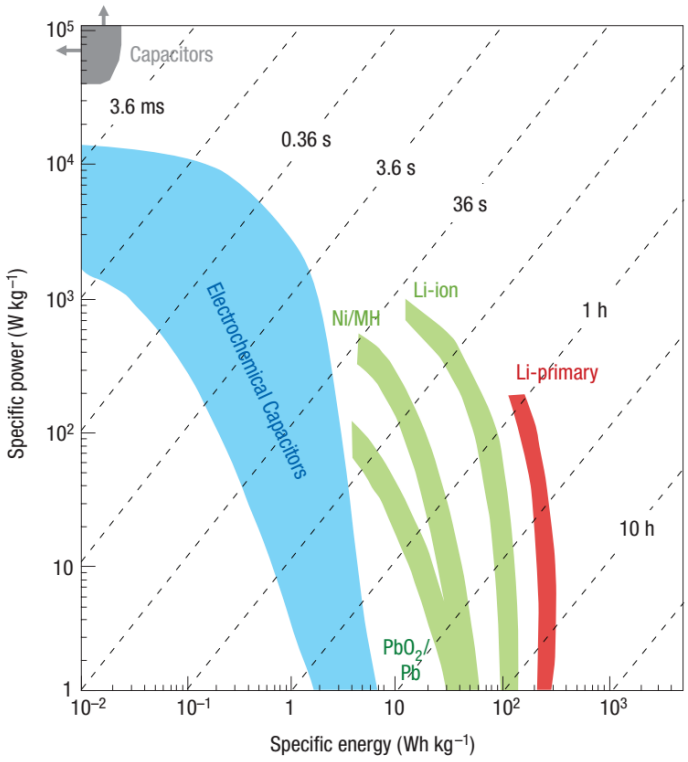

Figure 1.2.1 Ragone plot of specific power against specific energy demonstrating properties for different energy storage system[70]

From the Ragone plot above, it can be found that capacitors possess higher specific power but lower specific energy than other energy storage devices. The main advantage of batteries is their high specific energy. For electrochemical capacitors, they have higher energy density than conventional capacitors and greater power density than batteries. Conventional capacitors have been widely employed for quite a long time, due to the similar storage mechanism, the mathematical description and performance parameters for capacitors can be also applied to ECs. For a capacitor, the capacitance can be written as the equation below

$$C = \frac{Q}{V} \qquad 1.2.1$$

where C is the capacitance (F), Q is the quantity of electric charge (C), v is the potential difference between two electrodes (V). A typical capacitor consists of two parallel plane electrodes and a dielectric separator, the capacitance can be also defined as

$$C = \frac{\varepsilon_0 \varepsilon_r A}{D} \qquad 1.2.2$$

where ε_0 is the permittivity of vacuum, ε_r is the permittivity of the dielectric separator, A is the surface area of electrodes and D is the distance between the two electrodes. The important characterization parameters for capacitors are specific energy and specific power. Specific energy means how much energy can be stored in unit mass (Wh kg^{-1}) and specific power means how fast the energy can be transferred in unit mass (W kg^{-1}). The relation between capacitance (C) and energy (E) is

$$E = \frac{1}{2}CV^2 \qquad 1.2.3$$

where V is the potential difference (V) between the electrodes. When considering the power of a capacitor, the resistance needs to be considered. The resistance of components in a capacitor like current collector, electrode, dielectric (or electrolyte and separator in supercapacitor) can be obtained as equivalent series resistance (ESR). The test of power is usually conducted under matching impedance, that is to say, when load impedance is supposed to be the same as ESR, the maximum power P_{max} can be obtained.

$$P_{max} = \frac{V^2}{4ESR} \qquad 1.2.4$$

Due to the resistance of the components in capacitors, the output voltage will be lower and therefore the power will decrease as well. So, to decrease the ESR is a method to increase the power of a capacitor.

Based on the energy storage mechanism, supercapacitors can be classified into three types, electrical double layer capacitor (EDLC), pseudo-capacitor and hybrid capacitor. The relationship between them is shown in the figure 1.2.2.

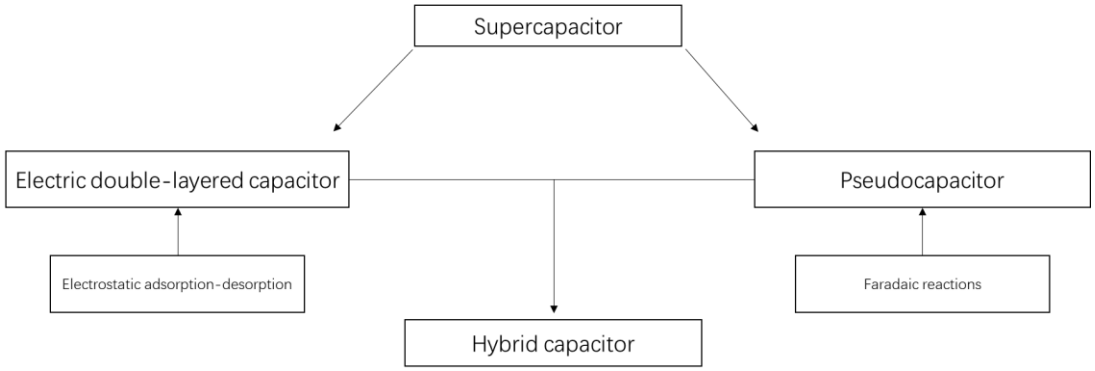

Figure 1.2.2 The classification of supercapacitors based on energy storage methods

1.2.1 Electric double-layer capacitor

The energy storage mechanism of EDLC is attributed to the electrostatic adsorption/desorption on the surface of electrodes. The concept of a supercapacitor was first proposed by Helmholtz in the 19th century.[71] The Helmholtz model is similar to the mechanism of conventional capacitor. In the Helmholtz model, it is stated that charge separation occurs on the interface of charged electrode and electrolyte, therefore a layer of charge will be absorbed on the surface of electrode. Then, Gouy and Chapman proposed that there is a diffusion layer on the interface of electrode/electrolyte rather than a compact layer of charge.[72,73] However, Gouy and Chapman model overestimates the capacitance of electric double layer structure, due to the thickness of diffusion layer is larger than a single charge layer, therefore more ions will be involved on the interface. Based on Helmholtz and Gouy-Chapman models, Stern put forward a new model to describe the adsorption on the interface.[74] In the Stern model, the interface is composed of the Stern layer (inner Helmholtz plane, IHP) and the diffusion layer (outer Helmholtz plane, OHP). The IHP is the compact ion layer most closely absorbed on the surface of electrode while the OHP means the layer of non-specifically adsorbed ion layer. The OHP layer is the boundary of the diffusion layer and the Stern layer.

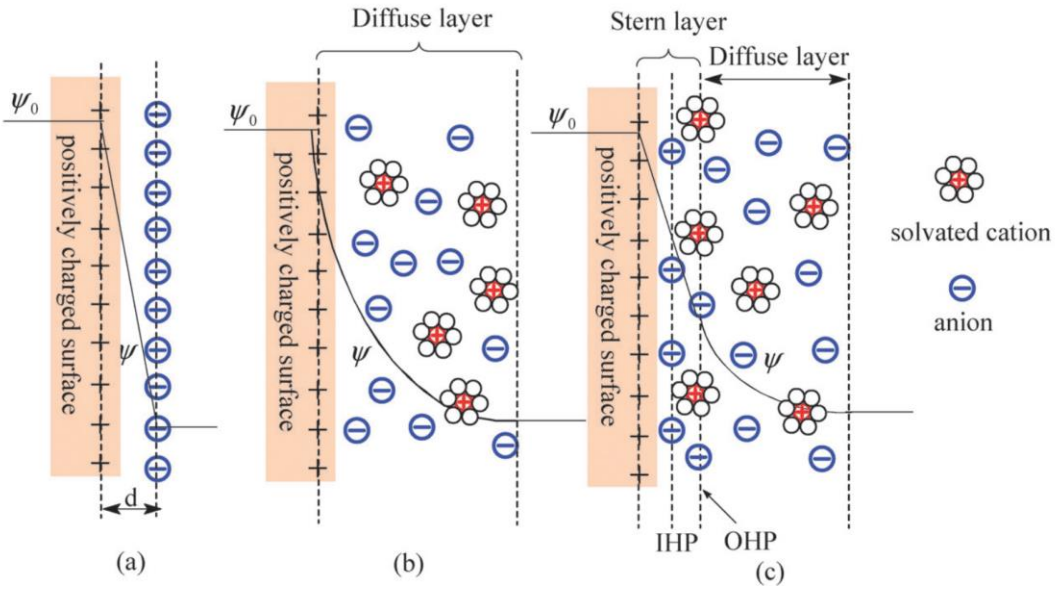

Figure 1.2.3 (a). Helmholtz model, (b). Gouy–Chapman model, and (c). Stern model[75]

From the schematic of EDLC working mechanism and capacitance calculation equation $C=\frac{\varepsilon_0\varepsilon_r A}{D}$, it can be understood why supercapacitors have much higher energy density than conventional capacitors. The first reason is that the porous structure of electrodes in SCs provides much larger surface area for ion adsorption, and secondly, the thickness of electric double layer (D in the equation) is at atomic level.

With the development of porous materials, mesoporous and microporous materials with high specific surface area are well studied and widely used as supercapacitor electrode materials. However, traditional Stern model based on parallel-plate model cannot fully interpret the capacitive performance of the mesoporous and microporous materials, thus Heuristic model was proposed. If pore width is large enough, pore curvature does not need to be considered, the adsorption/desorption process can be modeled by using parallel-plate model. when pore size decreases, pore curvature needs to be taken into account. Electric double-cylinder (EDC) structure formed by counter ions are used for modeling for mesopores, which is shown in figure 1.2.4 a). For micropores, electric wire-in-cylinder (EWC) model is used, shown in figure 1.2.4 b). The capacitance calculation of EDC and EWC model is given in equation 1.2.1.1 and 1.2.1.2, respectively.

$$C = \frac{\varepsilon_r\varepsilon_0}{b\ln[\frac{b}{b-d}]}A \qquad 1.2.1.1$$

$$C = \frac{\varepsilon_r\varepsilon_0}{b\ln[b/a_0]}A \qquad 1.2.1.2$$

where A is surface area, b and a are the radii of the outer and inner cylinders, respectively, and a_0 is the effective size of the counterions, i.e., the extent of electron density around the ions.

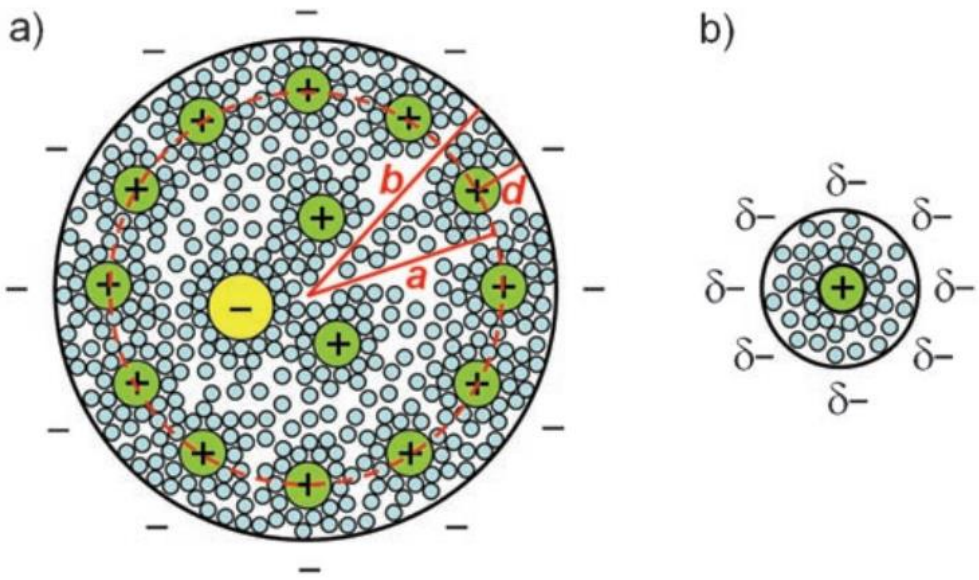

Figure 1.2.4 Schematic diagrams (top views) of a) a negatively charged mesopore with solvated cations approaching the pore wall to construct electric double-cylinder (EDC) structure with outer radium b and inner radium a of the cylinder., b) a negatively charged micropore of radius b with solvated cations of radius a_0 lining up to form an electric wire-in-cylinder structure (© Wiley InterScience, reprinted with permission).[76]

Heuristic model provides theoretical basis for interpreting the relationship between capacitive performance and pore structure of a material, as well as for supercapacitor electrode material designing. These theoretical studies are still desired for better understanding of EDLC energy storage mechanism and future EDLC researches.

1.2.2 Pseudo-capacitance

Different from electrostatic adsorption/desorption, the energy storage mechanism of pseudo-capacitance is attributed to the faradaic behavior of the electrode, that is to say, fast redox reactions on the surface of the electrode realize the energy conversion. Conway et al. proposed that pseudo-capacitor can be divided into three types, (I). Underpotential Deposition, (II). Redox reaction on the surface (2D), (III). Intercalation Pseudocapacitance (quasi-2D).[77]

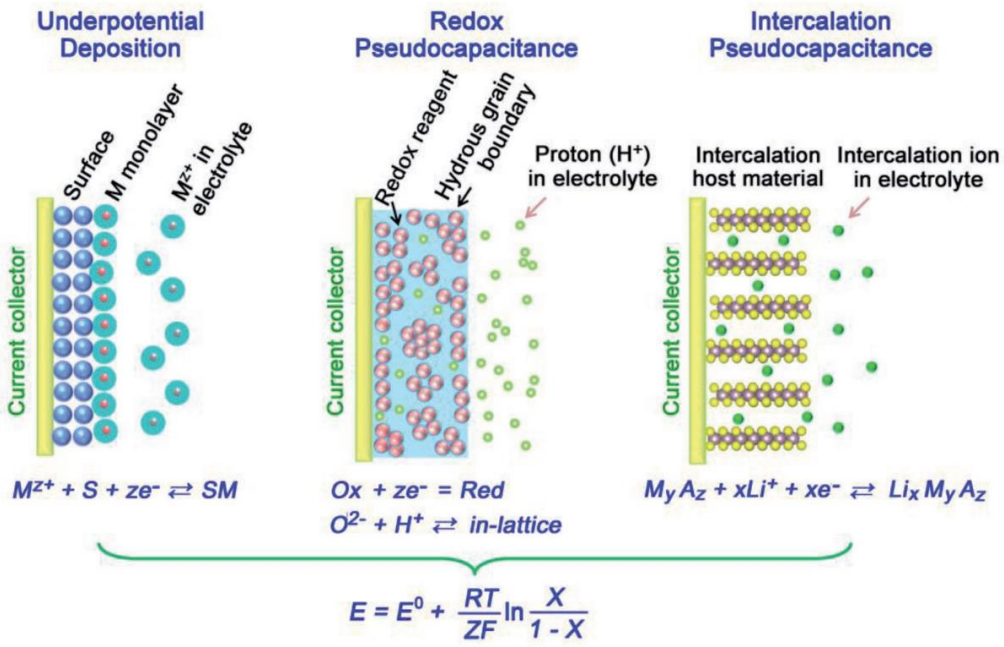

Figure 1.2.5 Schematic of different types of pseudocapacitance[78]

Underpotential deposition (type I) means when the interaction of M-S (M means deposition material and S means surface material) is stronger than the interaction of M-M, a layer of ions will be adsorbed on the surface because of reduction. Redox pseudocapacitance (type II) includes both ion adsorption and redox reaction. Intercalation pseudocapacitance (type III) is similar to electrode in lithium-ion battery, but the difference is there is no phase transformation during the reaction.

The relationship between potential of electrode and the extent of charge/discharge can be shown in the equation (5)[78]

$$E=E^0+\frac{RT}{ZF}ln\frac{X}{1-X} \qquad 1.2.2.1$$

In equation (5), E is Electrode potential (V), E^0 is standard electrode potential, R is the ideal gas constant (8.314 J mol^{-1} K^{-1}), T is temperature (K), Z is the number of transferred electrons in redox reaction, F is Faraday constant (96,485 C mol^{-1}), X is the occupancy fraction of the surface.

1.3 The introduction to carbon materials applied for supercapacitors

The research into carbon materials used as supercapacitor electrode materials had lasted

for decades. This intensive research has proposed some important conclusions and led to a great boosting effect on the development of supercapacitors as well. Carbonaceous materials are a wide range of materials with different morphologies, for instance, activated carbon is an amorphous porous carbon material while carbon fiber, carbon nanotubes and graphene are materials with different structures made up of carbon atoms. Currently, activated carbons are still the main materials for supercapacitor electrode manufacturing. Because of the low cost and moderate performance, activated carbon is identified to be the primary commercial material for supercapacitor electrode, especially for electric double layer capacitors. In order to improve the supercapacitive performance, activated carbon fiber, carbon nanotubes and graphene are employed to fabricate composite materials for supercapacitor electrodes as well.

1.3.1 Activated carbon

Activated carbon is produced from physical or chemical activation. The physical activation is usually conducted under temperature around 700 to 1200 °C.[79] Under the combined effects of high temperature and oxidization gas like steam or CO_2, the activated carbon with porous structure can be obtained. The chemical activation requires lower temperature (around 400 to 700 °C),[80] and the carbon precursor need to be mixed with activating agent like potassium hydroxide, zinc chloride, phosphoric acid, sodium hydroxide and sulfuric acid.[81–90] The porosity of activated carbon comes from the etched carbon network and the released gas that generated during the carbon network oxidation. As a porous material, activated carbon has high specific surface area and wide pore size distribution. The specific surface area of activated carbon can be as high as 3100 $m^2 g^{-1}$.[91] Micropores (< 2 nm), mesopores (2-50 nm) and macropores (>50 nm) all can be found in activated carbon.[92,93] To improve the supercapacitive performance of activated carbons, heteroatoms can be introduced into activated carbons through post-treatment on the surface. The oxygen functionalities can be obtained from the surface oxidation with concentrated nitric acid.[94] The nitrogen containing functional groups can be obtained from the thermal treatment[95] or hydrothermal reaction[96] together

with nitrogen enriched materials, like ammonia and amines, etc.. Similarly, sulphur can be used for activation carbons surface post treatment as well.[97] For example, Xu et al. prepared nitrogen-doped activated carbon nanofiber doping with ammonia.[98] The BET surface area is 701 m^2/g, and the specific capacitance is 197 F/g at 0.2 A/g and 143 F/g at 20 A/g (rate capability 72.1%). Shang et al. prepared phosphorous and nitrogen co-doped activated carbon doping with $NH_4H_2PO_4$.[99] The BET surface area is 1407 m^2/g and the specific capacitance is 227 F/g at 0.05 A/g. They also prepared oxygen and nitrogen co-doped activated carbon with BET surface 1433 m^2/g and specific capacitance 235 F/g at 0.05 A/g (rate capability 89.8% at 5 A/g). However, the post-treatments for activated carbon surface modification are complicated, high-cost and time consuming.[100] The other way to introduce functionalities into activated carbons is to use biomass materials as precursors. Biomass is organic materials that can be obtained from animals and plants, therefore these sustainable, renewable and inexpensive materials are environmentally friendly. Moreover, biomass materials contain abundant of heteroatom functionalities,[101] and the unique inherent structures from different biomass materials could result in the different pore structures of the derived activated carbons as well.[102] Currently, activated carbons derived from biomass are the research focus due to the advantages mentioned above. The results of activated carbons derived from biomass materials and fossil fuels used for EDLC application are listed in the table 1.3.1.

Materials	BET surface area (m^2/g)	Electrochemical test conditions	Capacitance (F/g)	Capability rate	Cycle stability	Reference
Pitch-based activated carbon with KOH and $KMnO_4$ activation (PAC_KM_1)	1750	6 M KOH aqueous solution/Symmetric two-electrode system	225.2 F/g at 5 mV/s	112.8 F/g at 100 mV/s (50%)	---	103
Coal tar pitch-based activated	2984	6 M KOH aqueous solution/three-	327 F/g at 1 mV/s	198 F/g at 200 mV/s	94% retention after 10000	104

carbons with $ZnCl_2$ and KOH activation (HPCs-5-800)		electrode system		(60.6%)	cycles at 10 A/g	
Nitrogen-doped coal-based activated carbon with melamine used as nitrogen source and KOH activation (MAC_N)	2129	6 M KOH aqueous solution/Symmetric two-electrode system	323 F/g at 0.5 A/g	214 F/g at 20.0 A/g (66%)	90.7% retention after 5000 cycles at 1 A/g	105
Coal-based activation carbon with KOH activation (AC4T800t2)	2457	6 M KOH aqueous solution/three-electrode system	384 F/g at 5 mV/s	279 F/g at 200 mV/s (73%)	95% retention after 5000 at 5 A/g	106
Popcorn derived activated carbon with KOH activation (PCF-900)	3301	6 M KOH aqueous solution/Symmetric two-electrode system	348 F/g at 0.2 A/g	286 F/g at 90 A/g (82%)	95% retention after 10 000 cycles at 5 A/g	107
Porous carbon materials from silk cocoon with KOH activation (N-PC-700)	3841	6 M KOH aqueous solution/Symmetric two-electrode system	408 F/g at 0.5 A/g	235 F/g at 30 A/g (58%)	96% retention after 20 000 cycles at 25 A/g	108
Activated carbon from waste coffee beans with $ZnCl_2$ activation	1019	1 M H_2SO_4 aqueous solution/two-electrode system	368 at 0.05 A/g	---	Retention is higher than 90% after 10,000 cycles at 5 A/g	109
Corncob derived activated porous carbon with (CC-AA-600)	800	1 M H_2SO_4 aqueous solution/three-electrode system	390 F/g at 0.5 A/g	250 F/g at 5 A/g (64%)	85% Retention after 5000 cycles at 10 A/g	110
Activated	2895	6 M KOH aqueous	275 F/g at 0.5	210 F/g at 50	99.1% retention	111

carbon derived from harmful aquatic plant (altemanthera philoxeroides) with KOH activation (APPC-3)		solution/three-electrode	A/g	A/g (76%)	after 5000 cycles at 10 A/g	

Table 1.3.1 The supercapacitive performance of activated carbons

The research into activated carbon has already laid a good foundation for future research due to some important conclusions being revealed. These conclusions are about the relationship between the structure of porosity and the performance in supercapacitors. Generally speaking, specific surface area is a primary parameter to describe a porous material, and the direct impression of a porous material usually is higher specific surface area means better performance. However, for the application of supercapacitor electrodes, it was pointed out that there is discrepancy between specific surface area and capacitance of activated carbon. Endo et al. had demonstrated that the pore size distribution is a more important parameter for activated carbon used as supercapacitor electrodes.[112] Furthermore, Largeot et al. revealed that the maximum capacitance of electric double layer capacitors can be achieved when pore size and electrolyte ion size matches.[113] In summary, activated carbon is a porous with high specific surface area. The structures of activated carbons can be influenced by raw materials and manufacturing methods. Although activated carbon could have high specific surface area, the wide pore size distribution and random connected pore structure decrease the supercapacitive performance of activated carbon.[114]

1.3.2 Templated carbon

In order to overcome these disadvantages to get carbon materials with more controllable pore structure, templating techniques for fabricating porous carbon with ordered structures has been developed. The preparation procedure of templated carbon can be divided into three steps, (1) carbon precursor is infiltrated into porous template, (2) the

precursor is treated with carbonization and (3) the template is removed to form a porous structure.

In comparison with activated carbon, templated carbon has an ordered structure at the microscopic level due to the arranged mesoporous or macroporous structures.[115]

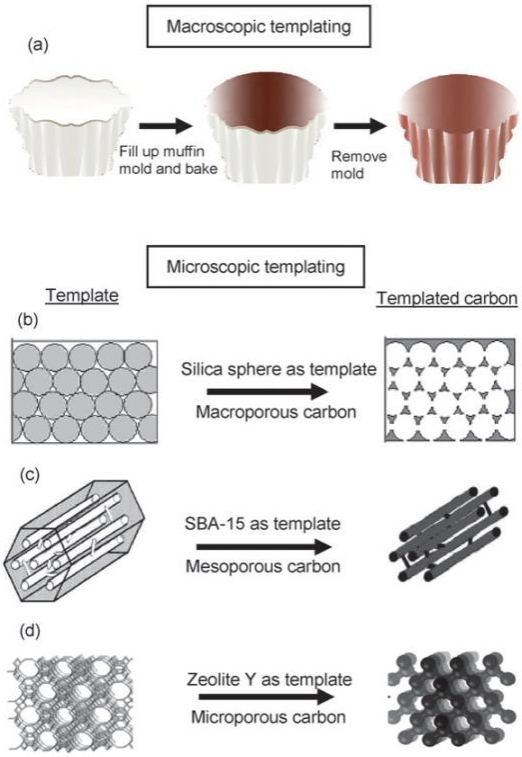

Figure 1.3.1 (a) The general concept of templating in macroscopic scale. (b) Macroporous templated carbon by using silica sphere. (c) Mesoporous templated carbon with SBA-15 as a template. (d) Zeolite Y used as template for producing microporous templated carbon.[116]

Just like normal activated carbon materials, micropores can be formed during the activating procedure as well. Therefore, templated carbons could have an ordered hierarchical pore structure. Because of this structural feature, templated carbon has an improved performance. The researches on templated carbons also revealed important conclusions for the development of supercapacitors. Compared with activated carbon, the interconnected molecule network of templated carbon could enhance the accessibility of electrolyte ions in the material, so better performance in power density, capacitance, and higher rate performance can be obtained.[117] Xia et al. found that if ordered interconnected mesopores with pore width 3-4 nm were introduced into

activated carbon, the specific capacitance can rise up to 223 F/g from 115 F/g.[118] In a hierarchical structure, the pores with different sizes play different roles. Wang et al. pointed out that in their designed hierarchical carbon material, the macropores (>50 nm) play the role of buffering reservoir of ions; the graphitic mesopores could overcome the kinetic limits of electrochemical process in porous electrode material to provide good electrical conductivity; the micropores are essential for boosting the capacitance.[119] The schematic of the 3-D hierarchical pore structure in their work is shown in the figure 1.3.2.

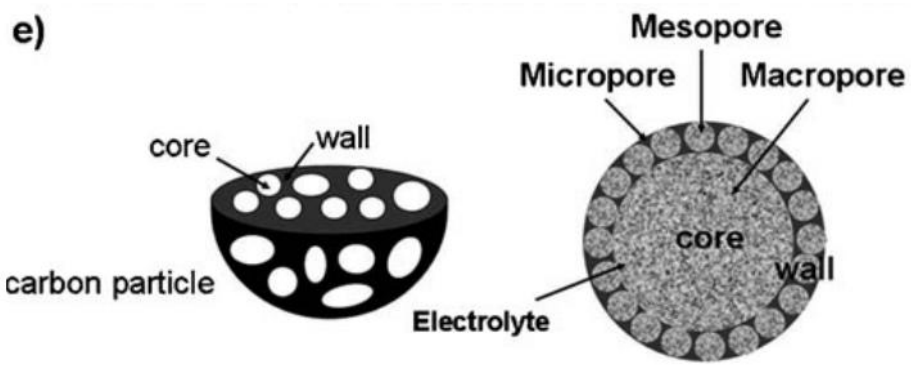

Figure 1.3.2 The schematic of the 3-D hierarchical pore structure[119]

The supercapacitive performance of templated carbons are listed in the table 1.3.2.

Materials	BET surface area (m^2/g)	Electrochemical test conditions	Capacitance (F/g)	Capability rate	Cycle stability	Reference
Nitrogen-doped ordered mesoporous Carbon (H-NMC-2.5)	537	1 M H_2SO_4 aqueous solution/three-electrode system	262 F/g at 0.2 A/g	63% at 5 A/g	---	120
Pore-adjustable mesoporous carbon (NPC-1)	765	1 M H_2SO_4 aqueous solution/three-electrode system	280 F/g at 0.5 A/g	64% at 10 A/g	96.5% retention after 10000 cycles at 10 A/g	121
Ordered microporous carbons produced with zeolite template	3040	1 M Et4NBF4 in PC (propylene carbonate)/three-electrode system	168 F/g at 0.05 A/g	91% at 2 A/g	---	122

(X-Ac)						
Ordered microporous carbons with three-dimensionally arrayed and mutually connected 1.2-nm nanopores (ZTC-L)	2910	1 M Et4NBF4 in PC/ three-electrode system	74 F/cm^3 at 0.01 A/g	64 F/cm^3 at 20 A/g (86%)	No capacitance losses after 2000 cycles at 1 A/g	123
Ordered mesoporous carbon derived from silicon carbide (mesoporous CDC, 700 ℃)	2250	tetraethylammonium tetrafluoroborate ($TEABF_4$) in acetonitrile/ Symmetric two-electrode system	170 F/g at 0.1 A/g	150 F/g at 17 A/g (88%)	---	124
Cubic ordered mesoporous carbon (H-CMK-8)	1217	2 M KOH aqueous solution/three-electrode system	246 F/g at 0.625 A/g	181 F/g at 6.25 A/g (74%)	81% retention after 2000 cycles at 1.25 A/g	125
Nitrogen-doped ordered mesoporous carbon spheres (N-OMCS)	439	6 M KOH aqueous solution/three-electrode system	288 F/g at 0.1 A/g	66% at 50 A/g	No obvious capacitance degradation after 25,000 cycles at 20 A/g	126

Table 1.3.2 Supercapacitive performance of templated carbons

In the table 1.3.2, it can be found that some ordered mesoporous carbons have the capability rate higher than 85%, indicating the enhanced ion diffusion in the ordered structures. In 2006, Sevilla et al. proposed the conclusion that the template mesoporous carbon have the limitation in specific surface area (1500-1600 m^2/g) as well as in specific capacitance obtained from aqueous electrolytes (around 220 F/g) after summarizing the papers related with template mesoporous carbon published before 2006.[127] This conclusion is a little outdated currently, as it can be seen that some of the ordered mesoporous carbon materials in the table 1.3.2 show BET surface area higher

than 2000 m^2/g, but none of them show capacitance higher than 300 F/g, so relatively low specific capacitance remain a problem for templated carbons. More importantly, the high cost and complex operation of template methods restrict the mass production of template carbons.

1.3.3 Carbon nanotubes

Since firstly reported in 1991,[128] carbon nanotubes have attracted extensive attentions of researchers due to their structural, electrical, mechanical properties and high chemical and thermal stability. Carbon nanotubes are regarded as a candidate for supercapacitor application due to their good conductivity and unique porous structures.[129,130] Carbon nanotubes can be divided into single-walled carbon nanotubes (SWCNTs) and multi-walled carbon nanotubes (MWCNTs), the structure schematic of them is shown below.

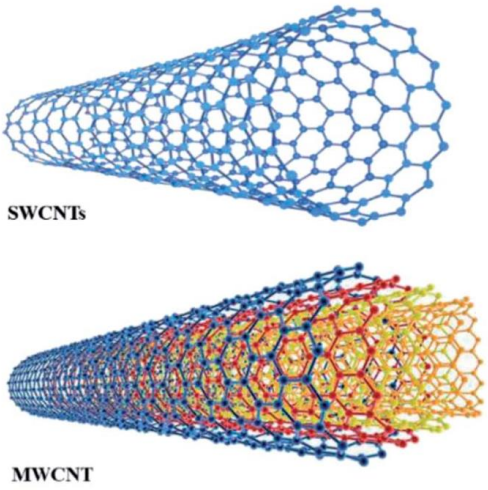

Figure 1.3.3 Nanostructures of SWCNTs and MWCNTs[131]

The chemical vapor deposition method and arc discharge method are common methods for carbon nanotube preparation.[132,133] To improve the supercapacitive performance, functionalities can be introduced into carbon nanotubes through thermal treatments, chemical activation methods and post-treatment methods that used for activated carbons.[134–140] The supercapacitive performance of some carbon nanotube-based

materials for EDLC are listed in the table 1.3.3.

Materials	BET surface area (m^2/g)	Electrochemical test conditions	Specific capacitance	Capability rate	Cycle stability	Reference
Single-walled carbon nanotubes film	---	PVA-H_3PO_4/ Symmetric two-electrode system	110 F/g at 1 mA/mg	33% (36 F/g) at 30 mA/mg	---	141
Carbon nanotubes ink for 3D printing	---	PVA-H_3PO_4/ Symmetric two-electrode system	4.69 mF/cm^2 at 50 mV/s	4.25 mF/cm^2 at 100 mV/s (91%)	Specific capacitance retention rate is no lower than 90% after 2000 cycles	142
Carbon nanotube yarn	---	PVA-H_3PO_4/ Symmetric two-electrode system	19.2 F/g at 100 mV/s	---	Specific capacitance retention rate is higher than 90% after 1000 cycles	143
Carbon nanotube with KOH activation (ACNT-5)	644	7 M KOH aqueous solution/Symmetric two-electrode system	53.6 F/g at 0.05 A/g	60% (32 F/g) at 5 A/g	---	144
Multi-walled carbon nanotube with H_2SO_4/HNO_3	208	1 M H_2SO_4 aqueous solution /three-electrode system	51.3 F/g at 100 mV/s	---	---	145

Table 1.3.3 Supercapacitive performance of carbon nanotubes

Compared with activated carbons, carbon nanotubes have relatively low specific surface area, theoretically, carbon nanotubes have an limit SSA of 1315 m2/g.[146] It is difficult to maintain the intrinsic properties of individual CNTs on a macroscopic scale,[130] therefore the performance of CNT monolithic electrodes fabricated with common method will be lower than the theoretical values, like specific surface area. The high cost for mass production of high quality CNT remains a challenge for the commercialization of CNT-based supercapacitors.[147]

1.3.4 Graphene

Since the publication of 'Electric Field Effect in Atomically Thin Carbon Films' in 2004, [148] graphene, the material with sp^2-hybridized carbon atoms formed two-dimensional hexagonal monolayer, has attracted worldwide attention due to its high electrical and thermal conductivity as well as strong mechanical properties. [149–151] For supercapacitor applications, the theoretical value of BET surface area is 2630 m^2/g and the theoretical value of specific capacitance is 550 F/g.[152,153] Graphene not only exist in monolayer form, it can be consisted of two or more single layers as well, while the graphene consists of more than ten single layers will be of less scientific interest.[154] It can be seen that the name of graphene is derived from graphite, graphite consists of stacked monolayer graphene bonded with weak van der Waals force, so graphene can be obtained from graphite exfoliation. In 2004, Graphene was prepared with repeating mechanical exfoliation of graphite, but this method is tedious and time consuming.[148] Typically, chemical vapor deposition (CVD),[155] Hummers method[156] and electrochemical exfoliation[157] are common methods for graphene preparation. For chemical vapor deposition method, the precursors are evaporated and carbonized first, then the vapor is cooled down and multilayer graphene can be obtained on the substrate (e.g., Ni or Cu foil). In terms of Hummers method, oxidation reaction occurs in the graphite due to the strong oxidation agents (potassium permanganate, sodium nitrate, sulfuric acid). The interaction between the graphite layers is weaken by the oxygen containing functional groups (e.g., hydroxyl group C-OH, carboxyl group C=O, and epoxy groups C-O) on the surface of individual layers, therefore the exfoliation of the graphite is easier. After exfoliation, graphene oxides (GO) can be obtained. Reduced graphene oxides (RGO) can be obtained through the reduction of graphene oxides, for example, using reducing agent like $NaBH_4$.[158] Compare with graphene, reduced graphene oxides have some defects in the structure and some properties may be influenced, for instance, the sp^3 hybridization may reduce the conductivity but the hydrophilicity may be increased by the hydrophilic groups.[159] For electrochemical exfoliation, Parvez et al. proposed a method conducted in inorganic salts aqueous

solution.[157] The graphite is soaked into the water solution of different inorganic salts, for example, like $(NH_4)_2SO_4$, Na_2SO_4, or K_2SO_4, then the graphite will be exfoliated by the gas (e.g. O_2, SO_2) generated in the electrolysis process of the inorganic salt. It is an easy and cost-effective method to produce multilayer graphene. The activation and post-treatment methods for activated carbons can be also used to graphene to enhance the performance in different applications.[160,161]

Materials	BET surface area (m^2/g)	Electrochemical test conditions	Specific capacitance	Capability rate	Cycle stability	Reference
Vertically oriented graphene nanosheet	1100	25 wt.% KOH aqueous solution/ Symmetric two-electrode system	2.9 F/cm^3 at 120 Hz	Ultra-high capability rate, phase angle -45° is reached at 15000 Hz	---	162
Graphene nanosheet (GNS55)	524	30 wt.% KOH aqueous solution/ three-electrode system	150 F/g at 0.1 A/g	Higher than 90% at 1 A/g	No capacitance losses after 500 cycles at 0.1 A/g	163
Nitrogen doped graphene via thermal treatment	---	0.5 M H_2SO_4 aqueous solution/ Symmetric two-electrode system	286 F/g at 0.2 A/g	189 F/g at 3 A/g (66%)	90.3% retention after 5000 cycles at 1 A/g	164
Sulfur and nitrogen co-doped graphene (m-NSG-5)	1278	1 M LiPF6 in ethylene carbonate/dimethyl carbonate (1:1 by volume)/ Symmetric two-electrode system	146.6 F/g at 0.8 A/g	118.0 F/g at 3.2 A/g (80%)	94.5% retention after 25,000 cycles at 3.2 A/g	165
Nitrogen-doped reduced graphene oxide	1007	1 M tetraethyl ammonium tetra-fluoroborate in acetonitrile /Symmetric two-electrode system	291 F/g at 1 A/g	261 F/g at 50 A/g (90%)	96% retention after 100,000 cycles at 20 A/g	166
Graphene with KOH activation	3100	1-butyl-3-methyl-imidazolium tetrafluoroborate (BMIM BF4) in	165 F/g at 1.4 A/g	166 F/g at 5.7 A/g (no capacitance losses)	97% retention after 10000 cycles at 2.5 A/g	167

		acetonitrile/ Symmetric two-electrode system				

Table 1.3.4 Supercapacitive capacitance of graphene

In terms of graphene, the agglomeration of individual sheet can prevent the theoretical specific surface area and specific capacitance from being reached.[168] Moreover, the cost of producing high-quality graphene remain much higher than that of producing activated carbons. Then, expected high leakage current results in the poor charge storage stability.[169] Although graphene is a promising material for supercapacitor, more researches are required to address the problems mentioned above before the real breakthrough of graphene used for supercapacitor applications.

1.3.5 Activated carbon fiber

Carbon fibers are carbonaceous materials with fibrous shape and a diameter 5-10 μm.[170] The carbon content of carbon fibers is no lower than 92% wt.[171] Carbon fibers are usually used for reinforcing advanced composite materials due to the outstanding tensile properties, good thermal and electrical conductivities, and excellent creep resistance.[172–175] Compared with carbon fibers, the most distinguishing feature of activated carbon fibers is high porosity but lower mechanical strength.[176] The physical and chemical activation methods used for activated carbons can be also used for activated carbon fibers manufacturing.[170,171] Activated carbon fibers can be derived from carbon fibers, for example, PAN-based carbon fibers[177,178] and pitch-based carbon fibers,[179,180] they can be also obtained from natural and synthetic polymer fibers, e.g., phenolic resin-based fiber,[181,182] and lignocellulosic fibers.[183,184] The supercapacitive performance of some activated carbon fibers are shown in the table 1.3.5.

Materials	BET surface area (m^2/g)	Electrochemical test conditions	Specific capacitance	Capability rate	Cycle stability	Reference
Anthracene oil-based pitch activated	1454	6 M KOH aqueous solution/Symmetric two-electrode	142 F/g at 0.2 A/g	53% at 20 A/g	---	185

carbon fiber with CO_2 activation (ACF)		system				
Anthracene oil-based pitch activated carbon fiber with NH_3 activation (N-ACF)	891	6 M KOH aqueous solution/Symmetric two-electrode system	146 F/g at 0.2 A/g	40% at 20 A/g	---	
Coal-based pitch activated carbon fiber with NaOH activation (ASF)	2460	1 M H_2SO_4 aqueous solution / Symmetric two-electrode system	143 F/g at 0.88 mA/ cm^2	63% at 88.50 mA/ cm^2	---	186
Phenolic resin-based activated carbon fiber with KOH activation (ACF-KOH-900)	1893	6 M KOH aqueous solution/Symmetric two-electrode system	214 F/g at 0.05 A/g	90% at 1 A/g	---	187
Activated carbon fibers derived from lignin with KOH activation (K-ACF)	---	6 M KOH aqueous solution/Symmetric two-electrode system	344 F/g at 10 mV/s	80% at 50 mV/s	96% after 5000 cycles at current density 4 A/g	188
Nomex-derived activated carbon fibers with H_3PO_4 and CO_2 activation (NP1-90)	2832	5.25 M sulfuric acid aqueous solution/three-electrode system	175 F/g at 5 mV/s	No obvious specific capacitance decrease is observed at 20 mV/s	---	189
Sisal-Activated Carbon Fibers with KOH activation (SC-750)		6 M KOH aqueous solution/ three-electrode system	415 F/g at 0.5 A/g	83% at 10 A/g	93% after 10000 cycles at current density 10 A/g	190

Table 1.3.5 Supercapacitive performance of activated carbon fibers

The most important advantage of activated carbon fibers is the mechanical flexibility,

this makes them ideal for fabricating of flexible and wearable electronic applications,[191] while the relatively low capacitance of activated carbon fiber and the high cost of production make them not the best candidate for common supercapacitor.[192,193]

1.3.6 Carbons derived from carbides

Carbides are composed of carbon and elements with less electronegativity which can be both metallic and nonmetallic, like aluminum carbide (Al_4C_3), titanium carbide (TiC), tungsten carbide (WC), zirconium carbide (ZrC), vanadium carbide (VC), boron carbide (B4C), silicon carbide (SiC), and so on. Due to the chemical composition of carbides, carbons can be obtained from carbides by removing the non-carbon components. Carbons derived from carbides (CDCs) are usually produced by chlorination of precursors, i.e., selective etching in chlorine gas in the temperature range of 200-1200 °C.[194–197] The porous structures of CDCs can be tuned by using different precursors and chlorination conditions. By tuning the precursors and chlorination temperature, both micro- and mesoporosity can be obtained, and the pore size distribution can be either broad or monodisperse.[194,195,198,199] To further improve the porosities of CDCs, physical and chemical activation methods for other carbonaceous materials can be applied to CDCs as well.[195,200–202] The supercapacitive performance of carbide derived carbons are shown in the table 1.3.6.

Materials	BET surface area (m^2/g)	Electrochemical test conditions	Specific capacitance	Capability rate	Cycle stability	Reference
Boron carbide derived carbons (CDC-1000-9)	1461	6 M KOH aqueous solution/ three-electrode system	172.2 F/g at 2 mV/s	82.3% at 50 mV/s	---	203
Titanium carbide derived carbons	1920	1 M H_2SO_4 aqueous solution / three-electrode system	132 F/g at 0.15 A/g	81.8% at 6 A/g	---	196
Silicon carbide derived carbon		1.5 M tetraethylammonium tetrafluoroborate	80 F/g at 20 mV/s	93.8% at 1 V/s	---	199

		(NEt_4BF_4) in acetonitrile/ Symmetric two-electrode system				
Monolithic carbide-derived carbon films	---	1 M aqueous sulfuric acid and 1 M tetraethylammonium tetrafluoroborate (TEABF4) in acetonitrile	At coating thickness around 2 μm: ~180 F/cm_3 in $TEABF_4$ and ~160 F/cm_3 in 1M H_2SO_4	---	---	204
Graphene/carbide-derived carbon film (GC 9010)	18	6 M KOH aqueous solution/ three-electrode system	At coating thickness 5 μm: ~250 F/g at 2mV/s	At coating thickness 5 μm: 83% at 100 mV/s	94% after 10000 cycles at current density 10 A/g	205
Graphene-like carbide derived carbon (CDC-G-1)	913	1.5 M tetraethylammonium tetrafluoroborate (NEt_4BF_4) in acetonitrile/ Symmetric two-electrode system	80 F/g at 20 mV/s	76% at 3 V/s	---	206
Vanadium carbide derived carbon (VC 800 ℃)	1286	1 M $(C_2H_5)_3CH_3NBF_4$ in acetonitrile/ Symmetric two-electrode system	127 F/g at 2 mA/cm^2	---	---	207
KOH activated carbide-derived carbons (600 ℃-activated)	1723	1.5 M tetraethylammonium tetrafluoroborate (NEt_4BF_4) in acetonitrile/ Symmetric two-electrode system	143 F/g at ~0.4 A/g	---	---	202

Table 1.3.6 Supercapacitive performance of carbide derived carbons

By employing different precursors and chlorination temperatures, the textures and pore structures of CDCs can be tuned. Moreover, corresponding chlorides can be obtained in mass-production of CDCs.[208] More importantly, in the development of CDC research,

Simon and Gogotsi revealed pores with sizes less than 1 nm could enhance the capacitance performance.[209] However, with the development of other supercapacitor materials, CDCs receive less attention in recent years due to low capacitance performance.

1.4 The introduction to porous organic polymers applied for supercapacitors

Due to the high porosity of the POPs, they are attractive to the supercapacitor applications. While the potential of POPs for supercapacitor electrodes materials is not noticed until 2011. In 2011. Kou et al. synthesized Aza-CMPs with ionothermal method and these samples showed much higher specific capacitance than that of the carbon materials at that time.[210] Since then, POPs used for supercapacitor applications began to develop. So far, the supercapacitor electrodes made from POPs and porous carbon derived from POPs already showed good performance confirming their potential for supercapacitor applications.

Aza-CMPs were reported to have ultra-high specific capacitance.[210] In terms of the synthesis of Aza-CMP, 1,2,4,5-benzenetetramine and triquinoyl hydrate are polymerized through ionothermal condensation reaction, then the ring fused Aza-structure can be obtained. The schematic of Aza-CMP synthesis is shown in the figure 1.4.1.

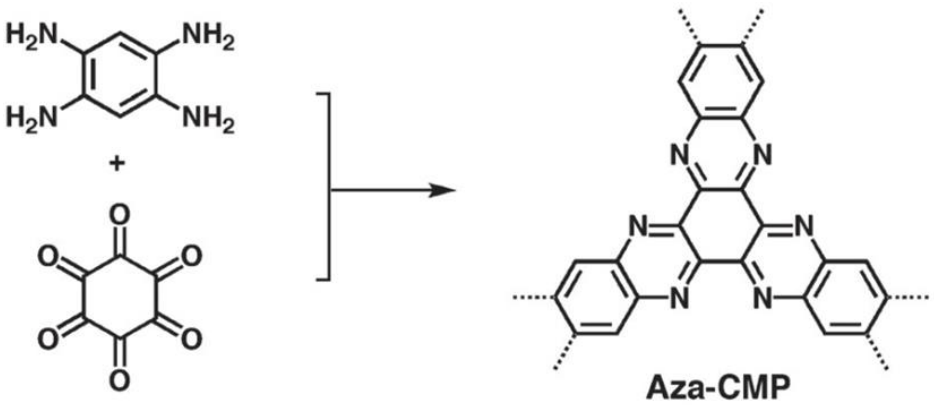

Figure 1.4.1 The scheme of monomers of Aza-CMP and its structure[210]

Aza-CMPs were synthesized under different temperatures which are used for marking these samples. Aza-CMP@300, Aza-CMP@350, Aza-CMP@400, Aza-CMP@450 and Aza-CMP@500 correspond to the synthesis temperature at 300 ℃, 350 ℃, 400 ℃, 450 ℃ and 500 ℃, respectively. The highest BET surface area of Aza-CMPs is 1227 m^2/g (Aza-CMP@500). The electrochemical test was conducted by using GCD method in a three-electrode system with 1 M H_2SO_4 aqueous solution as electrolyte.

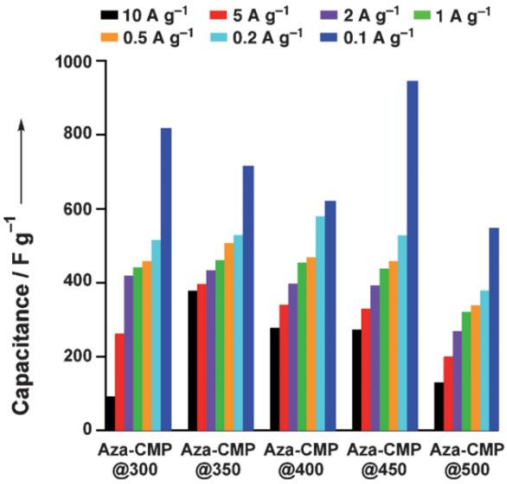

Figure 1.4.2 Specific capacitance of Aza-CMPs at different current densities[210]

It can be seen that Aza-CMP@450 has the highest specific capacitance at a current density of 0.1 A/g, 946 F/g. Aza-CMP@350 has the highest specific capacitance at a current density of 10 A/g, 378 F/g, indicating it has higher capability rate than other samples. The cycle stability of Aza-CMP@350 was performed with GCD method for 10000 times charge/discharge cycling at a current density of 5 A/g. The cycle stability test result is shown in figure 1.4.3.

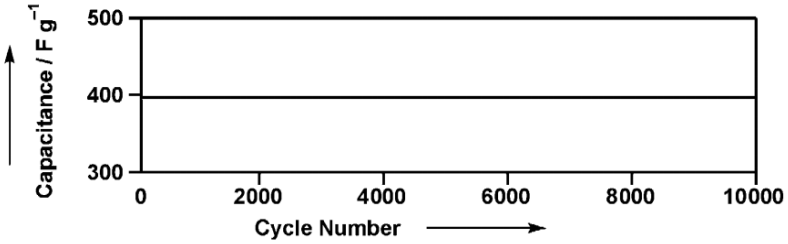

Figure 1.4.3 Cyclability test for Aza-CMP@350 at a current density of 5 A/g[210]

No capacitance losses were observed after 10000 times charge/discharge cycling demonstrates the excellent cycle stability of Aza-CMP@350.

The successful synthesis Aza-CMPs and the successful supercapacitor application of Aza-CMPs are quite important for the research to POPs used for supercapacitor electrodes as more people began to pay attention to these newly-developed polymer materials. The excellent supercapacitive performance of Aza-CMPs illustrate the high potential of POPs used for supercapacitor applications, but the expensive monomer, the complex operation and harsh conditions of ionothermal synthesis restrict the mass production of Aza-CMPs. While the outstanding advantage of POPs is there is always a possibility of synthesizing materials with low cost but good performance by combing an extensive variety of monomers and synthesis methods together.

Chaudhary et al. synthesized nanoporous nitrogen-enriched triazine containing polymer by using inexpensive melamine and cyanuric chloride as monomers.[211] DMSO was used as the solvent for the microwave assisted condensation reaction. The reaction was performed with a microwave power of 400 W and reaction time of 30 min. The obtained product was marked as NENP-1.

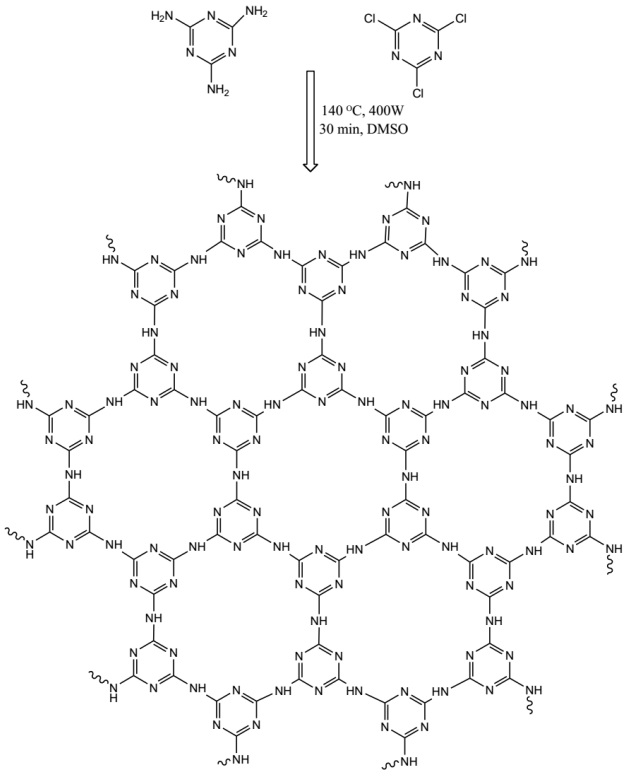

Figure 1.4.4 Schematic of NENP-1 synthesis[211]

The BET surface of NENP-1 is 838 m^2/g. The electrochemical performance of NENP-1 was measured by cyclic voltammetry with a three-electrode system in 0.1 M H_2SO_4 aqueous solution. The specific capacitance of NENP-1 is 1064 F/g at a scanning rate of 5 mV/s and 497 F/g at a scanning rate of 100 mV/s. The capability rate of NENP-1 from 5 mV/s to 100 mV/s is 47%. The cycle stability of NENP-1 was conducted by using GCD with 5000 charge/discharge cycles at a current density of 5 A/g. The specific capacitance retention rate after 5000 cycles at 5 A/g is 87.4%. The low-cost and good supercapacitive capacitance of NENP-1 indicate the POPs are promising to be the supercapacitor electrode materials with a good price-performance ratio. There are also more POPs used as supercapacitor electrodes without any treatment in recent years, the supercapacitive performance of them are shown in the table 1.4.1.

Materials	BET surface area (m^2/g)	Electrochemical test conditions	Specific capacitance	Capability rate	Cycle stability	Reference
Covalent triazine-based framework (TCNQ-CTF-800)	3663	1 M KOH aqueous solution /three-electrode system	383 F/g at 0.2 A/g	---	92% retention after 5000 cycles at 7 A/g	212
		1 M KOH aqueous solution /Symmetric two-electrode system	100 F/g at 0.1 A/g	39 F/g at 10 A/g (39%)		
Triazatruxene-based conjugated microporous polymer (TAT-CMP-2)	106	1 M Na_2SO_4 aqueous solution/three-electrode system	183 F/g at 1 A/g	137 F/g at 10 A/g (75%)	95% retention after 10 000 cycles at 10 A/g	213
Porous Schiff-base-type polymeric network (HPPN-400-30)	2870	1 M H_2SO_4 aqueous solution/ three-electrode system	313 F/g at 0.1 A/g	129 F/g at 10 A/g (41%)	99% retention after 10000 cycles at 10 A/g	214
Conjugated microporous polymer synthesized from Buchwald–Hartwig Coupling (PAQTA)	331	0.5 M H_2SO_4 aqueous solution/ three-electrode system	576 F/g at 1 A/g	410 F/g at 10 A/g (71%)	78% retention after 6000 cycles at 2 A/g	215
Triazine containing	317	2 M KOH aqueous	178 F/g at 0.5	77 F/g at 8	72.5%	216

porous organic polymer (POP_{M-TFP})		solution/ three-electrode system	A/g	A/g (43%)	retention after 4500 cycles at f 0.5 A/g	
β -Ketoenamine-Linked Covalent Organic Framework (DAB-TFP COF)	365	1 M H_2SO_4	14 F/g at 0.1 A/g	6 F/g at 2 A/g (43%)	87% retention after 5000 cycles at 0.1 A/g	217
DAAQ-TFP COF	1280		42 F/g at 0.1 A/g	14 F/g at 2 A/g (30%)	83% retention after 5000 cycles at 0.1 A/g	

Table 1.4.1 Supercapacitor performance of POPs without treatment

For the POPs without treatment, it can be seen that although some materials could have high specific capacitance, the cycle stability cannot meet the requirement of a supercapacitor, for instance, PAQTA and NENP-1. The reason for this is the initial structures of these samples were changed by the redox reactions occurred during the charge/discharge process thus the charge storage ability is reduced, similar to PANI based supercapacitors.[218–220] As some of the POPs have the limitation in electron conductivity,[221] an effective method for turning POPs into good supercapacitor electrode materials is to be produced into porous carbon materials with the same methods for producing activated carbons. The porous carbons derived from POPs also show good supercapacitive performance. In 2013, Liu et al. used the synthesized porous polymer from the condensation of 1,3,5-triformylbenzene and p-phenylenediamine as precursor for porous carbon producing.[222] The sample obtained under 800 ℃ has the best performance. The BET surface area of the final product is 525 m^2/g. The specific capacitance of it is 230 F/g at 0.5 A/g, and it decreased to 190 F/g at 3 A/g, the capability rate is 82.6% from 0.5 to 3 A/g. After 1500 cycles at 3 A/g, the capacitance retention is 93%. This performance is comparable with activated carbons. In 2016, Lee et al. used CMP-1 as precursor for carbonization under 800 ℃.[223] The CMP-1 was carbonized under nitrogen atmosphere and ammonia atmosphere and the carbonization time varied from 2 h to 6 h. The sample N3-CMP-1 has the best performance in specific capacitance

obtained from a three-electrode configuration with 1 M H_2SO_4 aqueous electrolyte, 175.3 F/g at 0.1 A/g and 148.6 F/g at 10 A/g. This sample did not show capacitance losses after 10000 cycles at 5 A/g, indicating good cycling stability. In recent years, there are more researches of porous carbon derived from POPs shown in the table 1.4.2.

Materials	BET surface area (m^2/g)	Electrochemical test conditions	Specific capacitance	Capability rate	Cycle stability	Reference
Porous carbons derived from covalent organic framework without chemical activation (TAPT–DHTA–COF0.1@PPZS900)	456	6 M KOH aqueous solution/three-electrode system	411 F/g at 0.5 A/g	182 F/g at 10 A/g (44%)	No capacitance losses after 10000 cycles at 10 A/g	224
Porous carbons derived from pyrene-based conjugated microporous polymer with KOH activation (SDBPy-800)	1520	6 M KOH aqueous solution/three-electrode system	301 F/g at 1 A/g	214 F/g at 10 A/g (71%)	92.6% retention after 10,000 cycles at 3 A/g	225
Microporous nitrogen-doped carbon synthesized from azine-linked covalent organic framework without chemical activation (carbonized ACOF1)	1596	6 M KOH aqueous solution/three-electrode system	234 F/g at 1 A/g	89% retention at 50 A/g	---	226
Porous carbons derived from hypercrosslinked polymer with KOH activation (CHCPB-K-600)	2739	6 M KOH aqueous solution/three-electrode system	379 F/g at 0.5 A/g	255 F/g at 60 A/g (67%)	91.2% retention after 3000 cycles at 2 A/g	227
Carbon derived from triazine-based porous organic polymer without	801	6 M KOH aqueous solution/three-electrode system	505 F/g at 0.5 A/g	101 F/g at 10 A/g (20%)	89% retention after 10,000 cycles at 3	228

chemical activation (N-MPC)					A/g	
Nitrogen and sulfur co-Doped porous carbon derived from hypercrosslinked pyrrole-thiophene copolymer with KOH activation (N, S-MC)	1339	6 M KOH aqueous solution/three-electrode system	455 F/g at 0.5 A/g	360 F/g at 10 A/g (79%)	92.1% retention after 10000 cycles at 10 A/g	229
Porous heteroatom-doped carbons derived from covalent organic framework with K_2CO_3 activation (ONC-T1-700)	3451	1 M H_2SO_4 aqueous solution/ three-electrode system	768 F/g	439 F/g at 500 A/g (57%)	98.3% retention after 10000 cycles at 10 A/g	230
ONC-T1-850	1518		1711 F/g	856 F/g at 500 A/g (50%)	No capacitance losses after 10000 cycles at 10 A/g	

Table 1.4.2 Supercapacitor performance of carbonized POPs

In the table 1.4.2, it can be seen the supercapacitive performance of these POPs-derived carbons are no worse than activated carbons, some of them have better performance than that of activated carbons which are shown in the previous part. Compared with the POPs without treatments, the cycle stability of the porous carbon materials derived from POPs show higher cycle stability. Similar to biomass derived carbons, the heteroatom doping can be realized by using the synthesized heteroatom containing precursors but not post-treatments. Moreover, as the structures of the precursors have significant influences to the porous structures of the carbons, the various porous structures of POPs originating from different monomers make the porous carbons derived from POPs more promising for supercapacitor. In terms of activated carbons, the low cost of biomass precursors makes activated carbons more competitive than the carbons derived from the POPs, while the high performance of the carbons derived from the POPs (e.g., ONC-T1-850) indicates the possible breakthrough brought by carbons derived from the POPs in the future. To my best knowledge, ONC-T1-850 is the carbon-based material

with the best supercapacitive performance so far. As discussed in previous part, templated carbons, carbon nanotubes, graphene, activated carbon fibers have their own advantages and disadvantages, while the activated carbons remain the overall best candidate for supercapacitor electrodes. With the development of POPs and carbons derived from POPs in the future, the price-performance ratio of carbons derived from the POPs can be increased, just like NENP-1 synthesized from melamine and cyanuric acid, therefore the research to POPs used for supercapacitor should be developed with focusing on both performance enhancing and cost reducing at the same time, for the purpose of being as competitive as activated carbons.

1.5 Thesis aims

To develop new supercapacitor electrode materials, both of the performance and cost of the materials need to be considered. Just like activated carbons derived from biomass precursors, using materials with low cost and investigating the methods for improvements of the supercapacitive performance can be a good idea for developing materials with a high cost-effectiveness. Hypercrosslinked polymers (HCPs) can be synthesized from a variety of inexpensive monomers with the low-cost synthesis method in mild conditions. Moreover, as the porous structures of activated carbons can be influenced by the inherent structures of their precursors, the high specific surface areas and controllable molecular structures of HCPs show promising potentials for being good supercapacitor electrode materials.

As discussed in part 1.2, due to the pore structure of a material is closely related with its supercapacitive performance, tuning the pore structures of HCPs can be used for achieving better supercapacitive performance. An HCP molecular network is formed by monomers and crosslinkers, so using monomers with different sizes and geometries and using different monomer to crosslinker ratios for HCP synthesis can be employed for structure controlling of HCPs. Because heteroatom-doped activated carbons have

shown increased supercapacitive performance, to introduce heteroatoms into HCPs is worth investigating and it can be achieved by using heteroatom containing monomers for HCP synthesis. Similar with the heteroatom-doped activated carbons derived from heteroatom-enriched biomass precursors, the heteroatom containing HCPs can be used as precursors for the heteroatom-doped carbons in the future.

The aims of this research are:

I. To obtain hypercrosslinked polymers with different pore structures and heteroatoms by synthesis.

II. The synthesized hypercrosslinked polymers should be used as precursor of porous carbons for supercapacitor electrode materials.

However, carbonization of the synthesized HCPs cannot be finished due to the pandemic, thus only the electrochemical tests from uncarbonized HCPs are completed.

The specific aims of each individual chapter are:

Chapter 3: To compare the influence of different monomer structures to pore structures and electrochemical performance of the uncarbonized HCPs

Chapter 4: To investigate the influence of different heteroatoms in monomers of same structure to pore structures and electrochemical performance of HCPs

Chapter 5: To explore the influence of different monomer-crosslinker ratios to pore structures and electrochemical performance of HCPs

Due to the large-scale application of supercapacitors, the materials for electrodes should be inexpensive. In chapter 3, the monomers with low cost and different structures, benzene, biphenyl, terphenyl, triphenylmethane, triphenylbenzene, diphenylmethane and fluorene were used for HCP synthesis. In order to explore the influence of heteroatoms, monomers contain nitrogen, sulfur, oxygen and have similar structures with triphenylmethane, diphenylmethane and fluorene were employed. Benzene, biphenyl, terphenyl, TPM, TPB were can be considered as the growth and combination of benzene rings in different ways, therefore, they were used as monomers in chapter 5 to study the influence of differences in monomeric structures and ratios of monomer-

crosslinker.

Reference

1 S. Kesraoui-Ouki, C. R. Cheeseman and R. Perry, *J. Chem. Technol. Biotechnol.*, 1994, **59**, 121–126.

2 J. Wen, H. Dong and G. Zeng, *J. Clean. Prod.*, 2018, **197**, 1435–1446.

3 H. Teng, H. C. Lin and H. Teng, *AIChE J.*, 1998, **44**, 1170–1177.

4 P. Chingombe, B. Saha and R. J. Wakeman, *Carbon N. Y.*, 2005, **43**, 3132–3143.

5 C. S. Diercks and O. M. Yaghi, *Science (80-.).*, 2017, **355**, eaal1585.

6 T. Ben and S. Qiu, *CrystEngComm*, 2013, **15**, 17–26.

7 P. M. Budd, E. S. Elabas, B. S. Ghanem, S. Makhseed, N. B. McKeown, K. J. Msayib, C. E. Tattershall and D. Wang, *Adv. Mater.*, 2004, **16**, 456–459.

8 P. Kuhn, M. Antonietti and A. Thomas, *Angew. Chemie - Int. Ed.*, 2008, **47**, 3450–3453.

9 M. G. Rabbani and H. M. El-Kaderi, *Chem. Mater.*, 2012, **24**, 1511–1517.

10 N. W. Ockwig, A. P. Co, M. O. Keeffe, A. J. Matzger and O. M. Yaghi, 2005, **310**, 1166–1171.

11 E. L. Spitler and W. R. Dichtel, *Nat. Chem.*, 2010, **2**, 672–677.

12 E. L. Spitler, M. R. Giovino, S. L. White and W. R. Dichtel, *Chem. Sci.*, 2011, **2**, 1588–1593.

13 N. Huang, P. Wang and D. Jiang, *Nat. Rev. Mater.*, 2016, **1**, 16068.

14 A. P. Côté, H. M. El-Kaderi, H. Furukawa, J. R. Hunt and O. M. Yaghi, *J. Am. Chem. Soc.*, 2007, **129**, 12914–12915.

15 Y. F. Xie, S. Y. Ding, J. M. Liu, W. Wang and Q. Y. Zheng, *J. Mater. Chem. C*, 2015, **3**, 10066–10069.

16 C. Xiong, H. Ning, G. Jia, X. Hong, X. Fei and J. Donglin, *Chem. Commun.*, 2014, **50**, 6161–6163.

17 S. B. Alahakoon, C. M. Thompson, A. X. Nguyen, G. Occhialini, G. T. McCandless and R. A. Smaldone, *Chem. Commun.*, 2016, **52**, 2843–2845.

18 Y. Wu, H. Xu, X. Chen, J. Gao and D. Jiang, *Chem. Commun.*, 2015, **51**, 10096–10098.

19 S. Kandambeth, D. B. Shinde, M. K. Panda, B. Lukose, T. Heine and R. Banerjee, *Angew. Chemie - Int. Ed.*, 2013, **52**, 13052–13056.

20 S. Wan, J. Guo, J. Kim, H. Ihee and D. Jiang, *Angew. Chemie - Int. Ed.*, 2009, **48**, 5439–5442.

21 S. Kandambeth, K. Dey and R. Banerjee, *J. Am. Chem. Soc.*, 2019, **141**, 1807–1822.

22 J. X. Jiang, F. Su, A. Trewin, C. D. Wood, N. L. Campbell, H. Niu, C. Dickinson, A. Y. Ganin, M. J. Rosseinsky, Y. Z. Khimyak and A. I. Cooper, *Angew. Chemie - Int. Ed.*, 2007, **46**, 8574–8578.

23 A. Laybourn, R. Dawson, R. Clowes, T. Hasell, A. I. Cooper, Y. Z. Khimyak and D. J. Adams, *Polym. Chem.*, 2014, **5**, 6325–6333.

24 Y. Xu, S. Jin, H. Xu, A. Nagai and D. Jiang, *Chem. Soc. Rev.*, 2013, **42**, 8012.

25 G. Cheng, T. Hasell, A. Trewin, D. J. Adams and A. I. Cooper, *Angew. Chemie - Int. Ed.*, 2012, **51**, 12727–12731.

26 Y. Xu, L. Chen, Z. Guo, A. Nagai and D. Jiang, *J. Am. Chem. Soc.*, 2011, 17622–17625.

27 J. X. Jiang, F. Su, A. Trewin, C. D. Wood, H. Niu, J. T. A. Jones, Y. Z. Khimyak and A. I. Cooper, *J. Am. Chem. Soc.*, 2008, **130**, 7710–7720.

28 C. Zheng, M. Du, F. Li, Y. Qi and J. Yi, *Sci. China Chem.*, 2015, **58**, 1227–1234.

29 C. Xu and N. Hedin, *J. Mater. Chem. A*, 2013, **1**, 3406–3414.

30 P. Pandey, A. P. Katsoulidis, I. Eryazici, Y. Wu, M. G. Kanatzidis and S. T. Nguyen, *Chem. Mater.*, 2010, **22**, 4974–4979.

31 S. Yuan, B. Dorney, D. White, S. Kirklin, P. Zapol, L. Yu and D. J. Liu, *Chem. Commun.*, 2010, **46**, 4547–4549.

32 J. X. Jiang, A. Trewin, D. J. Adams and A. I. Cooper, *Chem. Sci.*, 2011, **2**, 1777–1781.

33 L. Chen, Y. Honsho, S. Seki and D. Jiang, *J. Am. Chem. Soc.*, 2010, **132**, 6742–6748.

34 Q. Chen, M. Luo, T. Wang, J. X. Wang, D. Zhou, Y. Han, C. S. Zhang, C. G. Yan and B. H. Han, *Macromolecules*, 2011, **44**, 5573–5577.

35 V. A. Davankov, S. V. Rogoshin and M. P. Tsyurupa, *J Polym Sci Part C, Polym Symp*, 1974, **101**, 95–101.

36 N. Fontanals, J. Cortés, M. Galià, R. M. Marcé, P. A. G. Cormack, F. Borrull and D. C. Sherrington, *J. Polym. Sci. Part A Polym. Chem.*, 2005, **43**, 1718–1728.

37 L. Tan and B. Tan, *Chem. Soc. Rev.*, 2017, **46**, 3322–3356.

38 D. Zhang, L. Tao, J. Ju, Y. Wang, Q. Wang and T. Wang, *Polymer (Guildf).*, 2015, **60**, 234–240.

39 V. A. Davankov and M. P. Tsyurupa, *React. Polym.*, 1990, **13**, 27–42.

40 P. Veverka and K. Jeřábek, *React. Funct. Polym.*, 1999, **41**, 21–25.

41 J. H. Ahn, J. E. Jang, C. G. Oh, S. K. Ihm, J. Cortez and D. C. Sherrington, *Macromolecules*, 2006, **39**, 627–632.

42 B. Li, R. Gong, W. Wang, X. Huang, W. Zhang, H. Li, C. Hu and B. Tan, *Macromolecules*, 2011, **44**, 2410–2414.

43 L. Tan, B. Li, X. Yang, W. Wang and B. Tan, *Polymer (Guildf).*, 2015, **70**, 336–342.

44 Y. Luo, B. Li, W. Wang, K. Wu and B. Tan, *Adv. Mater.*, 2012, **24**, 5703–5707.

45 A. Stephenson, B. Li, L. Chen, R. Clowes, M. E. Briggs and A. I. Cooper, *J. Mater. Chem. A*, 2019, **7**, 25521–25525.

46 D. S. Ahmed, G. A. El-Hiti, E. Yousif, A. A. Ali and A. S. Hameed, *J. Polym. Res.*, 2018, **25**, 1–21.

47 F. Z. Cui, J. J. Xie, S. Y. Jiang, S. X. Gan, D. L. Ma, R. R. Liang, G. F. Jiang and X. Zhao, *Chem. Commun.*, 2019, **55**, 4550–4553.

48 J. Bai, X. Ma, H. Yan, J. Zhu, K. Wang and J. Wang, *Microporous Mesoporous Mater.*, 2020, **306**, 110441.

49 A. Ahmad, Q. Meng, S. Melhi, L. Mao, M. Zhang, B. H. Han, K. Lu and Z. Wei, *Electrochim. Acta*, 2017, **255**, 145–152.

50 Z. Yang, J. Han, R. Jiao, H. Sun, Z. Zhu, W. Liang and A. Li, *J. Colloid Interface Sci.*, 2019, **557**, 664–672.

51 C. Withagen, *Resour. Energy Econ.*, 1994, **16**, 235–242.

52 C. W. Landsea, *Nature*, 2005, **438**, E11–E12.

53 R. A. Kerr, *Science (80-.).*, 2007, **316**, 188–190.

54 O. I. Joensuu, *Science (80-.).*, 1971, **172**, 1027–1028.

55 G. M. Joselin Herbert, S. Iniyan, E. Sreevalsan and S. Rajapandian, *Renew. Sustain. Energy Rev.*, 2007, **11**, 1117–1145.

56 R. Saidur, N. A. Rahim, M. R. Islam and K. H. Solangi, *Renew. Sustain. Energy Rev.*, 2011, **15**, 2423–2430.

57 N. S. Lewis, *Science (80-.).*, 2007, **315**, 798–801.

58 L. Lakatos, G. Hevessy and J. Kovács, *World Futur. J. Gen. Evol.*, 2011, **67**, 395–408.

59 F. O. Rourke, F. Boyle and A. Reynolds, *Appl. Energy*, 2010, **87**, 398–409.

60 M. S. Chowdhury, K. S. Rahman, V. Selvanathan, N. Nuthammachot, M. Suklueng, A. Mostafaeipour, A. Habib, M. Akhtaruzzaman, N. Amin and K. Techato, *Environ. Dev. Sustain.*, 2021, **23**, 8179–8194.

61 J. W. Lund and D. H. Freeston, *Geothermics*, 2001, **30**, 29–68.

62 E. Barbier, *Renew. Sustain. Energy Rev.*, 2002, **6**, 3–65.

63 M. Slattery, J. Dunn and A. Kendall, *Resour. Conserv. Recycl.*, 2021, **174**, 105755.

64 M. D. Slater, D. Kim, E. Lee and C. S. Johnson, *Adv. Funct. Mater.*, 2013, **23**, 947–958.

65 J. Y. Hwang, S. T. Myung and Y. K. Sun, *Chem. Soc. Rev.*, 2017, **46**, 3529–3614.

66 H. Gao, L. Xue, S. Xin and J. B. Goodenough, *Angew. Chemie*, 2018, **130**, 5547–5551.

67 L. Xue, Y. Li, H. Gao, W. Zhou, X. Lü, W. Kaveevivitchai, A. Manthiram and J. B. Goodenough, *J. Am. Chem. Soc.*, 2017, **139**, 2164–2167.

68 A. G. Olabi, T. Wilberforce and M. A. Abdelkareem, *Energy*, 2021, **214**, 118955.

69 A. Ajanovic and R. Haas, *Int. J. Hydrogen Energy*, 2021, **46**, 10049–10058.

70 P. Simon and Y. Gogotsi, *Nat. Mater.*, 2008, **7**, 845–854.

71 H. Helmholtz, *Ann. der Phys. und Chemie*, 1853, **165**, 211–233.

72 M. Gouy, *J. Phys. Théorique Appliquée*, 1910, **9**, 457–468.

73 W. Silvestre-Alcantara, L. B. Bhuiyan, J. Jiang, J. Wu and D. Henderson, *Mol. Phys.*, 2014, **112**, 3144–3151.

74 L. Zhang, X. Hu, Z. Wang, F. Sun and D. G. Dorrell, *Renew. Sustain. Energy Rev.*, 2018, **81**, 1868–1878.

75 H. Du, X. Lin, Z. Xu and D. Chu, *Electric double-layer transistors: a review of recent progress*, Springer US, 2015, vol. 50.

76 J. Huang, B. G. Sumpter and V. Meunier, *Chem. - A Eur. J.*, 2008, **14**, 6614–6626.

77 B. E. Conway and W. G. Pell, *J. Solid State Electrochem.*, 2003, **7**, 637–644.

78 J. Liu, J. Wang, C. Xu, H. Jiang, C. Li, L. Zhang, J. Lin and Z. X. Shen, *Adv. Sci.*, , DOI:10.1002/advs.201700322.

79 C. Bouchelta, M. S. Medjram, O. Bertrand and J. P. Bellat, *J. Anal. Appl. Pyrolysis*, 2008, **82**, 70–77.

80 J. Hayashi, A. Kazehaya, K. Muroyama and A. P. Watkinson, *Carbon N. Y.*, 2000, **38**, 1873–1878.

81 Y. Sudaryanto, S. B. Hartono, W. Irawaty, H. Hindarso and S. Ismadji, *Bioresour. Technol.*, 2006, **97**, 734–739.

82 D. Lozano-Castelló, M. A. Lillo-Ródenas, D. Cazorla-Amorós and A. Linares-Solano, *Carbon N. Y.*, 2001, **39**, 741–749.

83 K. Mohanty, M. Jha, B. C. Meikap and M. N. Biswas, *Chem. Eng. Sci.*, 2005, **60**, 3049–3059.

84 Z. Yue, C. L. Mangun and J. Economy, *Carbon N. Y.*, 2002, **40**, 1181–1191.

85 Z. Yue, J. Economy and C. L. Mangun, *Carbon N. Y.*, 2003, **41**, 1809–1817.

86 S. Ichcho, E. Khouya, S. Fakhi, M. Ezzine, H. Hannache, R. Pallier and R. Naslain, *J. Hazard. Mater.*, 2005, **118**, 45–51.

87 I. A. Rahman, B. Saad, S. Shaidan and E. S. Sya Rizal, *Bioresour. Technol.*, 2005, **96**, 1578–1583.

88 M. A. Lillo-Ródenas, D. Lozano-Castelló, D. Cazorla-Amorós and A. Linares-Solano, *Carbon N. Y.*, 2001, **39**, 751–759.

89 S. Rio, C. Faur-Brasquet, L. Le Coq, P. Courcoux and P. Le Cloirec, *Chemosphere*, 2005, **58**, 423–437.

90 J. Guo and A. C. Lua, *Microporous Mesoporous Mater.*, 1999, **32**, 111–117.
91 T. Otowa, Y. Nojima and T. Miyazaki, *Carbon N. Y.*, 1997, **35**, 1315–1319.
92 C. Moreno-Castilla, *Carbon N. Y.*, 2004, **42**, 83–94.
93 G. Newcombe and M. Drikas, *Carbon N. Y.*, 1997, **35**, 1239–1250.
94 J. S. Noh and J. A. Schwarz, *Carbon N. Y.*, 1990, **28**, 675–682.
95 M. Abe, K. Kawashima, K. Kozawa, H. Sakai and K. Kaneko, *Langmuir*, 2000, **16**, 5059–5063.
96 J. Yang, M. R. Jo, M. Kang, Y. S. Huh, H. Jung and Y. M. Kang, *Carbon N. Y.*, 2014, **73**, 106–113.
97 C. Chen, Y. Duan, T. Huang, M. Zhu, X. Liu and H. Wei, *Energy and Fuels*, 2021, **35**, 9497–9508.
98 Q. Xu, X. Yu, Q. Liang, Y. Bai, Z. H. Huang and F. Kang, *J. Electroanal. Chem.*, 2015, **739**, 84–88.
99 T. X. Shang, X. X. Cai and X. J. Jin, *RSC Adv.*, 2015, **5**, 16433–16438.
100 D. Chen, L. Yang, J. Li and Q. Wu, *ChemistrySelect*, 2019, **4**, 1586–1595.
101 M. Demir, A. A. Farghaly, M. J. Decuir, M. M. Collinson and R. B. Gupta, *Mater. Chem. Phys.*, 2018, **216**, 508–516.
102 Y. Zhang, S. Liu, X. Zheng, X. Wang, Y. Xu, H. Tang, F. Kang, Q. H. Yang and J. Luo, *Adv. Funct. Mater.*, 2017, **27**, 1–8.
103 S. J. Kim, B. C. Bai, M. Il Kim and Y. S. Lee, *Carbon Lett.*, 2020, **30**, 585–591.
104 H. Liu, H. Song, W. Hou, Y. Chang, Y. Zhang, Y. Li, Y. Zhao and G. Han, *Mater. Chem. Phys.*, 2021, **265**, 124491.
105 D. Dong, Y. Zhang, Y. Xiao, T. Wang, J. Wang, C. E. Romero and W. ping Pan, *J. Colloid Interface Sci.*, 2020, **580**, 77–87.
106 Z. Peng, Z. Guo, W. Chu and M. Wei, *RSC Adv.*, 2016, **6**, 42019–42028.
107 J. Hou, K. Jiang, R. Wei, M. Tahir, X. Wu, M. Shen, X. Wang and C. Cao, *ACS Appl. Mater. Interfaces*, 2017, **9**, 30626–30634.
108 C. Long, J. Zhuang, Y. Xiao, M. Zheng, H. Hu, H. Dong, B. Lei, H. Zhang and Y. Liu, *J. Power Sources*, 2016, **310**, 145–153.
109 T. E. Rufford, D. Hulicova-Jurcakova, Z. Zhu and G. Q. Lu, *Electrochem. commun.*, 2008, **10**, 1594–1597.
110 M. Karnan, K. Subramani, P. K. Srividhya and M. Sathish, *Electrochim. Acta*, 2017, **228**, 586–596.
111 J. Li and Q. Wu, *Chem. Phys. Lett.*, 2018, **691**, 238–242.
112 M. Endo, T. Maeda, T. Takeda, Y. J. Kim, K. Koshiba, H. Hara and M. S. Dresselhaus, *J. Electrochem. Soc.*, 2001, **148**, A910.
113 C. Largeot, C. Portet, J. Chmiola, P. L. Taberna, Y. Gogotsi and P. Simon, *J. Am. Chem. Soc.*, 2008, **130**, 2730–2731.
114 H. Nishihara, H. Itoi, T. Kogure, P. X. Hou, H. Touhara, F. Okino and T. Kyotani, *Chem. - A Eur. J.*, 2009, **15**, 5355–5363.
115 J. Liu, H. Li, H. Zhang, Q. Liu, R. Li, B. Li and J. Wang, *J. Solid State Chem.*, 2018, **257**, 64–71.
116 L. L. Zhang and X. S. Zhao, *Chem. Soc. Rev.*, 2009, **38**, 2520.
117 E. Frackowiak, *Phys. Chem. Chem. Phys.*, 2007, **9**, 1774–1785.
118 K. Xia, Q. Gao, J. Jiang and J. Hu, *Carbon N. Y.*, 2008, **46**, 1718–1726.
119 D.-W. Wang, F. Li, M. Liu, G. Q. Lu and H.-M. Cheng, *Angew. Chemie*, 2008, **120**, 379–382.
120 J. Wei, D. Zhou, Z. Sun, Y. Deng, Y. Xia and D. Zhao, *Adv. Funct. Mater.*, 2013, **23**, 2322–2328.
121 S. Lei, Y. Lu, X. Zhang, P. Gao, X. Cui and Y. Yang, *Chem. Commun.*, 2019, **55**, 2305–2308.
122 H. Nishihara, H. Itoi, T. Kogure, P. X. Hou, H. Touhara, F. Okino and T. Kyotani, *Chem. - A Eur. J.*, 2009, **15**, 5355–5363.

123 H. Itoi, H. Nishihara, T. Kogure and T. Kyotani, *J. Am. Chem. Soc.*, 2011, **133**, 1165–1167.
124 Y. Korenblit, M. Rose, E. Kockrick, L. Borchardt, A. Kvit, S. Kaskel and G. Yushin, *ACS Nano*, 2010, **4**, 1337–1344.
125 J. W. Lang, X. Bin Yan, X. Y. Yuan, J. Yang and Q. J. Xue, *J. Power Sources*, 2011, **196**, 10472–10478.
126 J. G. Wang, H. Liu, H. Sun, W. Hua, H. Wang, X. Liu and B. Wei, *Carbon N. Y.*, 2018, **127**, 85–92.
127 M. Sevilla, S. Álvarez, T. A. Centeno, A. B. Fuertes and F. Stoeckli, *Electrochim. Acta*, 2007, **52**, 3207–3215.
128 S. Iijima, *Nature*, 1991, **354**, 56–58.
129 H. Zhang, G. Cao, Z. Wang, Y. Yang, Z. Shi and Z. Gu, *Nano Lett.*, 2008, **8**, 2664–2668.
130 D. N. Futaba, K. Hata, T. Yamada, T. Hiraoka, Y. Hayamizu, Y. Kakudate, O. Tanaike, H. Hatori, M. Yumura and S. Iijima, *Nat. Mater.*, 2006, **5**, 987–994.
131 M. N. Norizan, M. H. Moklis, S. Z. Ngah Demon, N. A. Halim, A. Samsuri, I. S. Mohamad, V. F. Knight and N. Abdullah, *RSC Adv.*, 2020, **10**, 43704–43732.
132 J. Kong, A. M. Cassell and H. Dai, *Chem. Phys. Lett.*, 1998, **292**, 567–574.
133 Z. Shi, Y. Lian, X. Zhou, Z. Gu, Y. Zhang, S. Iijima, L. Zhou, K. T. Yue and S. Zhang, *Carbon N. Y.*, 1999, **37**, 1449–1453.
134 E. Frackowiak, K. Metenier, V. Bertagna and F. Beguin, *Appl. Phys. Lett.*, 2000, **77**, 2421–2423.
135 Y. T. Kim, Y. Ito, K. Tadai, T. Mitani, U. S. Kim, H. S. Kim and B. W. Cho, *Appl. Phys. Lett.*, 2005, **87**, 1–3.
136 J. Y. Lee, K. H. An, J. K. Heo and Y. H. Lee, *J. Phys. Chem. B*, 2003, **107**, 8812–8815.
137 H. Pan, Y. P. Feng and J. Y. Lin, *J. Phys. Condens. Matter*, 2006, **18**, 5175–5184.
138 C. Zhou, S. Kumar, C. D. Doyle and J. M. Tour, *Chem. Mater.*, 2005, **17**, 1997–2002.
139 C. G. Liu, H. T. Fang, F. Li, M. Liu and H. M. Cheng, *J. Power Sources*, 2006, **160**, 758–761.
140 E. Frackowiak, S. Delpeux, K. Jurewicz, K. Szostak, D. Cazorla-Amoros and F. Béguin, *Chem. Phys. Lett.*, 2002, **361**, 35–41.
141 M. Kaempgen, C. K. Chan, J. Ma, Y. Cui and G. Gruner, *Nano Lett.*, 2009, **9**, 1872–1876.
142 W. Yu, H. Zhou, B. Q. Li and S. Ding, *ACS Appl. Mater. Interfaces*, 2017, **9**, 4597–4604.
143 Y. Shang, C. Wang, X. He, J. Li, Q. Peng, E. Shi, R. Wang, S. Du, A. Cao and Y. Li, *Nano Energy*, 2015, **12**, 401–409.
144 B. Xu, F. Wu, Y. Su, G. Cao, S. Chen, Z. Zhou and Y. Yang, *Electrochim. Acta*, 2008, **53**, 7730–7735.
145 Y. T. Kim and T. Mitani, *J. Power Sources*, 2006, **158**, 1517–1522.
146 A. Peigney, C. Laurent, E. Flahaut, R. R. Bacsa and A. Rousset, *Carbon N. Y.*, 2001, **39**, 507–514.
147 J. Li, X. Cheng, A. Shashurin and M. Keidar, *Graphene*, 2012, **01**, 1–13.
148 K. S. Novoselov, *Science (80-.).*, 2004, **306**, 666–669.
149 J. Xia, F. Chen, J. Li and N. Tao, *Nat. Nanotechnol.*, 2009, **4**, 505–509.
150 T. J. Booth, P. Blake, R. R. Nair, D. Jiang, E. W. Hill, U. Bangert, A. Bleloch, M. Gass, K. S. Novoselov, M. I. Katsnelson and A. K. Geim, *Nano Lett.*, 2008, **8**, 2442–2446.
151 A. King, G. Johnson, D. Engelberg, W. Ludwig and J. Marrow, *Science (80-.).*, 2008, **321**, 382–385.
152 G. Ning, Z. Fan, G. Wang, J. Gao, W. Qian and F. Wei, *Chem. Commun.*, 2011, **47**, 5976–5978.
153 S. K. Kandasamy and K. Kandasamy, *J. Inorg. Organomet. Polym. Mater.*, 2018, **28**, 559–584.
154 W. Choi, I. Lahiri, R. Seelaboyina and Y. S. Kang, *Crit. Rev. Solid State Mater. Sci.*, 2010, **35**, 52–71.
155 P. R. Somani, S. P. Somani and M. Umeno, *Chem. Phys. Lett.*, 2006, **430**, 56–59.
156 W. S. Hummers and R. E. Offeman, *J. Am. Chem. Soc.*, 1958, **80**, 1339.
157 K. Parvez, Z. S. Wu, R. Li, X. Liu, R. Graf, X. Feng and K. Müllen, *J. Am. Chem. Soc.*, 2014, **136**, 6083–

6091.
158 W. Gao, L. B. Alemany, L. Ci and P. M. Ajayan, *Nat. Chem.*, 2009, **1**, 403–408.
159 Y. Y. Gao, B. Han, W. Y. Zhao, Z. C. Ma, Y. Sen Yu and H. B. Sun, *Front. Chem.*, 2019, **7**, 1–5.
160 S. Wang, F. Tristan, D. Minami, T. Fujimori, R. Cruz-Silva, M. Terrones, K. Takeuchi, K. Teshima, F. Rodríguez-Reinoso, M. Endo and K. Kaneko, *Carbon N. Y.*, 2014, **76**, 220–231.
161 S. Liu, W. Peng, H. Sun and S. Wang, *Nanoscale*, 2014, **6**, 766–771.
162 J. R. Miller, R. A. Outlaw and B. C. Holloway, *Electrochim. Acta*, 2011, **56**, 10443–10449.
163 X. Du, P. Guo, H. Song and X. Chen, *Electrochim. Acta*, 2010, **55**, 4812–4819.
164 E. Haque, M. M. Islam, E. Pourazadi, M. Hassan, S. N. Faisal, A. K. Roy, K. Konstantinov, A. T. Harris, A. I. Minett and V. G. Gomes, *RSC Adv.*, 2015, **5**, 30679–30686.
165 A. G. Kannan, A. Samuthirapandian and D. W. Kim, *J. Power Sources*, 2017, **337**, 65–72.
166 H. C. Youn, S. M. Bak, M. S. Kim, C. Jaye, D. A. Fischer, C. W. Lee, X. Q. Yang, K. C. Roh and K. B. Kim, *ChemSusChem*, 2015, **8**, 1875–1884.
167 Y. Zhu, S. Murali, M. D. Stoller, K. J. Ganesh, W. Cai, P. J. Ferreira, A. Pirkle, R. M. Wallace, K. A. Cychosz, M. Thommes, D. Su, E. A. Stach and R. S. Ruoff, *Science (80-.).*, 2011, **332**, 1537–1542.
168 Y. Wang, Z. Shi, Y. Huang, Y. Ma, C. Wang, M. Chen and Y. Chen, *J. Phys. Chem. C*, 2009, **113**, 13103–13107.
169 W. Gu and G. Yushin, *Wiley Interdiscip. Rev. Energy Environ.*, 2014, **3**, 424–473.
170 M. F. Hassan, M. A. Sabri, H. Fazal, A. Hafeez, N. Shezad and M. Hussain, *J. Anal. Appl. Pyrolysis*, 2020, **145**, 104715.
171 T. Lee, C. H. Ooi, R. Othman and F. Y. Yeoh, *Rev. Adv. Mater. Sci.*, 2014, **36**, 118–136.
172 W. Qin, F. Vautard, L. T. Drzal and J. Yu, *Compos. Part B Eng.*, 2015, **69**, 335–341.
173 M. Wang, Q. Kang and N. Pan, *Appl. Therm. Eng.*, 2009, **29**, 418–421.
174 C. Unterweger, J. Duchoslav, D. Stifter and C. Fürst, *Compos. Sci. Technol.*, 2015, **108**, 41–47.
175 V. T. Do, H. D. Nguyen-Tran and D. M. Chun, *Compos. Struct.*, 2016, **150**, 240–245.
176 M. C. Yang and D. C. Yu, *J. Appl. Polym. Sci.*, 1998, **68**, 1331–1336.
177 M. A. do Amaral Junior, J. T. Matsushima, M. C. Rezende, E. S. Gonçalves, J. S. Marcuzzo and M. R. Baldan, *J. Aerosp. Technol. Manag.*, 2017, **9**, 423–430.
178 I. Martín-Gullón, R. Andrews, M. Jagtoyen and F. Derbyshire, *Fuel*, 2001, **80**, 969–977.
179 A. Oya, T. Wakahara and S. Yoshida, *Carbon N. Y.*, 1993, **31**, 1243–1247.
180 S. Shin, J. Jang, S. H. Yoon and I. Mochida, *Carbon N. Y.*, 1997, **35**, 1739–1743.
181 A. Oya, S. Yoshida, Y. Abe, T. Iizuka and N. Makiyama, *Carbon N. Y.*, 1993, **31**, 71–73.
182 A. Srivastava, M. Singh, K. Karsauliya, D. P. Mondal, P. Khare, S. Singh and S. Pratap Singh, *Environ. Nanotechnology, Monit. Manag.*, 2020, **14**, 100316.
183 J. S. Macedo, L. Otubo, O. P. Ferreira, I. de F. Gimenez, I. O. Mazali and L. S. Barreto, *Microporous Mesoporous Mater.*, 2008, **107**, 276–285.
184 C. Crestini, M. Crucianelli, M. Orlandi and R. Saladino, *Catal. Today*, 2010, **156**, 8–22.
185 K. Torchała, K. Kierzek, G. Gryglewicz and J. Machnikowski, *Electrochim. Acta*, 2015, **167**, 348–356.
186 N. Diez, P. Díaz, P. Álvarez, Z. González, M. Granda, C. Blanco, R. Santamaría and R. Menéndez, *Mater. Lett.*, 2014, **136**, 214–217.
187 R. Xue, J. Yan, X. Liu, Y. Tian and B. Yi, *J. Appl. Electrochem.*, 2011, **41**, 1357–1366.
188 S. Hu, S. Zhang, N. Pan and Y. Lo Hsieh, *J. Power Sources*, 2014, **270**, 106–112.
189 K. Leitner, A. Lerf, M. Winter, J. O. Besenhard, S. Villar-Rodil, F. Suárez-García, A. Martínez-Alonso and J. M. D. Tascón, *J. Power Sources*, 2006, **153**, 419–423.

190 M. Li, H. Xiao, T. Zhang, Q. Li and Y. Zhao, *ACS Sustain. Chem. Eng.*, 2019, **7**, 4716–4723.
191 Y. Li and C. Chen, *J. Mater. Sci.*, 2017, **52**, 12348–12357.
192 C. Kim, *J. Power Sources*, 2005, **142**, 382–388.
193 B. H. Kim, K. S. Yang, H. G. Woo and K. Oshida, *Synth. Met.*, 2011, **161**, 1211–1216.
194 V. Presser, M. Heon and Y. Gogotsi, *Adv. Funct. Mater.*, 2011, **21**, 810–833.
195 S. Osswald, C. Portet, Y. Gogotsi, G. Laudisio, J. P. Singer, J. E. Fischer, V. V. Sokolov, J. A. Kukushkina and A. E. Kravchik, *J. Solid State Chem.*, 2009, **182**, 1733–1741.
196 C. R. Pérez, S. H. Yeon, J. Ségalini, V. Presser, P. L. Taberna, P. Simon and Y. Gogotsi, *Adv. Funct. Mater.*, 2013, **23**, 1081–1089.
197 A. Jänes, T. Thomberg, H. Kurig and E. Lust, *Carbon N. Y.*, 2009, **47**, 23–29.
198 L. Borchardt, M. Oschatz, M. Lohe, V. Presser, Y. Gogotsi and S. Kaskel, *Carbon N. Y.*, 2012, **50**, 3987–3994.
199 J. Chmiola, C. Largeot, P.-L. Taberna, P. Simon and Y. Gogotsi, *Science (80-.).*, 2010, **328**, 480–483.
200 S. H. Yeon, S. Osswald, Y. Gogotsi, J. P. Singer, J. M. Simmons, J. E. Fischer, M. A. Lillo-Ródenas and Á. Linares-Solano, *J. Power Sources*, 2009, **191**, 560–567.
201 P. Yan, J. Xu, C. Wu, Y. Gu, X. Zhang, R. Zhang and Y. Song, *Electrochim. Acta*, 2016, **189**, 16–21.
202 C. Portet, M. Á. Lillo-Ródenas, A. Linares-Solano and Y. Gogotsi, *Phys. Chem. Chem. Phys.*, 2009, **11**, 4943–4945.
203 H. Wang and Q. Gao, *Carbon N. Y.*, 2009, **47**, 820–828.
204 Y. K. A. Lau, A. V Kvit, A. L. Schmitt, S. Jin, D. J. Chernak, M. J. Bierman, S. Jin, A. R. Harutyunyan, B. I. Yakobson, C. Growth, S. Publishing, N. Cabrera, C. Frank, L. E. Greene, J. C. Johnson, R. Saykally, P. D. Yang, J. H. Song, K. Keis, S. E. Lindquist, A. Hagfeldt, D. S. Boyle, P. B. Kenway, M. Dudley, D. Bliss, M. Callahan, M. Harris, G. M. Fuge, N. A. Fox, D. J. Riley, J. F. Banfield, H. P. Strunk, V. D. Heydemann, G. Pensl, J. D. Eshelby, J. D. Eshelby, C. M. Drum, T. B. Bateman, H. H. Teng, P. M. Dove, J. J. De Yoreo, C. Cottrell, S. Award and D. Young, 2010, **1060**, 480–484.
205 M. Alhabeb, M. Beidaghi, K. L. Van Aken, B. Dyatkin and Y. Gogotsi, *Carbon N. Y.*, 2017, **118**, 642–649.
206 P. C. Gao, W. Y. Tsai, B. Daffos, P. L. Taberna, C. R. Pérez, Y. Gogotsi, P. Simon and F. Favier, *Nano Energy*, 2015, **12**, 197–206.
207 T. Thomberg, A. Jänes and E. Lust, *J. Electroanal. Chem.*, 2009, **630**, 55–62.
208 W. Gu and G. Yushin, *Wiley Interdiscip. Rev. Energy Environ.*, 2014, **3**, 424–473.
209 P. Simon and Y. Gogotsi, in *Nanoscience and Technology*, Co-Published with Macmillan Publishers Ltd, UK, 2009, pp. 320–329.
210 Y. Kou, Y. Xu, Z. Guo and D. Jiang, *Angew. Chemie - Int. Ed.*, 2011, **50**, 8753–8757.
211 M. Chaudhary, A. K. Nayak, R. Muhammad, D. Pradhan and P. Mohanty, *ACS Sustain. Chem. Eng.*, 2018, **6**, 5895–5902.
212 W. Deng, Y. Li, S. Zheng, X. Liu, P. Li, L. Sun, R. Yang, S. Wang, Z. Wu and X. Bao, *Angew. Chemie Int. Ed.*, 2017, 1–6.
213 X.-C. Li, Y. Zhang, C.-Y. Wang, Y. Wan, W.-Y. Lai, H. Pang and W. Huang, *Chem. Sci.*, 2017, **8**, 2959–2965.
214 Y. Zhao, P. Liu, X. Zhuang, D. Wu, F. Zhang and Y. Su, *RSC Adv.*, 2017, **7**, 19934–19939.
215 Y. Liao, H. Wang, M. Zhu and A. Thomas, *Adv. Mater.*, 2018, **30**, 1–10.
216 L. Xu, R. Liu, F. Wang, S. Yan, X. Shi and J. Yang, 2019, 1586–1590.
217 C. R. Deblase, K. E. Silberstein, T. T. Truong, H. D. Abruña and W. R. Dichtel, *J. Am. Chem. Soc.*, 2013,

135, 16821–16824.

218 J. Yan, T. Wei, Z. Fan, W. Qian, M. Zhang, X. Shen and F. Wei, *J. Power Sources*, 2010, **195**, 3041–3045.

219 Q. Wang, J. L. Li, F. Gao, W. S. Li, K. Z. Wu and X. D. Wang, *Xinxing Tan Cailiao/ New Carbon Mater.*, 2008, **23**, 275–280.

220 M. Zhang, A. Nautiyal, H. Du, Z. Wei, X. Zhang and R. Wang, *Electrochim. Acta*, 2021, **376**, 138037.

221 J. S. M. Lee, M. E. Briggs, C. C. Hu and A. I. Cooper, *Nano Energy*, 2018, **46**, 277–289.

222 X. Liu, L. Zhou, Y. Zhao, L. Bian, X. Feng and Q. Pu, *ACS Appl. Mater. Interfaces*, 2013, **5**, 10280–10287.

223 J.-S. M. Lee, T.-H. Wu, B. M. Alston, M. E. Briggs, T. Hasell, C.-C. Hu and A. I. Cooper, *J. Mater. Chem. A*, 2016, **4**, 7665–7673.

224 Q. Xu, Y. Tang, L. Zhai, Q. Chen and D. Jiang, *Chem. Commun.*, 2017, **53**, 11690–11693.

225 Y. Zhao, F. Xie, C. Zhang, R. Kong, S. Feng and J. X. Jiang, *Microporous Mesoporous Mater.*, 2017, **240**, 73–79.

226 G. Kim, J. Yang, N. Nakashima and T. Shiraki, *Chem. - A Eur. J.*, 2017, 1–8.

227 C. Zhang, R. Kong, X. Wang, Y. Xu, F. Wang, W. Ren, Y. Wang, F. Su and J. X. Jiang, *Carbon N. Y.*, 2017, **114**, 608–618.

228 S. Vargheese, R. T. R. Kumar and Y. Haldorai, *Mater. Lett.*, 2019, **249**, 53–56.

229 Y. Lu, J. Liang, S. Deng, Q. He, S. Deng, Y. Hu and D. Wang, *Nano Energy*, 2019, **65**, 103993.

230 D. Yan, Y. Wu, R. Kitaura and K. Awaga, *J. Mater. Chem. A*, 2019, **7**, 26829–26837.

Chapter 2 Methods

2.1 Characterization methods

2.1.1 Nitrogen adsorption and desorption isotherm

Nitrogen adsorption/desorption isotherms were obtained by using a Micromeritics ASAP 2020Plus analyzer with high purity nitrogen at 77 K. The samples with the mass around 0.1 g were degassed at 120 °C under dynamic vacuum for overnight before analysis. The Brunauer-Emmett-Teller (BET) method was employed to calculate the surface areas of the samples and the relative pressure range is 0.01–0.15, as the HCPs discussed in this thesis have micropores. Therefore, the relative pressure range 0.01–0.15 is used to get more accurate results instead of the range of 0.05-0.35 which is commonly used for mesoporous materials. NLDFT (non-local density functional theory) was employed for calculating the differential pore sizes.

2.1.2 Solid state NMR spectroscopy

The 1H-13C cross-polarization magic angle spinning (CP/MAS) NMR was conducted at 125.76 MHz (500.13 MHz 1H) at a MAS rate of 10.0 kHz in a Bruker Avance III HD spectrometer with samples placed into 4 mm zirconia rotors. The 1H $\pi/2$ pulse was 3.4 μs, and two-pulse phase modulation (TPPM) decoupling was used during the acquisition. The Hartmann-Hahn condition was set using hexamethylbenzene. The spectra were measured using a contact time of 2.0 ms. The relaxation delay D1 for each sample was individually determined from the proton T1 measurement (D1 = 5 × T1). Samples were collected until sufficient signal to noise was observed, typically greater than 256 scans. The values of the chemical shifts are referred to that of TMS.

2.1.3 Infrared spectroscopy

Infrared spectra were obtained in a Perkin-Elmer 100 spectrometer with KBr pellet

method. KBr pellets were prepared with mixing approximate 1 mg of the samples with 100 mg pure KBr, then the pellets were holding at high pressure (9 tons) for 1 min. Before using, The KBr was dried in an oven at 100 °C overnight.

2.1.4 Elemental analysis

Elemental analysis was performed in the Elementar Vario MICRO Cube CHN/S analyzer with burning a sample in oxygen atmosphere. Combusted products were passed through a copper tube to remove excess oxygen and reduce NO_x to N_2 before separated with a Thermal Programmed Desorption column and detected by a thermal conductivity detector (TCD).

2.1.5 Thermogravimetric analysis (TGA)

TGA was carried out in Perkin Elmer Pyris 1. Around 5 mg of sample was used for the pyrolysis in nitrogen atmosphere. The temperature increased from 25 °C to 800 °C with the heating rate 10 °C/min.

2.1.6 Electrode preparation

Briefly, 80 wt% HCP sample (8 mg), 10 wt% activate carbon (1 mg), 10 wt% PTFE binder (1 mg, 1.7 μL of 60 wt% PTFE dispersion in water) and around 0.5 mL of acetone were homogenously mixed and grounded into a film-like paste. The paste was rolled onto the surface of nickel foam (2.5 cm x 3 cm) which was wetted with acetone. The electrode was dried under vacuum at 80 °C overnight.

2.1.7 Cyclic Voltammetry (CV)

The cyclic voltammetry was carried out in an AMETEK VersaSTAT 3 with a typical three-electrode system with 1 M Na_2SO_4 aqueous solution as electrolyte. The active material on nickel foam, a platinum electrode and an Ag/AgCl electrode (3 M KCl, 0.207 V vs. standard hydrogen electrode at 25 °C) were used as working electrode,

counter electrode and reference electrode, respectively. The CV tests were conducted with different scan rates 2, 10, 25, 50, 75, 100 and 200 mV/s in the voltage range of -0.2 V-0.8 V.

2.1.8 Electrochemical Impedance Spectroscopy (EIS)

The EIS was conducted in a Solartron 1286 combined with SI 1260 impedance analyzer with a typical three-electrode system with 1 M Na_2SO_4 aqueous solution as electrolyte. The active material on nickel foam, a platinum electrode and an Ag/AgCl electrode (3 M KCl, 0.207 V vs. standard hydrogen electrode at 25 °C) were used as working electrode, counter electrode and reference electrode, respectively. The EIS was performed with amplitude of 10 mV and frequency range 100 k Hz to 0.01 Hz.

2.2 Gas sorption theory

For porous materials, the characterization of porosity is important. So far, the gas adsorption method with high accuracy and convenient operation is commonly used for studying porous structures of materials. Gas adsorption on solid surface can be divided into physisorption and chemisorption. In terms of physisorption, gas molecules interact with solid surface through van der Waals force therefore physisorption is non-selective. For chemisorption, chemical bonds are formed when gas molecules are adsorbed on solid surface. Because of the weak interaction between solid surface and gas molecules of physisorption, the desorption is easier to take place. Thereby, the physisorption of inert gases (e.g., nitrogen, argon, krypton) at low temperatures is commonly used in porosity measurements. The gas adsorption on porous solid surface is shown in the figure 2.1.

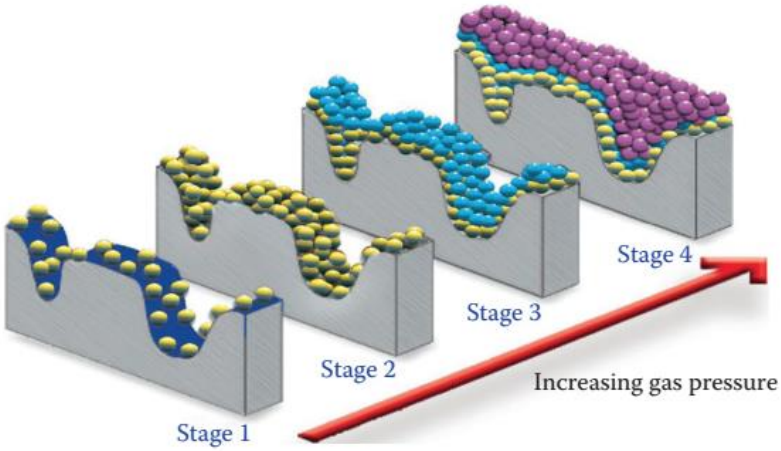

Figure 2.1 Schematic of gas adsorption at different pressures on porous solids, the adsorption state varies with increasing gas pressure[1]

With the increasing pressure, gas adsorption on porous solid can be divided into four stages. At very low pressure, the adsorption starts and the adsorption amount is low. In the second stage, the adsorption amount increases with the increasing pressure, the coverage of the adsorbed molecule monolayer is formed. In the third stage, multilayer adsorption is formed with the further increasing pressure. In stage 4, the pores are saturated at high pressure.

The development of the adsorption theories is significant for the porous structure analysis. In 1916, Irving Langmuir proposed Langmuir adsorption model, revealing the relationship between the adsorption and the pressure at constant temperature. The Langmuir model is built based on the following hypotheses.[2]

1. The surface of the adsorbent is homogeneous, i.e., all adsorption sites are equal in the adsorption probability.

2. There is no interaction between the adsorbed molecules, so the adsorption heat and the adsorption/desorption activation energy are independent with the occupancy fraction of adsorption sites.

3. Each adsorption site could carry only one adsorbed gas molecule, so the adsorption layer is monolayer.

4. The adsorption process and desorption process are simultaneous, so the adsorption equilibrium is dynamic equilibrium, the adsorption rate is equal to the desorption rate

when the equilibrium is reached.

The Langmuir equation can be derived from the adsorption kinetic. Firstly, the adsorption process is shown in the equation 2.2.1.

$$A(g) + B(s) \underset{k_d}{\overset{k_a}{\rightleftharpoons}} A\text{-}B \qquad 2.2.1$$

Where A(g) is the gas molecule, B(s) is the solid surface, and A-B means the adsorption state of the gas molecules on the solid surface. k_a represents rate constant of adsorption and k_d represents rate constant of desorption.

The occupancy fraction of adsorption sites is defined in equation 2.2.2,

$$\theta = \frac{n}{N} = \frac{V}{V_m} \qquad 2.2.2$$

where n is the amount of the occupied adsorption sites on the surface, N is the total amount of the adsorption sites on the surface, V is the equilibrium volume of the adsorbate at the partial pressure P_A of the adsorbate and V_m is the maximum capacity of the adsorbent surface, i.e., the completion of the monolayer adsorption. Therefore, the adsorption rate υ_a and the desorption rate υ_d can be obtained in equation 2.2.3 and 2.2.4.

$$\upsilon_a = k_a P_A(1-\theta) \qquad 2.2.3$$

$$\upsilon_d = k_d \theta \qquad 2.2.4$$

When the equilibrium is reached, $\upsilon_a = \upsilon_d$, equation 2.5 can be obtained

$$k_a P_A(1-\theta) = k_d \theta \qquad 2.2.5$$

Therefore, θ can be rewritten as

$$\theta = \frac{k_a P_A}{k_d + k_a P_A} \qquad 2.2.6$$

The equilibrium constant k_{eq} is defined as the ratio of the rate constant of adsorption k_a to the rate constant of desorption k_d.

$$k_{eq} = \frac{k_a}{k_d} \qquad 2.2.7$$

Then θ can be written as

$$\theta = \frac{k_{eq}P_A}{1+k_{eq}P_A} \qquad 2.2.8$$

According to the definition of the θ (equation 2.2), the equation 2.8 can be written as

$$V = \frac{V_m k_{eq}P_A}{1+k_{eq}P_A} \qquad 2.2.9$$

So, the equation 2.2.10 can be obtained

$$\frac{P_A}{V} = \frac{1}{k_{eq}V_m} + \frac{P_A}{V_m} \qquad 2.2.10$$

In equation 2.2.10, P_A can be replaced with the relative pressure p/p_0, the k_{eq} and the V_m can be obtained from the slope and the interception of the linear curve, therefore, the Langmuir surface area can be obtained.

The Langmuir theory laid the groundwork for gas adsorption, but it can only explain the phenomenon at low relative pressures. In 1938, Stephen Brunauer, Paul Hugh Emmett and Edward Teller proposed their theory (BET theory) based on the Langmuir theory.[3] To improve the Langmuir theory, the BET theory proposes the following hypotheses:

1. The multilayer adsorption can be formed by stacking of the monolayer adsorption, there is no interactions between the adsorbed molecules in the same layer, the molecules only interact with the molecules in the adjoining layers. The Langmuir theory can be applied to the formation each monolayer.

2. The first monolayer on the surface of the adsorbent has higher adsorption heat than other monolayers. The higher monolayers have the same adsorption heat equals to heat of liquefaction of them.

The equation of the BET theory is shown in equation 2.2.11,

$$\frac{p}{V(p_0-p)} = \frac{1}{V_m C} + \frac{C-1}{V_m C}\left(\frac{p}{p_0}\right) \qquad 2.2.11$$

where V is the volume of the adsorbed gas at the adsorption equilibrium, V_m is the volume of the adsorbed gas when monolayer adsorption is completed, p is the partial pressure of the adsorbed gas, p_0 is the saturated vapor pressure of the adsorbed gas. C is the constant related with the heat of the adsorption, shown in equation 2.2.12,

$$C = e^{\frac{E_1-E_L}{RT}} \qquad 2.2.12$$

where E_1 is the adsorption heat of the monolayer adjacent to the surface of the adsorbent

(the first layer) and E_L is the adsorption heat of the second and higher layers, equals to the heat of liquefaction or the heat of vaporization.

At a constant temperature, C and V_m are constants. Plot $\frac{p}{V(p_0-p)}$ vs $(\frac{p}{p_0})$, the slope of the linear curve is $\frac{C-1}{V_m C}$ and the interception is $\frac{1}{V_m C}$. Therefore, C and V_m can be obtained, shown in equation 2.2.13 and 2.2.14,

$$C = 1 + \frac{S}{I} \qquad 2.2.13$$

$$V_m = \frac{1}{S+I} \qquad 2.2.14$$

where S is the slope and I is the interception.

The BET theory is suitable for the relative pressure range of 0.05-0.35. The equation 2.2.15 shows the calculation of the BET surface area,

$$SA_{BET} = \frac{V_m N_A \sigma}{V_{MV} m} \qquad 2.2.15$$

where V_m is the volume of the adsorbed gas when monolayer adsorption is completed at STP, V_{MV} is the molar volume of the adsorbed gas at STP, N_A is Avogadro constant, σ is the adsorption cross section of the adsorbed gas and m is the mass of the adsorbent.

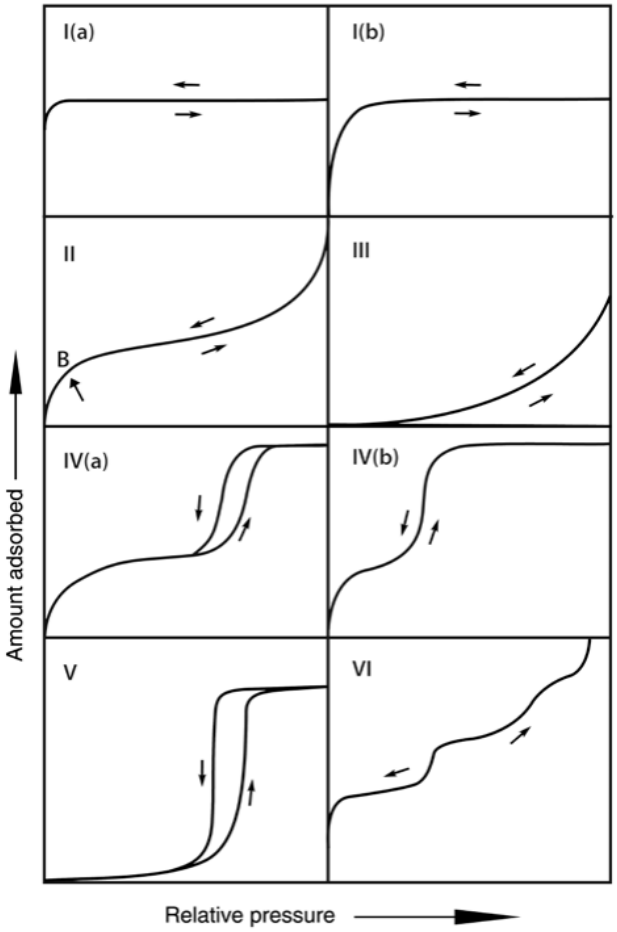

Figure 2.2 IUPAC classification of isotherm curves[4]

According to the IUPAC classification of isotherm in 1985 and the update in 2015,[5,4] the reversible Type I isotherm can be observed in microporous materials with small external surfaces, like some activated carbons, molecular sieve zeolites and porous oxides. The Type I isotherm shows a steep uptake at very low p/p_0 and reaches a maximum value. The steep uptake is due to the micropores could enhance the interaction between the adsorbent and the adsorbate, therefore the micropore can be filled at very low relative pressure. Because of the small external surfaces, the maximum uptake is controlled by the accessible micropore volume. For the nitrogen adsorption at 77 K and the argon adsorption at 87 K, the Type I(a) isotherm can be found in the microporous materials with pore width less than 1 nm while the Type I(b) isotherm can be seen in the materials have wider pore size distribution including micropores and mesopores with narrow pore width less than 2.5 nm.

The reversible Type II isotherm can be seen in the nonporous or macroporous materials

for physisorption of most gases. The shape of the Type II isotherm demonstrates the unrestricted monolayer-multilayer adsorption. The knee point of the Type II isotherm curve, Point B, indicates the completed monolayer adsorption and the beginning of the multilayer adsorption. If Point B is not distinctive, it confirms the existence of the overlap of the monolayer coverage before the beginning of the multilayer adsorption. The Type II isotherm shows the multilayer adsorption without limit at $p/p_0 = 1$.

In the Type III isotherm, due to the weak interaction between the adsorbent and the adsorbate, the adsorbed molecules aggregate around the most favorable sites on the surface of the nonporous or macroporous materials (like N_2 on polyethylene). Therefore, the monolayer adsorption is not identifiable and Point B disappears. Compared with the Type II, the multilayer adsorption at $p/p_0 = 1$ shows no limit as well.

The Type IV isotherms can be seen in mesoporous materials (e.g., mesoporous industrial adsorbent and molecular sieves). It can be found that the initial part of the Type IV isotherm shows monolayer-multilayer adsorption which is the same with the corresponding part in the Type II isotherm. The feature of the Type IV(a) isotherm is the hysteresis loop associated with capillary condensation occurring in mesopores. The hysteresis loop occurs when the pore width is larger than a certain critical width, which is dependent on the system and temperature (e.g., hysteresis loop occurs in the cylindrical pores with pore width larger than 4 nm in the nitrogen adsorption at 77 K and argon adsorption at 87 K). For the materials with smaller mesopore width, the completely reversible Type IV(b) isotherm without hysteresis loop can be obtained. Theoretically, the Type IV(b) isotherm can be also associated with conical and cylindrical meso pores with closed tapered end. The Type IV isotherms have a final saturation plateau with variable length, sometimes the saturation plateau can reduce to a mere inflexion point.

The Type V isotherm shows similarity with the Type III isotherm in the low p/p_0 range due to the weak interaction between the adsorbent and the adsorbate, but it is obtained with porous adsorbent.

The Type VI isotherms represent layer-by-layer adsorption on a highly uniform non-

porous surface, the step-height indicates the adsorption in each layer. The best example of the Type VI isotherm is argon or krypton adsorption on graphitized carbon blacks at low temperature. For example, the Type V isotherm can be observed for water adsorption on hydrophobic microporous or mesoporous adsorbent.

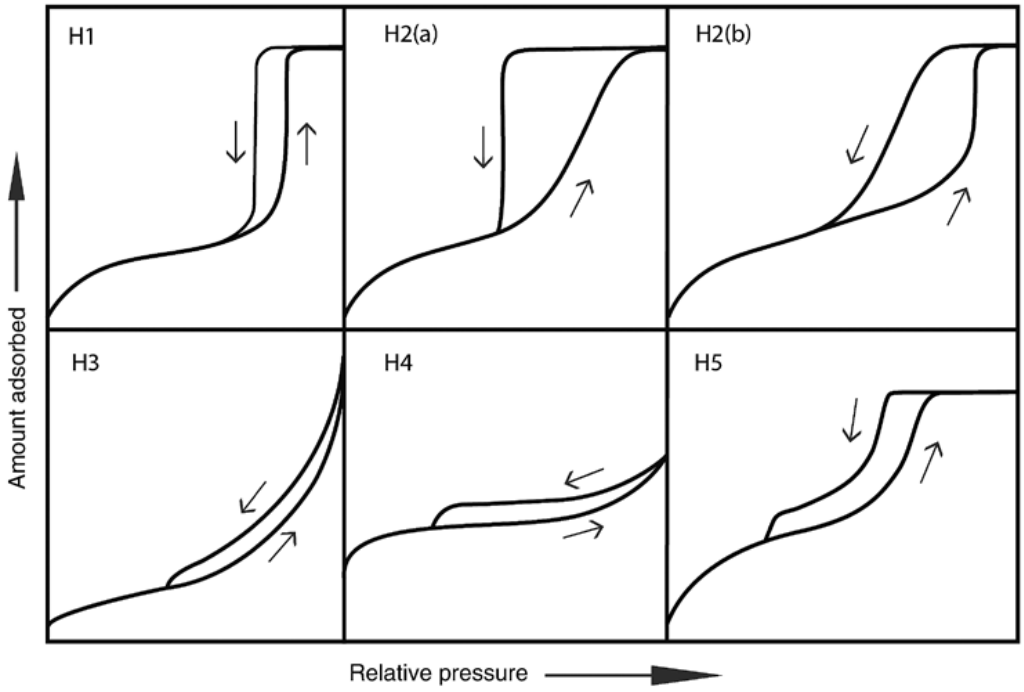

Figure 2.3 IUPAC classification of hysteresis loops[4]

The Type H1 loop can be found in the mesoporous materials with uniform pore size distribution and minimal network effects, like templated silicas, some controlled pore glasses and mesoporous carbons with ordered pore structure. The Type H1 hysteresis loop can be also seen in the materials with ink-bottle pores which have the neck size distribution similar to the width of the pore/cavity size distribution.

The Type H2 hysteresis loop can be seen in more complex pore structures in which network effects are significant. The steep desorption branch which is attributed to pore-blocking/percolation in a narrow range of pore necks or to cavitation-induced evaporation is the characteristic feature of H2(a) loops. The Type H2(a) loop can be found in many silica gels, some porous glasses (e.g., vycor) and some ordered mesoporous materials (like SBA-16 and KIT-5 silicas). The Type H2(b) hysteresis loop

can be also ascribed to pore blocking, but the neck width size distribution is larger. This type of hysteresis loop can be observed with mesocellular silica foams and some mesoporous ordered silicas after hydrothermal treatment.

For the Type H3 hysteresis loop, it takes the same path with the Type II isotherm in the adsorption branch. This type of loops can be given by non-rigid aggregates of plate-like particles (e.g., some clays) and the porous network consist of macropores which are not fully filled with pore condense.

The Type H4 hysteresis loop shows the adsorption branch with the combination of Type I and II isotherms. H4 loop can be often found with aggregated crystal of zeolites, some mesoporous zeolites, and micro-mesoporous carbons.

The Type H5 loop is associated with pore structures containing both open and partially blocked mesopore (e.g., plugged hexagonal templated silicas).

2.3 Electrochemical tests theory

2.3.1 Cyclic voltammetry

Voltametric methods are realized analyzing the relationship between controlled-potential and response current to the applied potential in a certain range. Cyclic voltammetry (CV) is a commonly used voltametric method for studying the charge transfer and mass transfer mechanisms at electrode/electrolyte interface.

The redox reactions at the interface of electrode/electrolyte can be expressed as $Ox + ne^- \leftrightarrow Red$. In a solution with concentration C_{bulk}, if the diffusion is faster, the concentration of the reduction product at the interface equals to concentration of the bulk solution, $[Red] = C_{bulk}$, the response current is controlled by kinetics and can be calculated by equation 2.3.1 [6]

$$i = nFAk_0[Red] \qquad 2.3.1$$

Where n is the number of electrons transferred in the redox reaction, F is the Faraday constant (96485 C/mol), A is the area of the electrode (m^2), k_0 is the rate of the oxidation

reaction.

If the kinetics are faster, the concentration of reduction product at the interface is zero, $[Red]$=0, the current is controlled by diffusion. The calculation of the relationship between current and concentration of reduction product is shown in equation 2.3.2 [6]

$$i = nFAD(\frac{d[Red]}{dx})_{x=0} \qquad 2.3.2$$

Where D (cm^2/s) is the diffusion coefficient.

The mechanism of the reaction occurs at the interface can be judged by CV. If the current is linearly proportional to the square root of scanning rate, the reaction is diffusion-controlled, as shown in Randles−Sevcik equation[7]

$$i_p = 2.69 \times 10^5 n^{\frac{3}{2}} A D^{\frac{1}{2}} C v^{\frac{1}{2}} \qquad 2.3.3$$

Where i_p is peak current, n is the number of moles of electrons transferred per mole of electroactive species, A is the area of the electrode, D is the diffusion coefficient (cm^2/s), C is the concentration (mol/cm^3), and v is scanning rate (V/s).

For supercapacitive performance, CV is a useful method for qualitative and quantitative analysis. For an ideal capacitor, the shape of CV curve is rectangular as shown in figure 2.4, indicating the feature of fast response.

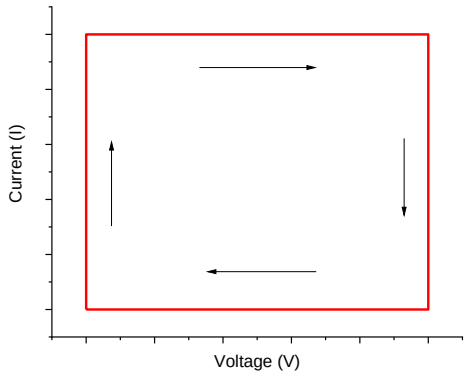

Fig 2.4. CV curve of an ideal capacitor

In reality, supercapacitors CV curves of will always show some deviations from rectangular due to resistance, faradaic reaction etc. Faradaic reaction could lead to

peaks in CV curves while resistance could result in rounded corners.

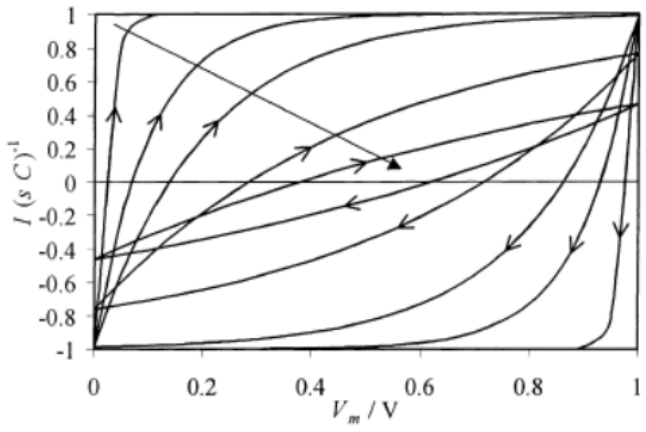

Fig 2.5 Shape deviation of simulated CV curves with increase in internal resistance (1, 5, 10,25, and 50 ohms) at scanning rate 20 mV/s (voltage range 0-1 V, C=1 F) (© Elsevier Limited, reprinted with permission)[8]

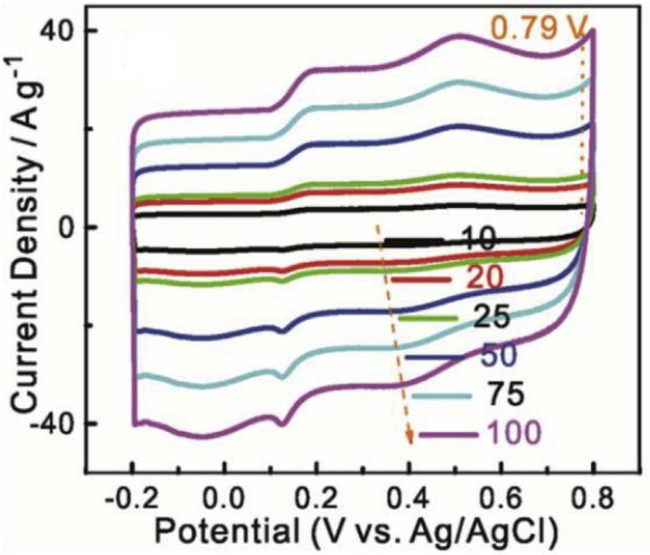

Figure 2.6 CV curves of N-S doped carbon derived from hypercrosslinked polymers at different scanning rates (10-100 mV/s).[9]

CV can be used to calculate specific capacitance in accordance with the equation 2.3.4

$$C = \frac{\int IdV}{2\nu\Delta Vm} \qquad 2.3.4$$

where C is the specific capacitance, $\int IdV$ is the integral area of the CV curve, ν is

the scanning rate, ΔV is the potential window and m corresponds to the mass of the active material.

Capacitance usually decreases with increasing scanning rates. Due to the amount of electrolyte ions penetrating into the electrodes will decrease when scanning rates are higher, that is to say, the surface area of the electrodes will be less utilized at higher scanning rates.

2.3.2 Electrochemical impedance spectroscopy (EIS)

Electrochemical impedance spectroscopy (EIS) is a useful electrochemical method for evaluating the interfacial behavior. For supercapacitors, the properties such as ohmic resistance, charge transfer resistance, diffusion impedance can be investigated by using EIS. Usually, a wide range of frequency like from 100 KHz to 0.01 Hz and a small amplitude of alternative potential varying from 5 ~ 10 mV are applied in EIS.

To analyze the EIS results, Randles model shown in figure 2.6 can be employed as equivalent circuit model of supercapacitors.

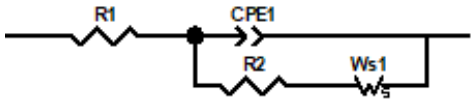

Figure 2.6 Randles circuit model

The Randles model involves four components. R1 is the sum of the resistances of the bulk electrolyte, and the contact resistance involved in the impedance test.[10] R2 is the sum of the charge transfer resistance and the internal resistance of the electrode materials.[11] CPE (constant phase angle element) is a model used to simulate the dispersion effect. Due to the existence of dispersion effect, the capacitance from the electric double layer is not a constant but dependent with the varying frequency. The surface roughness and the current distribution are related with the dispersion effect. CPE is commonly used to replace the capacitor element in equivalent circuit for better fitting results. The W_s is the Warburg element for describing the diffusion in the materials.

The complex capacitance C(ω) obtained from EIS reults is defined by equation 2.3.5. The real part and imaginary of the complex capacitance C'(ω) and C" (ω) is defined by equation 2.3.6 and 2.3.7, respectively.

$$C(\omega) = C'(\omega) - jC''(\omega) \quad 2.3.5$$

$$C'(\omega) = \frac{-Z''(\omega)}{\omega|Z|^2} \quad 2.3.6$$

$$C''(\omega) = \frac{Z'(\omega)}{\omega|Z|^2} \quad 2.3.7$$

Reference

1 Z. Chen and T. Bai, *Coal Prod. Process. Technol.*, 2015, 17–44.

2 I. Langmuir, *J. Am. Chem. Soc.*, 1916, **38**, 2221–2295.

3 S. Brunauer, P. H. Emmett and E. Teller, *J. Am. Chem. Soc.*, 1938, **60**, 309–319.

4 M. Thommes, K. Kaneko, A. V. Neimark, J. P. Olivier, F. Rodriguez-Reinoso, J. Rouquerol and K. S. W. Sing, *Pure Appl. Chem.*, 2015, **87**, 1051–1069.

5 K. S. W. Sing, *Pure Appl. Chem.*, 1985, **57**, 603–619.

6 B. E. Conway, *Electrochemical Supercapacitors*, Springer US, Boston, MA, 1999.

7 J. Wang, *Analytical Electrochemistry*, John Wiley & Sons, Inc., Hoboken, NJ, USA, 2006, vol. 53.

8 W. G. Pell and B. E. Conway, *J. Power Sources*, 2001, **96**, 57–67.

9 Y. Lu, J. Liang, S. Deng, Q. He, S. Deng, Y. Hu and D. Wang, *Nano Energy*, 2019, **65**, 103993.

10 R. Kötz and M. Carlen, *Electrochim. Acta*, 2000, **45**, 2483–2498.

11 Y. Zhou, P. Jin, Y. Zhou and Y. Zhu, *Sci. Rep.*, 2018, **8**, 1–7.

Chapter 3 Hypercrosslinked Polymers Synthesized from Different Monomers for Supercapacitor Applications

3.1 Introduction

Due to the environmental issues caused by the use of fossil fuel, the sustainable and green energy resources had been developed and commercialized, for example, wind energy and solar energy.[1–4] Supercapacitors are storage devices with fast charge/discharge rate and high power density. Due to the features of supercapacitors, they are widely used, for instance, driving heavy machinery,[5] energy recovery of electric vehicles,[6] energy buffer components for wind energy storage system,[7] etc. The energy storage of a supercapacitor is realized by charge accumulation at the interface of electrode/electrolyte. Therefore, the supercapacitor electrode requires materials with large specific surface area to enhance supercapacitive performance. Because of the low-cost and moderate supercapacitive performance, activated carbons have been used as supercapacitor electrode materials for a long time. With the development of porous organic polymers (POPs), more and more researches into POPs used for supercapacitor electrode materials have been reported, for example, covalent organic framework (COF),[8] covalent triazine-based framework (CTF)[9] and conjugated microporous polymer (CMP)[10] all have shown good supercapacitive performance. However, the widespread applications of these materials are limited by some shortcomings, i.e., some synthesis methods require harsh conditions, some synthesis of POPs require expensive monomers and catalysts. Hypercrosslinked polymers (HCPs) are a sub-class of POPs with amorphous porous structures, which are first reported in early 1970s.[11] The conventional synthesis method of HCPs can be summarized as the post-crosslinking of linear polymer chains in solvent. In 2011, Li et al. proposed a new synthesis method called 'knitting method'.[12] In this method, aromatic monomers are knitted together by external crosslinkers based on Friedel-Crafts alkylation. Because of the mild reaction condition and a wide range of low-cost monomers, HCPs synthesized with knitting

method used for supercapacitor are worthy of study. In this chapter, monomers with different structures and geometries are used for HCP synthesis, the porous structures and supercapacitive performance of the HCPs are discussed.

3.2 Experimental

3.2.1 Chemicals

Benzene and Polytetrafluoroethylene preparation 60 wt% in water were purchased from Sigma-Aldrich. Biphenyl and anhydrous sodium sulfate were purchased from Merck. p-Terphenyl and 1,2-dichloroethane were purchased from Acros. Diphenylmethane and 1,3,5-triphenylbenzene were obtained from Aldrich. Fluorene and triphenylmethane were purchased from Fluorochem. Formaldehyde diethyl acetal, anhydrous ferric chloride and carbon black were purchased from Alfa aesar. Methanol (HPLC) and acetone (SLR) were purchased from Fischer Scientific. All chemicals used in this work have purities over 97% and were used as received without further purification.

3.2.2 Synthesis

Synthesis of Benzene HCP

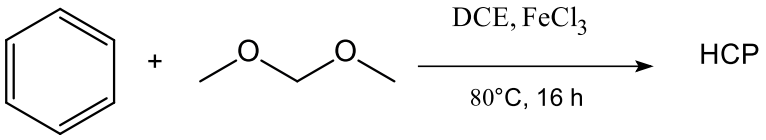

The synthesis of Benzene HCP was performed as follows. Ferric chloride (30 mmol, 4.87 g, 3 eq.) was added into a dried two-neck flask with a magnetic stirrer and a condenser. DCE (25 mL) and benzene (10 mmol, 0.90 mL, 1 eq.) were charged into the flask in sequence by syringes with stirring for 5 minutes to disperse the materials. Then, formaldehyde dimethyl acetal (FDA) (30 mmol, 2.65 mL, 3 eq.) was injected into the flask by syringes and the temperature was increased to 80 °C. The reaction was heated

for 20 hours. The reaction was conducted in atmospheric air. The HCP product was cooled and collected by vacuum filtration and washed with water, methanol, acetone. Then the product was transferred to a Soxhlet extractor and washed with methanol overnight. The product was dried under vacuum at 80 ℃ for overnight. Yield: 96.7%. Formula: C_9H_6. Calculated value of elemental analysis C: 94.70% H: 5.30%. Found value of elemental analysis C: 82.02% H: 5.82%

Synthesis of Biphenyl HCP

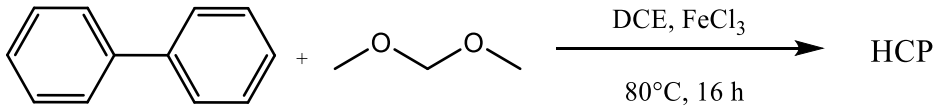

The synthesis of Biphenyl HCP was performed as follows. Biphenyl (5 mmol, 0.771 g, 1 eq.) and ferric chloride (25 mmol, 4.06 g, 5eq.) were added into a dried two-neck flask with a magnetic stirrer and a condenser. DCE (25 mL) was charged into the flask by a syringe with stirring for 5 minutes to disperse the materials. Then, formaldehyde dimethyl acetal (FDA) (25 mmol, 2.21 mL, 5 eq.) was injected into the flask by syringes and the temperature was increased to 80 ℃. The reaction was left for over 20 hours. The reaction was conducted in atmospheric air. The HCP product was cooled and collected by vacuum filtration and washed with water, methanol, acetone. Then the product was transferred to a Soxhlet extractor and washed with methanol overnight. The product was dried under vacuum at 80 ℃ for overnight. Yield: 102.1%. Formula: $C_{16}H_{10}$. Calculated value of elemental analysis C: 95.02% H: 4.98%. Found value of elemental analysis C: 79.81% H: 4.71%

Synthesis of p-Terphenyl (Terphenyl) HCP

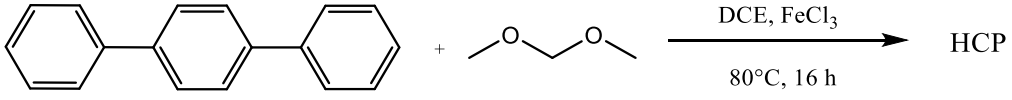

The synthesis of p-Terphenyl HCP was performed as follows. p-Terphenyl (5 mmol, 1.152 g, 1 eq.) and ferric chloride (35 mmol, 5.68 g, 7 eq.) were added into a dried two-neck flask with a magnetic stirrer and a condenser. DCE (25 mL) was charged into the

flask with stirring for 5 minutes to disperse the materials. Then, formaldehyde dimethyl acetal (FDA) (35 mmol, 3.10 mL, 7 eq.) was injected into the flask by syringes and the temperature was increased to 80 ℃. The reaction was left for over 20 hours. The reaction was conducted in atmospheric air. The HCP product was cooled and collected by vacuum filtration and washed with water, methanol, acetone. Then the product was transferred to a Soxhlet extractor and washed with methanol overnight. The product was dried under vacuum at 80 ℃ for overnight. Yield: 100.9%. Formula: $C_{23}H_{14}$. Calculated value of elemental analysis C: 95.14% H: 4.86%. Found value of elemental analysis C: 77.41% H: 4.96%

Diphenylmethane HCP

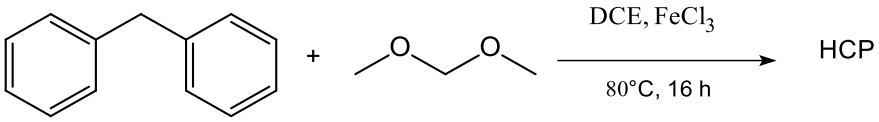

The synthesis of Diphenylmethane HCP was performed as follows. Ferric chloride (25 mmol, 4.06 g, 5 eq.) was added into a dried two-neck flask with a magnetic stirrer and a condenser. DCE (25 mL) and diphenylmethane (5 mmol, 0.84 mL 1 eq.) were charged into the flask in sequence by syringes with stirring for 5 minutes to disperse the materials. Then, formaldehyde dimethyl acetal (FDA) (25 mmol, 2.21 mL 5 eq.) was injected into the flask by syringes and the temperature was increased to 80 ℃. The reaction was heated for 20 hours. The reaction was conducted in atmospheric air. The HCP product was cooled and collected by vacuum filtration and washed with water, methanol, acetone. Then the product was transferred to a Soxhlet extractor and washed with methanol overnight. The product was dried under vacuum at 80 ℃ for overnight. Yield: 108.0%. Formula: $C_{18}H_{12}$. Calculated value of elemental analysis C: 94.70% H: 5.30%. Found value of elemental analysis C: 81.98% H: 5.60%

Fluorene HCP

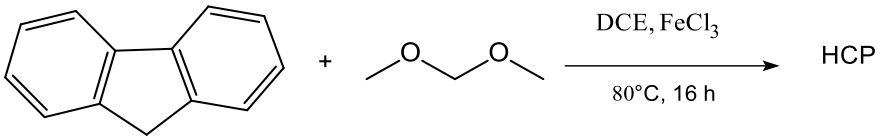

The synthesis of Fluorene HCP was performed as follows. Fluorene (5 mmol, 0.831 g, 1 eq.) and ferric chloride 20 mmol, 3.25 g, 4 eq.) were added into a dried two-neck flask with a magnetic stirrer and a condenser. DCE (25 mL) was charged into the flask by a syringe with stirring for 5 minutes to disperse the materials. Then, formaldehyde dimethyl acetal (FDA) (20 mmol, 1.77 mL 4 eq.) was injected into the flask by syringes and the temperature was increased to 80 ℃. The reaction was left for over 20 hours. The reaction was conducted in atmospheric air. The HCP product was cooled and collected by vacuum filtration and washed with water, methanol, acetone. Then the product was transferred to a Soxhlet extractor and washed with methanol overnight. The product was dried under vacuum at 80 ℃ for overnight. Yield: 109.6%. Formula: $C_{17}H_{10}$. Calculated value of elemental analysis C: 95.30% H: 4.70%. Found value of elemental analysis C: 80.61% H: 5.07%

Synthesis of Triphenylmethane (TPM) HCP

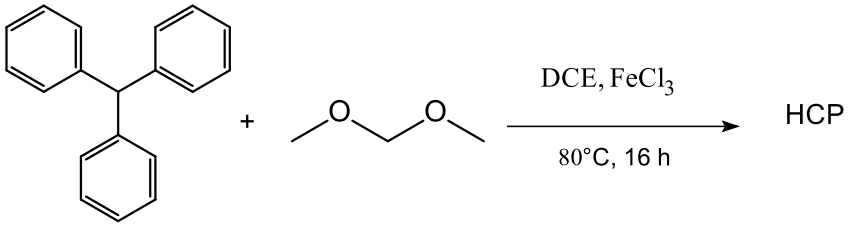

The synthesis of Triphenylmethane (TPM) HCP was performed as follows. Triphenylmethane (5 mmol, 1.22 g, 1 eq.) and ferric chloride (37.5 mmol, 6.08 g, 7.5 eq.) were added into a dried two-neck flask with a magnetic stirrer and a condenser. DCE (25 mL) was charged into the flask by a syringe with stirring for 5 minutes to disperse the materials. Then, formaldehyde dimethyl acetal (FDA) (37.5 mmol, 3.32 mL, 7.5 eq.) was injected into the flask by syringes and the temperature was increased to 80 ℃. The reaction was left for over 20 hours. The reaction was conducted in atmospheric air. The HCP product was cooled and collected by vacuum filtration and

washed with water, methanol, acetone. Then the product was transferred to a Soxhlet extractor and washed with methanol overnight. The product was dried under vacuum at 80 ℃ for overnight. Yield: 104.3%. Formula: $C_{26.5}H_{16}$. Calculated value of elemental analysis C: 95.21% H: 4.79%. Found value of elemental analysis C: 76.37% H: 5.54%

Synthesis of Triphenylbenzene (TPB) HCP

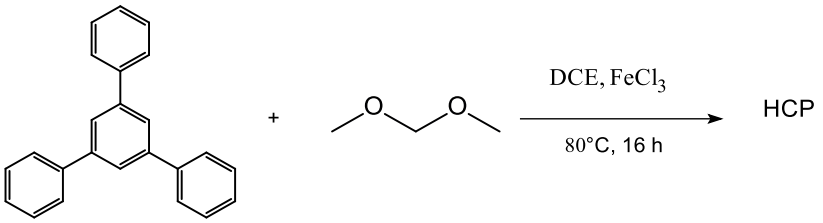

The synthesis of Triphenylbenzene (TPB) HCP was performed as follows. Triphenylbenzene (5 mmol, 1.53 g, 1 eq.) and ferric chloride (37.5 mmol, 6.08 g, 7.5 eq.) were added into a dried two-neck flask with a magnetic stirrer and a condenser. DCE (25 mL) was charged into the flask by a syringe with stirring for 5 minutes to disperse the materials. Then, formaldehyde dimethyl acetal (FDA) (37.5 mmol, 3.32 mL, 7.5 eq.) was injected into the flask by syringes and the temperature was increased to 80 ℃. The reaction was left for over 20 hours. The reaction was conducted in atmospheric air. The HCP product was cooled and collected by vacuum filtration and washed with water, methanol, acetone. Then the product was transferred to a Soxhlet extractor and washed with methanol overnight. The product was dried under vacuum at 80 ℃ for overnight. Yield: 101.7%. Formula: $C_{28.5}H_{18}$. Calculated value of elemental analysis C: 95.00% H: 5.00%. Found value of elemental analysis C: 83.60% H: 4.58%

3.3 Results and discussion

3.3.1 Synthesis

The HCPs were synthesized by Friedel-Crafts alkylation reaction with benzene,

biphenyl, p-terphenyl, diphenylmethane, fluorene, triphenylmethane and triphenylbenzene used as monomers, formaldehyde dimethyl acetal (FDA) used as an external crosslinker and anhydrous $FeCl_3$ used as a Lewis acid catalyst, in air atmosphere and at 80 ℃. Then the Benzene HCP, the Biphenyl HCP, the Terphenyl HCP, the Diphenylmethane HCP, the Fluorene HCP, the TPM HCP and the TPB HCP are obtained. The synthesis of HCPs with knitting method carried out in air atmosphere was reported in the previous literatures,[13,14] The HCPs could be synthesized in air atmosphere demonstrates the possibility for bringing down the cost of the potential mass production of HCPs in the future, for example, dry solvents can be replaced by common solvents for HCP synthesis. The yields and elemental analysis results of the HCPs synthesized from different monomers are performed in the table 3.1.

	Yield		Calculated value		Found value	
			C %	H %	C %	H %
Benzene HCP	96.7%	1.11 g	94.70	5.30	82.02	5.82
Biphenyl HCP	102.1%	1.09 g	95.02	4.98	79.81	4.71
Terphenyl HCP	100.9%	1.59 g	95.14	4.86	77.41	4.96
Diphenylmethane HCP	108.0%	1.34 g	94.70	5.30	81.98	5.60
Fluorene HCP	109.6%	1.17 g	94.70	5.30	80.61	5.07
TPM HCP	104.3%	1.74 g	95.21	4.79	76.37	5.54
TPB HCP	101.7%	2.02 g	95.00	5.00	83.60	4.58

Table 3.1 Yield and elemental analysis results of the HCPs

From the table 3.1, it can be seen that most of the HCPs have the yield higher than 100%, the Benzene HCP also has a yield close to 100%. The reason for the yields of these samples higher than 100% can be attributed to the incompletely reacted crosslinker residue, like -O-CH_3.[15] Due to existence of the extra oxygen atoms in the HCP networks, the yield can be higher than 100%. The incompletely reacted crosslinker residue also influence upon the elemental analysis results, the found values of the elemental analysis are lower than the calculated values, indicating the existence of the

crosslinker residues. In the synthesis of the HCPs, the crosslinker could react with the monomer rapidly to generate porous solid product, then steric hindrance was enhanced. The crosslinkers cannot react at both ends due to the steric hindrance and the crosslinker residues are formed. Some monomers and crosslinker cannot form large HCP particles because of the increased steric hindrance, as these small particles cannot be collected by filtration, some HCP samples will have a lower yield, like the Benzene HCP.

3.3.2 FTIR and ^{13}C Solid State NMR spectroscopy

The molecular structures of the HCPs synthesized from different monomers were analyzed and confirmed by using Fourier transform infrared (FTIR) and ^{13}C solid state NMR.

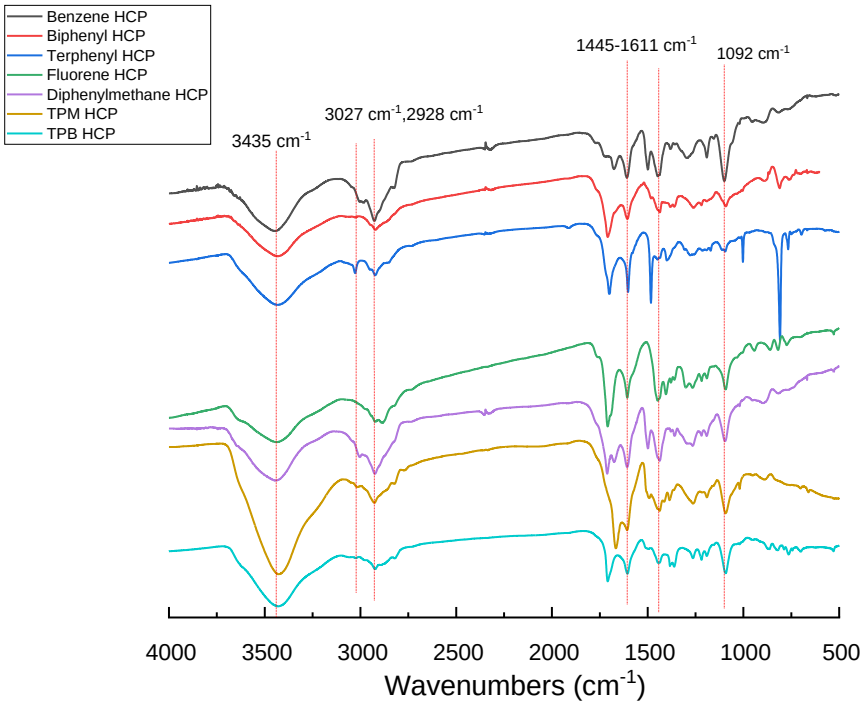

Figure 3.1 FTIR spectra of HCPs synthesized from different monomers

In the FTIR spectra the HCPs synthesized from different monomers, the peak at 2928 cm^{-1} can be assigned to C-H stretching in methylene bridges, and the weak peak at around 3027 cm^{-1} can be ascribed to C-H stretching in aromatic rings.[16–19] The peaks at 1445-1611 cm^{-1} correspond to the vibration of aromatic ring skeleton.[20–23] The peak at

1092 cm^{-1} is assigned to C-O stretching in crosslinker residue.[24] The peak at 3435 cm^{-1} can be attributed to the O-H stretching in physisorbed water which existed in the KBr disc and the porous structure of the HCPs.[25–28] For the molecule structures of HCPs synthesized from different monomers, the aromatic moieties, the methylene bridges, and the crosslinker residues had been confirmed by the FTIR spectra, therefore, the structures of these HCPs are consistent with the expected structure and the results of the previous literatures.

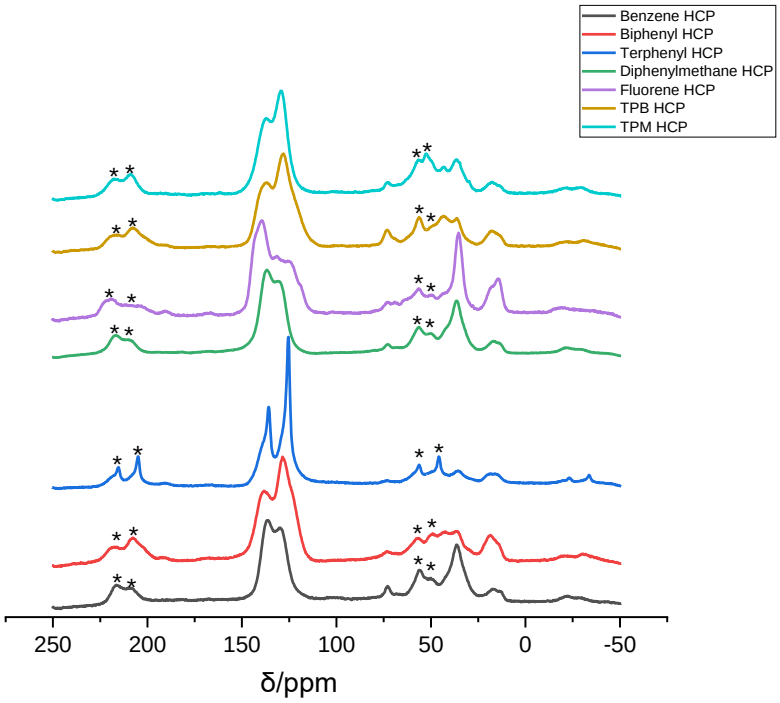

Figure 3.2 ^{13}C solid state NMR spectra of HCPs synthesized from different monomers (the asterisks denote spinning side bands)

In the ^{13}C NMR spectra of HCPs synthesized from different monomers, the peaks at around 137 ppm and 128 ppm can be assigned to the substituted aromatic carbon and the non-substituted aromatic carbon, respectively.[29–32] The peak at around 36 ppm is attributed to the carbon in methylene bridges.[33–36] For Biphenyl HCP, TPB HCP and TPM HCP, the peak at 42 ppm is due to the different substitution positions of methylene bridges.[37,38] The Fluorene showed a broader peak at 128 ppm due to the unsubstituted carbons in meta and ortho positions of fused ring in the fluorene molecule, the peaks of the aromatic carbons in the five-numbered fused ring overlapped with the peaks of the

substituted aromatic carbon at 137 ppm, while the peak of the -CH_2- in the five-numbered fused ring overlapped with the peak of the carbon in methylene bridges at 36 ppm.[39,40] The peak at 73 ppm and 18 ppm can be ascribed to carbon in the methylene group binding to oxygen atom of crosslinker residue and the methyl carbon at the end of crosslinker residue.[41] For the Biphenyl HCP, Terphenyl HCP, TPB HCP and TPM HCP, the relative intensity of the peak corresponds to the substituted aromatic is lower than that of the peak assigned to the unsubstituted aromatic carbon, indicating the unsubstituted aromatic carbon atoms are more than the substituted ones. This result agrees with the yield and elemental analysis results, i.e., the crosslinkers cannot fully reacted with the monomers due to the intense steric impediment arising from the formation of rigid HCP networks. The aromatic moieties, methylene bridges and the crosslinker residues had been confirmed by the ^{13}C solid state NMR spectra, corresponding to the results from the FTIR spectra. Therefore, the structures of these HCPs are consistent with the expected structure and the results of the previous literatures.

3.3.3 TGA

The thermal stability of the HCPs synthesized from different monomers was characterized by using thermalgravimetric analysis (TGA). The TGA was conducted

under a N_2 atmosphere and the samples were heated from 25 °C to 800 with a heating rate 10 °C/min.

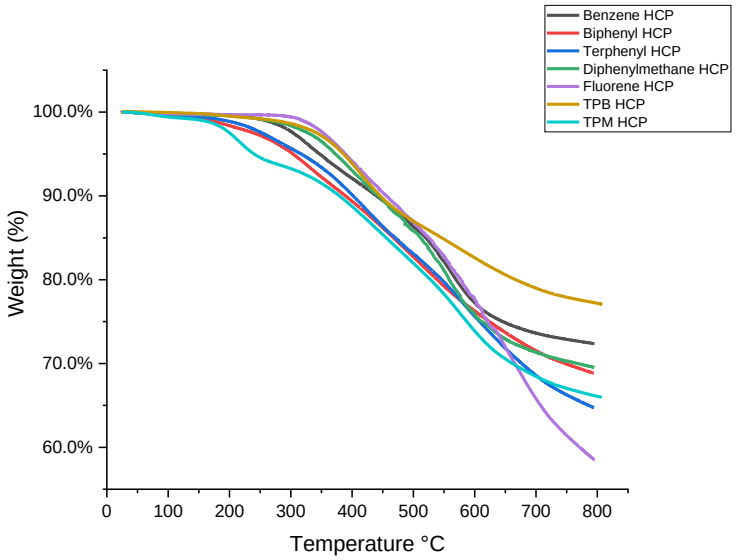

Fig 3.3 TGA spectra of HCPs synthesized from different monomers

From the TGA curves of the HCP samples, it can be seen that the weight residue of all samples is higher than 90% at 350 °C. The weight residue at 800 °C of Fluorene HCP is 55% while the weight residue of other samples is higher than 65% at this temperature.

3.3.4 N_2 Sorption

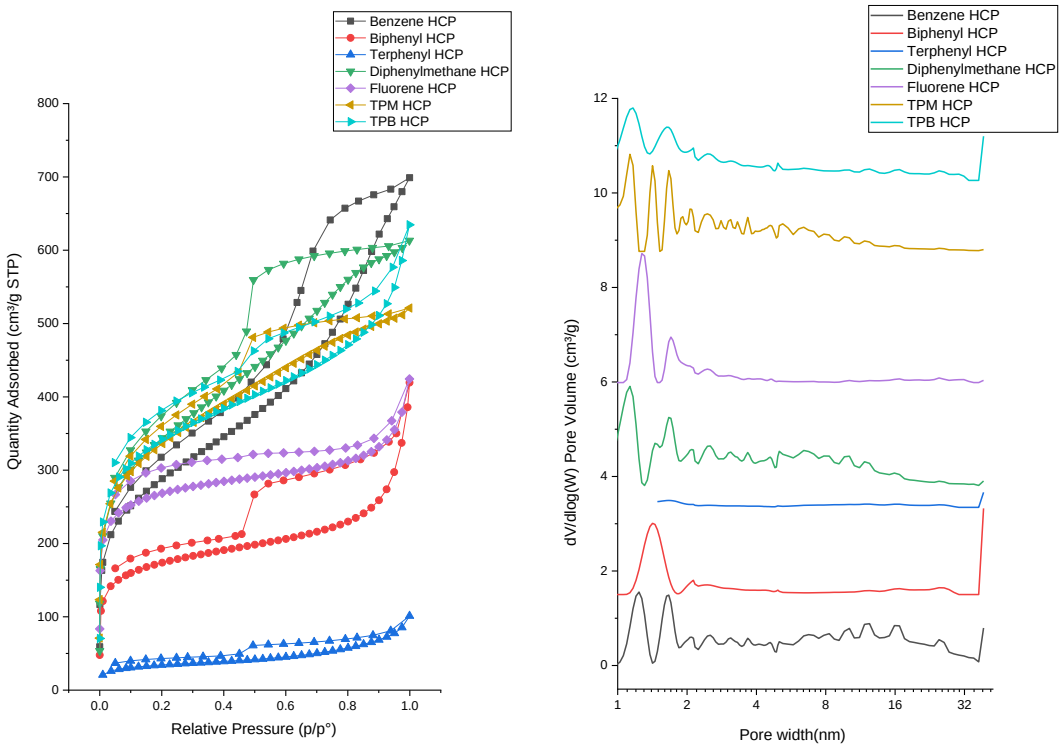

Figure 3.4 Isotherm and pore size distribution of HCPs synthesized from different monomers

The porosity of the HCPs synthesized from different monomers was characterized by N_2 sorption analysis at 77 K. In the figure 3.4, according to IUPAC definition, most of the HCPs showed the combined Type II and Type IV isotherm consisting of the rise at low relative pressure (P/P_0 <0.01) indicating the existence of microporous structure,[42,43] the hysteresis loop in the relative pressure range of 0.43-1.0 suggesting the existence of mesopores,[44] and the gradual rise in the relative pressure range of 0.9-1.0 demonstrating the existence of macropores.[45]

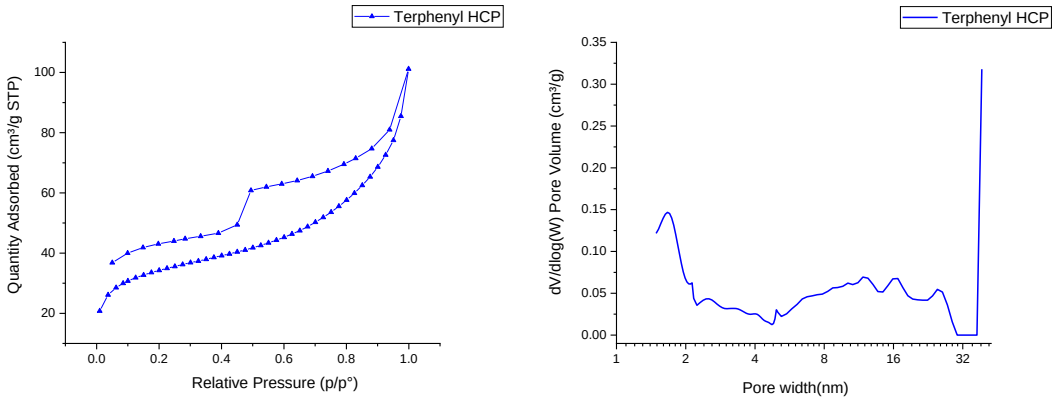

Figure 3.5 Isotherm and pore size distribution of the Terphenyl HCP

As the Terphenyl HCP has lower amount of N_2 adsorption, the isotherm and pore size distribution of it were shown separately in Figure 3.5. For the Terphenyl HCP, the weak rise in the N_2 uptake in the low relative pressure range $P/P_0<0.01$ can be seen, suggesting the low micropore volume proportion in the Terphenyl HCP. In the isotherm of the Fluorene HCP, the hysteresis loop is hard to be observed, indicating the low volume proportion of the mesopores in the Fluorene HCP.

In the pore size distribution curves of the HCPs synthesized from different monomers, it can be seen that the main peaks of each sample locate in the range of 1-2 nm. The pore size distribution can be also seen in the range of 2-32 nm. For the Fluorene HCP, the relative intensity of the pore size distribution in 2-32 nm is weaker than that of other sample, indicating the mesopore volume proportion in the Fluorene HCP is lower than that of other samples. This corresponds to the almost disappeared hysteresis loop in the isotherm curve of the Fluorene HCP. The BET surface area and total pore volume obtained at $p/p_0=0.99$ of the HCPs synthesized from different monomers are listed in the table 3.2

	BET surface area (m^2/g)	Single point adsorption total pore volume (cm^3/g) at p/p_0=0.99
Benzene HCP	1040.4	1.08
Biphenyl HCP	639.1	0.65
Terphenyl HCP	127.1	0.16
Diphenylmethane HCP	1240.8	0.95
Fluorene HCP	1003.9	0.66
TPM HCP	1219.1	0.81
TPB HCP	1255.6	0.98

Table 3.2 BET surface area and total pore volume of the HCPs synthesized from different monomers

The BET surface areas of the Benzene HCP, Biphenyl HCP, Terphenyl HCP, Diphenylmethane HCP, Fluorene HCP, TPM HCP and TPB HCP are 1040.4, 639.1, 127.1, 1240.8, 1003.9, 1219.1 and 1255.6 m^2/g, and the single point adsorption total pore volumes of them are 1.08, 0.65, 0.16, 0.95, 0.66, 0.81 and 0.98 cm^3/g, respectively. For benzene, biphenyl and terphenyl, with the increasing monomer sizes, the decreasing trend can be found in the BET surface areas and pore volumes of the Benzene HCP, Biphenyl HCP and Terphenyl HCP. From the Benzene HCP to Terphenyl HCP, the BET surface areas of them decreased from 1040.4 m^2/g to 127.1 m^2/g. It can be seen that the Terphenyl HCP has the lowest BET surface area among all the samples. Except for the Terphenyl HCP and Biphenyl HCP, all the samples have a BET surface area higher than 1000 m^2/g. The Benzene HCP has the highest total pore volume of 1.08 cm^3/g, while the Terphenyl HCP has the lowest total pore volume of 0.16 cm^3/g. The TPB HCP and Diphenylmethane HCP also have relatively higher total pore volumes, 0.98 cm^3/g and 0.95 cm^3/g, respectively.

To gain further insight into the pore volume of these samples, the pore volume of the pores with different pore widths are shown in the table 3.3 and the pore volume proportions of the HCPs synthesized from different monomers are shown in the figure 3.6. The pore volumes of the pores with pore widths less than 2 nm are obtained at

relative pressure p/p_0=0.2 and the pore volumes of the pores with pore widths less than 10 nm are obtained at p/p_0=0.8.

Material	Pore volume of the pores with pore width less than 2 nm (cm^3/g)	Pore volume of the pores with pore width 2-10 nm (cm^3/g)	Pore volume of the pores with pore width larger than 10 nm (cm^3/g)
Benzene HCP	0.44	0.37	0.27
Biphenyl HCP	0.27	0.09	0.29
Terphenyl HCP	0.05	0.04	0.07
Diphenylmethane HCP	0.53	0.34	0.08
Fluorene HCP	0.42	0.07	0.17
TPM HCP	0.52	0.23	0.06
TPB HCP	0.53	0.20	0.25

Table 3.3 The pore volumes of the pores with different pore widths of the HCPs synthesized from different monomers

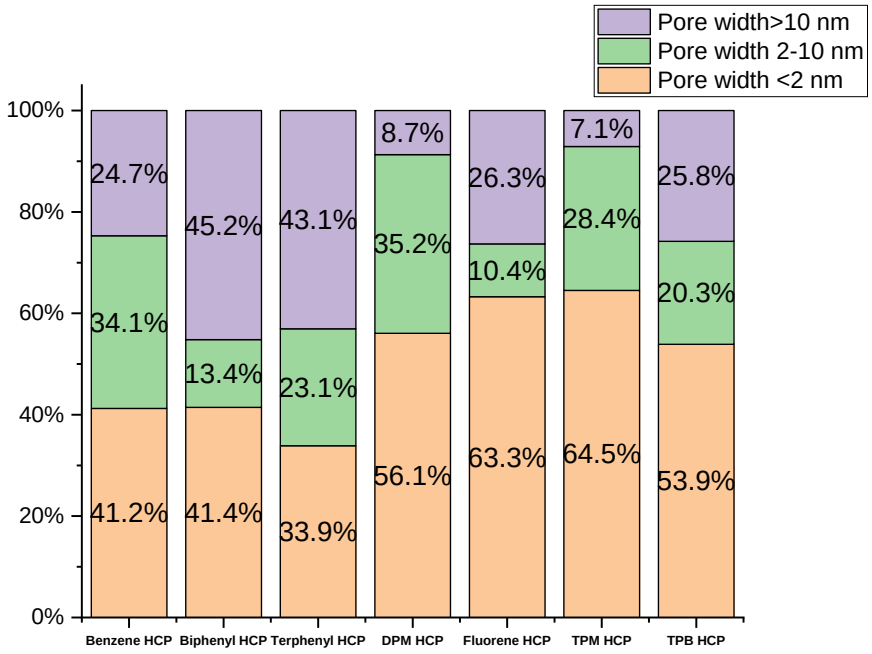

Figure 3.6 Pore volume proportions of the HCPs synthesized from different monomers

From the pore volume proportions of the HCPs synthesized from different monomers, it can be seen that the micropore volume proportions of the Benzene HCP, Biphenyl HCP, Terphenyl HCP, Diphenylmethane HCP, Fluorene HCP, TPM HCP and TPB HCP are 41.2%, 41.4%, 33.9%, 56.1%, 63.3%, 64.5% and 53.9%, the micropore volumes of them are 0.44, 0.27, 0.05, 0.53, 0.42, 0.52 and 0.53 cm^3/g, respectively. It can be found that the TPM HCP has the highest micropore volume proportion and the Fluorene HCP has a similar micropore volume proportion with the TPM HCP. The TPB HCP and Diphenylmethane (DPM) HCP have the highest micropore volume followed by the TPM HCP. For the Benzene HCP, Biphenyl HCP and Terphenyl HCP, the micropore volume of them also showed a decreasing trend with the increasing monomer size. It can be seen that the Terphenyl HCP has the lowest micropore volume proportion and the lowest micropore volume among all the samples, corresponding to the weak N_2 uptake of the Terphenyl HCP at low relative pressure P/P_0 <0.01. The pore volume proportions of the pores with pore diameter 2-10 nm of the Benzene HCP, Biphenyl HCP, Terphenyl HCP, Diphenylmethane HCP, Fluorene HCP, TPM HCP and TPB HCP are 34.1%, 13.4%, 23.1%, 35.2%, 10.4%, 28.4% and 20.3%, the pore volumes of the pores with pore diameter 2-10 nm of these samples are 0.37, 0.09, 0.04, 0.34, 0.07, 0.23 and 0.20, respectively. It can be seen that the Fluorene HCP has the lowest volume proportion of the pores with pore diameter 2-10 nm, corresponding to the almost disappeared hysteresis loop in the isotherm curve of the Fluorene HCP. For the Benzene HCP, Biphenyl HCP and Terphenyl HCP, the decreasing trend can be also seen in the pore volume of the pores with pore diameter 2-10 nm. For the pores with pore width larger than 10 nm, the pore volume proportion of the Benzene HCP, Biphenyl HCP, Terphenyl HCP, Diphenylmethane HCP, Fluorene HCP, TPM HCP and TPB HCP is 24.7%, 45.2%, 43.1%, 8.7%, 26.3%, 7.1% and 25.8%, the pore volume of the pore width larger than 10 nm of these samples is 0.27, 0.29, 0.07, 0.08, 0.17, 0.06 and 0.25 cm^3/g, respectively. The Biphenyl HCP and Terphenyl HCP has much higher pore volume proportion of the pore width larger than 10 nm than other HCPs, while the Diphenylmethane HCP and TPB HCP have a much lower volume proportion of the

pores with pore width larger than 10 nm.

3.3.5 Cyclic Voltammetry

The electrochemical properties of the HCPs were evaluated by a typical three-electrode system with 1 M Na_2SO_4 aqueous solution as electrolyte. The active material on nickel foam, a platinum electrode and an Ag/AgCl (3 M KCl, 0.207 V vs. standard hydrogen electrode at 25 °C) electrode were used as working electrode, counter electrode and reference electrode, respectively. The CV tests were conducted with different scan rates 2, 10, 25, 50, 75, 100 and 200 mV/s in the voltage range of -0.2 V-0.8 V.

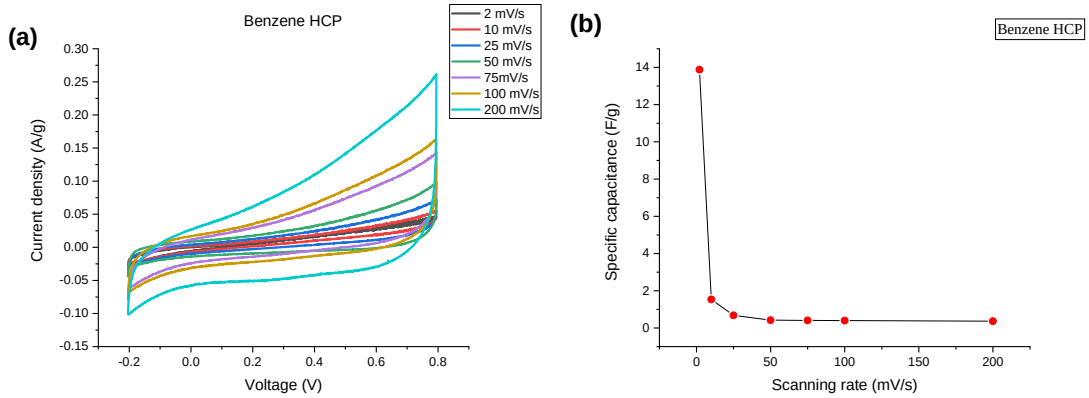

Figure 3.7 (a) CV curves at different scanning rate, and (b) Specific capacitance obtained at different scanning rates of the Benzene HCP

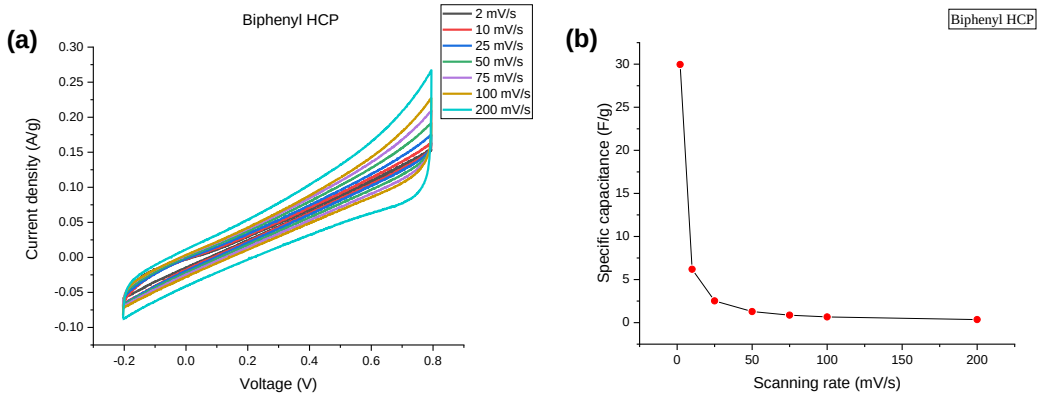

Figure 3.8 (a) CV curves at different scanning rate, and (b) Specific capacitance obtained at different scanning rates of the Biphenyl HCP

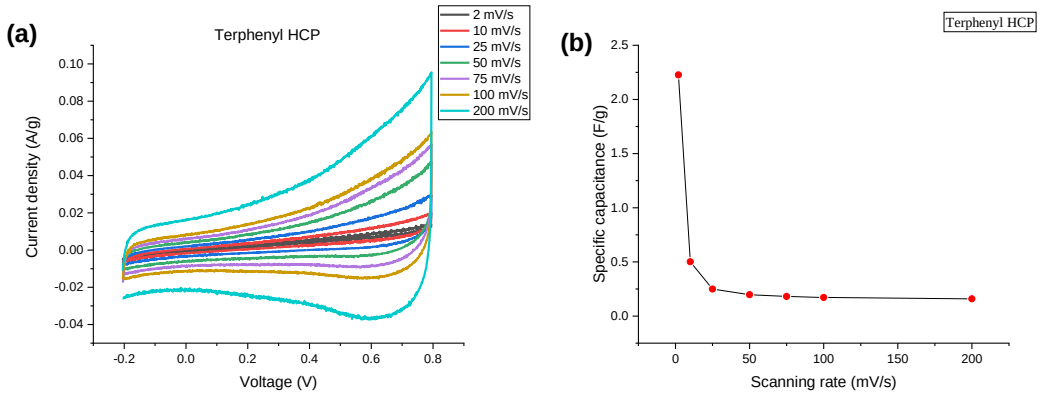

Figure 3.9 (a) CV curves at different scanning rate, and (b) Specific capacitance obtained at different scanning rates of the Terphenyl HCP

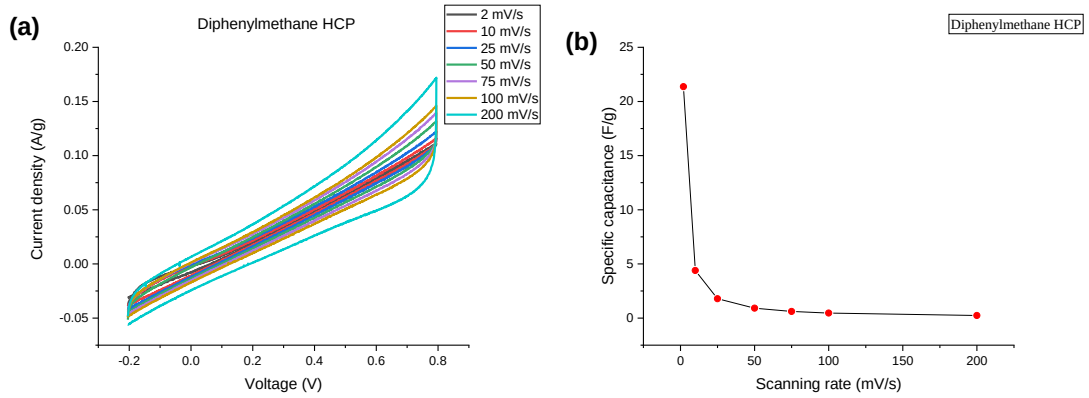

Figure 3.10 (a) CV curves at different scanning rate, and (b) Specific capacitance obtained at different scanning rates of the Diphenylmethane HCP

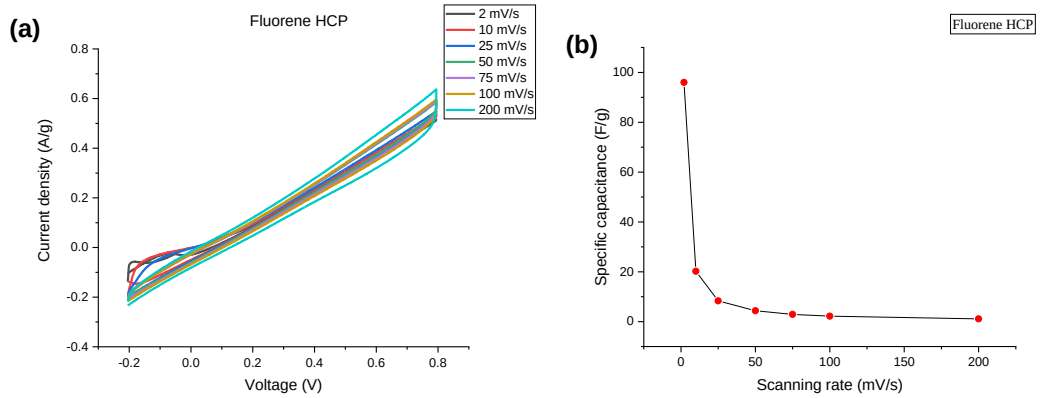

Figure 3.11 (a) CV curves at different scanning rate, and (b) Specific capacitance obtained at different scanning rates of the Fluorene HCP

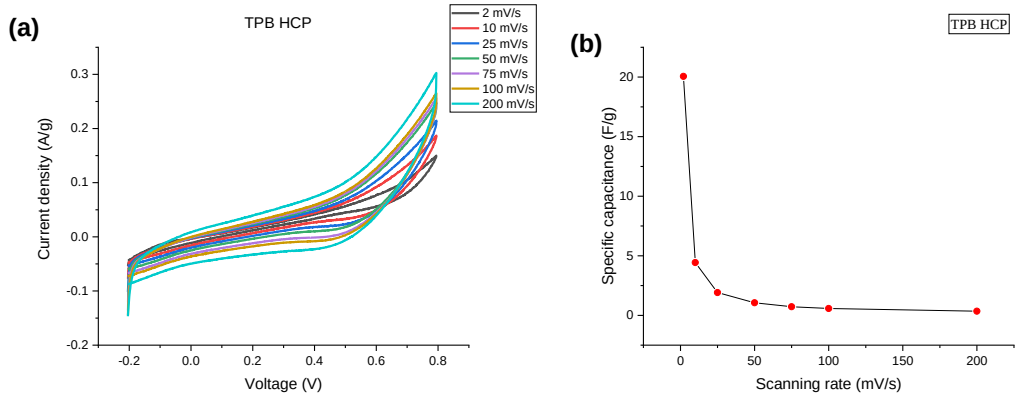

Figure 3.12 (a) CV curves at different scanning rate, and (b) Specific capacitance obtained at different scanning rates of the TPB HCP

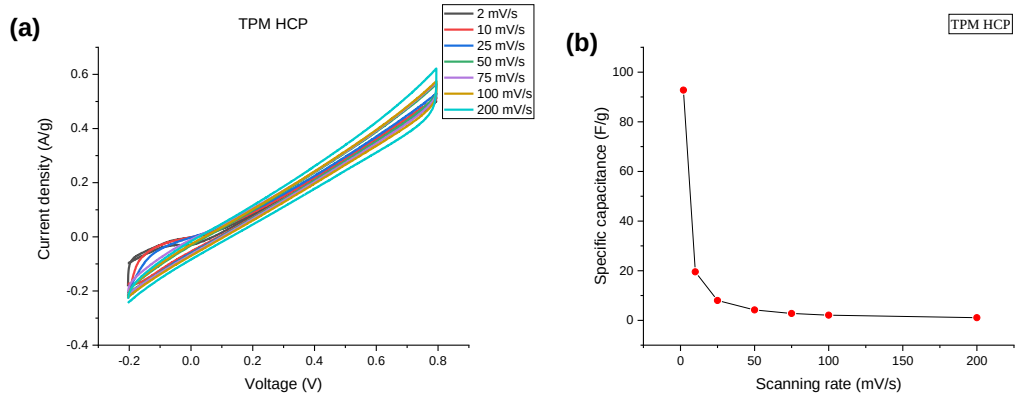

Figure 3.13 (a) CV curves at different scanning rate, and (b) Specific capacitance obtained at different scanning rates of the TPM HCP

	Specific capacitance obtained at different scanning rates (F/g)							
Scanning rates (mV/s) / Material	2	10	25	50	75	100	200	Retention of capacitance at 200 mV/s
Benzene HCP	13.9	1.5	0.7	0.4	0.4	0.4	0.4	2.9%
Biphenyl HCP	30.0	6.2	2.5	1.3	0.9	0.7	0.3	1.0%
Terphenyl HCP	2.2	0.5	0.2	0.2	0.2	0.2	0.2	9.1%
Diphenylmethane HCP	21.4	4.4	1.8	0.9	0.6	0.5	0.2	0.9%
Fluorene HCP	96.0	20.2	8.3	4.4	2.9	2.2	1.1	1.1%

TPB HCP	20.1	4.4	1.9	1.1	0.7	0.6	0.3	1.5%
TPM HCP	92.7	19.6	8.0	4.2	2.8	2.1	1.1	1.2%

Table 3.4 Specific capacitance obtained at different scanning rates

The specific capacitance at 2 mV/s of the Benzene HCP, Biphenyl HCP, Terphenyl HCP, Diphenylmethane HCP, Fluorene HCP, TPB HCP and TPM HCP is 13.9, 30.0, 2.2, 21.4, 96.0, 20.1 and 92.7 F/g, and the capacitance retention from 200 mV/s to 2 mV/s of these HCPs are 2.9%, 1.0%, 9.1%, 0.9%, 1.1%, 1.5% and 1.2%, respectively, suggesting the poor rate performance of the HCPs caused by the poor conductivity. The Fluorene HCP has the highest capacitance followed by the TPM HCP. It can be found that the BET surface area and the total pore volume of the Fluorene HCP (1003.9 m^2/g, 0.66 cm^3/g) and TPM HCP (1219.1 m^2/g, 0.81 cm^3/g) are not the highest. The micropore volume of the Fluorene HCP (0.42 cm^3/g) and the TPM HCP (0.52 cm^3/g) is not the highest as well. The Fluorene HCP (63.3%) and TPM HCP (64.5%) have higher micropore volume proportion than other HCP samples, this may result in the high specific capacitance of the Fluorene HCP and TPM HCP. For the Diphenylmethane HCP and the Triphenylbenzene HCP, the micropore volume proportion of them (56.1% and 53.9%, respectively) is higher than 50% while the specific capacitance of them is much lower than that of the Fluorene HCP and the TPM HCP. The BET surface area and the total pore volume of the Diphenylmethane HCP (1240.8 m^2/g, 0.95 cm^3/g) and the TPB HCP (1255.6 m^2/g, 0.98 cm^3/g) are higher than those of the Fluorene HCP and the TPM HCP. It can be also found that the micropore volume of the Diphenylmethane HCP (0.53 cm^3/g) and the TPB HCP (0.53 cm^3/g) is higher than that of the Fluorene HCP and the TPM HCP. The Benzene HCP has higher BET surface area, total pore volume and micropore volume (1040.4 m^2/g, 1.08 cm^3/g, and 0.44 cm^3/g) than those of the Biphenyl HCP (639.1 m^2/g, 0.65 cm^3/g, and 0.27 cm^3/g). It can be also found that the Benzene HCP and the Biphenyl HCP have similar micropore volume proportion (41.2% and 41.4%, respectively), while the Biphenyl HCP has higher specific capacitance than the Benzene HCP. The Terphenyl HCP has the lowest BET surface area (127.1 m^2/g), total pore volume (0.16 cm^3/g), micropore volume (0.05 cm^3/g) and micropore volume

proportion (33.9%) among all the samples, the specific capacitance of the Terphenyl HCP is the lowest as well. It can be seen that the monomers with different sizes and geometries have influences to the capacitances of HCPs, while the variation in the capacitances of the HCPs is independent with the variations in the porosity of the HCPs. The reason for this is as the differences in the adsorption in gas phase and liquid phase, the results obtained from the N_2 adsorption/desorption cannot fully explain the results from the adsorption occurred in the liquid phase. More importantly, the porous structures of HCPs cannot be fully used when the electrodes are charged due to the high internal resistance of HCPs, leading to it is more difficult to compare the volumetric results with the electrochemical results. The disordered porous structure of the HCPs could have unpredictable impacts on the electrochemical results.

The CV curves of the HCPs synthesized from different monomers showed deviation from the rectangular shape, shown in the figure 3.14.

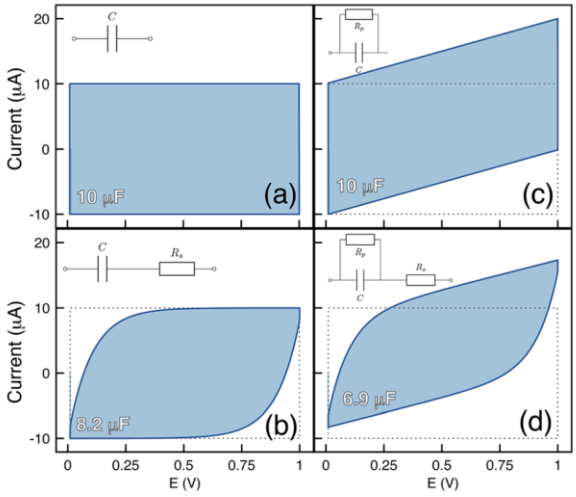

Figure 3.14 Cyclic voltammograms (CVs) calculated from variations of equivalent circuits to represent the non-ideal behavior of supercapacitors.[46]

For an ideal capacitor, the shape of the CV curve is rectangular. When the capacitor is connected with a resistor in parallel, i.e., the internal resistance of the capacitor electrode is taken into consideration, the CV curve will tilt. If the capacitor is connected with a resistor in serial, that is to say, the unavoidable resistance generated in the test (e.g., the contact resistance) is taken into consideration, the shape of CV curve will

deviate diagonally. For the HCPs, the tilted CV curves suggest the high internal resistance of them.

The capacity kinetic of the HCPs is analyzed by using the relationship between response current and scanning rate. The kinetic of the capacity is dominated by fast surface-controlled process if the response current is linear with scanning rate, whereas the linear relationship between response current and scanning root square root suggests the kinetic of the capacity is dominated by slow diffusion-controlled process.[47,48] The relationship between the response current and scanning rate of the HCPs is listed the figure 3.15.

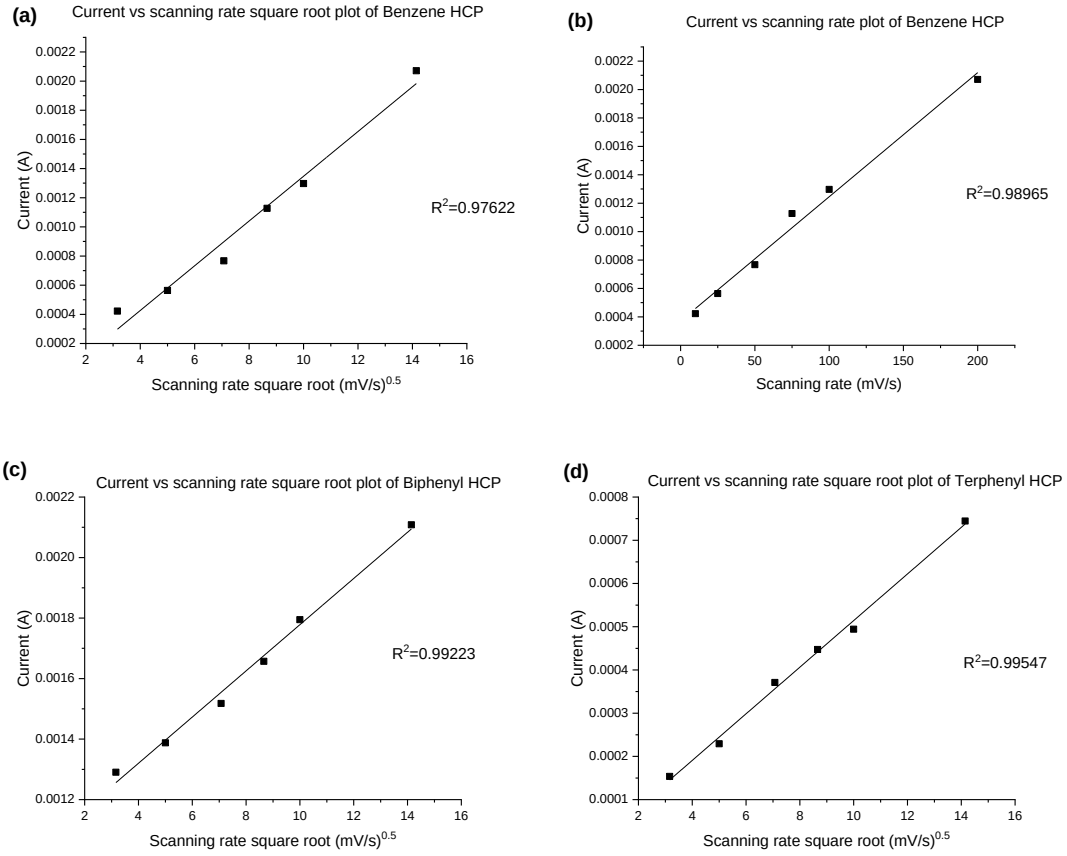

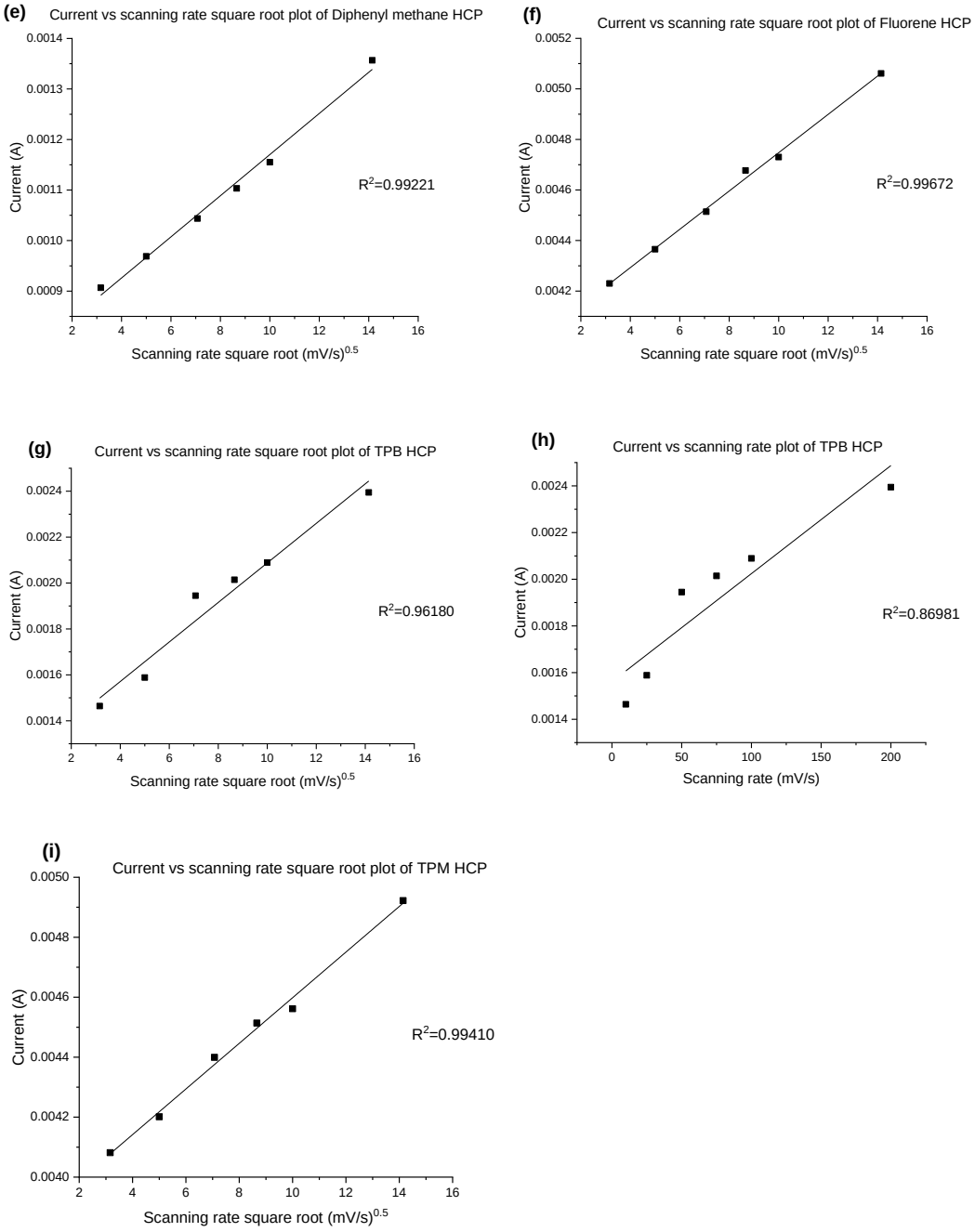

Figure 3.15 The relationship between response current and scanning rate plot of the HCPs synthesized from different monomers. (a). current vs scanning rate square root plot and (b). current vs scanning rate plot of Benzene HCP. (c). and (d). current vs scanning rate plot of Biphenyl HCP and Terphenyl HCP. (e). and (f). current vs scanning rate square root plot of Diphenyl methane and Fluorene HCP. (g). and (h). current vs scanning rate square root plot and current vs scanning rate plot of TPB HCP. (i). current vs scanning rate square root plot of TPM HCP.

From the figure 3.15, it can be seen that the coefficient of determination R^2 of the

response current vs scanning rate square root plot of the Biphenyl HCP, Terphenyl HCP, Diphenylmethane HCP, Fluorene HCP and TPM HCP is 0.99223, 0.99547, 0.99221, 0.99672 and 0.99410, respectively, showing the good linear relationship between the response current and scanning rate square root. Therefore, the capacity kinetic of these samples are dominated by diffusion-controlled process, corresponding to the poor rate performance of these samples. For the Benzene HCP, the R^2 of the response current vs scanning rate square root plot is 0.97622, lower than that of other samples. So, the response current vs scanning rate plot of Benzene HCP is shown to find out the capacity kinetic of it. It can be seen that the R^2 of response current vs scanning rate plot of Benzene HCP is 0.98965, higher than that of the response current vs scanning rate square root plot, indicating the Benzene HCP showed a mixed capacity kinetic involves both diffusion-controlled process and surface-controlled process. For the TPB HCP, the R^2 of the response current vs scanning rate square root plot is 0.96180, lower than that of other samples, while the R^2 of the response current vs scanning rate plot is 0.86981. This demonstrates the TPB HCP also showed a mixed capacity kinetic, but the capacitance of the TPB HCP mainly came from the diffusion-controlled process. The results above correspond to the results from the previous literatures: the poor electrical conductivity could result in the low specific capacitance and the capacitance is realized through the sluggish diffusion-controlled process, thus the rate performance will be poor as well.[49,50]

3.3.6 Electrochemical impedance spectroscopy (EIS)

To further investigate the electrochemical performance of the HCPs synthesized from different monomers, electrochemical impedance spectroscopy (EIS) was carried out with amplitude of 10 mV and frequency range 100 k Hz to 0.01 Hz. The Nyquist and Bode plots of the HCPs are listed the figure 3.16.

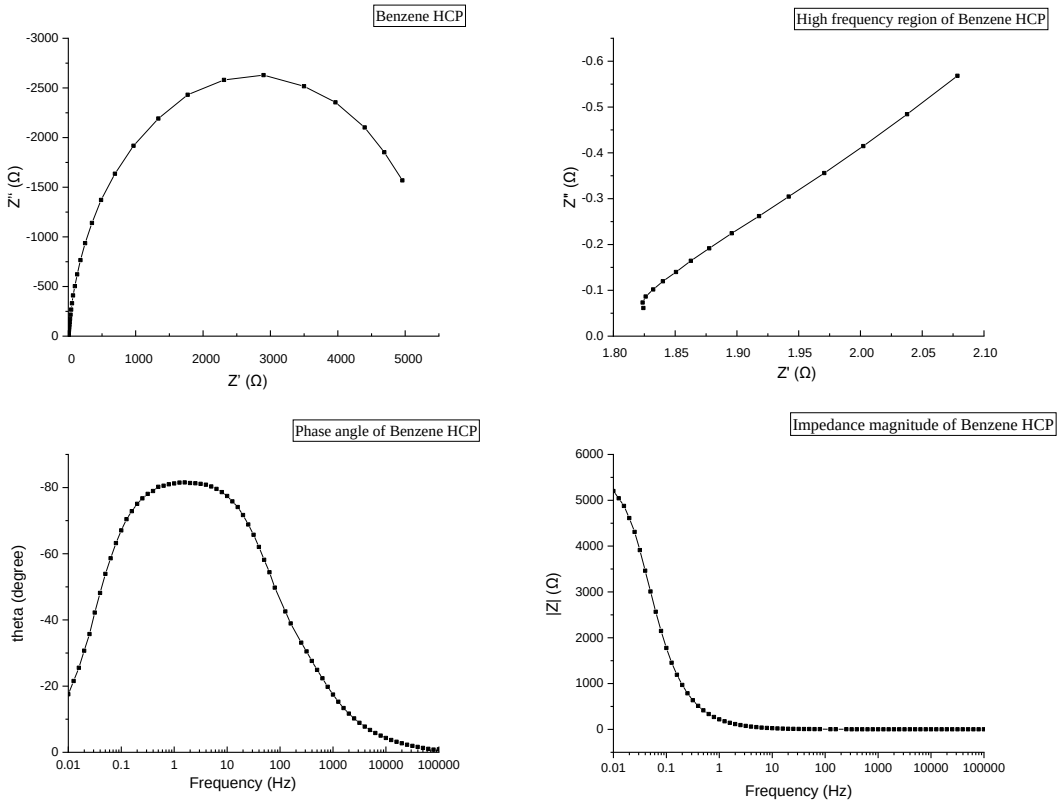

Figure 3.16 The Nyquist and Bode plot of the Benzene HCP

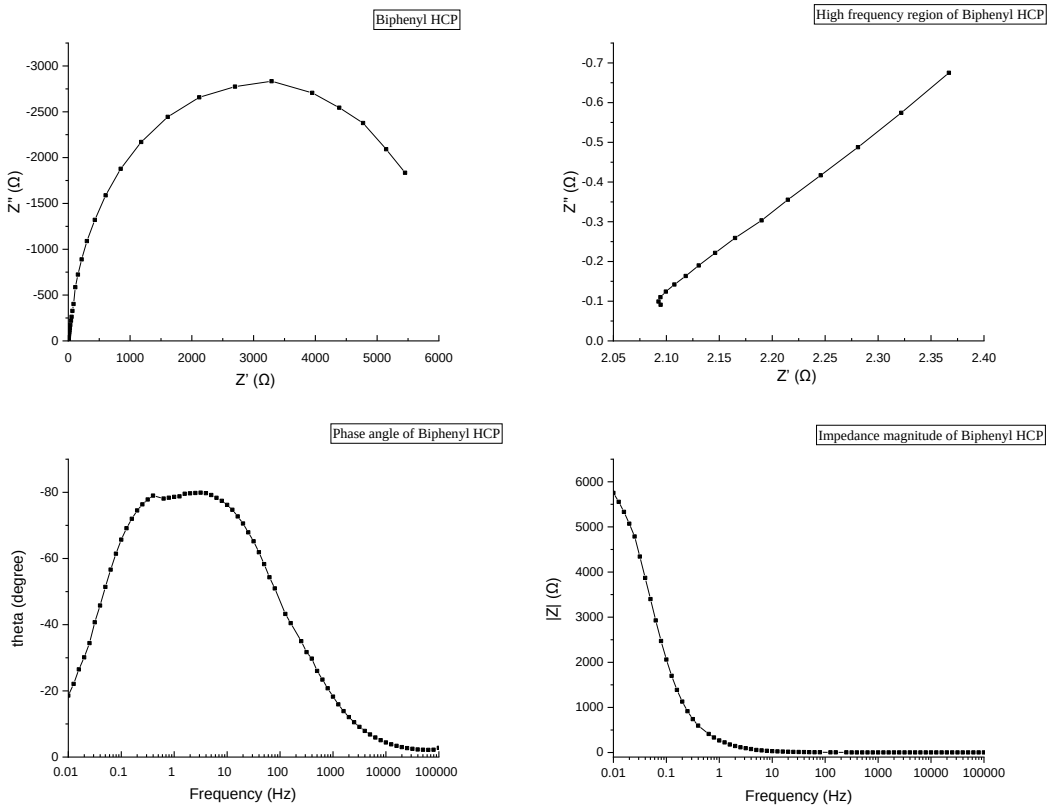

Figure 3.17 The Nyquist and Bode plot of the Biphenyl HCP

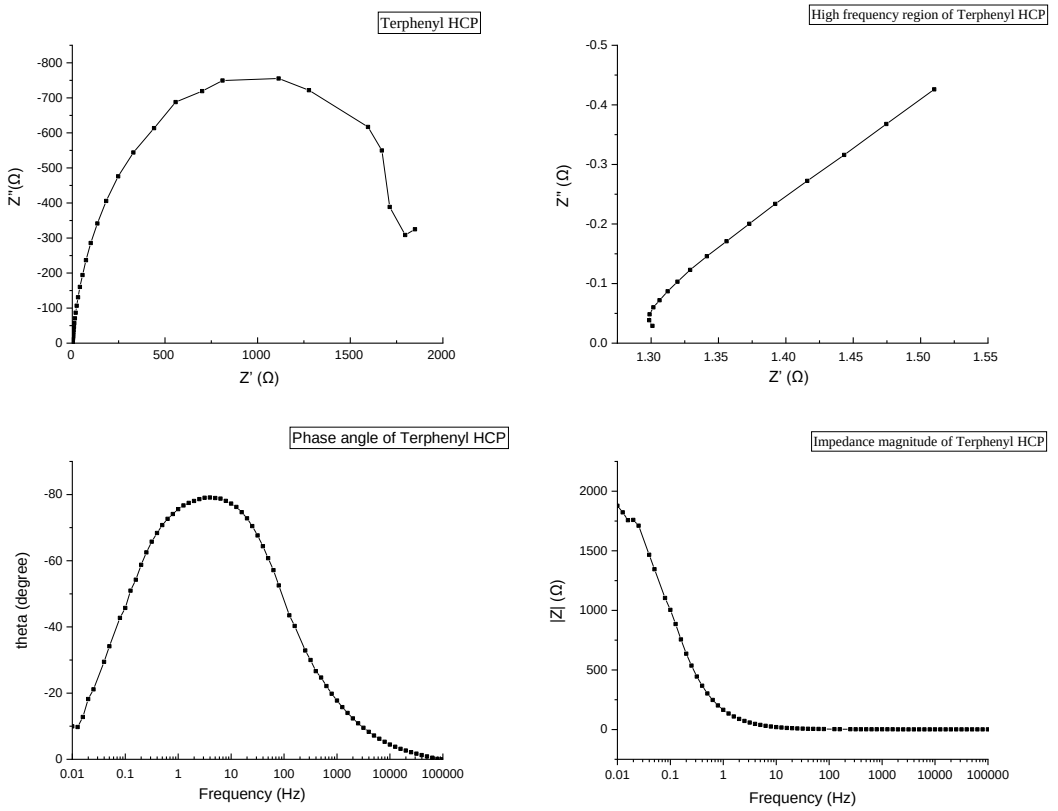

Figure 3.18 The Nyquist and Bode plot of the Terphenyl HCP

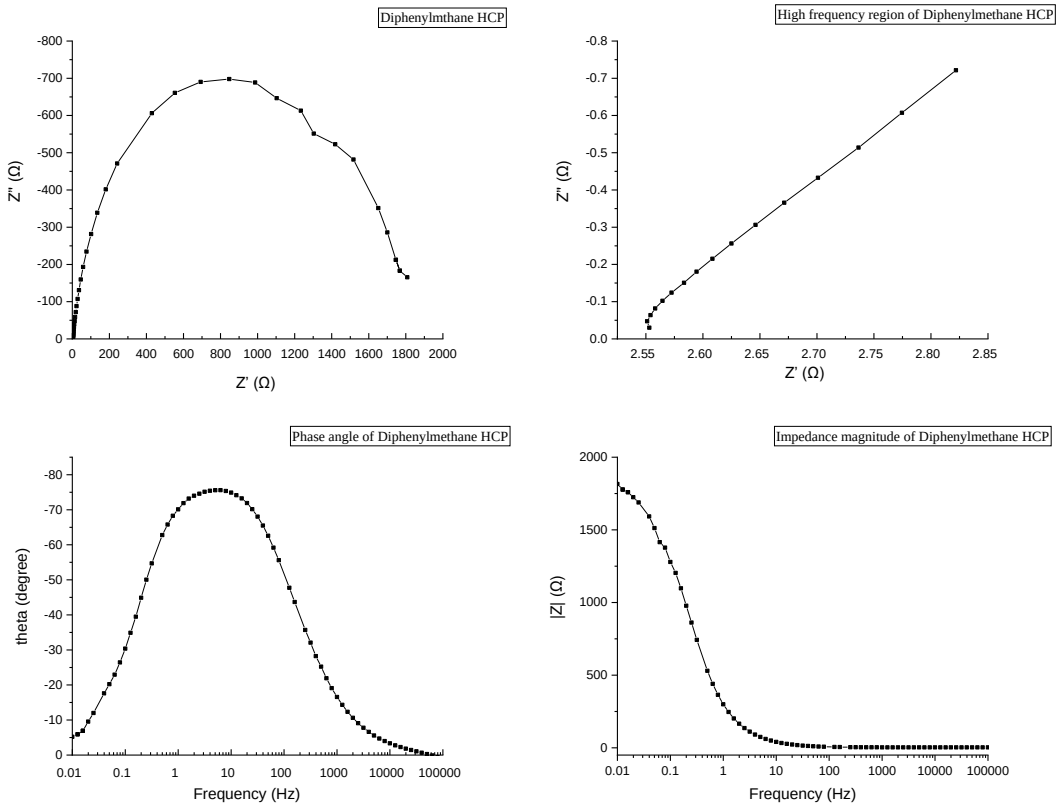

Figure 3.19 The Nyquist and Bode plot of the Diphenylmethane HCP

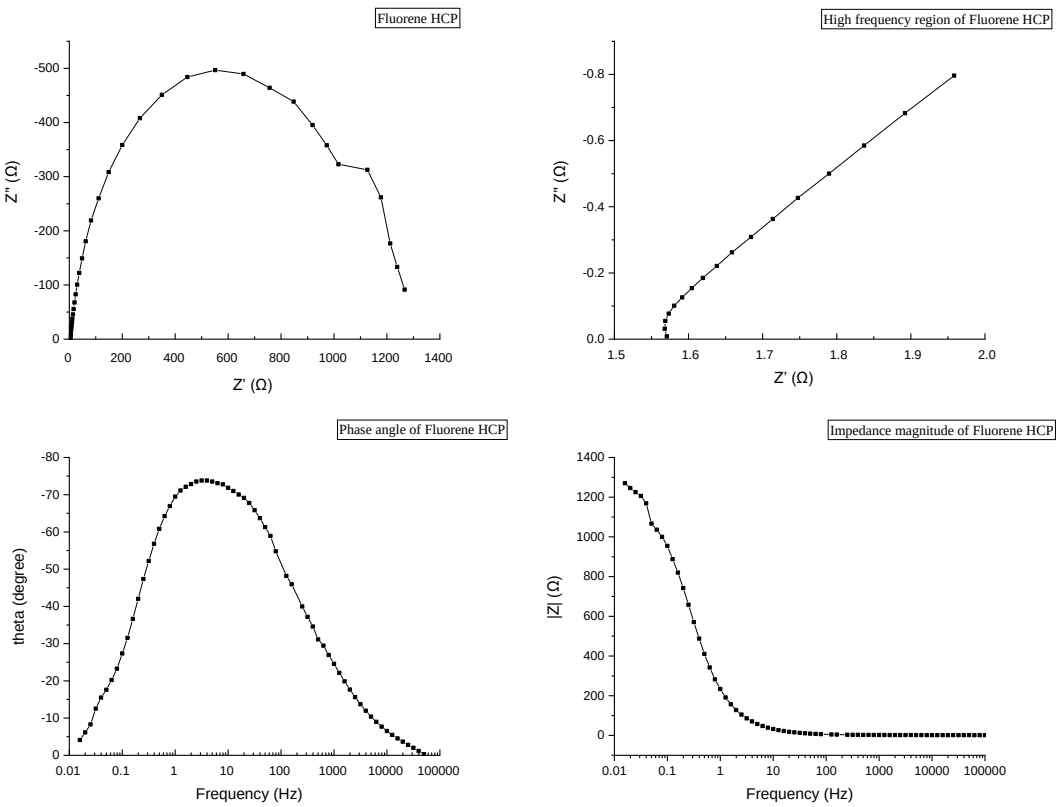

Figure 3.20 The Nyquist and Bode plot of the Fluorene HCP

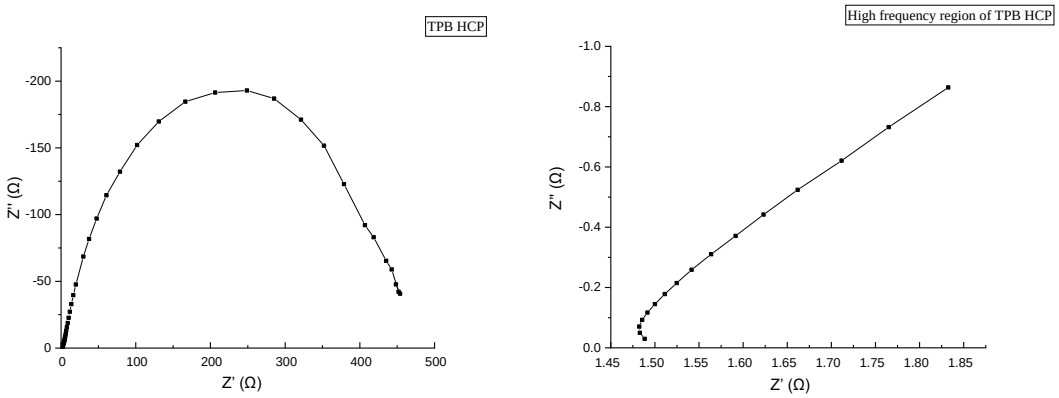

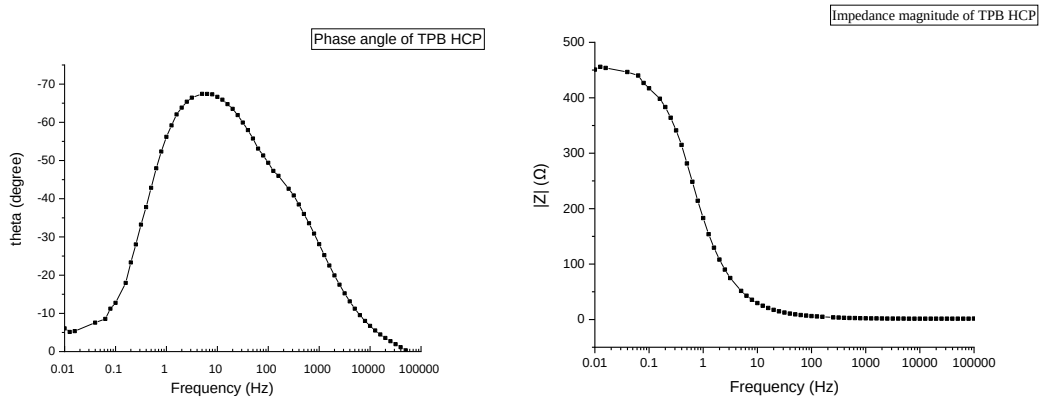

Figure 3.21 The Nyquist and Bode plot of the TPB HCP

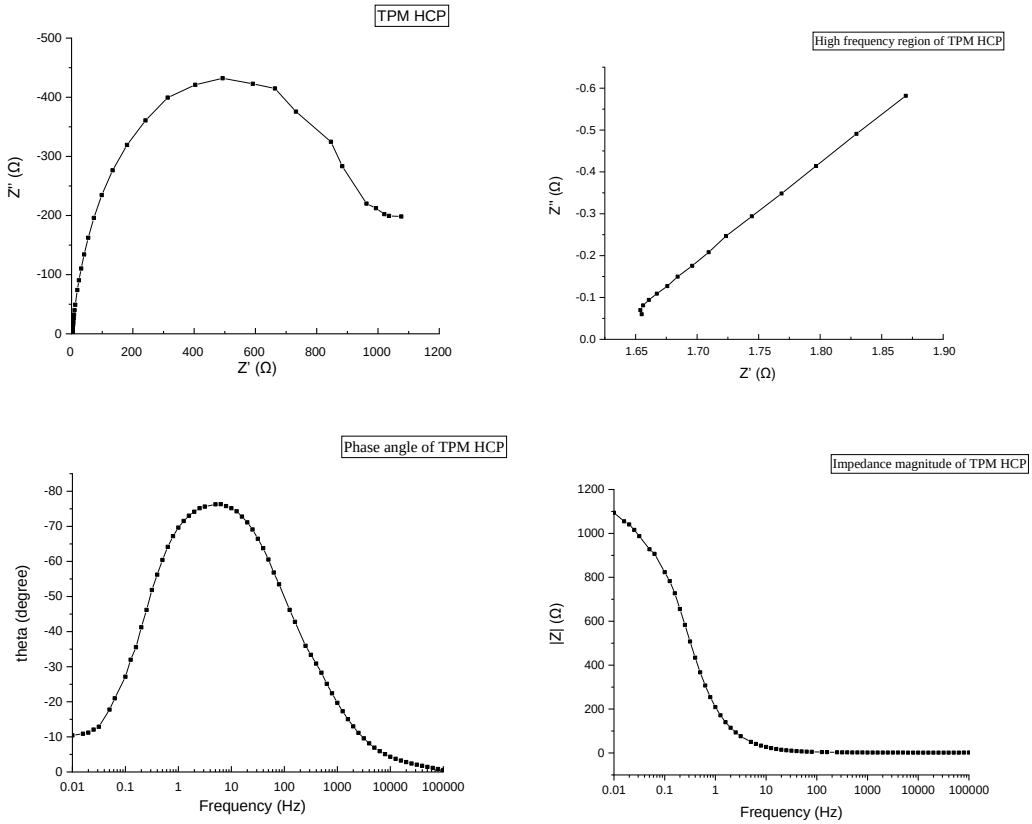

Figure 3.22 The Nyquist and Bode plot of the TPM HCP

	Whether the semicircle can be observed at	Whether the Nyquist plot is vertical or near vertical	The phase angle value of the curve apex	Phase angle at 0.01 Hz	Impedance magnitude at 0.01 Hz (Ω)

	high frequencies?	to Z'' axis at low frequencies?			
Benzene HCP	No	No	-81°	-19°	5201
Biphenyl HCP	No	No	-80°	-19°	5753
Terphenyl HCP	No	No	-79°	-10°	1878
Diphenylmethane HCP	No	No	-76°	-5°	1815
Fluorene HCP	No	No	-74°	-3°	1270
TPB HCP	No	No	-67°	-5°	451
TPM HCP	No	No	-76°	-10°	1094

Table 3.5 The results from Nyquist and Bode plot of different HCPs

For an ideal capacitor, the Nyquist plot is a straight line vertical to the Z' axis. For a common supercapacitor, the Nyquist plot is shown in the figure 3.23.

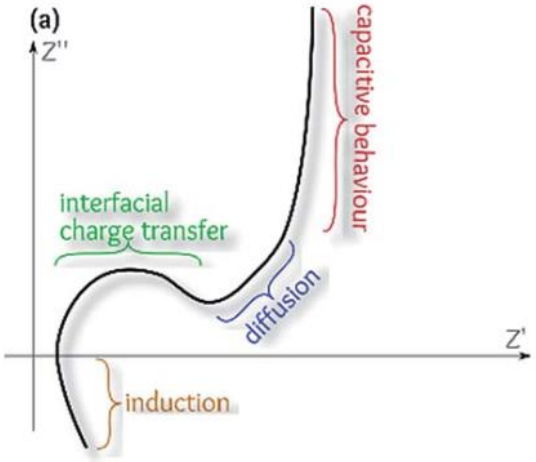

Figure 3.23 The Nyquist plot of supercapacitors[51]

The Nyquist plot of a common supercapacitor consists of a semi-circle in the high frequency region caused by the charge transfer resistance at the interface of electrode/electrolyte. If the charge transfer resistance is low enough, the semi-circle in the high frequency region will disappear.[52] The semi-circle is followed by a straight line with a slope in the intermediate and low frequency region corresponding to the diffusion process in the porous structure of the electrode. In the low frequency region, the vertical or nearly vertical line is the feature of the capacitor behaviour indicating the

supercapacitor is fully charged. The intersection of the straight line with a slope corresponding to the diffusion process and the vertical line in the low frequency region defines to the knee frequency: below this frequency, the maximum capacitance can be reached.[53] For the Nyquist plots of HCPs synthesized from different monomers, it can be seen that there was no sharp rise 'tail' paralleling to Z" axis which indicates the supercapacitor was fully charged. That is to say, the HCPs did not behave like a supercapacitor.

For a resistor, the phase angle is always 0°, whereas for an ideal supercapacitor, the highest phase angle curve is -90°. The degree of -90° indicates the capacitor behaviour, i.e., the voltage lags behind the current for 90 degree when an ideal capacitor is connected in the AC circuit. Although -90° is quite hard to be reached, the closer to -90°, the closer to capacitor behavior. The phase angle of a common supercapacitor should not change after reaching the highest point with the decreasing frequency, as shown in the figure 3.24.

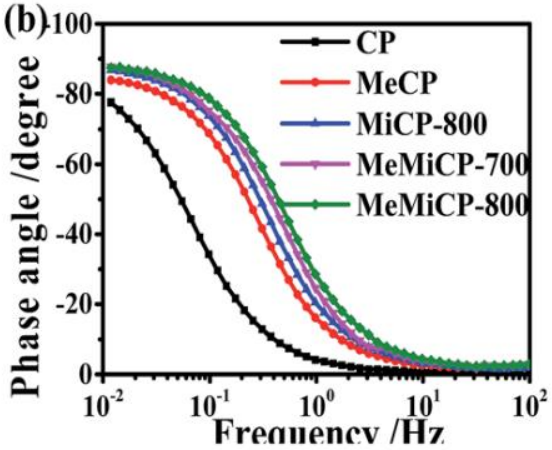

Figure 3.24 The phase angle of nitrogen-doped porous carbon nanorods[54]

The highest point of the phase angles curves of HCPs are close to -80°. It can be observed that the phase angle curves of HCPs decreased after reaching the highest phase angle, illustrating the HCPs did not behave like supercapacitors. While the phase angle did not decrease to 0°, this means the HCPs showed some capacitance at low frequency. The impedance magnitudes of HCPs at 0.01 Hz are quite high. Based on the quasi-semicircle shape of the Nyquist plots and the formula of impedance magnitude

calculation, it can be found that the internal resistance of HCPs accounts for a large proportion in the impedance magnitudes obtained at low frequencies. Because of the high internal resistances of the HCPs synthesized from different monomers, the absence of the semi-circle in the high frequency region should be attributed to the ohmic contact between the current collector and the active materials.[55]

In order to see the poor conductivity of the HCPs synthesized from the different monomers more directly, the fitting results are performed in the figure 3.25 and table 3.6. The Randles circuit model is employed as the equivalent circuit model used for the fitting of the HCPs.

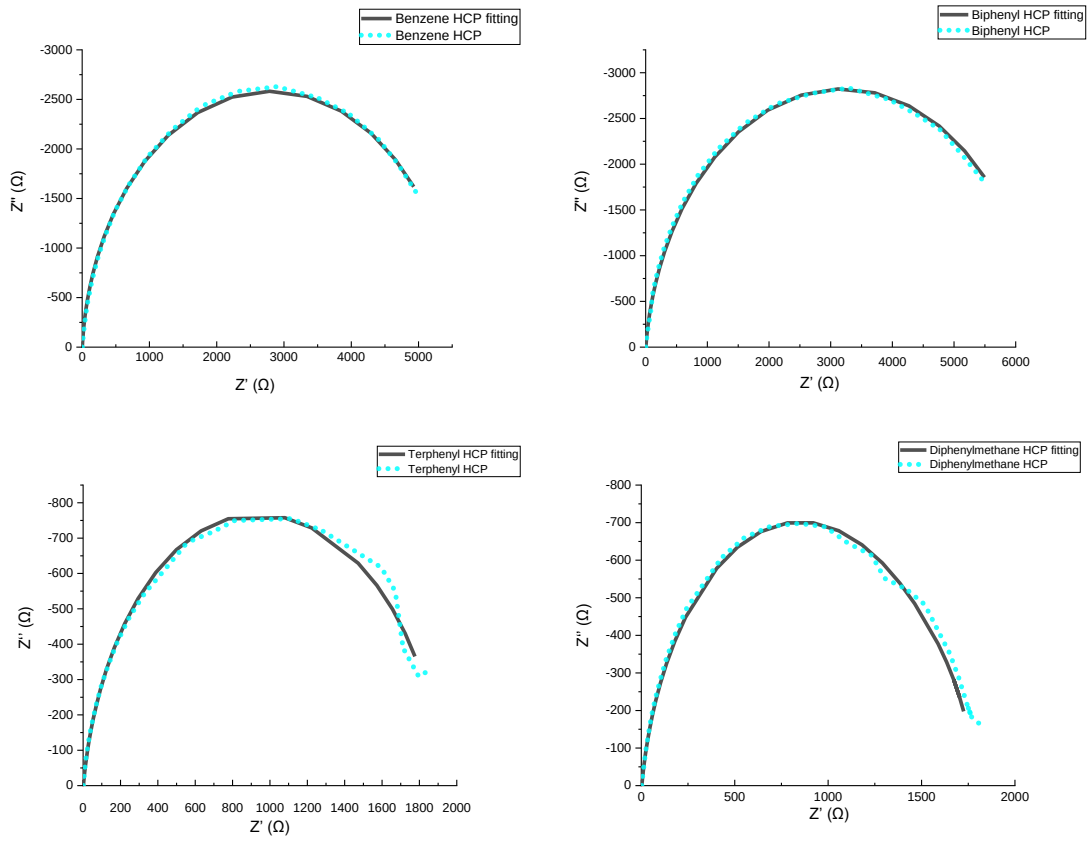

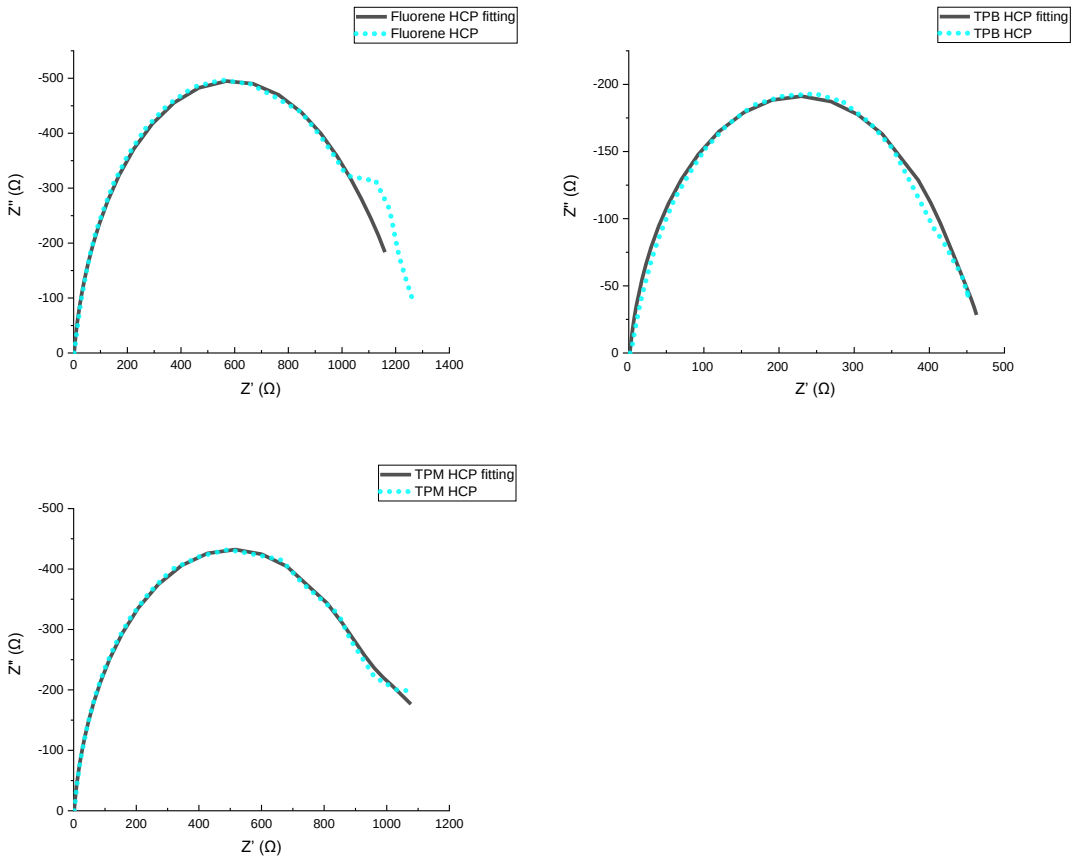

Figure 3.25 The impedance fitting curves of the HCPs synthesized from different monomers

From the fitting curves in the figure 3.25, it can be found that the fitting results in the high and intermediate frequency region are better that those in the low frequency region. The deviations in the fitting results in the low frequency region can be found due to no proper model can be used to describe the diffusion behaviours in the disordered hierarchical porous structures of the HCPs with poor conductivity.

	R1 (Ω)	CPE1-T (F)	CPE1-P	R2 (Ω)	Ws1-R (Ω)	Ws1-T (s)	Ws1-P
Benzene HCP	1.998	0.00083276	0.95511	5463.3	134.2	13.3	0.5
Biphenyl HCP	2.304	0.00071572	0.93047	6214.1	152.8	15.6	0.5
Terphenyl HCP	1.435	0.0011862	0.89712	1733.2	189.1	13.9	0.5
Diphenylmethane HCP	2.672	0.0006422	0.8869	1664.3	142.7	13.4	0.5
Fluorene HCP	1.743	0.00087917	0.8971	1146.8	89.1	17.3	0.5
TPB HCP	1.539	0.0011694	0.8992	445.4	25.3	18.7	0.5
TPM HCP	1.771	0.00094522	0.9101	964.9	221.4	33.6	0.5

Table 3.6 The impedance fitting results of the HCPs synthesized from different monomers

Although the fitting results are not perfect, the poor conductivity of the HCPs can be seen from the large R2 values in the table 3.6.

To further study the electrochemical performance of HCPs synthesized from the different monomers under alternating current, the complex capacitances of the HCPs are performed. The complex capacitance C(ω) is defined by equation 3.3.6.1. The real part and imaginary of the complex capacitance C'(ω) and C" (ω) is defined by equation 3.3.6.2 and 3.3.6.3, respectively.

$$C(\omega) = C'(\omega) - jC''(\omega) \qquad 3.3.6.1$$

$$C'(\omega) = \frac{-Z''(\omega)}{\omega|Z|^2} \qquad 3.3.6.2$$

$$C''(\omega) = \frac{Z'(\omega)}{\omega|Z|^2} \qquad 3.3.6.3$$

The complex capacitance curves of the HCPs are listed in the figure 3.26.

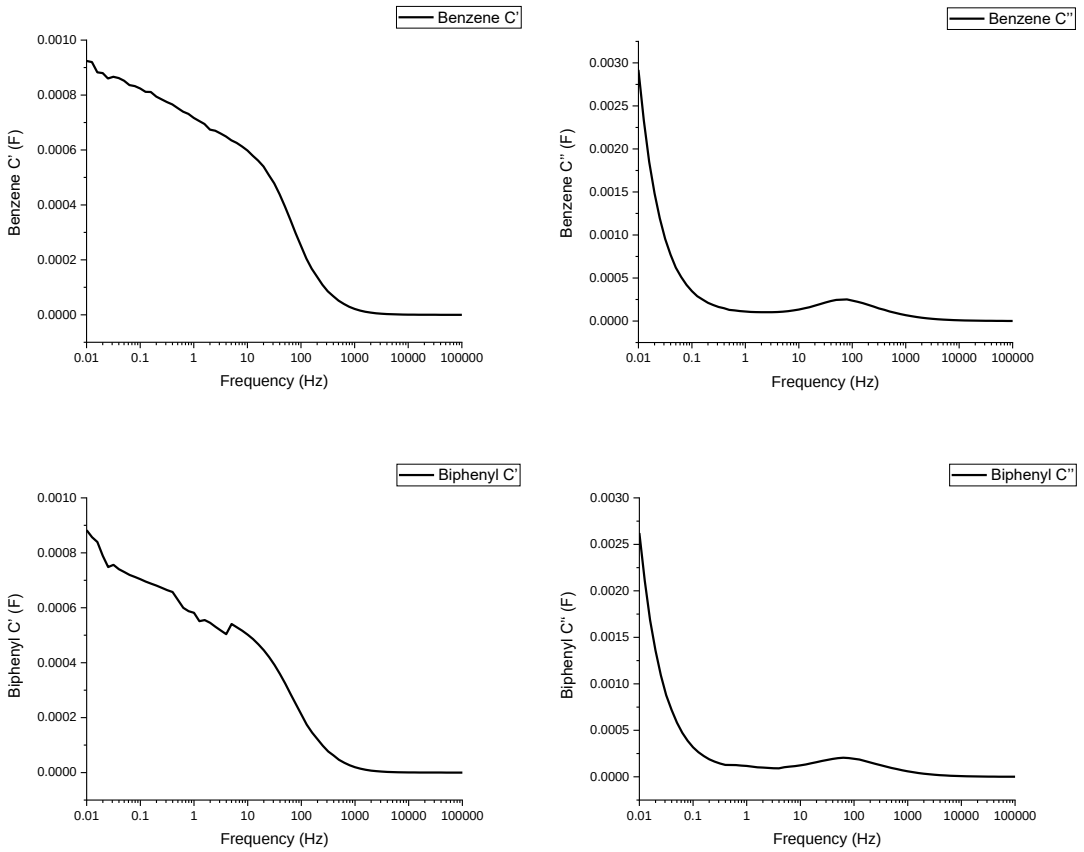

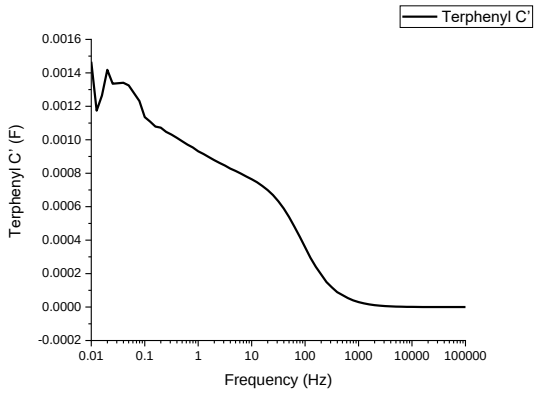
Terphenyl C'
Terphenyl C' (F)
Frequency (Hz)

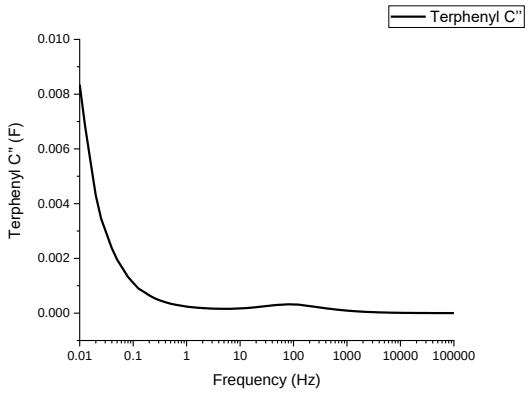
Terphenyl C''
Terphenyl C'' (F)
Frequency (Hz)

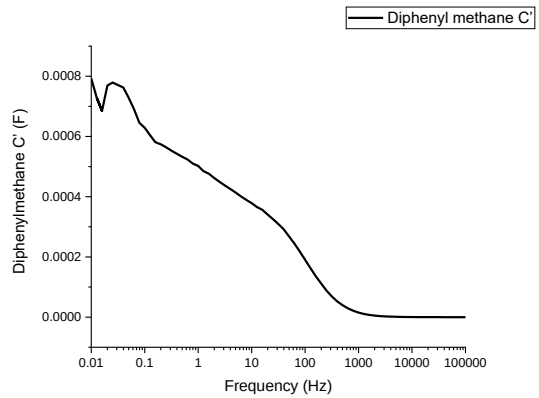
Diphenyl methane C'
DiphenylmethaneC' (F)
Frequency (Hz)

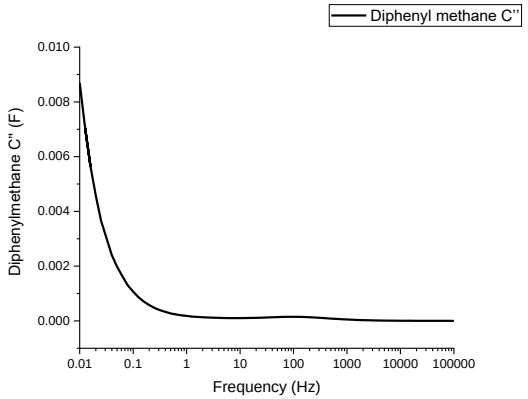
Diphenyl methane C''
DiphenylmethaneC'' (F)
Frequency (Hz)

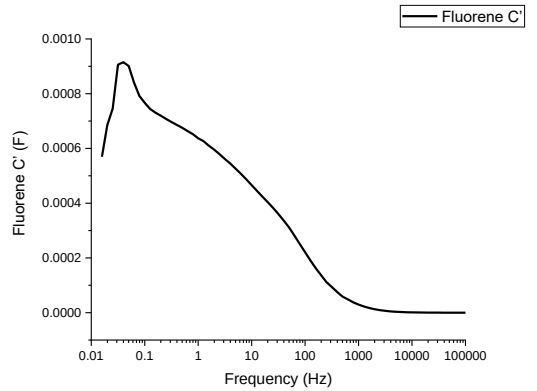
Fluorene C'
Fluorene C' (F)
Frequency (Hz)

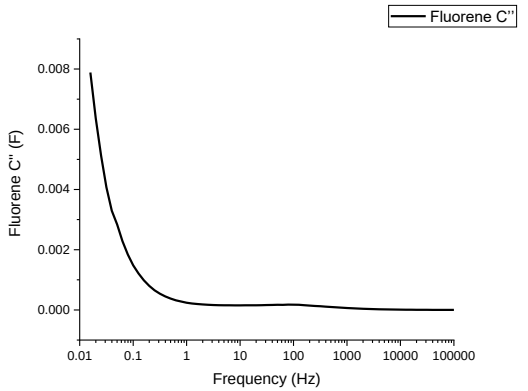
Fluorene C''
Fluorene C'' (F)
Frequency (Hz)

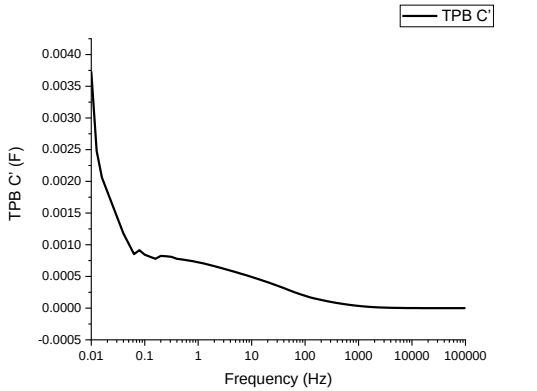
TPB C'
TPB C' (F)
Frequency (Hz)

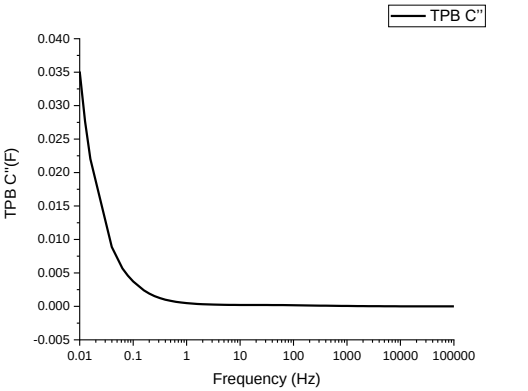
TPB C''
TPB C''(F)
Frequency (Hz)

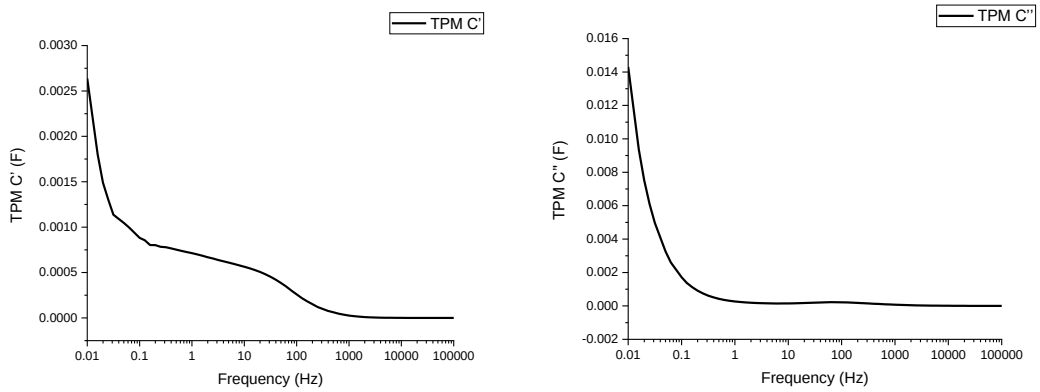

Figure 3.26 The complex capacitance of the HCPs

Firstly, the complex capacitance of common supercapacitors is shown in the figure 3.27.

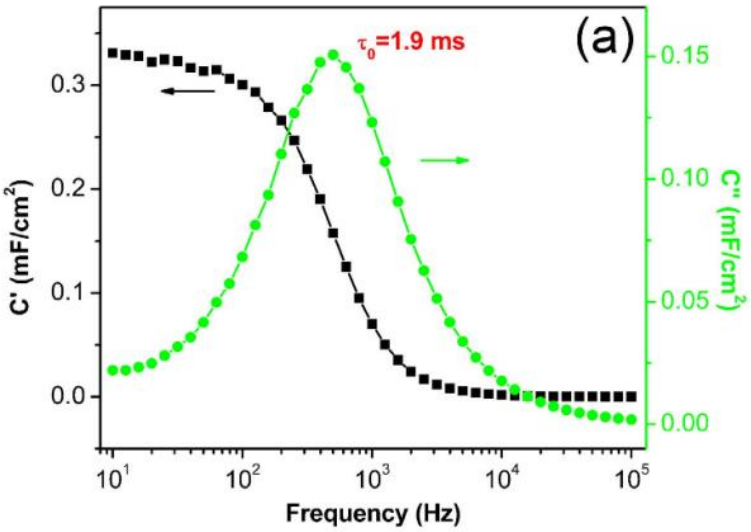

Figure 3.27 The complex capacitance of a graphene-based supecapacitor[56]

The real part of the complex capacitance C' shows the capacitance variation with the decreasing frequency. For a common supercapacitor, the C' showed the resistor behaviour in the high frequency region, therefore the capacitance is zero. With the decreasing frequency, C' rises sharply at first then gradually becomes less dependent with frequency at low frequencies as the maximum capacitance can be reached in the low frequency region.

The imaginary part of the complex capacitance C" correspond to energy dissipation. For a common supercapacitor, it has no resistance to alternating current in the high frequency region, so the C" is zero at high frequencies. With the decreasing frequency,

the C" increases and attains the peak at the frequency f_0 which corresponds to -45°. The phase angle of -90° indicates the pure capacitor behaviour and the phase angle of 0° demonstrates the pure resistor behaviour. From 0° to -45°, the charge/discharge of the supercapacitor starts with the decreasing frequency. As the frequency is still high, the voltage direction changes rapidly leading to a hysteresis, therefore the energy dissipation occurs and it becomes higher with the decreasing frequency. The energy losses is similar to the dielectric losses in water molecule rotation or movement which is the reason of food getting hot under microwave heating.[53] The energy dissipation reaches the maximum at -45°. With the decreasing frequency from -45° to -90°, the supercapacitor has more sufficient time to realize the charge/discharge process, so the energy losses decreases. At -90°, the supercapacitor can be fully charge and the maximum capacitance can be reached, so the phase angle of -45° indicates the supercapacitor reaches the half of its low-frequency capacitance. The frequency f_0 corresponding to the maximum C" can be used to define the relaxation time τ_0 (equation 3.3.6.4), i.e., the time of the capacitor to reach the half of its low-frequency capacitance. The shorter this time, the better rate performance of the supercapacitor.

$$\tau_0 = \frac{1}{f_0} \qquad 3.3.6.4$$

For the HCPs synthesized from the different monomers, the fluctuation can be seen in the low frequency region. The fluctuations of the C' in the low frequency region indicate the low frequency capacitances of the HCPs are not stable, that is to say, the accessibility rates of the pore structures of the HCPs are unstable due to the high internal resistance of the HCPs. This corresponds to the capacitances obtained from CV results are independent with the BET surface areas and the pore volumes of HCP samples. The inhomogeneous porosity of the HCPs may have unpredictable impacts on the utilization rate of the pore structures of the HCPs under the condition of poor conductivity. Moreover, it can be also found that the capacitance at very low frequencies in the real part of the complex capacitance is much lower than that obtained from CV results. This

suggests the HCPs can only produce quite small response to the voltage that employed in the impedance test due to the high internal resistance.

The C" of the HCPs remain at zero in the high frequency region indicating the resistor behaviour. With the decreasing frequency, a weak peak corresponding to the phase angle -45° appeared, and the C" curves showed a sharp rise in the low frequency region, indicating the increased energy losses at low frequencies originating from the high internal resistance of the HCPs, it also corresponds to the decreasing of the phase angle curves after reaching the highest phase angle, i.e., the tendency of behaving like a pure resistor due to the high internal resistance originated from amorphous structure and the non-conjugated methylene bridges of the HCPs. As the C" of the HCPs reached the maximum at 0.01 Hz, according to equation 3d, the relaxation time τ_0 of the HCPs is 100 s, indicating the poor rate performance due to the high internal resistance of the HCPs.

For the supercapacitive performance of the POPs without carbonization in the previous literatures, like conjugated microporous polymer synthesized from Buchwald–Hartwig coupling (PAQTA) which has specific capacitances of 576 F/g at 1 A/g and 410 F/g at 10 A/g,[57] Triazatruxene-based conjugated microporous polymer (TAT-CMP-2) which has specific capacitances of 183 F/g at 1 A/g and 137 F/g at 10 A/g,[58] β-ketoenamine-linked conjugated microporous polymer (KECMP-1) with specific capacitances of 252 F/g at 1 A/g and 126 F/g at 100 A/g,[59] they all show higher specific capacitances and better rate performance than the HCPs synthesized in this chapter. The common ground of them is that they all have a fully conjugated molecular structure, suggesting the low specific capacitances and rate performance of the HCPs are caused by the unconjugated methylene bridges which cannot provide good electronic conductivity.

3.4 Conclusion

The HCPs synthesized from monomers with different structure show various pore

structures which result in the differences in electrochemical performance. Most of the HCPs have high BET surface area no lower than 1000 m^2/g, while Terphenyl HCP has the lowest BET surface area of 127.1 m^2/g among all these samples. The single point adsorption total pore volume of these HCPs ranges from 0.16 to 1.08 cm^3/g. The micropore volume proportions of the total pore volumes varies from 33.87% to 64.54%. In the CV results, the specific capacitances obtained at 2 mV/s of these samples varies from 2.2 to 96.0 F/g. The Terphenyl HCP has the lowest specific capacitance of 2.2 F/g while the Fluorene HCP has the highest specific capacitance of 96.0 F/g, followed by the TPM HCP with a specific capacitance of 92.7 F/g. The capacitance retention rates from 2 mV/s to 200 mV/s of most of the HCPs are around 1%, indicating the quite poor rate performance of the HCPs.

The analyses of the relationship between response current and scanning rate of the HCPs show, the capacitances of the HCPs are dominated by slow diffusion-controlled process due to the high internal resistance of the HCPs, corresponding to the poor rate performance of the HCPs.

In the EIS results, the Nyquist plots of the HCPs do not show the 'tail' paralleling with the Z" axis, suggesting the HCPs do not show a supercapacitor behaviour. From the impedance magnitudes of the HCPs, the high internal resistances of the HCPs can be seen. The phase angle curves of the HCPs also demonstrate they do not show the supercapacitor behaviour as well, as the phase angles increase to close to 0° at low frequencies, illustrating that the HCPs behave like a pure resistor in the low frequency region. In the complex capacitances, the pore structures of the HCPs cannot be fully used due to their high internal resistances is confirmed by the fluctuations in the low frequency region of the C' curves and the poor rate performance of the HCPs are reaffirmed by the C" curves.

For the HCPs synthesized from monomers with different sizes and geometries, thermal treatment is required before they are used as supercapacitor electrode materials, but it is interesting to see these HCPs have various specific capacitances caused by their different porous structures. If the HCPs are used as precursors for manufacturing

carbons, the various porous structures of the HCPs can be used to control the porosity of the carbons derived from them.

Reference

1 G. M. Joselin Herbert, S. Iniyan, E. Sreevalsan and S. Rajapandian, *Renew. Sustain. Energy Rev.*, 2007, **11**, 1117–1145.

2 R. Saidur, N. A. Rahim, M. R. Islam and K. H. Solangi, *Renew. Sustain. Energy Rev.*, 2011, **15**, 2423–2430.

3 N. S. Lewis, *Science (80-.).*, 2007, **315**, 798–801.

4 L. Lakatos, G. Hevessy and J. Kovács, *World Futur. J. Gen. Evol.*, 2011, **67**, 395–408.

5 P. J. Corral-Vega, P. García-Triviño and L. M. Fernández-Ramírez, *Energy*, , DOI:10.1016/j.energy.2019.115863.

6 L. Kouchachvili, W. Yaïci and E. Entchev, *J. Power Sources*, 2018, **374**, 237–248.

7 M. Hassanalieragh, T. Soyata, A. Nadeau and G. Sharma, *IEEE Access*, 2016, **4**, 542–557.

8 A. M. Khattak, Z. A. Ghazi, B. Liang, N. A. Khan, A. Iqbal, L. Li and Z. Tang, *J. Mater. Chem. A*, 2016, **4**, 16312–16317.

9 W. Deng, Y. Li, S. Zheng, X. Liu, P. Li, L. Sun, R. Yang, S. Wang, Z. Wu and X. Bao, *Angew. Chemie Int. Ed.*, 2017, 1–6.

10 Y. Kou, Y. Xu, Z. Guo and D. Jiang, *Angew. Chemie - Int. Ed.*, 2011, **50**, 8753–8757.

11 V. A. Davankov, S. V. Rogoshin and M. P. Tsyurupa, *J Polym Sci Part C, Polym Symp*, 1974, **101**, 95–101.

12 B. Li, R. Gong, W. Wang, X. Huang, W. Zhang, H. Li, C. Hu and B. Tan, *Macromolecules*, 2011, **44**, 2410–2414.

13 S. Hou, S. Razzaque and B. Tan, *Polym. Chem.*, 2019, **10**, 1299–1311.

14 G. Ji, Z. Yang, X. Yu, Y. Zhao, F. Zhang and Z. Liu, *ACS Sustain. Chem. Eng.*, 2020, **8**, 16320–16326.

15 L. Tan, B. Li, X. Yang, W. Wang and B. Tan, *Polymer (Guildf).*, 2015, **70**, 336–342.

16 G. Wang, B. Dou, J. Wang, W. Wang and Z. Hao, *RSC Adv.*, 2013, **3**, 20523–20531.

17 Y. Liu, X. Chen, X. Jia, X. Fan, B. Zhang, A. Zhang and Q. Zhang, *Ind. Eng. Chem. Res.*, 2018, **57**, 17259–17265.

18 J. He, G. Zhao, P. Mu, H. Wei, Y. Su, H. Sun, Z. Zhu, W. Liang and A. Li, *Sol. Energy Mater. Sol. Cells*, , DOI:10.1016/j.solmat.2019.110111.

19 D. Chen, S. Gu, Y. Fu, Y. Zhu, C. Liu, G. Li, G. Yu and C. Pan, *Polym. Chem.*, 2016, **7**, 3416–3422.

20 X. Fu, Y. Liu, X. Jiang, Q. Wang, Y. Luo and Y. Lyu, *Thermochim. Acta*, 2018, **665**, 111–118.

21 J. Bai, W. Zhang, X. Ma, L. Chen, L. Liu and C. Zhang, *Microporous Mesoporous Mater.*, 2020, **294**, 109892.

22 B. Li, R. Gong, W. Wang, X. Huang, W. Zhang, H. Li, C. Hu and B. Tan, *Macromolecules*, 2011, **44**, 2410–2414.

23 R. Lu, C. Xu, Q. Wang, Y. Wang, Y. Zhang, D. Gao, J. Bi and G. Fan, *Int. J. Hydrogen Energy*, 2018, **43**, 18253–18260.

24 C. Wilson, M. J. Main, N. J. Cooper, M. E. Briggs, A. I. Cooper and D. J. Adams, *Polym. Chem.*, 2017, **8**, 1914–1922.

25 R. Dawson, T. Ratvijitvech, M. Corker, A. Laybourn, Y. Z. Khimyak, A. I. Cooper and D. J. Adams, *Polym. Chem.*, 2012, **3**, 2034–2038.

26 Y. Shigemasa, H. Matsuura, H. Sashiwa and H. Saimoto, *Int. J. Biol. Macromol.*, 1996, **18**, 237–242.

27 L. Pan, Q. Chen, J. H. Zhu, J. G. Yu, Y. J. He and B. H. Han, *Polym. Chem.*, 2015, **6**, 2478–2487.

28 H. Wei, F. Wang, H. Sun, Z. Zhu, C. Xiao, W. Liang, B. Yang, L. Chen and A. Li, *J. Mater. Chem. A*, 2018, **6**, 8633–8642.
29 Y. Luo, S. Zhang, Y. Ma, W. Wang and B. Tan, *Polym. Chem.*, 2013, **4**, 1126–1131.
30 R. V. Law, D. C. Sherrington, C. E. Snape, I. Ando and H. Kurosu, *Macromolecules*, 1996, **29**, 6284–6293.
31 L. Ding, H. Gao, F. Xie, W. Li, H. Bai and L. Li, *Macromolecules*, 2017, **50**, 956–962.
32 Y. Cheng, S. Razzaque, Z. Zhan and B. Tan, *Chem. Eng. J.*, 2021, **426**, 130731.
33 S. Krishnan and C. V. Suneesh, *Mater. Today Commun.*, 2021, **27**, 102251.
34 S. Xu, K. Song, T. Li and B. Tan, *J. Mater. Chem. A*, 2015, **3**, 1272–1278.
35 G. Liu, Y. Wang, C. Shen, Z. Ju and D. Yuan, *J. Mater. Chem. A*, 2015, **3**, 3051–3058.
36 S. Seo, W. Chaikittisilp, N. Koike, T. Yokoi and T. Okubo, *Microporous Mesoporous Mater.*, 2019, **278**, 212–218.
37 R. Rego, P. J. Adriaensens, R. A. Carleer and J. M. Gelan, *Polymer (Guildf).*, 2004, **45**, 33–38.
38 T. Yoshida and Y. Maekawa, *Fuel Process. Technol.*, 1987, **15**, 385–395.
39 S. Hug, M. B. Mesch, H. Oh, N. Popp, M. Hirscher, J. Senker and B. V. Lotsch, *J. Mater. Chem. A*, 2014, **2**, 5928–5936.
40 S. Dey, A. Bhunia, D. Esquivel and C. Janiak, *J. Mater. Chem. A*, 2016, **4**, 6259–6263.
41 J. H. Zhu, Q. Chen, Z. Y. Sui, L. Pan, J. Yu and B. H. Han, *J. Mater. Chem. A*, 2014, **2**, 16181–16189.
42 H. Xu, J. Wu, B. Zheng, W. Mai, F. Xu, L. Chen, H. Liu, R. Fu, D. Wu and K. Matyjaszewski, *Chem. Commun.*, 2017, **53**, 5294–5297.
43 W. Wang, W. Wang, S. Zhang, Z. Li, C. Wang and Z. Wang, *J. Chromatogr. A*, 2018, **1556**, 47–54.
44 P. Puthiaraj and W. S. Ahn, *Ind. Eng. Chem. Res.*, 2016, **55**, 7917–7923.
45 N. Zhang, F. Liu, S. Da Xu, F. Y. Wang, Q. Yu and L. Liu, *J. Mater. Chem. A*, 2017, **5**, 22631–22640.
46 D. Boonpakdee, C. F. Guajardo Yévenes, W. Surareungchai and C. La-O-Vorakiat, *J. Mater. Chem. A*, 2018, **6**, 7162–7167.
47 W. Lv, M. Guo, M. H. Liang, F. M. Jin, L. Cui, L. Zhi and Q. H. Yang, *J. Mater. Chem.*, 2010, **20**, 6668–6673.
48 V. Augustyn, P. Simon and B. Dunn, *Energy Environ. Sci.*, 2014, **7**, 1597–1614.
49 X. Lu, G. Wang, T. Zhai, M. Yu, J. Gan, Y. Tong and Y. Li, *Nano Lett.*, 2012, **12**, 1690–1696.
50 T. Kou, B. Yao, T. Liu and Y. Li, *J. Mater. Chem. A*, 2017, **5**, 17151–17173.
51 A. Eftekhari, *J. Mater. Chem. A*, 2018, **6**, 2866–2876.
52 D. Yan, Y. Wu, R. Kitaura and K. Awaga, *J. Mater. Chem. A*, 2019, **7**, 26829–26837.
53 P. L. Taberna, P. Simon and J. F. Fauvarque, *J. Electrochem. Soc.*, 2003, **150**, A292.
54 M. Ni, Z. Huang, X. Zhang, J. Liu, L. Qiao and W. Yang, *RSC Adv.*, 2017, **7**, 22447–22453.
55 Z. Bo, Z. Wen, H. Kim, G. Lu, K. Yu and J. Chen, *Carbon N. Y.*, 2012, **50**, 4379–4387.
56 Z. Wu, L. Li, Z. Lin, B. Song, Z. Li, K. S. Moon, C. P. Wong and S. L. Bai, *Sci. Rep.*, 2015, **5**, 1–7.
57 Y. Liao, H. Wang, M. Zhu and A. Thomas, *Adv. Mater.*, 2018, **30**, 1–10.
58 X.-C. Li, Y. Zhang, C.-Y. Wang, Y. Wan, W.-Y. Lai, H. Pang and W. Huang, *Chem. Sci.*, 2017, **8**, 2959–2965.
59 S. Chai, N. Hu, Y. Han, X. Zhang, Z. Yang, L. Wei, L. Wang and H. Wei, *RSC Adv.*, 2016, **6**, 49425–49428.

Chapter 4 Heteroatom containing Hypercrosslinked Polymers for Supercapacitor Applications

4.1 Introduction

In order to improve the supercapacitive energy storage performance of the electrode materials, introducing functional groups containing heteroatoms is a common method. The benefits from heteroatoms includes: (i) enhance the wettability of the materials; (ii) increase the conductivity of the materials and (iii) provide additional pseudo-capacitance.[1–3] For carbon materials, there are two main methods for introducing heteroatoms containing functional groups into the materials, one is using heteroatom enriched biomass (e.g. seaweed[4] and popcorn[5]) as precursor for carbonization and another one is to introduce heteroatoms through surface modification, for instance, the oxygen functionalities can be obtained by surface oxidation[6] while the nitrogen functional groups can be obtained from thermal treatment together with nitrogen enriched materials like ammonia or melamine.[7,8] However, the post-treatments for surface modification of carbonaceous materials are complicated, high-cost and time consuming.[9] Compared with the surface modifications, using heteroatom-enriched biomass materials as precursors for manufacturing heteroatom-doped activated carbons is a more convenient and cost-effective method. For porous organic polymers, it is easy to get a porous network with controllable functionalities by employing different monomers, like quinone and triazine containing POPs.[10,11] In order to explore the influence of different heteroatoms to the properties of the HCPs, a controlled experiment with three groups of monomers were employed. In each group, the monomers have similar structure but different heteroatoms. The structures of the monomers are derived from fluorene, diphenylmethane and triphenylmethane, respectively. The porous structures and supercapacitive performance of the heteroatom containing HCPs are discussed in this chapter.

4.2 Experimental

4.2.1 Chemicals

Dibenzofuran was purchased from Fluorochem. Dibenzothiophene, triphenylmethanol and triphenylmethanethiol were obtained from Aldrich. Triphenylmethylamine was obtained from Sigma. Diphenyl ether and diphenylamine were purchased from Sigma-Aldrich. Diphenyl sulfide was purchased from Merck. Carbazole was purchased from Alfa aesar.

4.2.2 Synthesis

Carbazole HCP

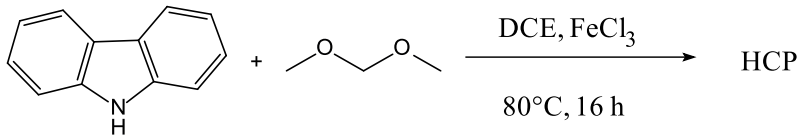

The synthesis of Carbazole HCP was performed as follows. Carbazole (5 mmol, 0.836 g, 1 eq.) and ferric chloride (20 mmol, 3.25 g, 4 eq.) were added into a dried two-neck flask with a magnetic stirrer and a condenser. DCE (25 mL) was charged into the flask by a syringe with stirring for 5 minutes to disperse the materials. Then, formaldehyde dimethyl acetal (FDA) (20 mmol, 1.77 mL, 4 eq.) was injected into the flask by syringes and the temperature was increased to 80 ℃. The reaction was heated for 20 hours. The reaction was conducted in atmospheric air. The HCP product was cooled and collected by vacuum filtration and washed with water, methanol, acetone. Then the product was transferred to a Soxhlet extractor and washed with methanol overnight. The product was dried under vacuum at 80 ℃ for overnight. Yield:1.13 g, 105.1%. Formula: $C_{16}H_9N$. Calculated value of elemental analysis C: 89.28% H: 4.21% N: 6.51%. Found value of elemental analysis C: 73.23%% H: 5.03% N: 4.78%.

Dibenzothiophene HCP

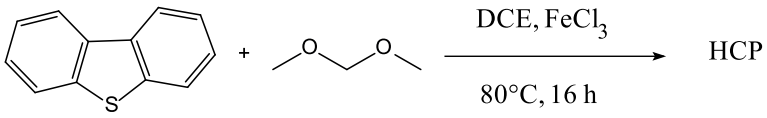

The synthesis of Dibenzothiophene HCP was performed as follows. Dibenzothiophene (5 mmol, 0.921 g, 1 eq.) and ferric chloride (20 mmol, 3.25 g, 4 eq.) were added into a dried two-neck flask with a magnetic stirrer and a condenser. DCE (25 mL) was charged into the flask by a syringe with stirring for 5 minutes to disperse the materials. Then, formaldehyde dimethyl acetal (FDA) (20 mmol, 1.77 mL, 4 eq.) was injected into the flask by syringes and the temperature was increased to 80 ℃. The reaction was heated for 20 hours. The reaction was conducted in atmospheric air. The HCP product was cooled and collected by vacuum filtration and washed with water, methanol, acetone. Then the product was transferred to a Soxhlet extractor and washed with methanol overnight. The product was dried under vacuum at 80 ℃ for overnight. Yield: 0.16 g, 13.8 %. Formula: $C_{16}H_8S$. Calculated value of elemental analysis C: 82.73% H: 3.47% S: 13.80%. Found value of elemental analysis C: 69.90% H: 3.94% S: 11.58%

Dibenzofuran HCP

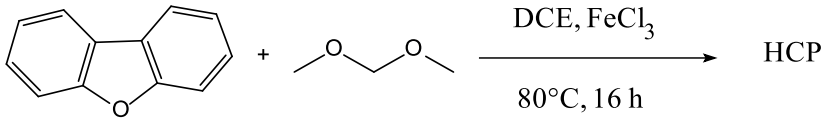

The synthesis of Dibenzofuran HCP was performed as follows. Dibenzofuran (5 mmol, 0.841 g, 1 eq.) and ferric chloride (20 mmol, 3.25 g, 4 eq.) were added into a dried two-neck flask with a magnetic stirrer and a condenser. DCE (25 mL) was charged into the flask by a syringe with stirring for 5 minutes to disperse the materials. Then, formaldehyde dimethyl acetal (FDA) (20 mmol, 1.77 mL, 4 eq.) was injected into the flask by syringes and the temperature was increased to 80 ℃. The reaction was heated for 20 hours. The reaction was conducted in atmospheric air. The HCP product was cooled and collected by vacuum filtration and washed with water, methanol, acetone.

Then the product was transferred to a Soxhlet extractor and washed with methanol overnight. The product was dried under vacuum at 80 ℃ for overnight. Yield: 1.03 g, 95.4 %. Formula: $C_{16}H_8O$. Calculated value of elemental analysis C: 88.87% H: 3.37%, O: 7.40%. Found value of elemental analysis C: 77.35% H: 4.44% O: ---

Diphenylamine HCP

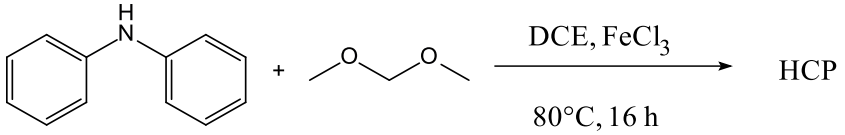

The synthesis of Diphenylamine HCP was performed as follows. Diphenylamine (5mmol, 0.846 g, 1 eq.) and ferric chloride (25 mmol, 4.06 g, 5 eq.) were added into a dried two-neck flask with a magnetic stirrer and a condenser. DCE (25 mL) was charged into the flask by a syringe with stirring for 5 minutes to disperse the materials. Then, formaldehyde dimethyl acetal (FDA) (25 mmol, 2.21 mL, 5 eq.) was injected into the flask by syringes and the temperature was increased to 80 ℃. The reaction was heated for 20 hours. The reaction was conducted in atmospheric air. The HCP product was cooled and collected by vacuum filtration and washed with water, methanol, acetone. Then the product was transferred to a Soxhlet extractor and washed with methanol overnight. The product was dried under vacuum at 80 ℃ for overnight. Yield: 0.89 g, 78%. Formula: $C_{17}H_{11}N$. Calculated value of elemental analysis C: 89.05% H: 4.84 N: 6.11%. Found value of elemental analysis C: 75.82% H: 5.47% N:5.98%

Diphenyl sulfide HCP

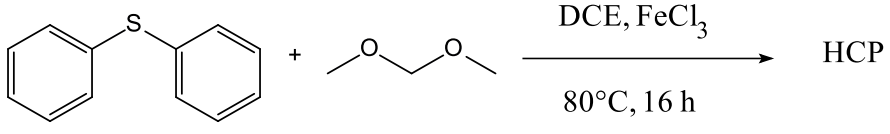

The synthesis of Diphenyl sulfide HCP was performed as follows. Ferric chloride (25 mmol, 4.06 g, 5 eq.) was added into a dried two-neck flask with a magnetic stirrer and

a condenser. DCE (25 mL) and diphenyl sulfide (5mmol, 0.84 mL, 1 eq.) were charged into the flask by syringes in sequence with stirring for 5 minutes to disperse the materials. Then, formaldehyde dimethyl acetal (FDA) (25 mmol, 2.21 mL, 5 eq.) was injected into the flask by syringes and the temperature was increased to 80 ℃. The reaction was left for over 20 hours. The reaction was conducted in atmospheric air. The HCP product was collected by vacuum filtration, but no solid product was found. Yield: 0 %.

Diphenyl ether HCP

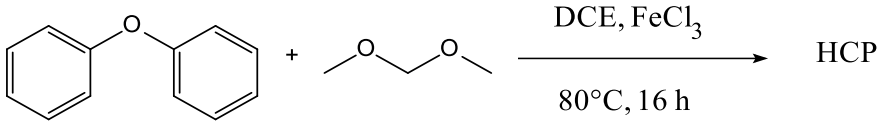

The synthesis of Diphenyl ether HCP was performed as follows. Ferric chloride (25 mmol, 4.06 g, 5 eq.) was added into a dried two-neck flask with a magnetic stirrer and a condenser. DCE (25 mL) and diphenyl ether (5mmol, 0.79 mL, 1 eq.) were charged into the flask in sequence by syringes with stirring for 5 minutes to disperse the materials. Then, formaldehyde dimethyl acetal (FDA) (25 mmol, 2.21 mL, 5 eq.) was injected into the flask by syringes and the temperature was increased to 80 ℃. The reaction was heated for 20 hours. The reaction was conducted in atmospheric air. The HCP product was cooled and collected by vacuum filtration and washed with water, methanol, acetone. Then the product was transferred to a Soxhlet extractor and washed with methanol overnight. The product was dried under vacuum at 80 ℃ for overnight. Yield: 1.22 g, 105.7%. Formula: $C_{17}H_{10}O$. Calculated value of elemental analysis C: 88.67% H: 4.38% O: 6.95%. Found value of elemental analysis C: 75.74% H: 4.97% O: ---

Triphenylmethylamine (TPMA) HCP

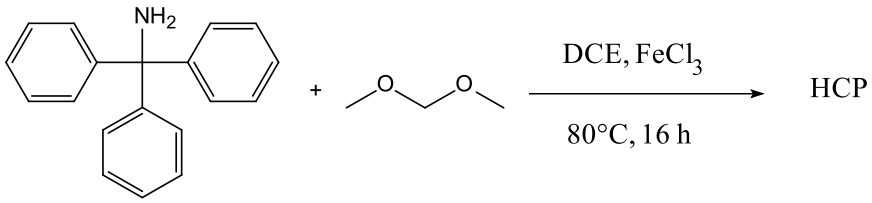

The synthesis of Triphenylmethylamine (TPMA) HCP was performed as follows. Triphenylmethylamine (5 mmol, 1.297 g, 1 eq.) and ferric chloride (37.5 mmol, 6.08 g, 7.5 eq.) were added into a dried two-neck flask with a magnetic stirrer and a condenser. DCE (25 mL) was charged into the flask by a syringe with stirring for 5 minutes to disperse the materials. Then, formaldehyde dimethyl acetal (FDA) (37.5 mmol, 3.32 mL, 7.5 eq.) was injected into the flask by syringes and the temperature was increased to 80 ℃. The reaction was heated for 20 hours. The reaction was conducted in atmospheric air. The HCP product was cooled and collected by vacuum filtration and washed with water, methanol, acetone. Then the product was transferred to a Soxhlet extractor and washed with methanol overnight. The product was dried under vacuum at 80 ℃ for overnight. Yield: 1.59 g, 90.9%. Formula: $C_{26.5}H_{17}N$. Calculated value of elemental analysis C: 91.12% H: 4.87% N 4.01%. Found value of elemental analysis C: 80.47% H: 5.55% N: 0.96%

Triphenylmethanethiol (TPMT) HCP

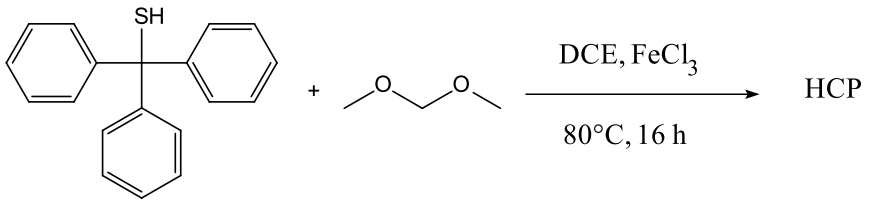

The synthesis of Triphenylmethanethiol (TPMT) HCP was performed as follows. Triphenylmethanethiol (5 mmol, 1.382 g, 1 eq.) and ferric chloride (37.5 mmol, 6.08 g, 7.5 eq.) were added into a dried two-neck flask with a magnetic stirrer and a condenser. DCE (25 mL) was charged into the flask by a syringe with stirring for 5 minutes to disperse the materials. Then, formaldehyde dimethyl acetal (FDA) (37.5 mmol, 3.32

mL, 7.5 eq.) was injected into the flask by syringes and the temperature was increased to 80 ℃. The reaction was heated for 20 hours. The reaction was conducted in atmospheric air. The HCP product was cooled and collected by vacuum filtration and washed with water, methanol, acetone. Then the product was transferred to a Soxhlet extractor and washed with methanol overnight. The product was dried under vacuum at 80 ℃ for overnight. Yield: 1.71 g, 93.2%. Formula: $C_{26.5}H_{16}S$. Calculated value of elemental analysis C: 86.89% H: 4.37% S: 8.74%. Found value of elemental analysis C: 79.45% H: 4.84% S: 3.57%

Triphenylmethanol (TPMO) HCP

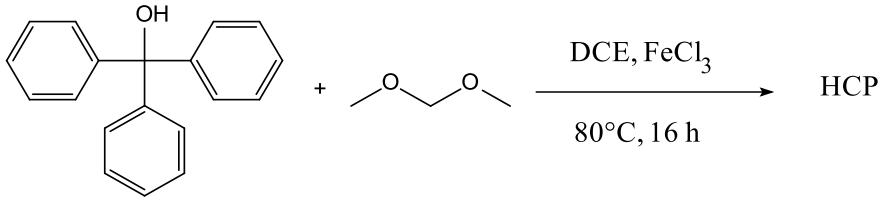

The synthesis of Triphenylmethanol (TPMO) HCP was performed as follows. Triphenylmethanol (5 mmol, 1.302 g, 1 eq.) and ferric chloride (37.5 mmol, 6.08 g, 7.5 eq.) were added into a dried two-neck flask with a magnetic stirrer and a condenser. DCE (25 mL) was charged into the flask by a syringe with stirring for 5 minutes to disperse the materials. Then, formaldehyde dimethyl acetal (FDA) (37.5 mmol, 3.32 mL, 7.5 eq.) was injected into the flask by syringes and the temperature was increased to 80 ℃. The reaction was heated for 20 hours. The reaction was conducted in atmospheric air. The HCP product was cooled and collected by vacuum filtration and washed with water, methanol, acetone. Then the product was transferred to a Soxhlet extractor and washed with methanol overnight. The product was dried under vacuum at 80 ℃ for overnight. Yield: 1.60 g, 91.6%. Formula: $C_{26.5}H_{16}O$. Calculated value of elemental analysis C: 90.86% H: 4.57% O: 4.57%. Found value of elemental analysis C: 75.29% H: 4.99% O: ---

4.3 Result and discussion

4.3.1 Synthesis

The heteroatom containing monomers are used as monomers of Friedel-Crafts alkylation reaction with formaldehyde dimethyl acetal (FDA) used as an external crosslinker and anhydrous $FeCl_3$ used as a Lewis acid catalyst for heteroatom containing HCPs synthesis, in air atmosphere and at 80 ℃. The synthesis of HCPs with knitting method conducted in air atmosphere was also reported in the previous literatures.[12,13] The HCPs can be synthesized in air atmosphere indicates the cost of the potential mass production of HCPs in the future could be reduced, e.g., dry solvents can be replaced by common solvents for HCP synthesis. The yields of these samples were calculated and the elemental analysis was performed in the table 4.1.

	Yield		Calculated value			Found value		
			C %	H %	Heteroatom content%	C %	H %	Heteroatom content%
Carbazole HCP	1.13 g	105.1%	89.28%	4.21%	N: 6.51%	73.23%	5.03%	N: 4.78%
Dibenzothiophene HCP	0.16 g	13.8%	82.73%	3.47%	S: 13.80%	69.90%	3.94%	S: 11.58%
Dibenzofuran HCP	1.03 g	95.4%	88.87%	3.37%	O: 7.40%	77.35%	4.44%	O: ---
Diphenylamine HCP	0.89 g	78.0%	88.25%	7.07%	N: 4.68%	75.82%	5.47%	N: 5.98%
Diphenyl sulfide HCP	0 g	---	---	---	---	---	---	---
Diphenyl ether HCP	1.22 g	105.7%	88.67%	4.38%	O: 6.95%	75.74%	4.97%	O: ---
Triphenylmethylamine (TPMA) HCP	1.59 g	90.9%	91.12%	4.87%	N: 4.01%	80.47%	5.55%	N: 0.96%
Triphenylmethanethiol (TPMT) HCP	1.71 g	93.2%	86.89%	4.37%	S: 8.74%	79.45%	4.84%	S: 3.57%
Triphenylmethanol (TPMO) HCP	1.60 g	91.6%	90.86%	4.57%	O: 4.57%	75.29%	4.99%	O: ---

Table 4.1 The yields and elemental analysis results of the heteroatom containing HCPs

In the table 4.1, it can be seen that the monomer of diphenyl sulfide could not generate solid HCP network under the synthesis condition of the Friedel-Crafts alkylation reaction used for other samples. For another sulfur-containing sample, the Dibenzothiophene HCP shows a much lower yield than other samples, 13.8%. The

reason for this can be attributed to the 3d orbital of the S atom participates in the hybridization, which reduces the electron cloud density on aromatic rings.[14] The nitrogen-containing Diphenylamine HCP also shows a lower yield, 78%, this can be attributed to chelate coordination of the nitrogen atoms and Fe^{3+} destroying the catalytic performance of ferric chloride.[15] Although the sulfur and nitrogen atoms could influence the aromatic electrophilic substitution reaction, it depends on the configuration of them, for instance, the Carbazole HCP shows a high yield, 105.1%. The Diphenyl ether HCP also presents a high yield, 105.7%.

The reason for the yield higher than 100% can be ascribed to the incompletely reacted crosslinker residue, like -O-CH_3.[16] Due to the existence of the unexpected extra oxygen atoms in the network of the synthesized HCPs, the yield can be higher than 100%. For other samples which have yields higher than 90% but lower than 100%, the crosslinker residues also exist in their molecular network as it can be confirmed by the elemental analysis. In the elemental analysis results, it can be seen that the experimental values of C% and H% are lower than those of the calculated values, indicating the existence of the incompletely reacted crosslinker residues. It can be found that the sulfur content in the Dibenzothiophene HCP and the nitrogen content in the Diphenylamine are higher than the calculated value, indicating the amount of the crosslinkers connected with these two monomers is lower than calculated, i.e., the lower crosslinking density in these two HCP samples.

The reason for the formation of the incompletely reacted crosslinker residue is due to the intense steric impediment. The reaction rate of Friedel-Crafts alkylation reaction for HCP synthesis is fast, therefore the HCP network with high rigidity can be formed rapidly. After the rigid HCP networks are formed, the intense steric impediment limits the accessibility of crosslinkers and monomers, some crosslinker only react with aromatic monomers at one end, thus the incompletely reacted crosslinker residues are formed, meanwhile some small HCP particles cannot grow larger and hence will be lost in the washing and filtration process, resulting in some samples have a yield lower than 100%.

4.3.2 FTIR and ^{13}C Solid State NMR spectroscopy

The molecular structures of heteroatom containing HCPs were analyzed and confirmed by using Fourier transform infrared (FTIR) and ^{13}C solid state NMR.

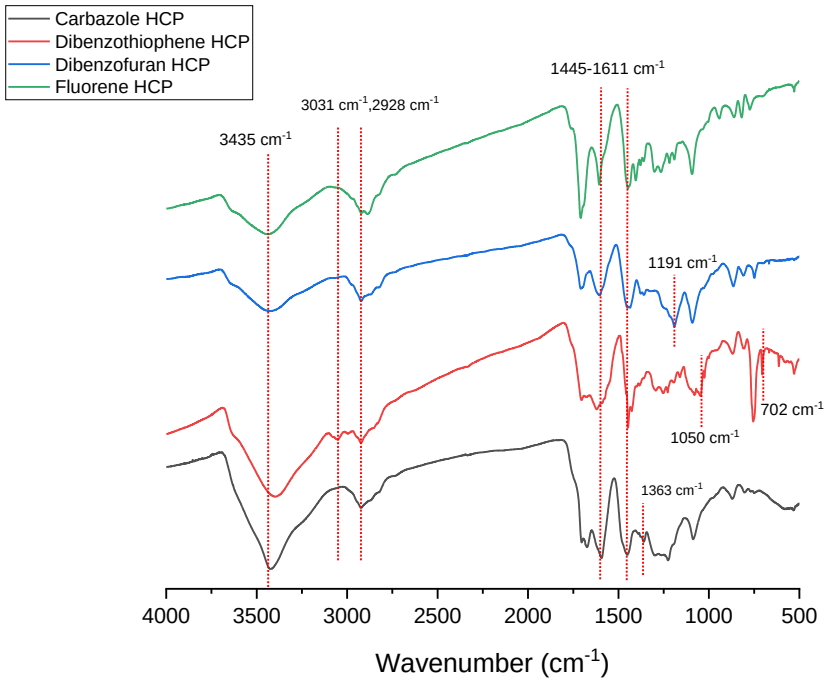

Figure 4.1 FTIR spectra of HCPs synthesized from fluorene-liked heteroatom containing monomers

In the FTIR spectra of HCPs synthesized from fluorene-liked heteroatom containing monomers, the peak at 2928 cm^{-1} can be assigned to C-H stretching in methylene bridges and the weak peak at 3031 cm^{-1} could be ascribed to C-H stretching in aromatic rings.[17–20] The peaks at 1445-1611 cm^{-1} can be assigned to the vibration of aromatic ring skeletons.[21–24] The peak at 1092 cm^{-1} corresponds to C-O stretching in crosslinker residue.[25] The peak at 3435 cm-1 could be attributed to the O-H stretching in physisorbed water which existed in the KBr disc and the porous structure of the HCPs.[26–29] For Dibenzofuran HCP, the peak at 1191 cm^{-1} corresponds to the C-O-C stretching in dibenzofuran.[30] In terms of Dibenzothiophene HCP, the peaks at 1050 cm^{-1} and 702 cm^{-1} are assigned to the stretching of C-S-C.[31,32] As for carbazole HCP, the peak at 1383 cm^{-1} correspond to the stretching of C-N-C.[33,34]

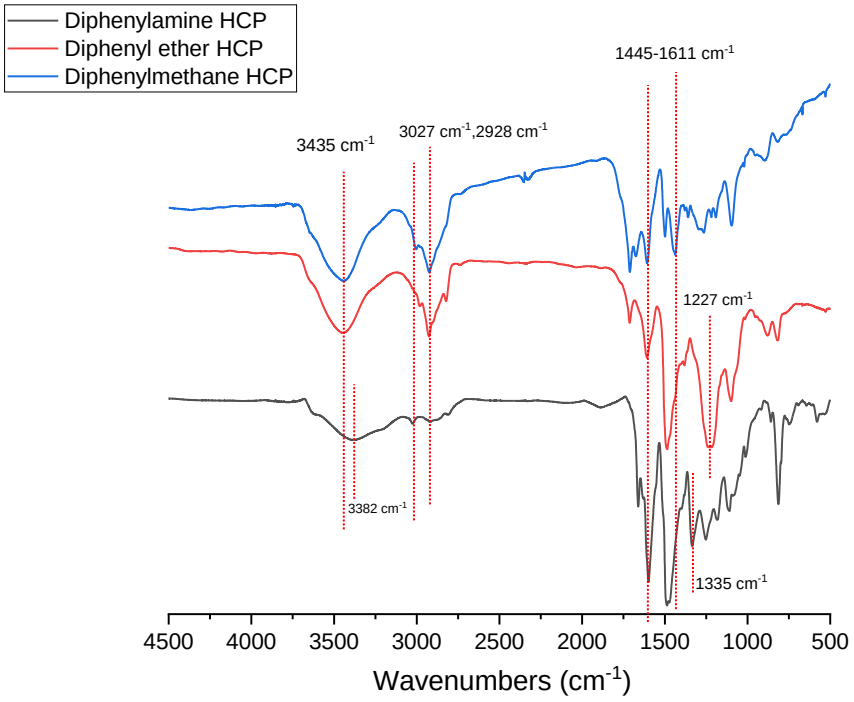

Figure 4.2 FTIR spectra of HCPs synthesized from diphenylmethane-liked heteroatom containing monomers

In the FTIR spectra of HCPs synthesized from diphenylmethane-liked heteroatom containing monomers, the peak at 2928 cm^{-1} and the weak peak at 3027 cm^{-1} correspond to C-H stretching in the methylene bridge and C-H stretching in aromatic rings, respectively. For Diphenylmethane HCP, the peaks at 1445-1611 cm^{-1} are assigned to the vibration of aromatic ring skeletons, while for Diphenyl ether HCP and Diphenylamine HCP, the peak at 1445 cm^{-1} shift to 1485 cm^{-1}, this is in consistency with previous literatures.[35,36] The peak at 1092 cm^{-1} corresponds to C-O stretching in crosslinker residue. For Diphenylmethane HCP and Diphenyl ether HCP, the peak at 3435 cm-1 could be attributed to the O-H stretching in physisorbed water which existed in the KBr disc and the porous structure of the HCPs, while in terms of diphenyl amine HCP, the peak at 3382 cm^{-1} can be assigned to N-H stretching of diphenyl amine moieties.[37] For Diphenyl ether HCP, the peak at 1227 cm^{-1} corresponds to aromatic C-O stretching in diphenyl ether building blocks.[38] For Diphenylamine HCP, the peak at 1335 cm^{-1} is ascribed to aromatic C-N stretching in diphenylamine.[39]

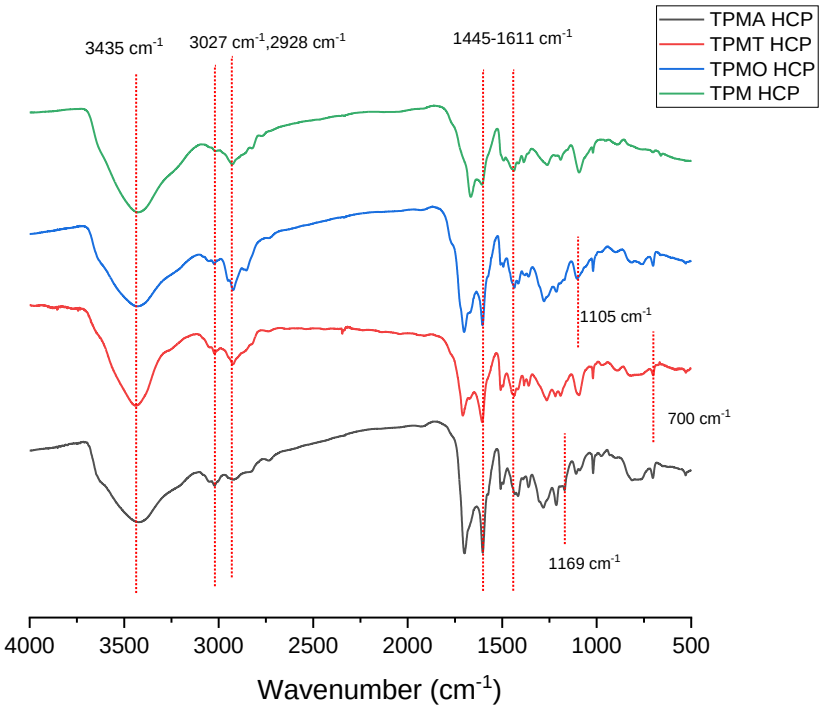

Figure 4.3 FTIR spectra of HCPs synthesized from triphenylmethane (TPM)-liked heteroatom containing monomers

In the FTIR spectra of HCPs synthesized from TPM-liked heteroatom containing monomers, the peak at 2928 cm^{-1} and the weak peak at 3027 cm^{-1} could be ascribed to C-H stretching in methylene bridges and C-H stretching in aromatic rings, respectively. The peaks at 1445-1611 cm^{-1} are ascribed to the vibration of aromatic ring skeletons. The peak at 1092 cm^{-1} corresponds to C-O stretching in crosslinker residue. For TPMO HCP, the peak at 1109 cm^{-1} corresponds to C-O stretching.[40] For TPMA HCP, the peak at 1169 cm^{-1} is assigned to C-N stretching.[41] For TPMT HCP, the absence of the peak at around 2570 cm^{-1} which corresponds to S-H stretching is in consistency with the results of the TPMT HCP synthesized by He et al., and the explanation given by them is the formation of disulfide linkages during the thermal reaction.[42] The peak at 700 cm^{-1} can be ascribed to C-S stretching of TPMT,[43] but the peak at this position can be also attributed to the C-H out-of-plane bending vibration of the monosubstituted benzene,[44] so this peak can be also observed for other samples in this group.

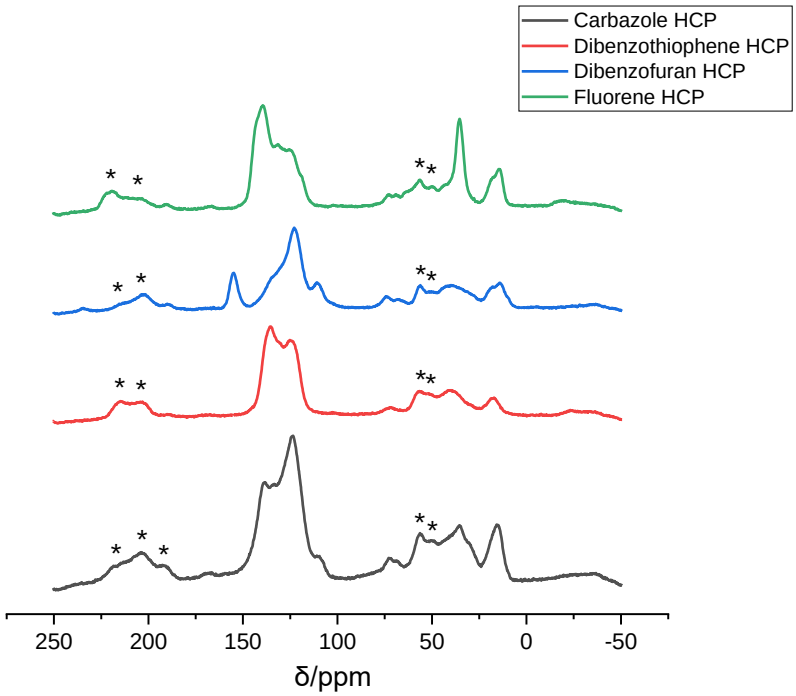

Figure 4.4 ^{13}C solid state NMR spectra of HCPs synthesized from fluorene-liked heteroatom containing monomers (the asterisks denote spinning side bands)

In the ^{13}C solid state NMR spectra of HCPs synthesized from fluorene-liked heteroatom containing monomers, the peaks at around 135 ppm and 125 ppm correspond to substituted aromatic carbon and the non-substituted aromatic carbon, respectively.[45–48] The peak at around 36 ppm is attributed to the carbon in methylene bridges.[49–52] The peak at 73 ppm and 18 ppm can be ascribed to carbon in the methylene group binding to oxygen atom of crosslinker residue and the methyl carbon at the end of crosslinker residue.[53] For the Dibenzofuran HCP, the peak at 155 ppm corresponds to the aromatic carbon connected with the oxygen atom and the peak at 110 ppm is assigned to the carbon in the meta position of the five-numbered ring.[54] For the Carbazole HCP, the peak at 139 ppm is assigned to the aromatic carbon directly connected to the nitrogen atom, and the peak at 110 ppm corresponds to the carbon (the one not in the five-numbered ring) adjacent to the carbon directly connected to the nitrogen atom.[55] For the Dibenzothiophene HCP, the peak corresponds to carbon connected with the sulfur atom almost overlaps with the peak assigned to the crosslinker substituted aromatic carbon at around 138 ppm.[56]

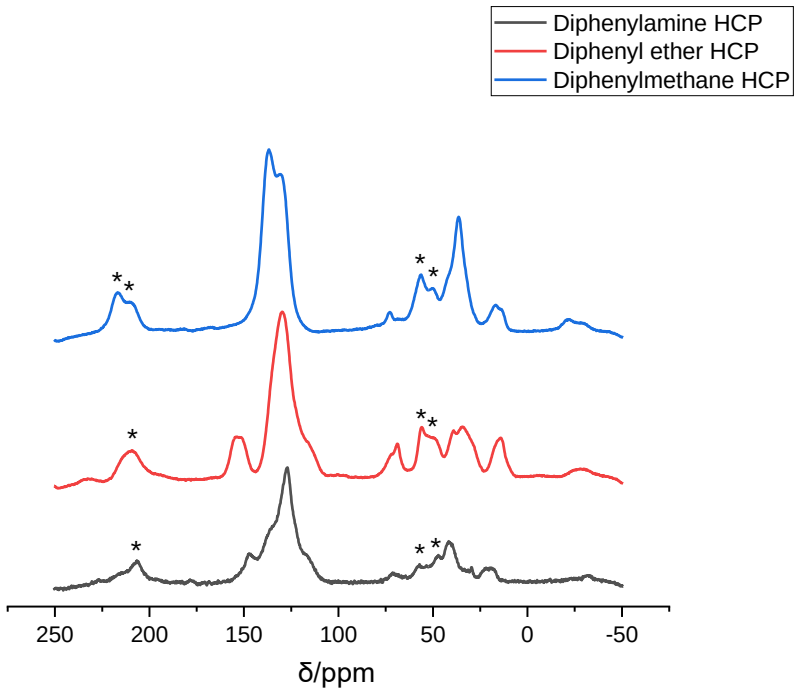

Figure 4.5 ^{13}C solid state NMR spectra of HCPs synthesized from diphenylmethane-liked heteroatom containing monomers (the asterisks denote spinning side bands)

In the ^{13}C solid state NMR spectra of the Diphenyl ether HCP and the Diphenylamine HCP, it can be seen that the gap between the peaks assigned to substituted aromatic carbon at around 135 ppm and the peaks at around 125 ppm corresponding to non-substituted aromatic carbon disappeared. The peak at around 36 ppm is attributed to the carbon in methylene bridges. The peak at 73 ppm and 18 ppm can be ascribed to carbon in the methylene group binding to oxygen atom of crosslinker residue and the methyl carbon at the end of crosslinker residue. For the Diphenyl ether HCP, the peak at 153 pm is ascribed to the carbon connected with the oxygen atom and the peak shoulder at 112 ppm corresponds to the carbon in the ortho position of the carbon connected with the oxygen atom.[57] In terms of the Diphenylamine HCP, the peak at 147 ppm corresponds to the carbon directly connected with the nitrogen atom and the peak shoulder at 116 ppm can be ascribed to the carbon in the ortho position of carbon connected with the nitrogen atom.[58]

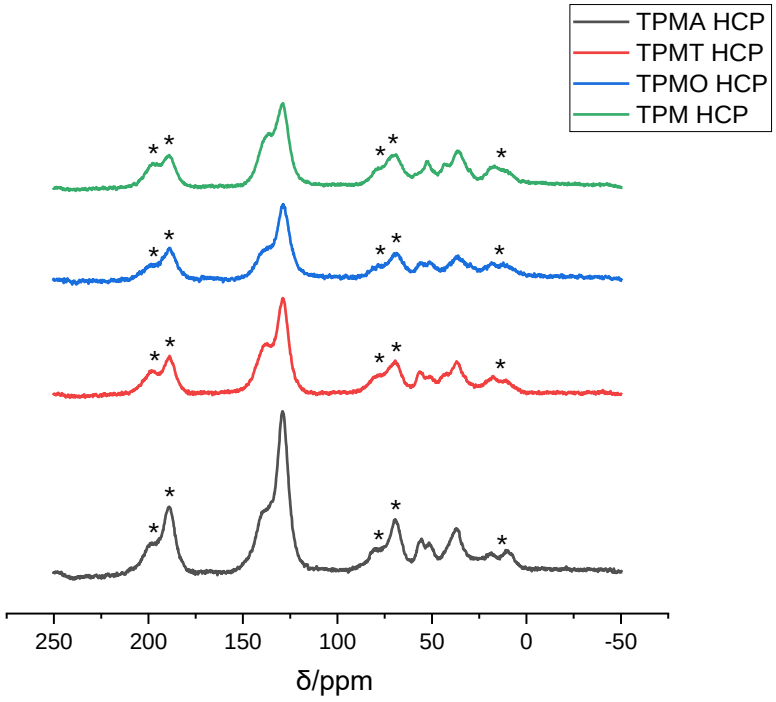

Figure 4.6 ^{13}C solid state NMR spectra of HCPs synthesized from triphenylmethane (TPM)-liked heteroatom containing monomers obtained with a MAS rate of 7.5 kHz (the asterisks denote spinning side bands)

In the ^{13}C solid state NMR spectra of HCPs synthesized from TPM-liked heteroatom containing monomers obtained with 7.5 kHz MAS, the peaks at around 135 ppm and 125 ppm correspond to substituted aromatic carbon and the non-substituted aromatic carbon, respectively. The peak at around 36 ppm is attributed to the carbon in methylene bridges. The peak at 73 ppm can be ascribed to carbon in the methylene group binding to oxygen atom of crosslinker residue, the peak at 51 ppm can be attributed to the carbon in completely reacted methylene bridges binding with phenyl, and the methyl carbon at the end of crosslinker residue.[53] Compared with the TPM HCP, the TPMO HCP has a peak at 56 ppm corresponding to the carbon connected with the hydroxyl group.[59] It can be seen that the TPMT HCP and the TPMA HCP also have a peak at around 56 ppm, corresponding to the carbon connected with the heteroatom containing functional groups.

4.3.3 TGA

The thermal stability of the heteroatom containing HCPs was characterized by using thermalgravimetric analysis (TGA). The TGA was conducted under a N_2 atmosphere and the samples were heated from 25 °C to 800 with a heating rate 10 °C/min.

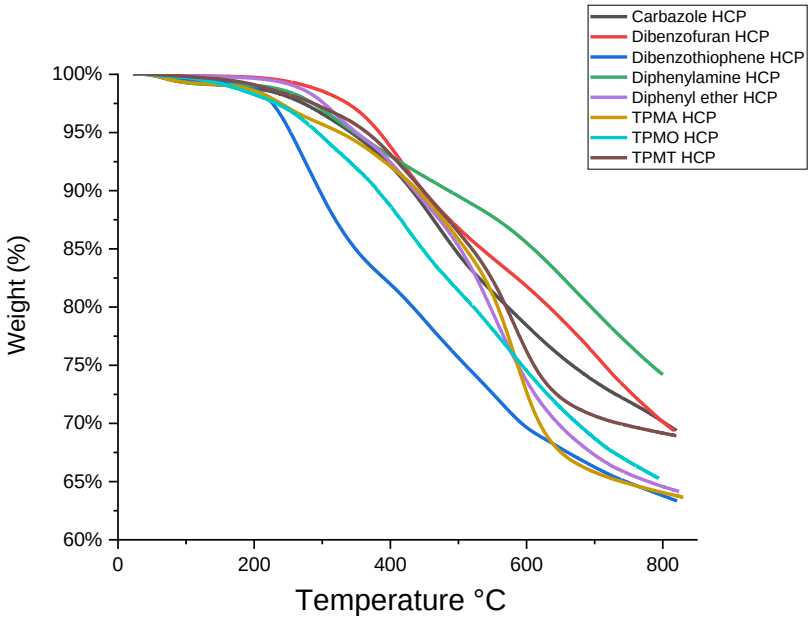

Fig 4.7 TGA spectra of heteroatom containing HCPs

From the TGA curves of the heteroatom containing HCPs, it can be found that the weight residue of these samples is higher than 90% at 300 °C. At 800 °C, the weight residue of these samples is higher than 60 %. The Dibenzothiophene HCP has a lower onset temperature, this can be ascribed to its low crosslinking density which is discussed in the synthesis analysis part.

4.3.4 N_2 Sorption

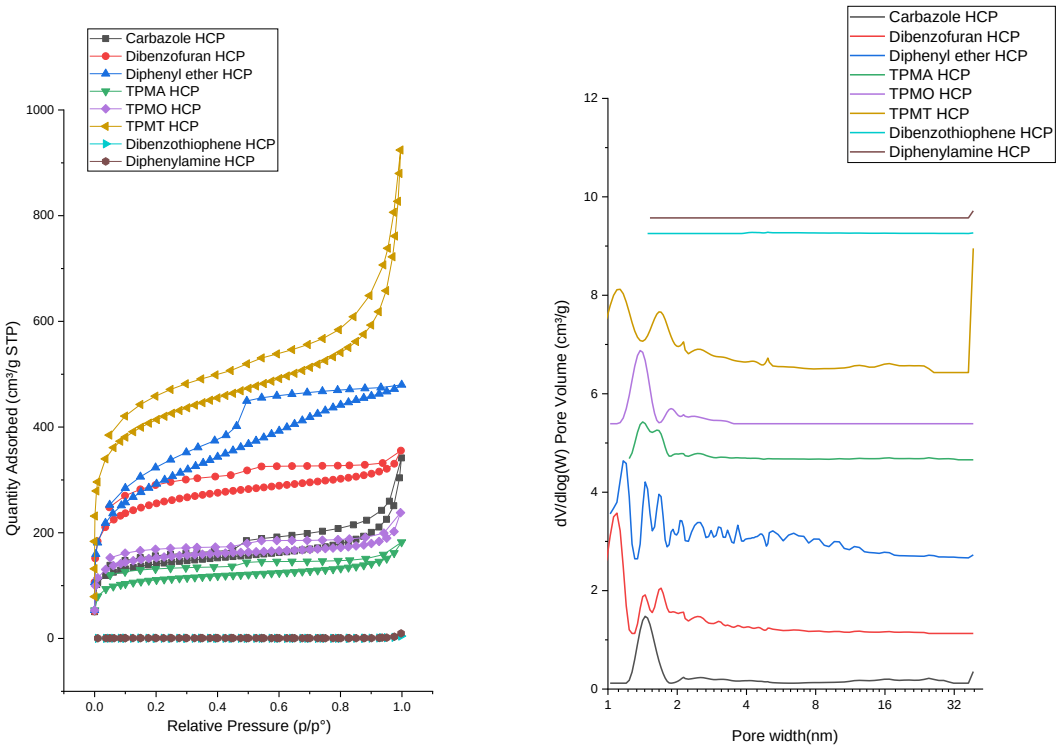

Figure 4.8 Isotherm and pore size distribution of heteroatom containing HCPs

The porosity of the HCPs synthesized from heteroatom containing monomers was characterized by N_2 sorption analysis at 77 K. According to IUPAC definition, most of these samples showed a Type II and Type IV combined isotherm. The N_2 uptake in very low relative pressure region ($p/p_0<0.01$) indicates the existence of the microporous structure,[60] the hysteresis loop in the relative pressure range 0.43-1.0 indicating the existence of mesopores.[61] The gradual rise in the relative pressure range of 0.9-1.0 demonstrating the existence of macropores.[62] From the quite low N_2 adsorption amount of Diphenylamine HCP and Diphenylamine HCP, it can be seen that these two samples have very low specific surface area.

In the pore size distribution curves of the heteroatom containing HCPs, it can be seen that most of the samples show main peaks in the range of 1-2 nm, indicating the microporosity in these samples. For Diphenylamine HCP and Diphenylamine HCP, no peak is shown in their pore size distribution curve, corresponding to their non-porosity

property. The single point adsorption total pore volumes of the HCPs synthesized from heteroatom containing monomers obtained at p/p_0=0.99 and the BET surface areas of them are shown in the table 4.2.

	BET surface area (m^2/g)	Single point adsorption total pore volume at p/p_0=0.99 (cm^3/g)
Fluorene HCP	1003.9	0.66
Carbazole HCP	523.4	0.53
Dibenzofuran HCP	945.9	0.55
Diphenylmethane HCP	1240.8	0.95
Diphenyl ether HCP	1049.2	0.74
TPM HCP	1219.1	0.81
TPMA HCP	412.6	0.28
TPMT HCP	1520.5	1.43
TPMO HCP	574.3	0.37
Dibenzothiophene HCP	1.6	--
Diphenylamine HCP	2.8	--

Table 4.2 BET surface area and total pore volume of the heteroatom containing HCPs

The BET surfaces of the Carbazole HCP, Dibenzofuran HCP, Diphenyl ether HCP, TPMA HCP, TPMT HCP and TPMO HCP are 523.4, 945.9, 1049.2, 412.6, 1520.5 and 574.3 m^2/g, the total pore volumes of them are 0.53, 0.55, 0.74, 0.28, 1.43 and 0.37 cm^3/g, respectively. The BET surface of the Dibenzothiophene HCP and the Diphenylamine HCP are 1.6 m^2/g and 2.8 m^2/g, the non-porous property of these two samples indicates the predominant linear structures of them, this result agrees with the conclusion from the elemental analysis, i.e., the low crosslinking density of these two samples. The BET surface areas of the Fluorene HCP, Diphenylmethane HCP, and TPM HCP are 1003.9, 1240.8, and 1219.1 m^2/g, and the total pore volumes of them are 0.66,

0.95 and 0.81 cm^3/g, respectively. Compared with the Fluorene HCP, the Carbazole HCP and Dibenzofuran HCP show lower BET surfaces and total pore volumes. Although the Carbazole HCP has a much lower BET surface than the Dibenzofuran HCP, the total pore volume of the Carbazole HCP is similar to that of the Dibenzofuran HCP. In the previous literature review, carbazole HCP has a BET surface area of 445 m^2/g,[59] lower than that of the Carbazole HCP in my work.

Compared with the Diphenylmethane HCP, the Diphenyl ether HCP also shows a lower BET surface area and total pore volume. Compared with the TPM HCP, the nitrogen containing TPMA HCP and the oxygen containing TPMO HCP show much lower BET surface areas and total pore volumes, while the sulfur containing TPMT HCP shows a much higher BET surface area and a total pore volume than the TPM HCP. The triphenylmethanol HCP synthesized by James et al. has a BET surface area of 781 m^2/g,[59] higher than the TPMO HCP synthesized in my work. The triphenylmethanethiol HCP synthesized by He et al. has a BET surface area of 649 m^2/g,[42] lower than that of the TPMT HCP synthesized in my work.

The pore volumes of the pores with different pore widths and pore volume proportions of them are performed in the table 4.3 and figure 4.9 for further insight into the pore volume compositions of the heteroatom containing HCPs.

Material	Pore volume of the pores with pore width less than 2 nm (cm^3/g)	Pore volume of the pores with pore width 2-10 nm (cm^3/g)	Pore volume of the pores with pore width larger than 10 nm (cm^3/g)
Fluorene HCP	0.42	0.07	0.17
Carbazole HCP	0.22	0.06	0.25
Dibenzofuran HCP	0.40	0.07	0.08
Diphenylmethane HCP	0.53	0.34	0.08
Diphenyl ether HCP	0.45	0.23	0.06

TPM HCP	0.52	0.23	0.06
TPMA HCP	0.17	0.03	0.08
TPMT HCP	0.64	0.20	0.59
TPMO HCP	0.24	0.03	0.10

Table 4.3 The pore volumes of the pores with different pore widths of the heteroatom containing HCPs

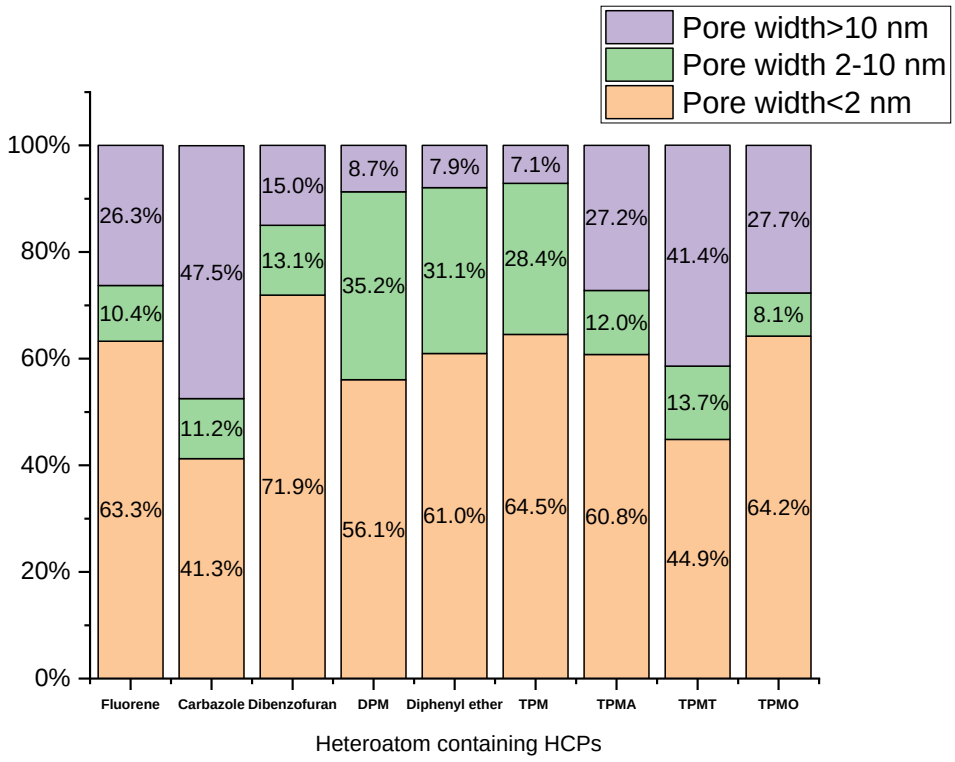

Figure 4.9 Pore volume proportions of heteroatom containing HCPs

For the Carbazole HCP, the volume proportions of the micropores, pores with the pore width 2-10 nm and the pores with diameter larger than 10 nm are 41.3%, 11.2% and 47.5%, the pore volumes of these pores are 0.22, 0.06 and 0.25 cm^3/g, respectively. For the Dibenzofuran HCP, the volume proportions of these pores are 71.9%, 13.1% and 15.0% and the pore volumes of these pores are 0.40, 0.07 and 0.08 cm^3/g, respectively. For the Fluorene HCP, the micropore volume proportion and micropore volume are 63.3% and 0.42 cm^3/g, the volume proportion of the pores with the pore width 2-10 nm and the pore volume of them are 10.4% and 0.07 cm^3/g, the volume proportions of the pores with diameter larger than 10 nm and the pore volumes of them are 26.3% and

0.17 cm^3/g.

Therefore, the Fluorene HCP has the highest micropore volume among the three samples (the Carbazole HCP, the Dibenzofuran HCP, and the Fluorene HCP). Although the Dibenzofuran HCP has the highest micropore proportion among the three samples, whereas it has lower micropore volume than the Carbazole HCP which has the lowest micropore volume proportion among the three samples. The volume proportions of the pores with the pore width 2-10 nm in these three samples are similar, the pore volumes of these pores are similar as well, while it can be found that the Carbazole HCP has slightly higher pore volume of the pores with the pore width 2-10 nm than other two samples. The Carbazole HCP has the highest volume proportion and the highest pore volume of the pores with diameter larger than 10 nm among all the three samples. For the Diphenyl ether HCP, the pore volume proportions and the pore volumes of the micropores, pores with the pore width 2-10 nm and the pores with diameter larger than 10 nm are 61.0%, 31.1%, 7.9%, and 0.45, 0.23, 0.06 cm^3/g, respectively, while the volume proportion and the pore volume of the Diphenylmethane HCP is 56.1%, 35.2%, 8.7%, and 0.53, 0.34 and 0.08 cm^3/g, respectively. Therefore, the similarity in the pore volume proportions of the Diphenylmethane HCP and Diphenyl ether HCP can be seen, while the Diphenyl ether HCP shows lower pore volumes of the pores with different diameters. For the TPMA HCP, the volume proportions and the pore volumes of the micropores, pores with the pore width 2-10 nm and the pores with diameter larger than 10 nm are 60.8%, 12.0%, 27.2% and 0.17, 0.03, 0.08 cm^3/g, respectively. The volume proportions and the pore volumes of the pores with different pore diameters in the TPMT HCP are 44.9%, 13.7% 41.4% and 0.64, 0.20, 0.59 cm^3/g, respectively, and the volume proportions and the pore volumes of these pores in the TPMO HCP are 64.2%, 8.1%, 27.7% and 0.24, 0.03, 0.10 cm^3/g, respectively. The volume proportions and the pore volumes of the micropores, pores with the pore width 2-10 nm and the pores with diameter larger than 10 nm in the TPM HCP are 64.5%, 28.4%, 7.1% and 0.52, 0.23, 0.06 cm^3/g, respectively. It can be seen that the TPMT HCP and TPMO HCP have similar pore volume proportions with the TPM HCP, and they all have a volume

proportion of the micropores higher than 60%. The pore volumes of the pores with different pore diameters in the TPMA HCP and TPMO HCP are lower than that in the TPM HCP. The TPMT HCP showed a different pore volume composition, a lower micropore volume proportion and a higher pore volume proportion of the pores with pore width larger than 10 nm. Except for the pore volume of the pores with diameter 2-10 nm, the micropore volume and the volume of the pores with diameter larger than 10 nm in the TPMT HCP are the highest among these four samples (i.e., TPM HCP, TPMA HCP, TPMT HCP and TPMO HCP).

4.3.5 Cyclic Voltammetry

The electrochemical properties of HCPs were evaluated by a typical three-electrode system with 1 M Na_2SO_4 aqueous solution as electrolyte. The active material on nickel foam, a platinum electrode and an Ag/AgCl (3 M KCl, 0.207 V vs. standard hydrogen electrode at 25 °C) electrode were used as working electrode, counter electrode and reference electrode, respectively. The CV tests were conducted with different scan rates 2, 10, 25, 50, 75, 100 and 200 mV/s in the voltage range of -0.2 V-0.8 V.

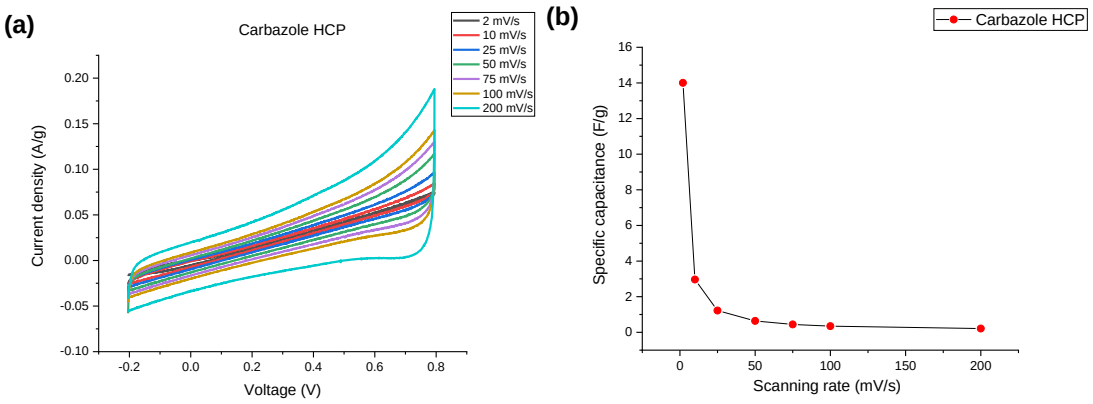

Figure 4.10 (a) CV curves at different scanning rate, and (b) Specific capacitance obtained at different scanning rates of the Carbazole HCP

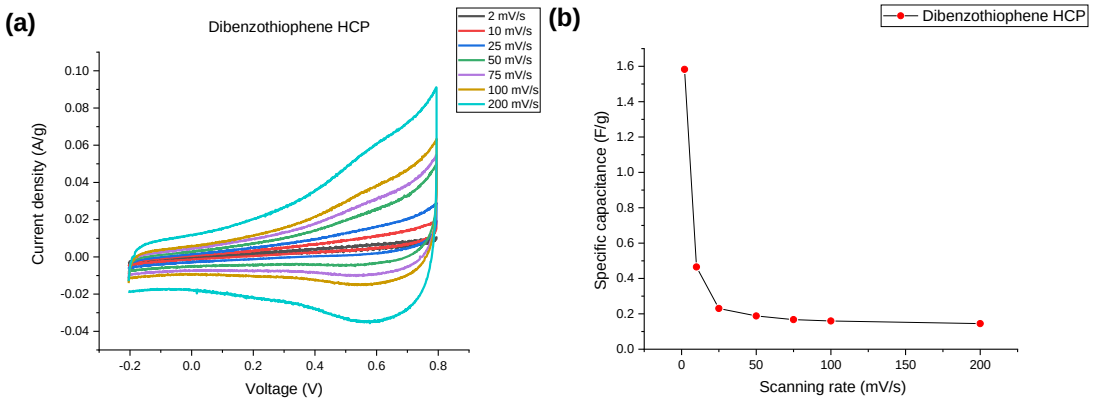

Figure 4.11 (a) CV curves at different scanning rate, and (b) Specific capacitance obtained at different scanning rates of the Dibenzothiophene HCP

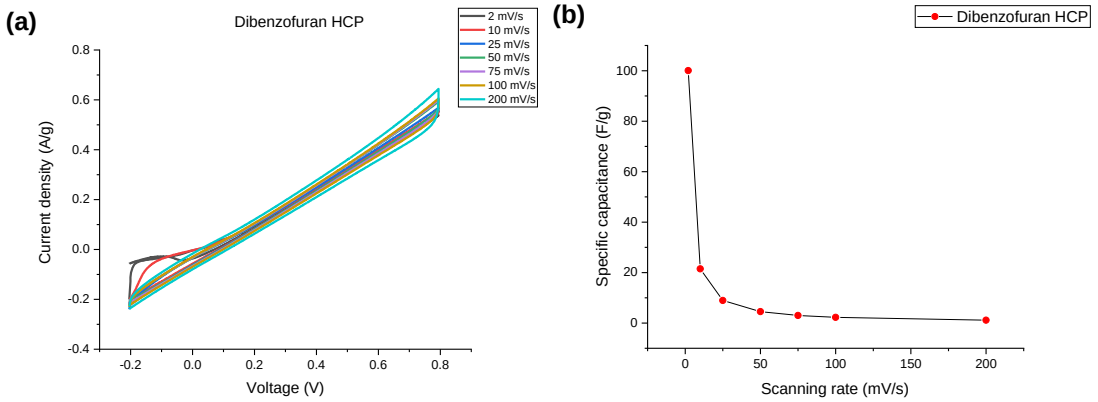

Figure 4.12 (a) CV curves at different scanning rate, and (b) Specific capacitance obtained at different scanning rates of the Dibenzofuran HCP

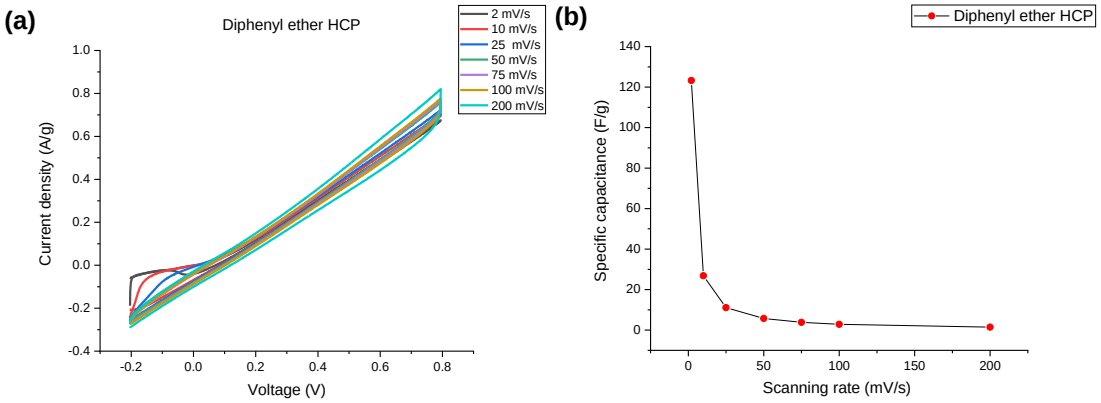

Figure 4.13 (a) CV curves at different scanning rate, and (b) Specific capacitance obtained at different scanning rates of the Diphenyl ether HCP

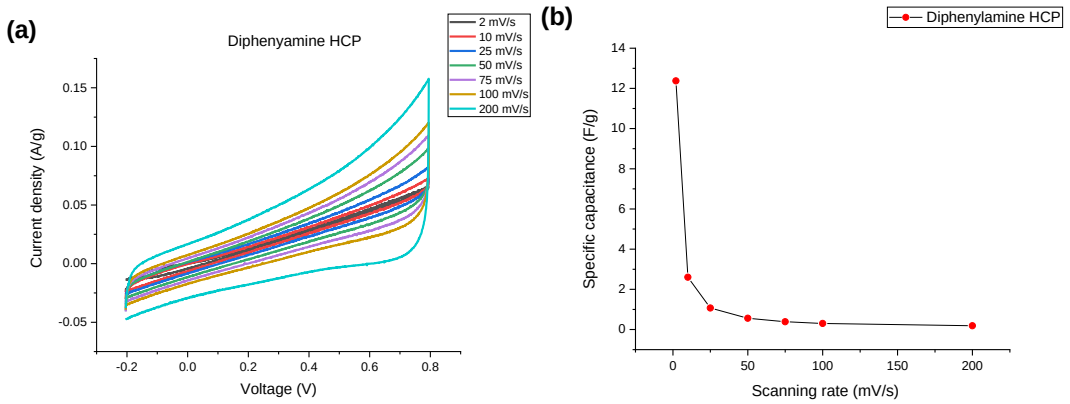

Figure 4.14 (a) CV curves at different scanning rate, and (b) Specific capacitance obtained at different scanning rates of the Diphenylamine HCP

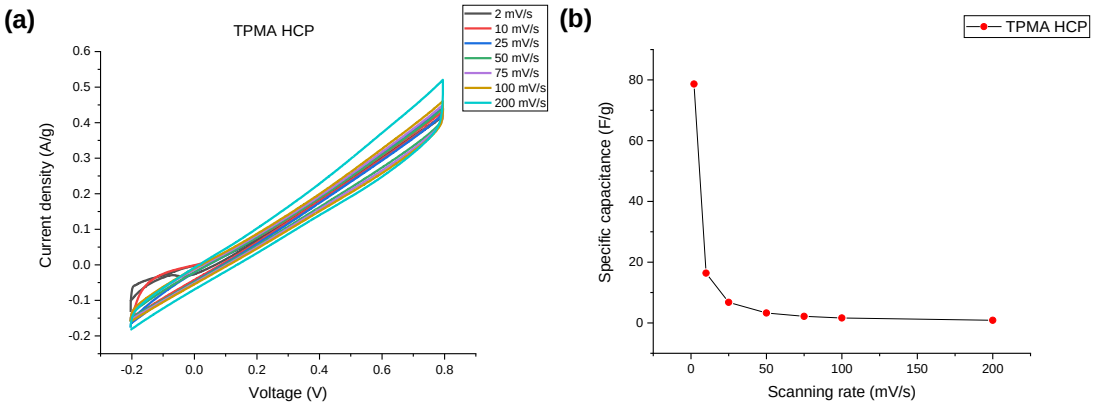

Figure 4.15 (a) CV curves at different scanning rate, and (b) Specific capacitance obtained at different scanning rates of the TPMA HCP

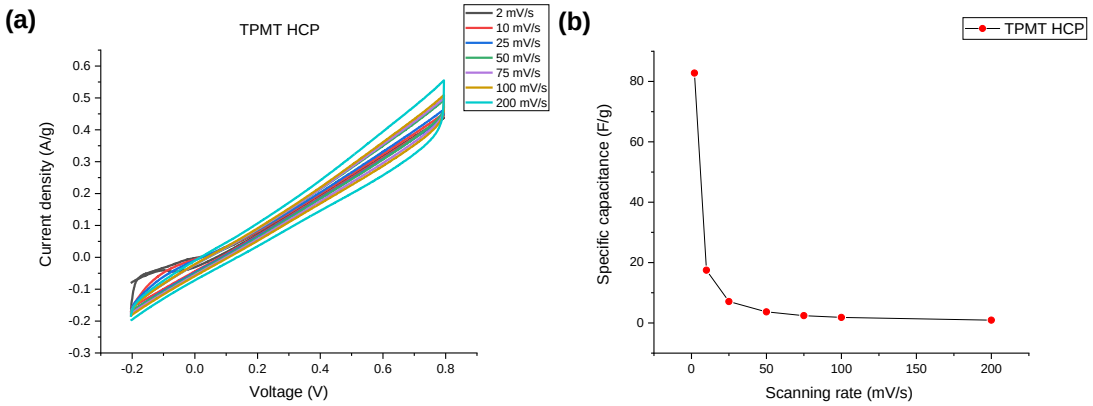

Figure 4.16 (a) CV curves at different scanning rate, and (b) Specific capacitance obtained at different scanning rates of the TPMT HCP

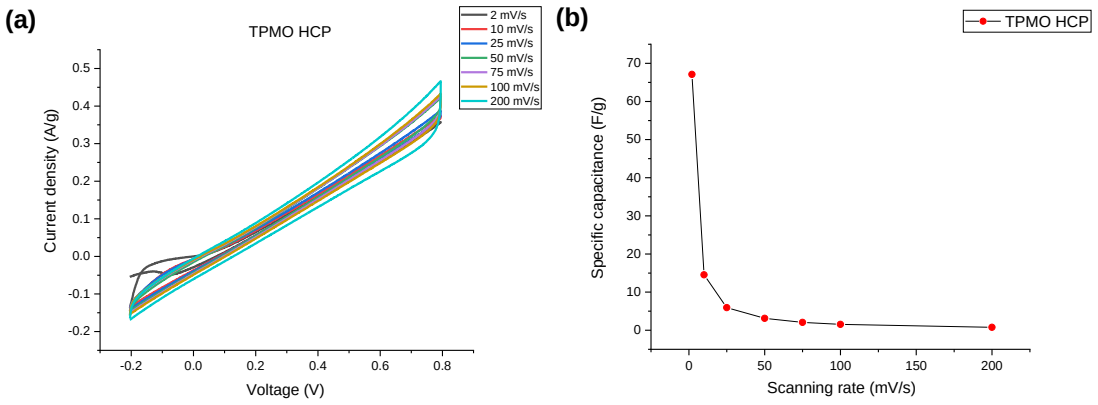

Figure 4.17 (a) CV curves at different scanning rate, and (b) Specific capacitance obtained at different scanning rates of the TPMO HCP

	Specific capacitance obtained at different scanning rates (F/g)							
Scanning rates (mV/s) / Material	2	10	25	50	75	100	200	Retention of capacitance at 200 mV/s
Fluorene HCP	96.0	20.2	8.3	4.4	2.9	2.2	1.1	1.1%
Carbazole HCP	14.0	3.0	1.2	0.6	0.4	0.3	0.2	1.4%
Dibenzothiophene HCP	1.6	0.5	0.2	0.19	0.17	0.16	0.14	8.9%
Dibenzofuran HCP	100.1	21.5	8.9	4.5	3.0	2.3	1.1	1.1%
Diphenylmethane HCP	21.4	4.4	1.8	0.9	0.6	0.5	0.2	0.9%
Diphenyl ether HCP	123.3	26.8	11.1	5.7	3.8	2.9	1.4	1.1%
Diphenylamine HCP	12.4	2.6	1.1	0.6	0.4	0.3	0.2	1.6%
TPM HCP	92.7	19.6	8.0	4.2	2.8	2.1	1.1	1.2%
TPMA HCP	78.7	16.4	6.8	3.3	2.2	1.6	0.9	1.1%
TPMT HCP	82.8	17.5	7.1	3.7	2.4	1.8	0.9	1.0%
TPMO HCP	67.1	14.5	5.9	3.1	2.1	1.5	0.8	1.2%

Table 4.4 Specific capacitance of heteroatom containing HCPs obtained at different scanning rates

The specific capacitance at 2 mV/s of the Carbazole HCP, Dibenzothiophene HCP and Dibenzofuran HCP is 14.0, 1.6, and 100.1 F/g, respectively, and the specific capacitance

at 2 mV/s of the Fluorene HCP is 96.0 F/g. Therefore, the Dibenzofuran HCP has the highest specific capacitance among these four samples. The BET surface and the total pore volume of the Dibenzofuran HCP (945.9 m^2/g, 0.55 cm^3/g) are lower than those of the Fluorene HCP (1003.9 m^2/g, 0.66 cm^3/g). The non-porous structure of the Dibenzothiophene HCP (1.6 m^2/g) resulted in the low capacitance of it. Although the Carbazole HCP has lower BET surface (523.4 m^2/g), the total pore volume of it (0.53 m^3/g) is similar to that of the Dibenzofuran HCP, while the specific capacitance of the Carbazole is much lower. From the cumulative pore volume results, it can be found that the micropore volume proportion and the micropore volume of the Fluorene HCP (63.3%, 0.42 cm^3/g) and the Dibenzofuran HCP (71.9%, 0.40 cm^3/g) are higher than those of the Carbazole HCP (41.3%, 0.22 cm^3/g). This may be the main reason of the low capacitance of the Carbazole HCP.

The specific capacitance at 2 mV/s of the Diphenyl ether HCP and the Diphenylamine HCP is 123.3 and 12.4 F/g, and the specific capacitance at 2 mV/s of the Diphenylmethane HCP is 21.4 F/g. The lowest BET surface area of the Diphenylamine HCP (2.8 m^2/g) among these three samples led to the Diphenylamine HCP has the lowest capacitance of these three samples. The BET surface area and the total pore volume of the Diphenylmethane HCP (1240.8 m^2/g, 0.95 cm^3/g) are higher than those of the Diphenyl ether HCP (1049.2 m^2/g, 0.74 cm^3/g), while the specific capacitance of the Diphenyl ether HCP is much higher than that of the Diphenylmethane HCP. The micropore volume proportion of the Diphenyl ether HCP (61.0%) is slightly higher than that of the Diphenylmethane HCP (56.1%), the volume proportion of the pores with diameter 2-10 nm of the Diphenyl ether HCP (31.1%) is slightly lower than that of the Diphenylmethane HCP (35.2%), and they have similar volume proportion of the pores with diameter larger than 10 nm. Generally speaking, the Diphenyl ether HCP has similar pore volume composition with the Diphenylmethane HCP. It can be also found that the Diphenylmethane HCP has higher micropore volume (0.53 cm^3/g) than the Diphenyl ether HCP (0.45 cm^3/g). Therefore, the variation in the capacitance of the

Diphenyl ether HCP and the Diphenylmethane HCP is independent with the variation in their porosities.

The specific capacitance at 2 mV/s of the TPMA HCP, TPMT HCP, and the TPMO HCP is 78.7, 82.8, and 67.1 F/g, respectively, and the specific capacitance at 2 mV/s of the TPM HCP is 92.7 F/g. The BET surface area and the total pore volume of the TPM HCP (1219.1 m^2/g, 0.81 cm^3/g) are higher than those of the TPMA HCP (412.6 m^2/g. 0.28 cm^3/g) and the TPMO HCP (574.3 m^2/g, 0.37 cm^3/g), the specific capacitance of the TPM HCP is higher than that of the TPMA HCP and TPMO HCP as well. The TPMO HCP has higher BET surface area and the TPMA HCP, while the TPMO HCP has lower specific capacitance. The TPMT HCP has much higher BET surface area and total pore volume (1520.5 m^2/g, 1.43 cm^3/g) than the TPM HCP, whereas the TPMT HCP has lower specific capacitance than the TPM HCP. In the cumulative pore volume of these four samples, it can be found that the TPM HCP, TPMA HCP and TPMO HCP have similar micropore volume proportion (64.5%, 60.8% and 64.2%, respectively). As the TPM HCP has higher total pore volume, it has higher micropore volume (0.52 cm^3/g) than the TPMA HCP (0.17 cm^3/g) and the TPMO HCP (0.24 cm^3/g). Although the TPMT HCP has lower micropore volume proportion (44.9%) than other three samples, it has the highest micropore volume (0.64 cm^3/g) among these four samples. This may be associated with that the TPMT HCP has higher specific capacitance than the TPMA HCP and TPMO HCP, but it cannot explain the TPM HCP has higher specific capacitance. However, it can be found that the TPM HCP has higher volume proportion of the pores with diameter 2-10 nm (28.4%) than the TPMA HCP (12.0%) and the TPMO HCP (8.1%), the TPM HCP also has the lowest pore volume proportion of the pores with diameter larger than 10 nm (7.1%) among these four HCPs. Although it is uncertain, the lower volume proportion of the pores with diameter larger than 10 nm and higher volume proportion of the pores with diameter 2-10 nm of the TPM HCP may be associated with its higher capacitance.

In these heteroatom containing HCPs, the Diphenyl ether HCP and the Dibenzofuran HCP have higher specific capacitances than other samples in this group, the specific

capacitances of the Diphenyl ether HCP and Dibenzofuran HCP are higher than that of the Diphenylmethane HCP and Fluorene HCP, respectively. Even if the TPMT HCP has higher BET surface area than the Diphenyl ether HCP and Dibenzofuran HCP, the specific capacitance of TPMT HCP is lower. Unlike the Diphenyl ether HCP and the Dibenzofuran HCP, the TPMO HCP has lower specific capacitance than the TPMT HCP. Therefore, it can be seen that the oxygen atom directed connected with an aromatic ring or involved in a heterocyclic ring could have more influence to the materials than the oxygen atom connected with an aliphatic carbon. As for the nitrogen containing HCPs, due to the very low specific surface area of the Diphenylamine HCP, it has low specific capacitance. Although the Carbazole HCP has higher BET surface area, the specific capacitance of the Carbazole HCP is low as well. The TPMA HCP has similar BET surface with the Carbazole HCP, but it has higher specific capacitance. It indicates that the nitrogen atom directed connected with an aromatic ring or involved in a heterocyclic ring could have more significant impact on the materials than the nitrogen atom connected with an aliphatic carbon, similar to the oxygen containing HCPs. Moreover, the independent relationship between the capacitances of the heteroatom containing HCPs and the porosities of these samples can be found here as well.

The independent relationship between the capacitances and the porosities of these samples can be attributed to: (1) The differences between the adsorption in gas phase and the adsorption in liquid phase result in the nitrogen adsorption/desorption results cannot fully explain the adsorption/desorption results in aqueous solutions. (2) The porosities of HCP cannot be fully used when the electrodes are charged due to the high internal resistance of HCPs. (3) Under the condition of poor conductivity, the inhomogeneous porosities of HCPs also have unpredictable limitations to the diffusion of electrolyte ions.

The rate performance of the heteroatom containing HCPs are quite low, the capacity kinetics of these samples were analyzed by using the relationship between response current and scanning rate. The linear relationship between response current and scanning rate indicates the capacity kinetic is dominated by fast surface-controlled

process, whereas the linear relationship between response current and scanning root square root demonstrates the kinetic of the capacity is determined by slow diffusion-controlled process.[63,64] The response current vs scanning rate plots of the heteroatom containing HCPs are listed in the figure 4.18.

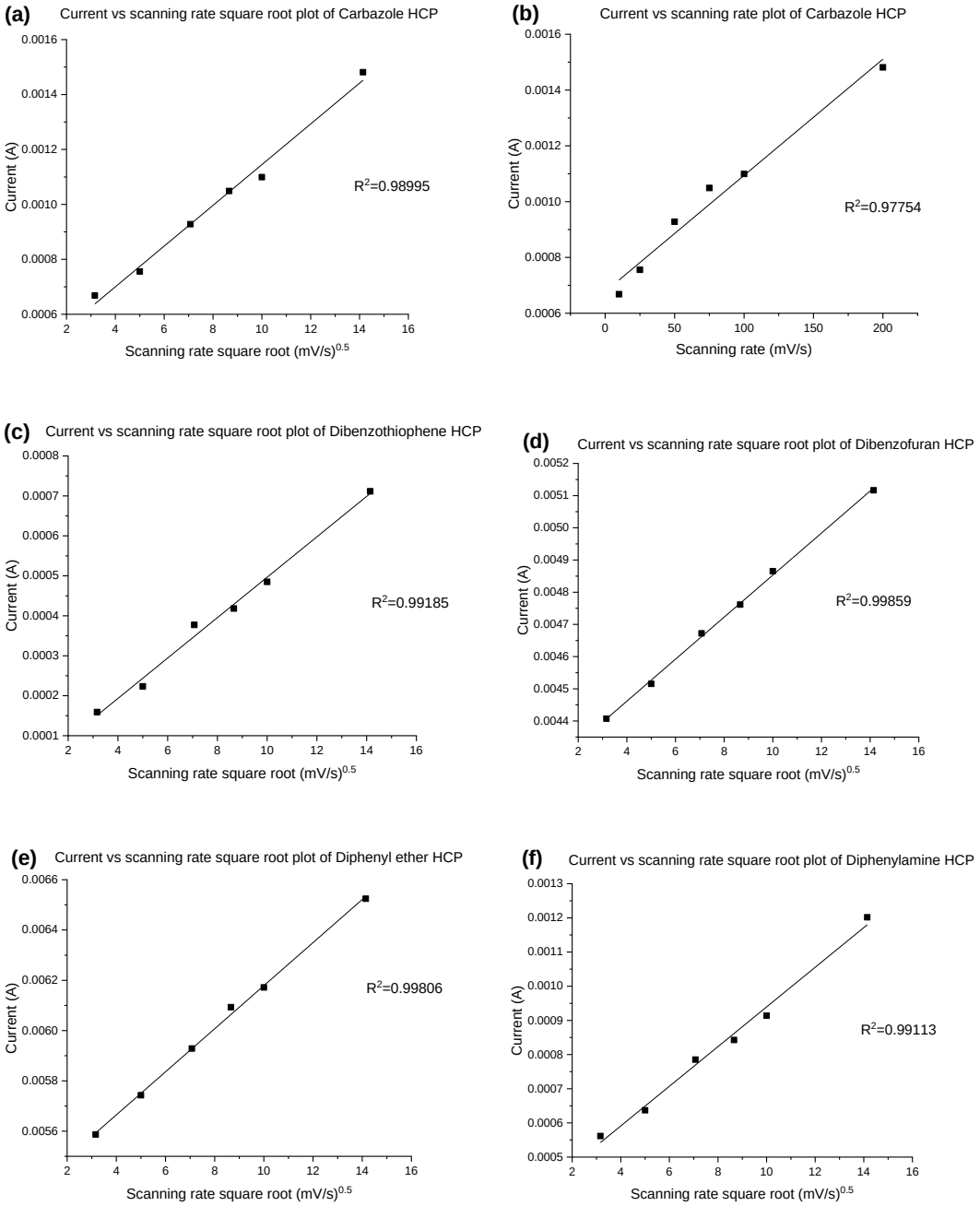

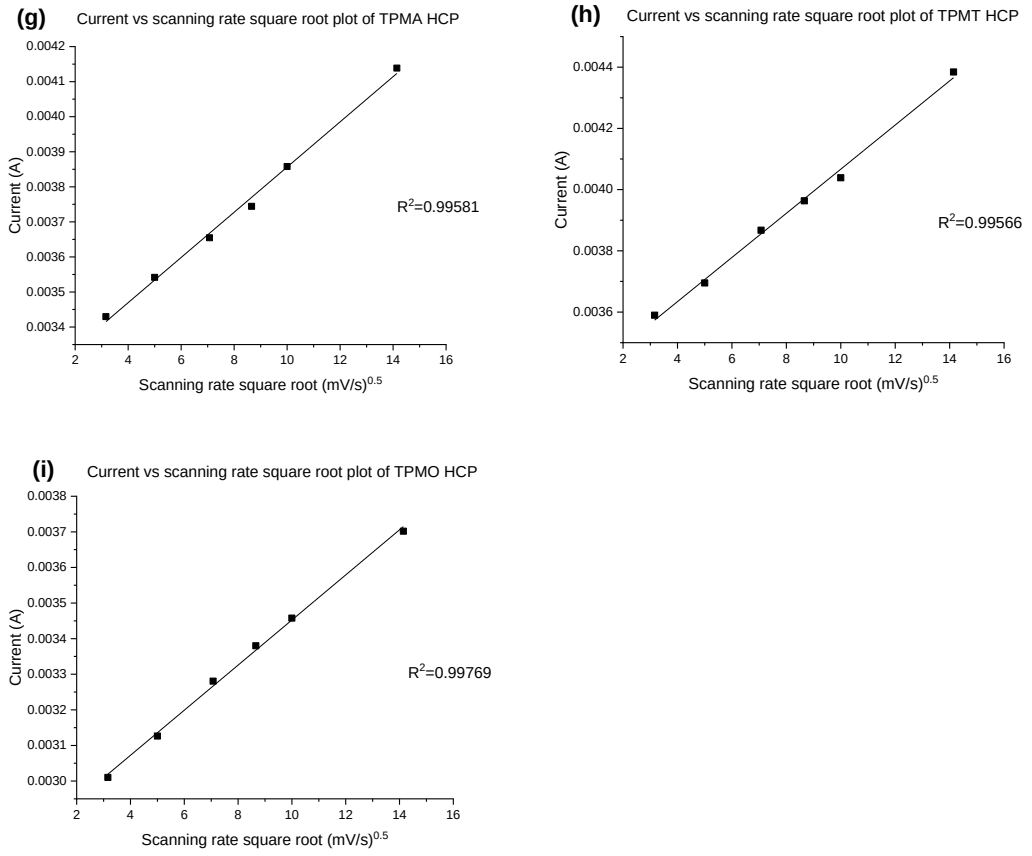

Figure 4.18 The relationship between response current and scanning rate of heteroatom containing HCPs. (a). current vs scanning rate square root plot and (b). current vs scanning rate plot of Carbazole HCP. (c). - (i). current vs scanning rate square root plot of Dibenzothiophene HCP, Dibenzofuran HCP, Diphenyl ether HCP, Diphenylamine HCP, TPMA HCP, TPMT HCP, and TPMO HCP.

Most of the heteroatom HCPs show a good linear relationship in the plots of response current vs scanning rate square root, the coefficient of determination R^2 of the Dibenzothiophene HCP, Dibenzofuran HCP, Diphenyl ether HCP, Diphenylamine HCP, TPMA HCP, TPMT HCP and TPMO HCP is 0.99185, 0.99859, 0.99806, 0.99113, 0.99581, 0.99566 and 0.99769, respectively. It can be seen that the Dibenzothiophene HCP and the Diphenylamine HCP show lower R^2 than other samples, corresponding to the proportion of the capacitance contributed by slow diffusion-controlled process is lower. The Carbazole HCP has the lowest coefficient of determination R^2 of the response current vs scanning rate square root plot among all these samples, 0.98995, the R^2 of the response current vs scanning plot of the Carbazole HCP is 0.97754, lower

than the former one. Therefore, the capacity kinetic of Carbazole is dominated by diffusion-controlled process, but the proportion of the capacitance attributed to fast surface-controlled process in the Carbazole HCP is higher than other samples in this group. The slow diffusion-controlled process dominated capacity kinetic of these samples corresponds to the low rate performance of the heteroatom containing HCP samples.

4.3.6 Electrochemical impedance spectroscopy (EIS)

To further investigate the electrochemical performance of the HCPs synthesized from different monomers, electrochemical impedance spectroscopy (EIS) was carried out with amplitude of 10 mV and frequency range 100 k Hz to 0.01 Hz. The Nyquist and Bode plots of the HCPs are shown in the figures from 4.19 to 4.26.

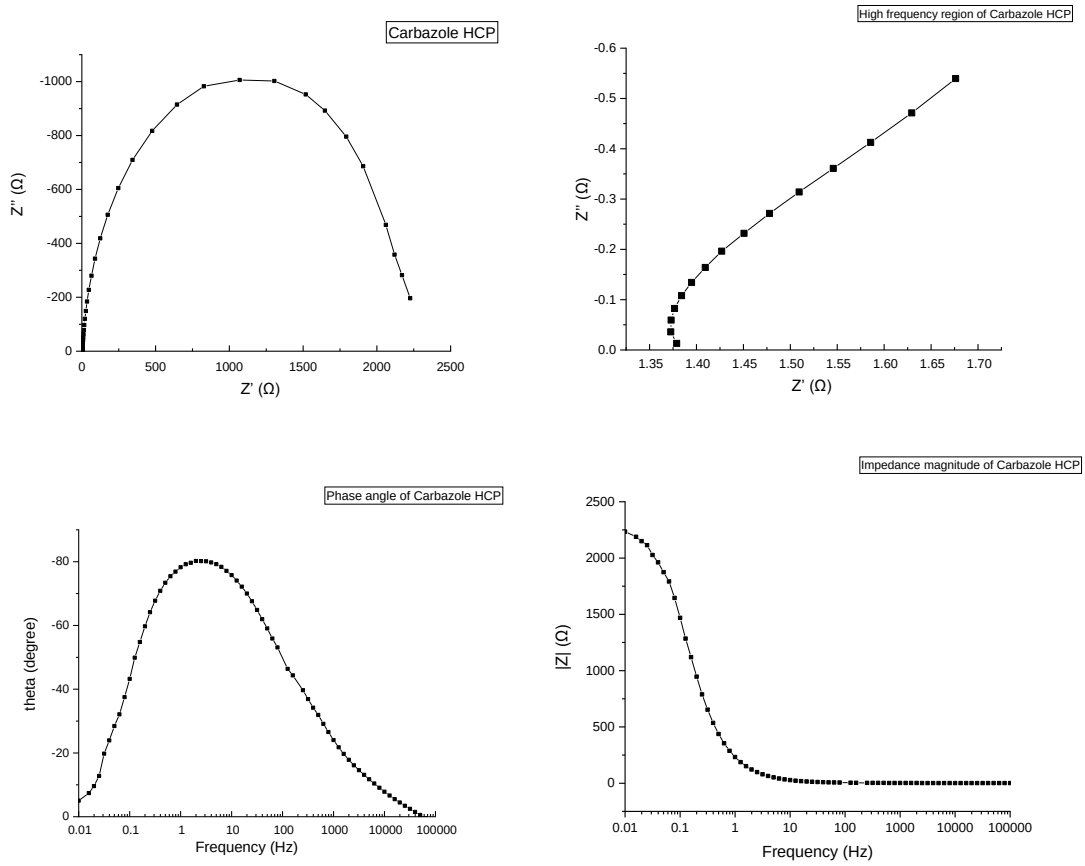

Figure 4.19 The Nyquist and Bode plot of Carbazole HCP

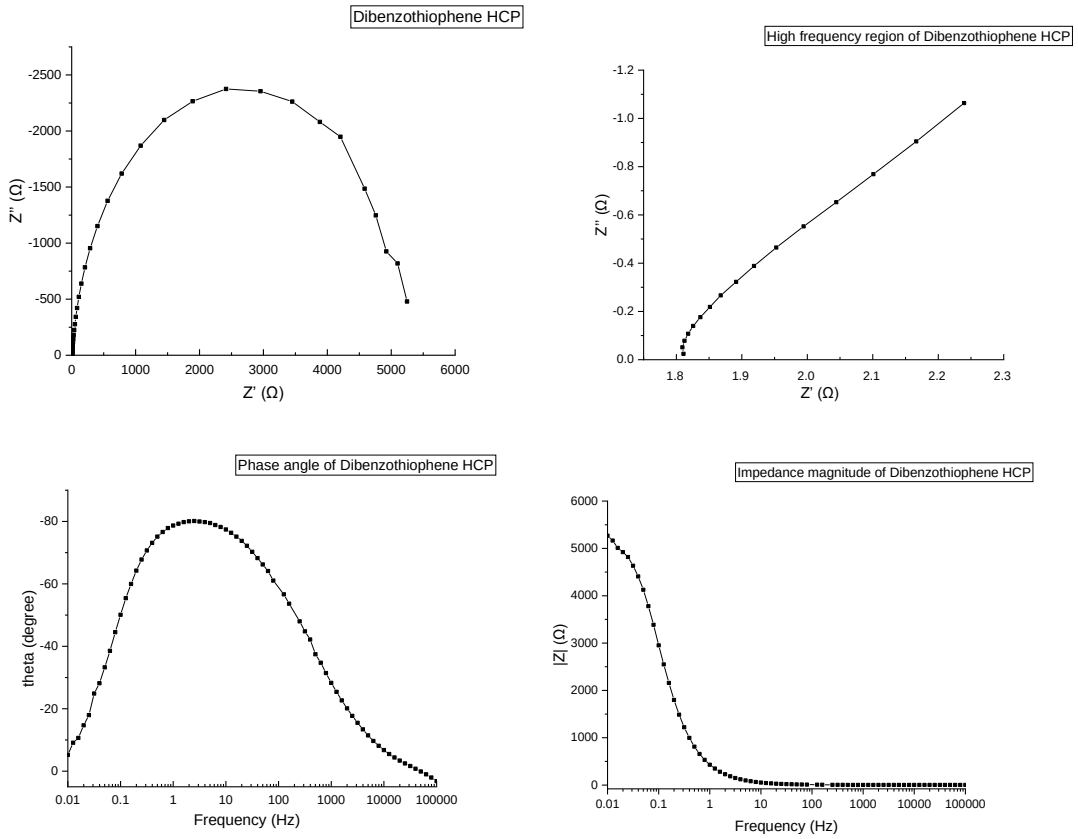

Figure 4.20 The Nyquist and Bode plot of Dibenzothiophene HCP

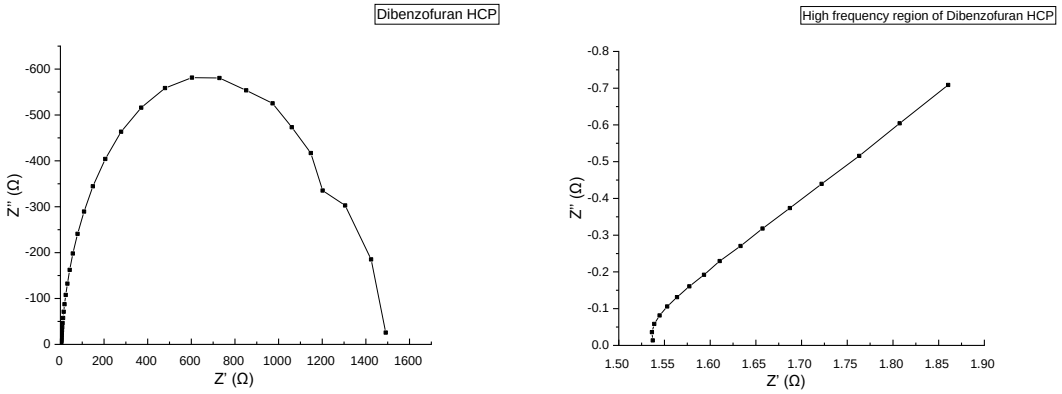

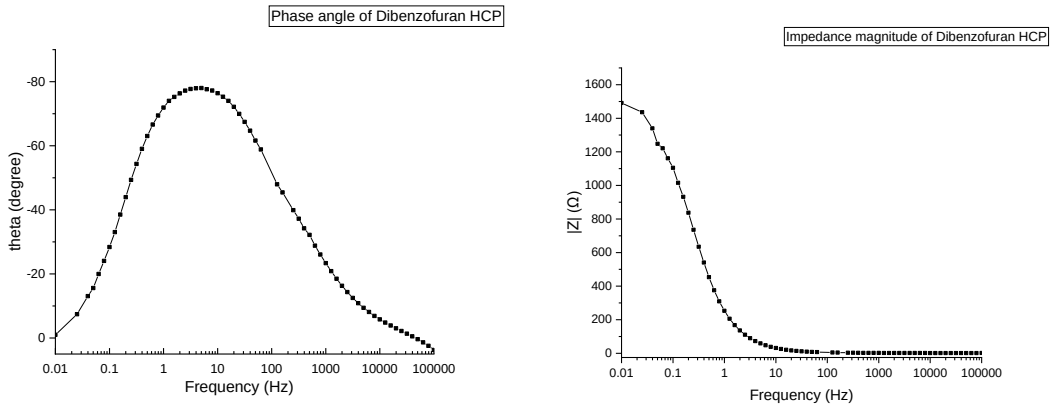

Figure 4.21 The Nyquist and Bode plot of Dibenzofuran HCP

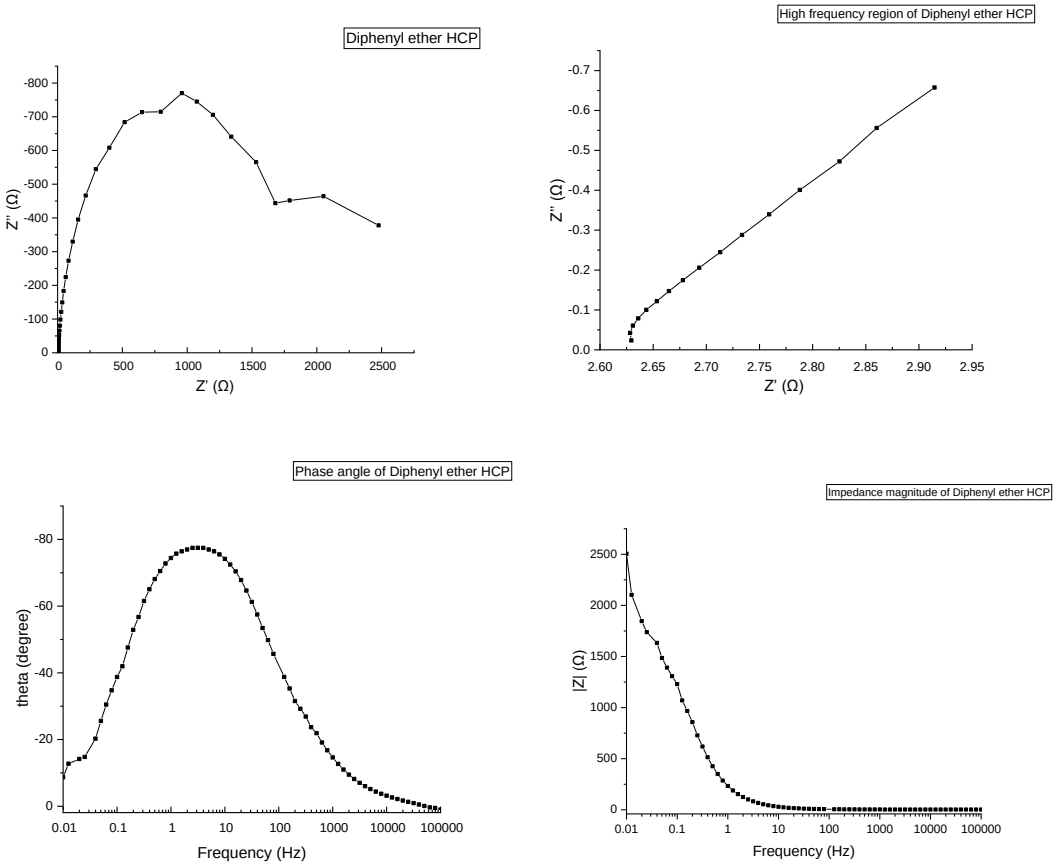

Figure 4.22 The Nyquist and Bode plot of Diphenyl ether HCP

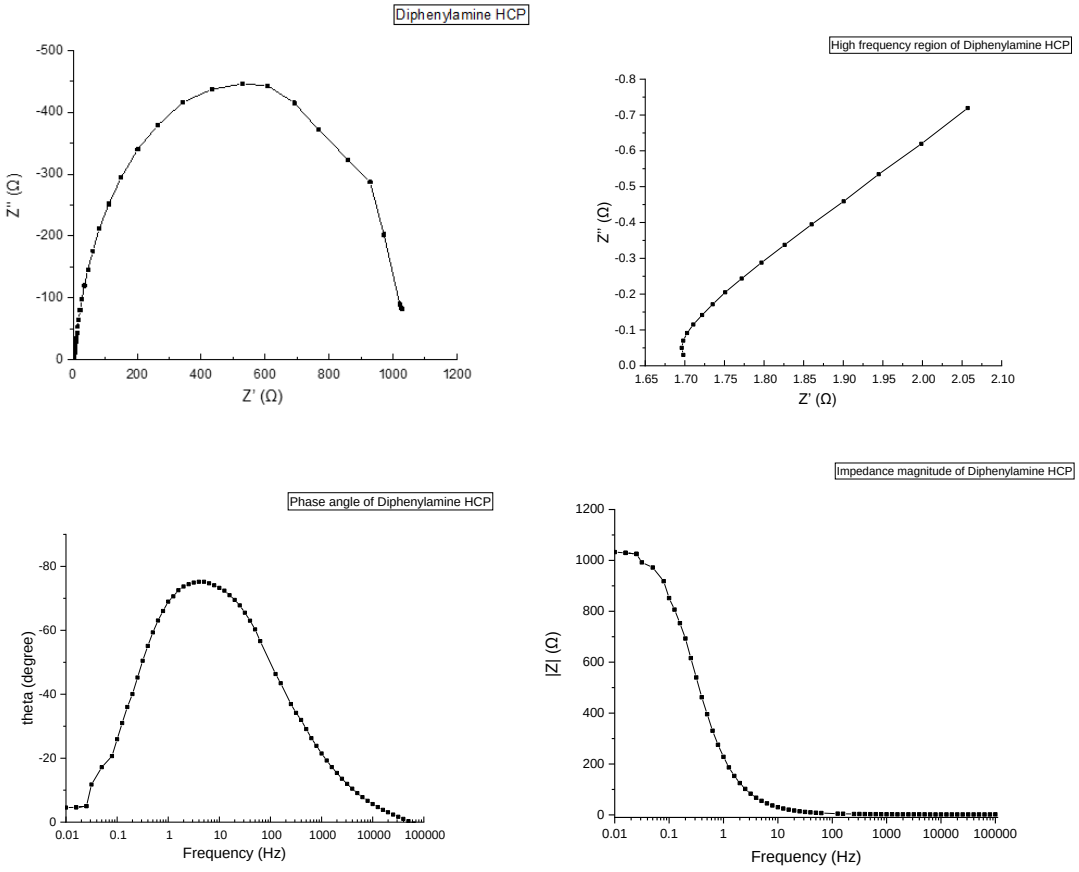

Figure 4.23 The Nyquist and Bode plot of Diphenylamine HCP

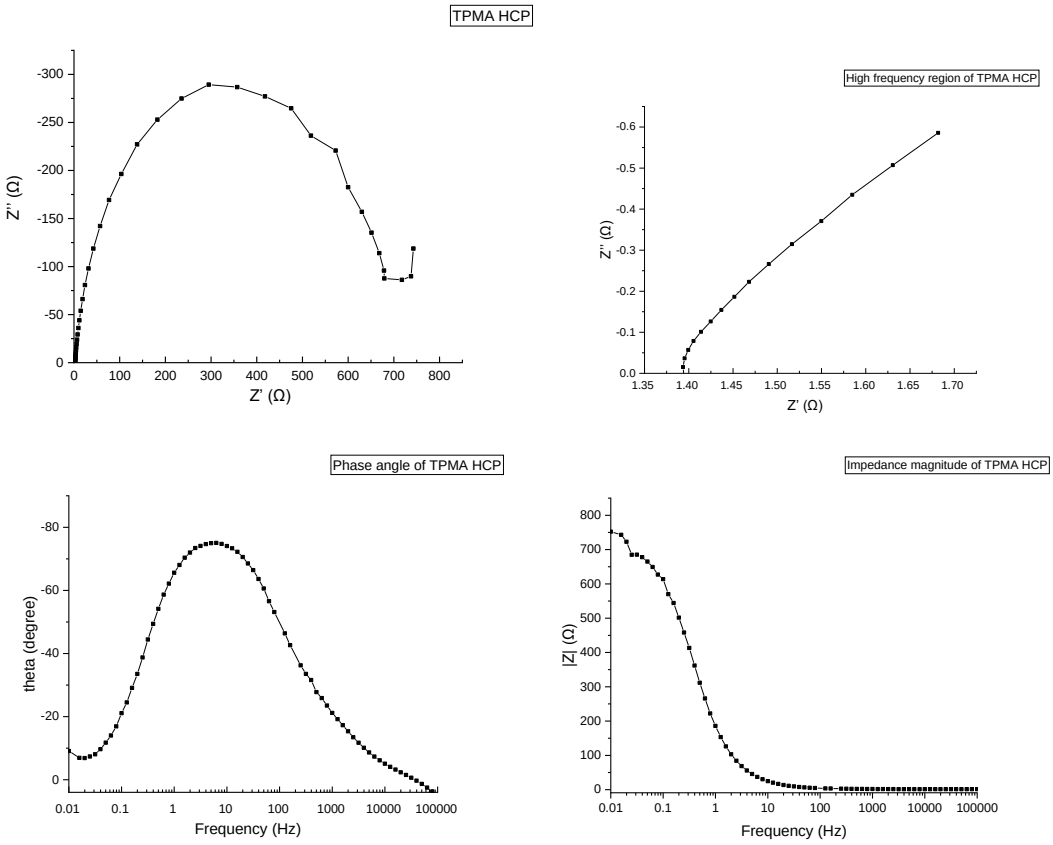

Figure 4.24 The Nyquist and Bode plot of TPMA HCP

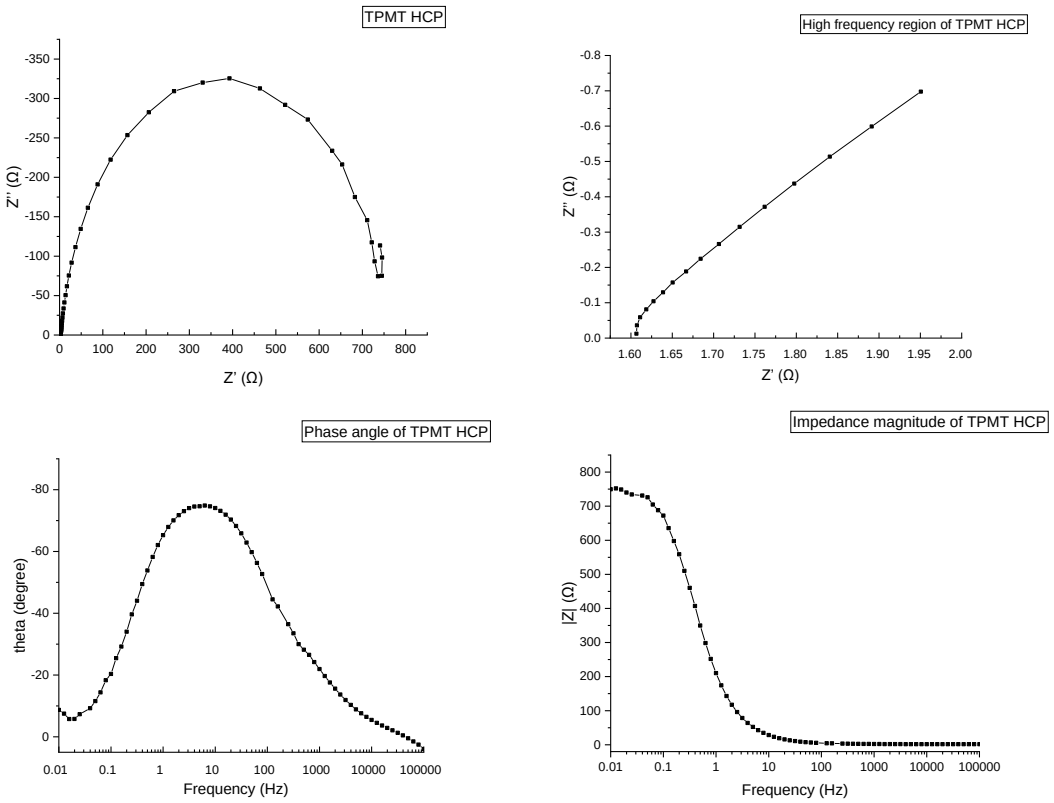

Figure 4.25 The Nyquist and Bode plot of TPMT HCP

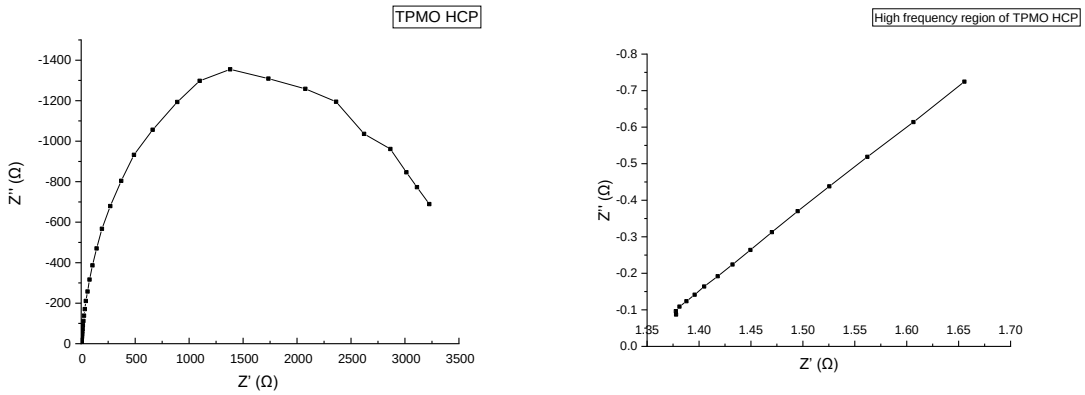

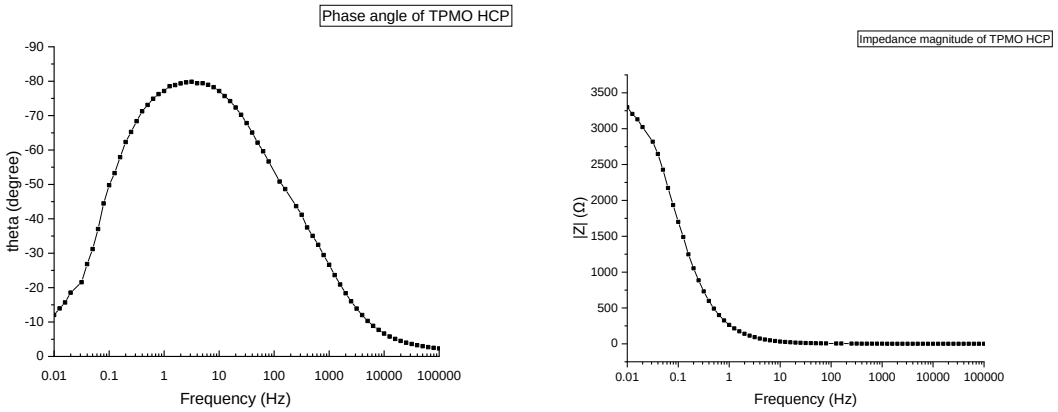

Figure 4.26 The Nyquist and Bode plot of TPMO HCP

	Whether the semicircle can be observed at high frequencies?	Whether the Nyquist plot is vertical or near vertical to Z" axis at low frequencies?	The phase angle value of the curve apex	Phase angle at 0.01 Hz	Impedance magnitude at 0.01 Hz (Ω)
Carbazole HCP	No	No	-80°	-5°	2234
Dibenzothiophene HCP	No	No	-80°	-5°	5269
Dibenzofuran HCP	No	No	-78°	-1°	1491
Diphenyl ether HCP	No	No	-77°	-9°	2505
Diphenylamine HCP	No	No	-75°	-5°	1032
TPMA HCP	No	No	-75°	-9°	752
TPMT HCP	No	No	-75°	-9°	750
TPMO HCP	No	No	-80°	-12°	3298

Table 4.5 The results from Nyquist and Bode plot of different heteroatom containing HCPs

For the heteroatom containing HCPs, the absence of the 'tail' paralleling to Z" axis in the intermediate and low frequency region in Nyquist plots indicates the HCPs did not show supercapacitor behaviour. The highest points of the phase angle curves of the heteroatom containing HCPs vary from -75° to -80° illustrating the HCPs show

deviations from pure capacitor behaviour. The phase angle curves decrease to the angle close to 0° after reaching the highest point with the decreasing frequency demonstrates the behaviours of the HCPs behave like resistors at low frequencies, while the phase angles do not decrease to 0° illustrates the HCPs show some capacitance at low frequencies. The impedance magnitudes of the HCPs are quite high, from the variation trend of the phase angles of the HCPs it can be found that the high impedance in the low frequency region of these HCPs is mainly contributed by the internal resistances of the HCPs. The absence of the semi-circle in the high frequency region can be attributed to the ohmic contact between the current collector and the active materials.[65]

In order to show the poor conductivity of the heteroatom containing HCPs more directly, the fitting results are shown in the figure 4.27 and table 4.6. The Randles circuit model is used as the equivalent circuit for the impedance fitting.

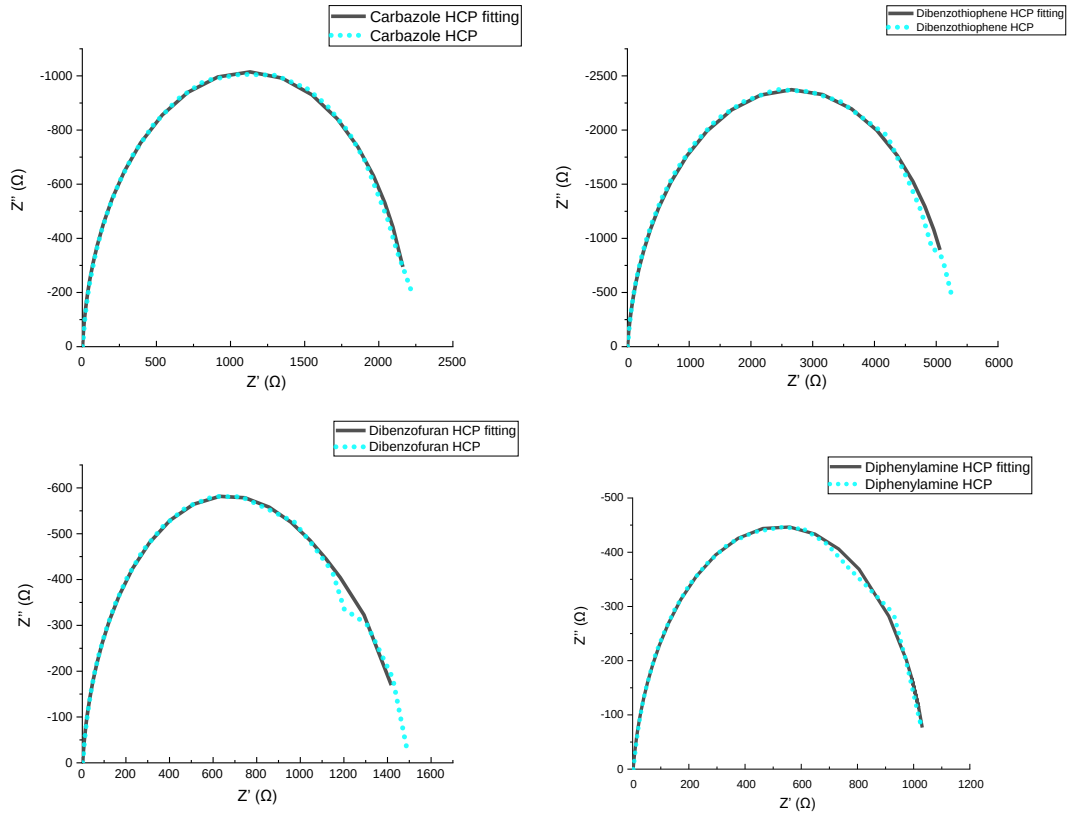

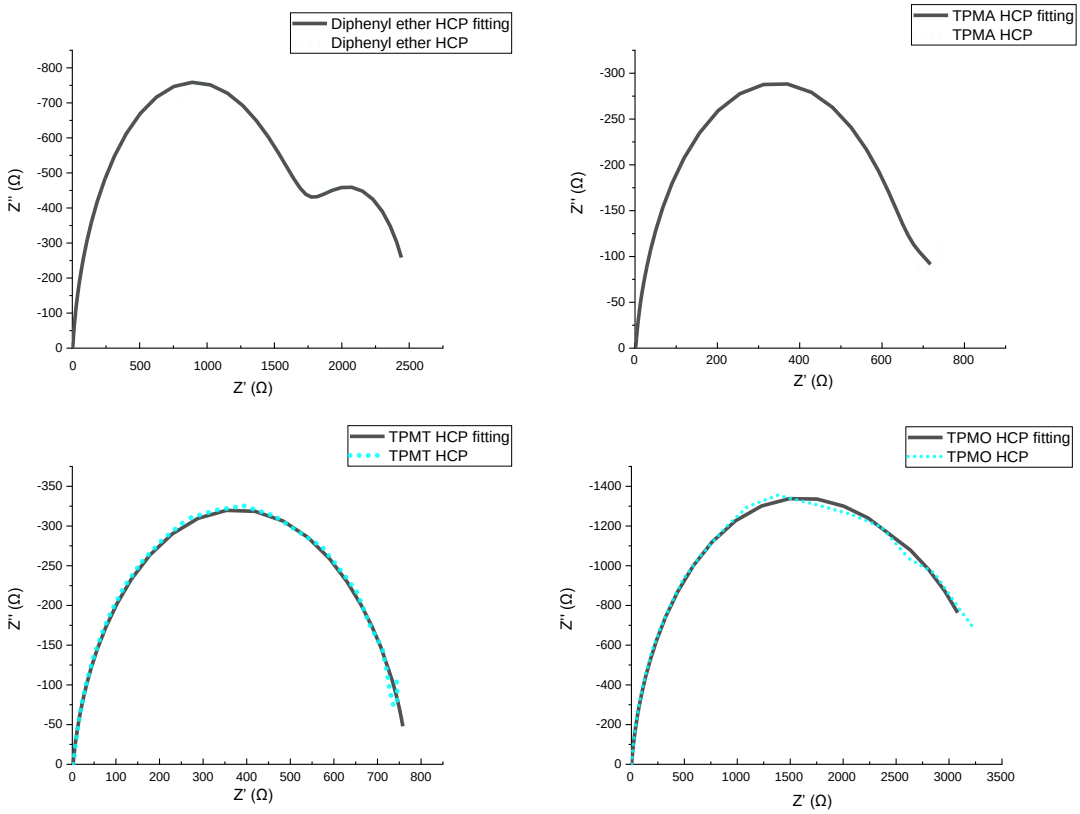

Figure 4.27 The fitting and experimental curves of the heteroatom containing HCPs

In the fitting curves of the HCPs, the deviations can be found in the low frequency region as the poor conductivity and the disordered porous structure of HCPs made the diffusion is hard to be precisely predicted.

	R1 (Ω)	CPE1-T (F)	CPE1-P	R2 (Ω)	Ws1-R (Ω)	Ws1-T (s)	Ws1-P
Carbazole HCP	1.635	0.00083836	0.9502	2128.2	97.3	4.2	0.5
Dibenzothiophene HCP	1.995	0.00044167	0.92965	5218.1	103.8	4.2	0.5
Dibenzofuran HCP	1.713	0.00077929	0.92747	1258.9	206.5	12.9	0.5
Diphenylamine HCP	1.881	0.00088106	0.9063	1018.3	27.2	2.1	0.5
Diphenyl ether HCP	2.839	0.00085891	0.90857	1671.1	853.4	129.9	0.5
TPMA HCP	1.548	0.0010647	0.89914	665.4	113.9	39.8	0.5
TPMT HCP	1.798	0.00094739	0.89839	747.7	18.6	8.3	0.5
TPMO HCP	1.515	0.0007506	0.91191	2927.5	523.2	21.7	0.5

Table 4.6 The impedance fitting results of heteroatom containing HCPs

From the table 4.6, it can be found that the high values of R2, suggesting the high

internal resistance of heteroatom containing HCPs.

To further study the electrochemical performance of the heteroatom containing HCPs under alternating current, the complex capacitances of the HCPs are performed. The complex capacitance C(ω) is defined by equation 4a. The real part and imaginary of the complex capacitance C'(ω) and C" (ω) is defined by equation 4b and 4c, respectively.

$$C(\omega) = C'(\omega) - jC''(\omega) \qquad 4.3.6.1$$

$$C'(\omega) = \frac{-Z''(\omega)}{\omega|Z|^2} \qquad 4.3.6.2$$

$$C''(\omega) = \frac{Z'(\omega)}{\omega|Z|^2} \qquad 4.3.6.3$$

The complex capacitance curves of the HCPs are shown in the figure 4.28.

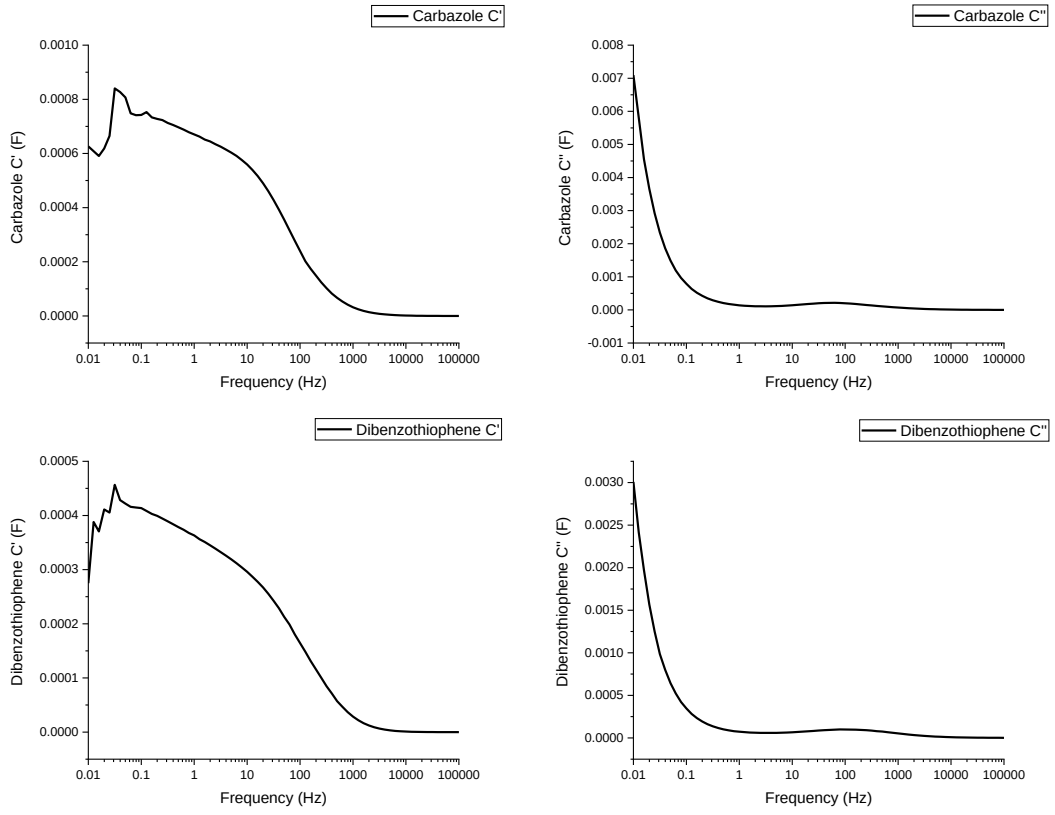

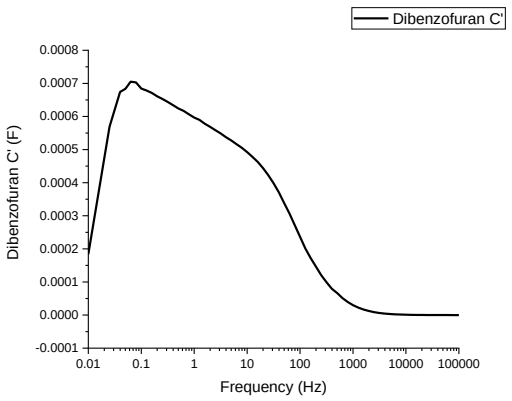
Dibenzofuran C'
Dibenzofuran C' (F)
Frequency (Hz)

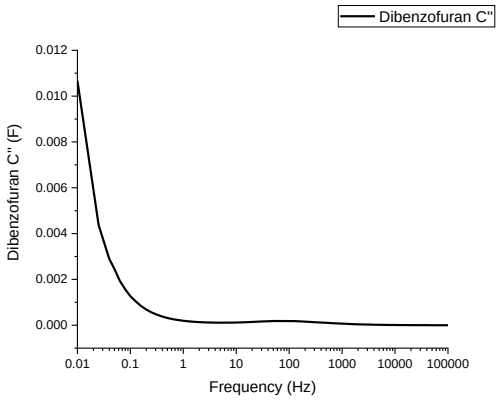
Dibenzofuran C''
Dibenzofuran C'' (F)
Frequency (Hz)

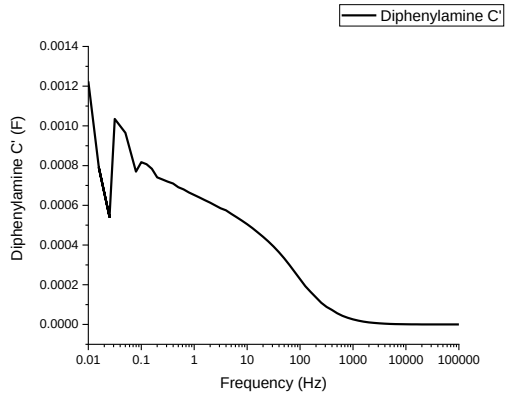
Diphenylamine C'
Diphenylamine C' (F)
Frequency (Hz)

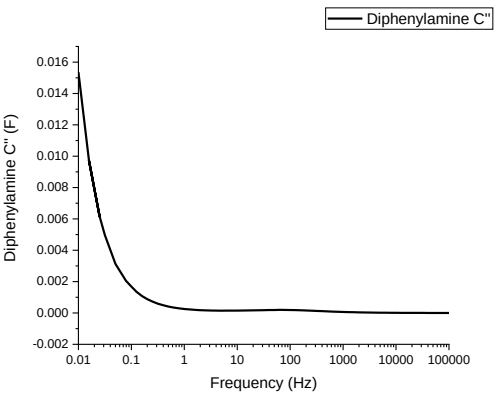
Diphenylamine C''
Diphenylamine C'' (F)
Frequency (Hz)

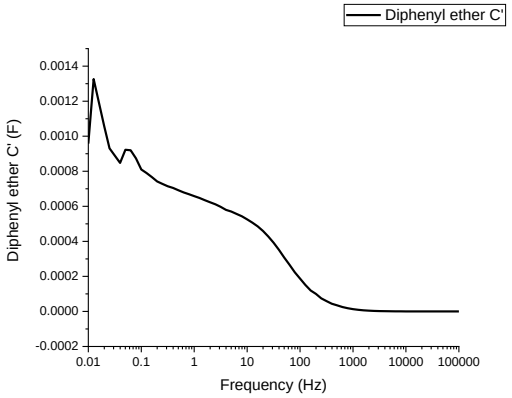
Diphenyl ether C'
Diphenyl ether C' (F)
Frequency (Hz)

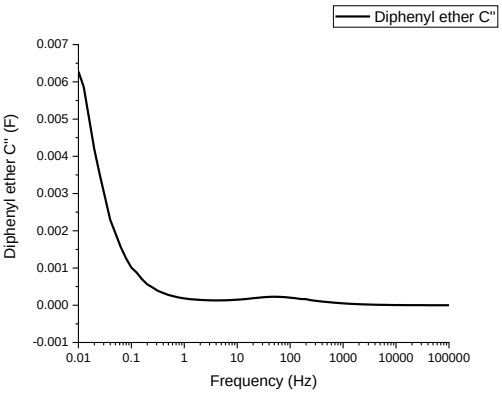
Diphenyl ether C''
Diphenyl ether C'' (F)
Frequency (Hz)

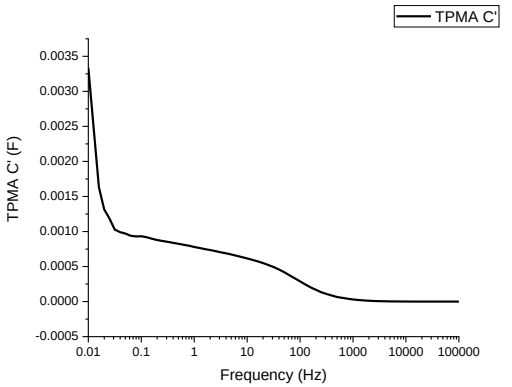
TPMA C'
TPMA C' (F)
Frequency (Hz)

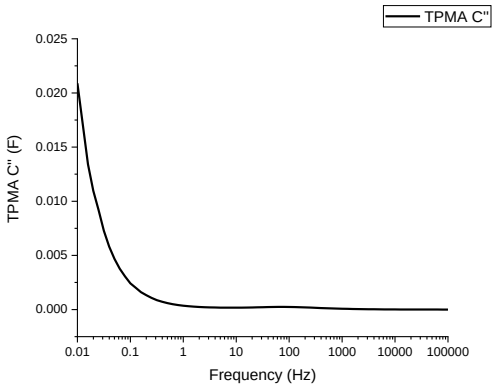
TPMA C''
TPMA C'' (F)
Frequency (Hz)

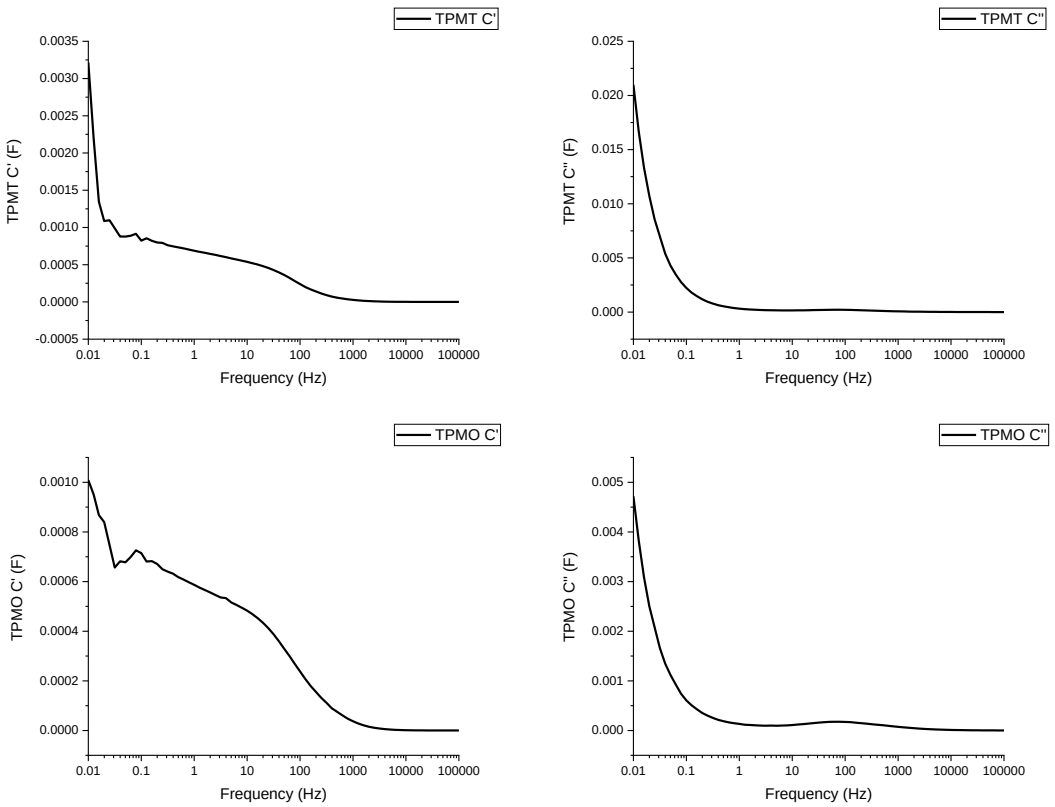

Figure 4.28 The complex capacitance of the heteroatom containing HCPs

The real part of the complex capacitance C' shows the capacitance variation with the decreasing frequency. It can be seen that the variation trend of C' of the heteroatom containing HCPs is same with a common supercapacitor in the high and intermediate frequency region, while significant fluctuations can be seen in the low frequency region, indicating the capacitances of the HCPs obtained at low frequencies are not stable, i.e., the utilization rate of the porous structures of the HCPs are not stable because of the poor conductivity of these samples. This corresponds to the specific capacitances of these HCPs obtained from CV tests are independent with the BET surface areas and pore volumes. It can be also found that the capacitance at very low frequencies in the real part of the complex capacitance is much lower than that obtained from CV tests. The voltage amplitude used in impedance tests is 10 mV, this indicates the HCPs can only produce quite small response at a low voltage due to the high internal resistance.

The imaginary part of the complex C'' corresponds to energy dissipation. With the decreasing frequency, the peak corresponding to phase angle -45° appeared then the C''

curves began to rise in the low frequency region and reached the maximum at 0.01 Hz, demonstrating the increased energy losses in the low frequency region caused by poor conductivity of the HCPs. This corresponds to the decreasing in the phase angle in the low frequency region. The frequency f_0 at which the C" reaches the maximum can be used to define the relaxation time to assess the rate performance of the materials. The relaxation time was defined in the equation 4d.

$$\tau_0 = \frac{1}{f_0} \qquad 4.3.6.4$$

The relaxation time τ_0 of the heteroatoms containing HCPs is 100 s, indicating the rate performance of the HCPs is not good due to their poor conductivity. This result corresponds to the results from the CV tests.

In this chapter, the Diphenyl ether HCP has the highest specific capacitance of 123.3 F/g, followed by the Dibenzofuran HCP with a specific capacitance of 100.1 F/g. Compared with the Fluorene HCP and Diphenylmethane HCP, these two oxygen doped HCPs show increases in the specific capacitances. However, compared with the POPs with fully conjugated molecular networks, for instance, Buchwald–Hartwig coupling (PAQTA) which has specific capacitances of 576 F/g at 1 A/g and 410 F/g at 10 A/g,[10] β-ketoenamine-linked conjugated microporous polymer (KECMP-1) with specific capacitances of 252 F/g at 1 A/g and 126 F/g at 100 A/g,[66] the HCPs synthesized with heteroatom containing monomers show lower specific capacitances and rate performance due to the high internal resistance caused by unconjugated methylene bridges.

4.4 Conclusion

Compared with the non-doped HCPs, the BET surface areas and pore volumes of most of the heteroatom containing HCPs show a downward tendency, while the TPMT HCP has a higher BET surface and a higher total pore volume than the TPM HCP. The diphenyl sulfide cannot be used as a monomer for HCP synthesis with knitting method as no solid product can be obtained after synthesis. The non-porous Dibenzothiophene

HCP with a low yield of 13.8% indicates the dibenzothiophene is not a good candidate for HCP synthesis. In addition, the Diphenylamine HCP is also a non-porous material. Therefore, it can be seen that there are limitations in the selection of heteroatom containing monomers for HCP synthesis. In terms of the influences of the heteroatoms to the specific capacitance of the heteroatom containing HCPs, the Diphenyl ether HCP has the highest specific capacitance of 123.3 F/g, followed by the Dibenzofuran HCP with a specific capacitance of 100.1 F/g. These two oxygen-containing HCPs show higher specific capacitances than the non-doped HCPs, Diphenylmethane HCP (21.4 F/g) and Fluorene HCP (96.0 F/g). All the heteroatom containing HCPs show a very low rate performance. By analyzing the relationship between response current and scanning rate, it can be seen the capacity kinetic of the heteroatom containing HCPs is dominated by diffusion-controlled process, corresponding to the low rate performance of these samples.

In the EIS results, the absence of the 'tail' paralleling with the Z" axis in Nyquist plots of the heteroatom containing HCPs suggests the HCPs do not show a supercapacitor behaviour. The high internal resistances of the HCPs can be seen from the impedance magnitudes of the HCPs. The phase angles of the heteroatom containing HCPs increase to close to 0° at low frequencies, illustrating that the HCPs tend to behave like a pure resistor in the low frequency region. In the complex capacitances, the pore structures of the HCPs cannot be fully used due to their high internal resistances is confirmed by the fluctuations in the low frequency region of the C' curves and the poor rate performance of the HCPs are reaffirmed by the C" curves.

The thermal treatment is required for the HCPs synthesized from heteroatom containing monomers, to solve the problem of the high internal resistance caused by unconjugated methylene bridges. For the nitrogen containing and sulfur containing HCPs, the heteroatom contents in these sample do not improve the supercapacitive performance of these materials, but if they are used as precursors for activated carbons, the porous carbons could have nitrogen or sulphur doping which may improve the supercapacitive performance of these carbons. There are some limitations in heteroatom containing

monomer selection for HCP synthesis with knitting method, as some heteroatoms with specific configurations could have impacts on the electron density of the conjugation system of aromatic monomers, so the selection of heteroatom containing monomers for HCP synthesis should be given more consideration.

Reference

1 A. G. Pandolfo and A. F. Hollenkamp, *J. Power Sources*, 2006, **157**, 11–27.

2 X. Gang, M. Krishnamoorthy, W. Jiang, J. Pan, Z. Pan and X. Liu, *Carbon N. Y.*, 2021, **171**, 62–71.

3 L. L. Zhang and X. S. Zhao, *Chem. Soc. Rev.*, 2009, **38**, 2520.

4 E. Raymundo-Piñero, F. Leroux and F. Béguin, *Adv. Mater.*, 2006, **18**, 1877–1882.

5 J. Hou, K. Jiang, R. Wei, M. Tahir, X. Wu, M. Shen, X. Wang and C. Cao, *ACS Appl. Mater. Interfaces*, 2017, **9**, 30626–30634.

6 J. S. Noh and J. A. Schwarz, *Carbon N. Y.*, 1990, **28**, 675–682.

7 M. Abe, K. Kawashima, K. Kozawa, H. Sakai and K. Kaneko, *Langmuir*, 2000, **16**, 5059–5063.

8 J. Yang, M. R. Jo, M. Kang, Y. S. Huh, H. Jung and Y. M. Kang, *Carbon N. Y.*, 2014, **73**, 106–113.

9 D. Chen, L. Yang, J. Li and Q. Wu, *ChemistrySelect*, 2019, **4**, 1586–1595.

10 Y. Liao, H. Wang, M. Zhu and A. Thomas, *Adv. Mater.*, 2018, **30**, 1–10.

11 R. Xue, H. Guo, T. Wang, X. Wang, J. Ai, L. Yue, Y. Wei and W. Yang, *Mater. Lett.*, 2017, **209**, 171–174.

12 S. Hou, S. Razzaque and B. Tan, *Polym. Chem.*, 2019, **10**, 1299–1311.

13 G. Ji, Z. Yang, X. Yu, Y. Zhao, F. Zhang and Z. Liu, *ACS Sustain. Chem. Eng.*, 2020, **8**, 16320–16326.

14 Y. Wang, Y. Cao, X. Zeng, J. Huang and Y. N. Liu, *Ind. Eng. Chem. Res.*, 2021, **60**, 931–938.

15 R. Shen, X. Yan, Y. J. Guan, W. Zhu, T. Li, X. G. Liu, Y. Li and Z. G. Gu, *Polym. Chem.*, 2018, **9**, 4724–4732.

16 L. Tan, B. Li, X. Yang, W. Wang and B. Tan, *Polymer (Guildf).*, 2015, **70**, 336–342.

17 G. Wang, B. Dou, J. Wang, W. Wang and Z. Hao, *RSC Adv.*, 2013, **3**, 20523–20531.

18 Y. Liu, X. Chen, X. Jia, X. Fan, B. Zhang, A. Zhang and Q. Zhang, *Ind. Eng. Chem. Res.*, 2018, **57**, 17259–17265.

19 J. He, G. Zhao, P. Mu, H. Wei, Y. Su, H. Sun, Z. Zhu, W. Liang and A. Li, *Sol. Energy Mater. Sol. Cells*, , DOI:10.1016/j.solmat.2019.110111.

20 D. Chen, S. Gu, Y. Fu, Y. Zhu, C. Liu, G. Li, G. Yu and C. Pan, *Polym. Chem.*, 2016, **7**, 3416–3422.

21 X. Fu, Y. Liu, X. Jiang, Q. Wang, Y. Luo and Y. Lyu, *Thermochim. Acta*, 2018, **665**, 111–118.

22 J. Bai, W. Zhang, X. Ma, L. Chen, L. Liu and C. Zhang, *Microporous Mesoporous Mater.*, 2020, **294**, 109892.

23 B. Li, R. Gong, W. Wang, X. Huang, W. Zhang, H. Li, C. Hu and B. Tan, *Macromolecules*, 2011, **44**, 2410–2414.

24 R. Lu, C. Xu, Q. Wang, Y. Wang, Y. Zhang, D. Gao, J. Bi and G. Fan, *Int. J. Hydrogen Energy*, 2018, **43**, 18253–18260.

25 C. Wilson, M. J. Main, N. J. Cooper, M. E. Briggs, A. I. Cooper and D. J. Adams, *Polym. Chem.*, 2017, **8**,

1914–1922.

26 R. Dawson, T. Ratvijitvech, M. Corker, A. Laybourn, Y. Z. Khimyak, A. I. Cooper and D. J. Adams, *Polym. Chem.*, 2012, **3**, 2034–2038.

27 Y. Shigemasa, H. Matsuura, H. Sashiwa and H. Saimoto, *Int. J. Biol. Macromol.*, 1996, **18**, 237–242.

28 L. Pan, Q. Chen, J. H. Zhu, J. G. Yu, Y. J. He and B. H. Han, *Polym. Chem.*, 2015, **6**, 2478–2487.

29 H. Wei, F. Wang, H. Sun, Z. Zhu, C. Xiao, W. Liang, B. Yang, L. Chen and A. Li, *J. Mater. Chem. A*, 2018, **6**, 8633–8642.

30 J. Xu, W. Zhou, J. Hou, S. Pu, Z. Wei and J. Wang, *Mater. Lett.*, 2006, **60**, 2569–2572.

31 Y. Wang, Y. Cao, X. Zeng, J. Huang and Y. N. Liu, *Ind. Eng. Chem. Res.*, 2021, **60**, 931–938.

32 J. Zhang, K. Dong, W. Luo and H. Guan, *Fuel*, 2018, **234**, 664–673.

33 A. G. Al Lafi and J. N. Hay, *J. Mol. Struct.*, 2019, **1175**, 152–162.

34 L. Shao, Y. Sang, N. Liu, Q. Wei, F. Wang, P. Zhan, W. Luo, J. Huang and J. Chen, *Sep. Purif. Technol.*, 2021, **262**, 118352.

35 A. G. Al Lafi, *Polym. Degrad. Stab.*, 2014, **105**, 122–133.

36 P. Sett, A. K. De, S. Chattopadhyay and P. K. Mallick, *Chem. Phys.*, 2002, **276**, 211–224.

37 K. Chadwick, R. J. Davey, G. Dent, R. G. Pritchard, C. A. Hunter and D. Musumeci, *Cryst. Growth Des.*, 2009, **9**, 1990–1999.

38 S. G. Kini, A. R. Bhat, B. Bryant, J. S. Williamson and F. E. Dayan, *Eur. J. Med. Chem.*, 2009, **44**, 492–500.

39 T. C. Wen, C. Sivakumar and A. Gopalan, *Mater. Lett.*, 2002, **54**, 430–441.

40 J. S. Huberty and R. J. Madix, *Surf. Sci.*, 1996, **360**, 144–156.

41 H. Y. Low and H. Ishida, *J. Polym. Sci. Part B Polym. Phys.*, 1998, **36**, 1935–1946.

42 J. He, S. Razzaque, S. Jin, I. Hussain and B. Tan, *ACS Appl. Nano Mater.*, 2019, **2**, 546–553.

43 D. Li and J. Li, *New J. Chem.*, 2003, **27**, 498–501.

44 A. Cherdoud-Chihani, M. Mouzali and M. J. M. Abadie, *J. Appl. Polym. Sci.*, 2003, **87**, 2033–2051.

45 Y. Luo, S. Zhang, Y. Ma, W. Wang and B. Tan, *Polym. Chem.*, 2013, **4**, 1126–1131.

46 R. V. Law, D. C. Sherrington, C. E. Snape, I. Ando and H. Kurosu, *Macromolecules*, 1996, **29**, 6284–6293.

47 L. Ding, H. Gao, F. Xie, W. Li, H. Bai and L. Li, *Macromolecules*, 2017, **50**, 956–962.

48 Y. Cheng, S. Razzaque, Z. Zhan and B. Tan, *Chem. Eng. J.*, 2021, **426**, 130731.

49 S. Krishnan and C. V. Suneesh, *Mater. Today Commun.*, 2021, **27**, 102251.

50 S. Xu, K. Song, T. Li and B. Tan, *J. Mater. Chem. A*, 2015, **3**, 1272–1278.

51 G. Liu, Y. Wang, C. Shen, Z. Ju and D. Yuan, *J. Mater. Chem. A*, 2015, **3**, 3051–3058.

52 S. Seo, W. Chaikittisilp, N. Koike, T. Yokoi and T. Okubo, *Microporous Mesoporous Mater.*, 2019, **278**, 212–218.

53 J. H. Zhu, Q. Chen, Z. Y. Sui, L. Pan, J. Yu and B. H. Han, *J. Mater. Chem. A*, 2014, **2**, 16181–16189.

54 L. Xiang, Y. Zhu, S. Gu, D. Chen, X. Fu, Y. Zhang, G. Yu, C. Pan and Y. Hu, *Macromol. Rapid Commun.*, 2015, **36**, 1566–1571.

55 R. R. Zhang, Q. Yin, H. P. Liang, Q. Chen, W. H. Luo and B. H. Han, *Polymer (Guildf).*, 2018, **143**, 87–95.

56 S. K. Das, S. Chatterjee, S. Mondal and A. Bhaumik, *Mol. Catal.*, 2019, **475**, 110483.

57 X. Fu and F. J. Schmitz, *J. Nat. Prod.*, 1996, **59**, 1102–1103.

58 X. Qian, B. Wang, Z. Q. Zhu, H. X. Sun, F. Ren, P. Mu, C. Ma, W. D. Liang and A. Li, *J. Hazard. Mater.*, 2017, **338**, 224–232.

59 A. M. James, J. Reynolds, D. G. Reed, P. Styring and R. Dawson, *Materials (Basel).*, , DOI:10.3390/ma14071605.

60 H. Xu, J. Wu, B. Zheng, W. Mai, F. Xu, L. Chen, H. Liu, R. Fu, D. Wu and K. Matyjaszewski, *Chem. Commun.*, 2017, **53**, 5294–5297.

61 P. Puthiaraj and W. S. Ahn, *Ind. Eng. Chem. Res.*, 2016, **55**, 7917–7923.

62 N. Zhang, F. Liu, S. Da Xu, F. Y. Wang, Q. Yu and L. Liu, *J. Mater. Chem. A*, 2017, **5**, 22631–22640.

63 W. Lv, M. Guo, M. H. Liang, F. M. Jin, L. Cui, L. Zhi and Q. H. Yang, *J. Mater. Chem.*, 2010, **20**, 6668–6673.

64 V. Augustyn, P. Simon and B. Dunn, *Energy Environ. Sci.*, 2014, **7**, 1597–1614.

65 Z. Bo, Z. Wen, H. Kim, G. Lu, K. Yu and J. Chen, *Carbon N. Y.*, 2012, **50**, 4379–4387.

66 S. Chai, N. Hu, Y. Han, X. Zhang, Z. Yang, L. Wei, L. Wang and H. Wei, *RSC Adv.*, 2016, **6**, 49425–49428.

Chapter 5 Hypercrosslinked Polymers Synthesized with Different Ratios of Monomer to Crosslinker for Supercapacitor Applications

5.1 Introduction

Supercapacitors are considered to be one of the most promising energy storage devices due to the fast charge/discharge, high power density and remarkably long life-span.[1,2] The pore structures of the supercapacitor electrode materials are important for the capacitance and rate performance of the supercapacitor.[3] According to the literatures, the micropores are closely associated with the capacitance of the material,[4,5] it was also found that if the pores match the size of the solvated electrolyte ions, the capacitance of the material could be enhanced.[6,7] The mesopores and macropores could reduce the diffusion distance of the electrolyte ions to the enhanced ions transport, thus the rate performance can be enhanced.[8,9,10] For activated carbons, in order to get the ordered hierarchical porous structure, the template method is commonly used for the supercapacitor electrode materials. Briefly, the mesoporous structures can be obtained from the removal of the template material from the mixture of the active material and the template material.[11] The ordered mesoporous templated carbons have shown the increased rate performance and capacitance compared with amorphous activated carbons.[12,13,14,15] However, the cost and the manufacturing process of the template method make the scale-up of template carbon materials is difficult. As a sub-class of POP materials with low-cost and convenient synthesis, HCPs synthesized with knitting method have also shown good potential for structure controlling, for example, by using different ratios of crosslinker to monomer for synthesis,[16,17] but there are very few researches into how different pore structures that are obtained using different ratios of crosslinker to monomer of the HCPs influence the supercapacitive performance of these HCPs. In this chapter, benzene, biphenyl, p-terphenyl, triphenylmethane and 1,3,5-triphenylbenzene are employed as monomers for HCP synthesis, and these HCPs are

synthesized with different ratios of crosslinker to monomer. The porous structures and supercapacitive performance of these HCPs are discussed.

5.2 Benzene HCPs

5.2.1 Synthesis of Benzene HCPs

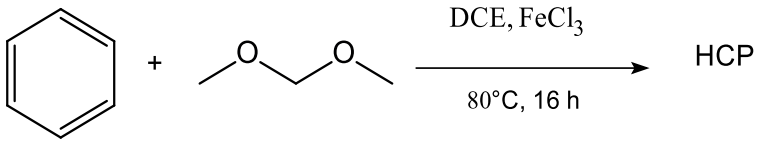

The synthesis of Benzene HCPs was performed as follows. Ferric chloride (10-60 mmol, 1-6 eq.) was added into a dried two-neck flask with a magnetic stirrer and a condenser. DCE (25 mL) and benzene (10 mmol, 1 eq.) were charged into the flask in sequence by syringes with stirring for 5 minutes to disperse the materials. Then, formaldehyde dimethyl acetal (FDA) (10-60 mmol, 1-6 eq.) was injected into the flask by a syringe and the temperature was increased to 80 ℃. The reaction was heated for 20 hours. The reaction was conducted in atmospheric air. The HCP product was cooled and collected by vacuum filtration and washed with water, methanol, acetone. Then the product was transferred to a Soxhlet extractor and washed with methanol overnight. The product was dried under vacuum at 80 ℃ overnight.

Benzene 1-1 HCP: benzene (10 mmol, 0.90 mL, 1 eq.), FDA (10 mmol, 0.89 mL, 1 eq.), ferric chloride (10 mmol, 1.63 g, 1eq.). Yield: 0.71 g, 79%. Formula: C_7H_6. Calculated value of elemental analysis C: 93.29% H: 6.71%. Found value of elemental analysis C: 89.42% H: 5.89%

Benzene 1-2 HCP: benzene (10 mmol, 0.90 mL, 1 eq.), FDA (20 mmol, 1.77 mL, 2 eq.), ferric chloride (20 mmol, 3.25 g, 2 eq.). Yield: 1.07 g, 104%. Formula: C_8H_6. Calculated value of elemental analysis C: 94.08% H: 5.92%. Found value of elemental analysis C: 84.23% H: 5.6%

Benzene 1-4 HCP: benzene (10 mmol, 0.90 mL, 1 eq), FDA (40 mmol, 3.54 mL, 4eq.),

ferric chloride (40 mmol, 6.50 g, 4 eq.). Yield: 1.25 g, 109%. Formula: C_9H_6. Calculated value of elemental analysis C: 94.70% H: 5.30%. Found value of elemental analysis C: 77.63% H: 5.40%

Benzene 1-5 HCP: benzene (10 mmol, 0.90 mL, 1 eq), FDA (50 mmol, 4.45 mL, 5 eq.), ferric chloride (50 mmol, 8.13 g, 5 eq.). Yield: 1.30 g, 113%. Formula: C_9H_6. Calculated value of elemental analysis C: 94.70% H: 5.30%. Found value of elemental analysis C: 79.95% H: 5.56%

Benzene 1-6 HCP: benzene (10 mmol, 0.90 mL, 1 eq), FDA (60 mmol, 5.34 mL, 6 eq.), ferric chloride (60 mmol, 9.75 g, 6 eq.). Yield: 1.38 g, 120%. Formula: C_9H_6. Calculated value of elemental analysis C: 94.70% H: 5.30%. Found value of elemental analysis C: 73.65% H: 5.29%

5.2.2 Results and discussion

5.2.2.1 Synthesis

Benzene HCPs were synthesized by Friedel-Crafts alkylation reaction with benzene used as monomer, formaldehyde dimethyl acetal (FDA) used as an external crosslinker and anhydrous $FeCl_3$ used as a Lewis acid catalyst, in air atmosphere and at 80 ℃. The synthesis of HCPs with knitting method performed in air atmosphere was also used in the previous literatures.[18,19] The HCPs can be synthesized under an air atmosphere indicates the cost of the potential industrial scale-up of HCPs in the future could be reduced, for instance, dry solvents can be replaced by common solvents for HCP synthesis. In Chapter 3, Benzene HCP was synthesized with a ratio of benzene to FDA 1:3. In order to explore the influence of different crosslinking density, Benzene HCPs are synthesized with different ratios of benzene to FDA 1:1, 1:2, 1:4, 1:5 and 1:6 in this chapter. Therefore, the HCPs are marked as Benzene 1-1 HCP, Benzene 1-2 HCP, Benzene 1-4 HCP, Benzene 1-5 HCP and Benzene 1-6 HCP, respectively. The yields of the HCPs are calculated and elemental analysis is performed in the table 5.2.1.

	Yield %		Calculated value		Found value	
			C %	H %	C %	H %
Benzene 1-1 HCP	79%	0.71 g	93.29	6.71	89.42	5.89
Benzene 1-2 HCP	104%	1.07 g	94.08	5.92	84.23	5.60
Benzene 1-3 HCP	96.7%	1.11 g	94.70	5.30	82.02	5.82
Benzene 1-4 HCP	109%	1.25 g	94.70	5.30	77.63	5.40
Benzene 1-5 HCP	113%	1.30 g	94.70	5.30	79.95	5.56
Benzene 1-6 HCP	120%	1.38 g	94.70	5.30	73.65	5.29

Table 5.2.1 Yield and elemental analysis results of Benzene HCPs

In the table 5.2.1, it can be seen that the Benzene 1-1 HCP has the lowest yield of 79%. The Benzene 1-6 HCP has the yield of 120% which is the highest among all samples in this group. With the increasing ratio of FDA to benzene, the overall variation of the yield of the Benzene HCPs shows an upward tendency, and the gap between the experimental values the found values of elemental analysis increases.

The samples with yield higher than 100% indicate the existence of incompletely reacted crosslinker residues due to the steric hindrance which was reported previously,[20] e.g., -O-CH_3. Because of the unexpected oxygen atoms in HCP networks, the yield can be higher than 100%, and the calculated values of the elemental analysis are different from the experimental values.

The low yield of the Benzene 1-1 HCP can be ascribed to the low content of crosslinker residues, as the found values of the Benzene 1-1 HCP in the elemental analysis are closer to the expected values than other samples, it can be also confirmed by the ^{13}C solid state NMR spectrum of the Benzene 1-1 HCP, it can be seen that the intensity of the peaks at 17 ppm and 73 ppm which correspond to the crosslinker residues is much lower. Due to the low ratio of FDA to benzene of Benzene 1-1 HCP and the increased steric hindrance, some monomers and crosslinkers cannot form a high molecular weight HCP network with large particle size, these HCP particles are too small to be collected by using vacuum filtration, thus the yield of the Benzene 1-1 HCP is lower. In the synthesis of HCPs, the crosslinker could react with the monomer rapidly to generate

porous solid product, then the steric hindrance is enhanced by the rigidity structure of the formed HCP networks. Therefore, some crosslinkers cannot be completely reacted thus crosslinker residues are formed, meanwhile, some monomers and crosslinkers may not be reacted as expected to form HCP networks with high molecular weight due to the intense steric impediment, therefore some small HCP particles that are hard to collect will be formed, leading to a lower yield. The increasing ratio of crosslinker to monomer could result in higher incompletely reacted crosslinker residues is also observed in the previous literatures.[21,22] The increasing amount of crosslinkers could accelerate the generation of porous solid product, hence more monomers and crosslinkers cannot be reacted as expected. As a result of increasing amount of crosslinkers, the yields of Benzene HCPs are higher due to the increasing crosslinker residue content and the gap between the calculated values and the found values of the elemental analysis is further enlarged. The synthesis of benzene HCPs can be analyzed from the perspective of Carothers theory as well. For multifunctional monomers, the number-average value of the degree of polymerization can be written as equation 5.2.2.1.

$$x_n = \frac{2}{2-pf_{av}} \qquad 5.2.2.1$$

Where p is extent of reaction, and f_{av} is average functionality, defined by equation 5.2.2.2.

$$f_{av} = \frac{\sum N_i f_i}{\sum N_i} \qquad 5.2.2.2$$

Where N is the number of molecules of the monomers, f is functionality of the monomers. In Carothers theory, the degree of polymerization at the gel point is infinite, and the extent of reaction is $\frac{2}{f_{av}}$. For Benzene 1-1, 1-2, 1-3, 1-4, 1-5, 1-6 HCP, the average functionality is 2, 2.67, 3, 2.8, 2.67, 2.57, respectively. It is well known that the average functionality has strong influence to the molecular structure of reaction product. In theory, when average functionality is 2, only linear structure product can be produced, this conclusion corresponds to the discussion of Benzene 1-1 HCP above. With the increasing amount of crosslinker, the average functionality increases as well, indicating

crosslinked networks were formed. These different average functionalities demonstrate using different monomer-crosslinked ratios is somewhat useful for controlling the structures of HCPs. With the increasing amount of crosslinkers.

It can be also found that the extent of reaction decreases with the increasing amount of crosslinkers from the ratio 1-1 to 1-6, corresponding to the steric hindrance caused by the rigidity of HCP network.

5.2.2.2 FTIR and ^{13}C Solid State NMR spectroscopy

The molecular structures of Benzene HCPs were analyzed and confirmed by using

Fourier transform infrared (FTIR) and ^{13}C solid state NMR.

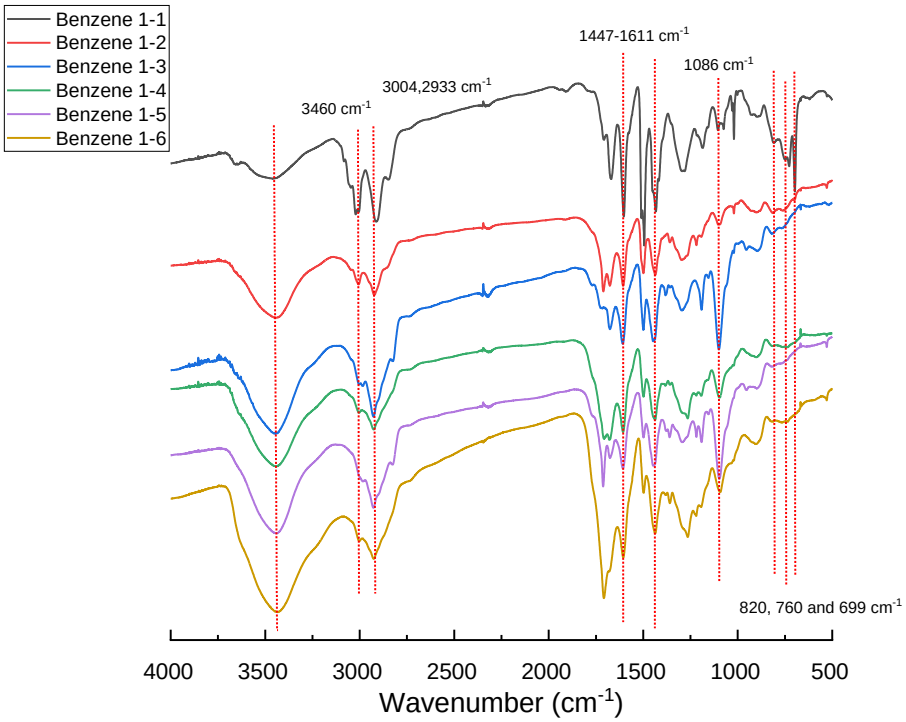

Figure 5.2.1 FTIR spectra of Benzene HCPs

For FTIR spectrum of Benzene HCPs, the peaks at 3004 and 2933 cm^{-1} are attributed to C-H stretching vibration in aromatic ring and methylene bridge obtained from Friedel-Crafts reaction, respectively.[23] The peaks at 1445-1611 cm^{-1} are attributed to the skeleton vibration of aromatic rings.[24] The peak at 1086 cm^{-1} can be ascribed to C-O stretching of the crosslinker residue.[22] It can be seen the intensity of the peak at 3004 cm^{-1} reduces with the increasing ratio of the crosslinker to benzene, this was also observed in the previous literature.[17] The broad and strong peaks at 3454 cm^{-1} is ascribed to the water residue in KBr disc and the porous samples.[25]

In the spectrum of Benzene 1-1 HCP, the peak at 1501 cm^{-1} together with the peak at 820 cm^{-1} corresponds to para-substituted aromatic ring,[26] and the peaks at 760 cm^{-1} and 699 cm^{-1} are related with mono-substituted aromatic ring.[27] With the increasing ratio of FDA to benzene, it can be seen that these peaks were weakened or disappeared indicating more crosslinker reacted with the benzene when the amount of crosslinkers used in the Benzene synthesis was higher. Therefore, the FTIR spectra of the Benzene HCPs are consistent with the expected structure.

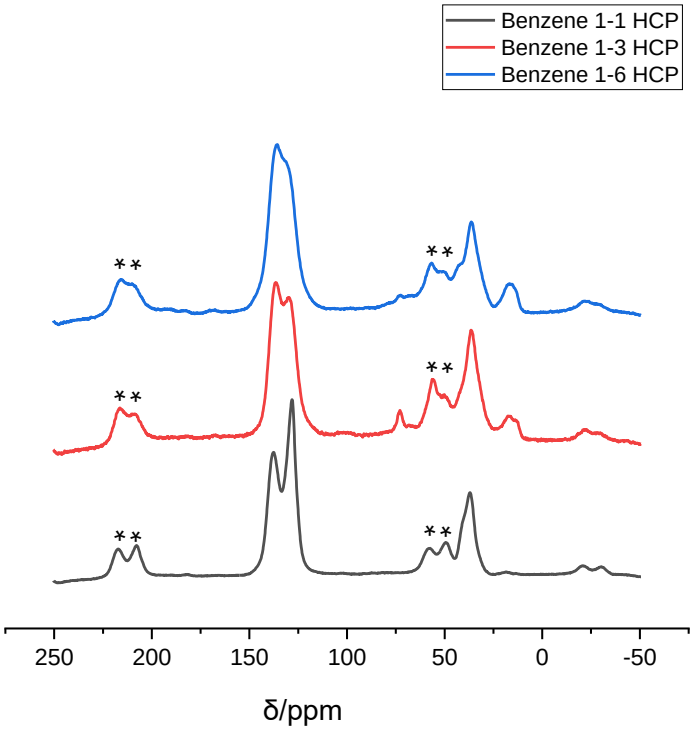

Figure 5.2.2 ^{13}C solid state NMR spectra of Benzene HCPs (the asterisks denote spinning side bands)

The structural information of Benzene HCPs can be also obtained from ^{13}C solid state NMR spectra. The peaks at 137 ppm and 130 ppm are assigned to the substituted aromatic carbon and the non-substituted aromatic carbon, respectively.[28] The peak at 36 ppm is ascribed to the carbon in the methylene bridge of the network.[29] As discussed in Chapter 3, the peak at 73 ppm corresponds to carbon in the methylene group binding to the oxygen atom of the incompletely reacted crosslinker, and the peak at 17 ppm is ascribed to the methyl carbon in the end of incompletely reacted crosslinker.[22] For Benzene 1-1 HCP, the peak at 17 ppm is much weaker than that of Benzene 1-3 and 1-6 HCP and the peak at 73 ppm disappears, suggesting the crosslinkers are easier to completely react with benzene at low ratio of the crosslinker to benzene. Comparing Benzene 1-3 HCP and Benzene 1-6 HCP, it can be found that the intensity of the non-substituted aromatic carbon peak is higher than that of the substituted aromatic carbon peak, indicating there are more aromatic carbons reacted with the crosslinkers with the increasing ratio of the crosslinker to benzene which is in consistent with FTIR results. Based on the analysis above, it can be confirmed that the benzene hyper-crosslinker

polymers with desired structure were obtained from Friedel-Crafts reaction.

5.2.2.3 TGA

The thermal stability of Benzene HCPs was characterized by using thermalgravimetric analysis (TGA). The TGA was conducted under a N_2 atmosphere and the samples were heated from 25 °C to 800 with a heating rate 10 °C/min.

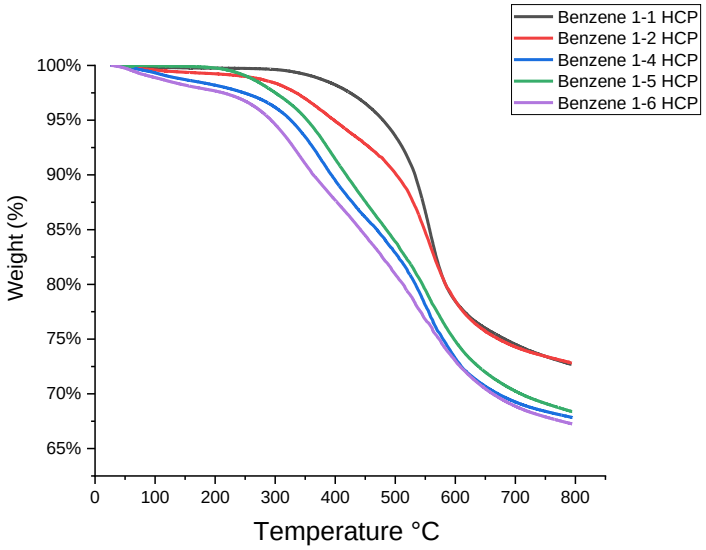

Figure 5.2.3 TGA curves of Benzene HCPs

In the figure above, Benzene HCPs showed good thermal stability. The weight residue of the Benzene HCPs is higher than 90% at 350 °C. It can be found that the onset temperature of the Benzene HCPs decreased with the increasing ratio of FDA to benzene. The decrease in onset temperature can be attributed to higher content of incompletely reacted crosslinker residues. At 800 °C, the Benzene 1-1 HCP and Benzene 1-2 HCP showed higher weight residue of 73%, and the weight residue of the Benzene 1-4, 1-5 and 1-6 HCP is around 67%, lower than that of Benzene 1-1 and 1-2 HCP.

5.2.2.4 N_2 Sorption

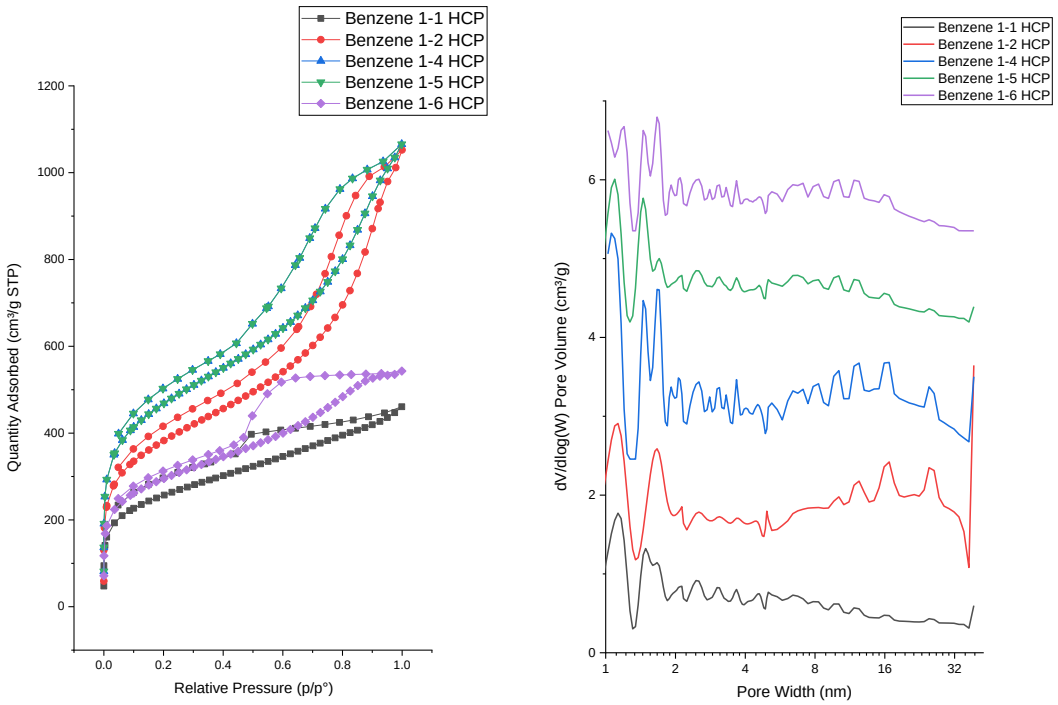

Figure 5.2.4 Isotherm and pore size distribution of Benzene HCPs

The pore structures of Benzene HCPs were characterized by using N_2 adsorption-desorption isotherms measured at 77 K. The Benzene HCPs exhibited the combined Type II and Type IV isotherms. The isotherm curves of Benzene HCPs show a steep rise of N_2 adsorption at very low relative pressure ($P/P_0<0.01$), which indicates the existence of microporous structures in these samples.[30,31] The hysteresis loop in the intermediate region demonstrating the mesopores in the structures of these samples.[32] The N_2 uptake with gradual rise in the relative pressure range of 0.9-1.0 suggesting the macroporous structures in these samples.[33] From the pore size distribution of Benzene HCPs, it can be found that the dominant pore width of the samples located at the interval of 1-2 nm indicating microporous structures in these samples. The relatively weaker peaks found at the pore size range of 2-32 nm suggesting the existence of mesoporous structures in the Benzene HCPs.

The single point adsorption total pore volumes of the Benzene HCPs obtained at $p/p_0=0.99$ and the BET surface areas of them are shown in the table 5.2.2.

	BET surface area (m^2/g)	Single point adsorption total pore volume at p/p_0=0.99 (cm^3/g)
Benzene 1-1 HCP	931.4	0.71
Benzene 1-2 HCP	1381.9	1.63
Benzene 1-3 HCP	1040.4	1.08
Benzene 1-4 HCP	1698.4	1.65
Benzene 1-5 HCP	1085.2	0.91
Benzene 1-6 HCP	1072.3	0.84

Benzene HCPs in previous literatures	BET surface area (m^2/g)	Reference
benzene-FDA 1:2	1270	[16]
benzene-FDA 1:3	1391	[16]
benzene-FDA 1:3	823.9	[17]

Table 5.2.2 BET surface area and single point adsorption total pore volume of Benzene HCPs

In the table 5.2.2, The BET surface areas of Benzene 1-1, 1-2, 1-4, 1-5 and 1-6 HCP were calculated to be 931.4, 1381.9, 1698.4, 1085.2 and 1072.3 m^2/g, respectively. The single point adsorption total pore volumes of Benzene 1-1, 1-2, 1-4, 1-5, 1-6 HCPs were found to be 0.71, 1.63, 1.65, 0.91 and 0.84 cm^3/g, respectively. For Benzene 1-3 HCP in chapter 3, the BET surface area is 1040.4 m^2/g and the single point adsorption total pore volume is 1.08 cm^3/g. When these samples are compared together, Benzene 1-1 HCP has the lowest BET surface and the single point adsorption total pore volume while Benzene 1-4 HCP shows the highest BET surface area, 1698.4 m^2/g, and the highest pore volume, 1.65 cm^3/g. The Benzene 1-2 and 1-4 HCP have the BET surface area of 1381.9 and 1698.4 m^2/g and the single point adsorption total pore volume of 1.63 and 1.65 cm^3/g which are higher than those of Benzene 1-3 HCP. With the ratio of FDA to benzene increased from 4-1 to 6-1, the BET surface area of the samples decreased from 1698.4 m^2/g to 1072.3 m^2/g and the pore volume decreased from 1.65 to 0.84 cm^3/g. The benzene HCP synthesize with a ratio of benzene to FDA 1-2 by Li et al. has a BET

surface area of 1270 m^2/g,[16] lower than that of the Benzene 1-2 HCP in my work, while the benzene HCP synthesized by them with a benzene to FDA ratio 1-3 has a BET surface area of 1391 m^2/g,[16], higher than that of the Benzene 1-3 HCP. The benzene HCP synthesized with a benzene to FDA ratio 1-3 by Penchah et al. has a lower BET surface area, 823.9 m^2/g.[17]

For further insight of the porous structures of Benzene HCPs, the pore volumes of the pores with different pore widths are shown in the table 5.2.3 and pore volume proportions of Benzene HCPs are performed in the figure 5.2.5, revealing the composition of total pore volumes of Benzene HCPs. The pore volumes of the pores with pore widths less than 2 nm are obtained at relative pressure p/p_0=0.2 and the pore volumes of the pores with pore widths less than 10 nm are obtained at p/p_0=0.8.

Material	Pore volume of the pores with pore width less than 2 nm (cm^3/g)	Pore volume of the pores with pore width 2-10 nm (cm^3/g)	Pore volume of the pores with pore width larger than 10 nm (cm^3/g)
Benzene 1-1 HCP	0.40	0.21	0.10
Benzene 1-2 HCP	0.59	0.48	0.55
Benzene 1-3 HCP	0.44	0.37	0.27
Benzene 1-4 HCP	0.73	0.51	0.41
Benzene 1-5 HCP	0.47	0.30	0.14
Benzene 1-6 HCP	0.46	0.29	0.09

Table 5.2.3 The pore volumes of the pores with different pore widths of Benzene HCPs

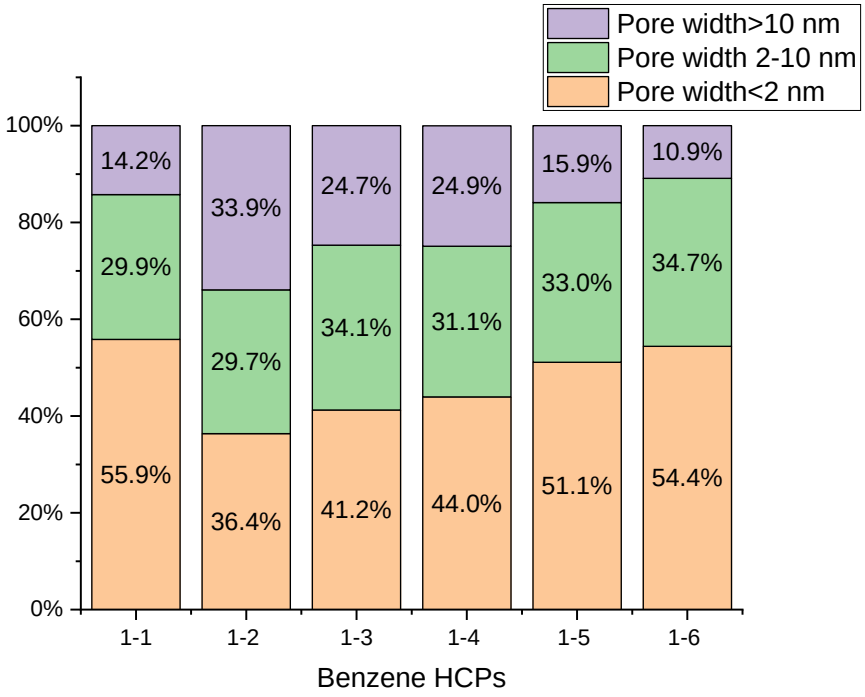

Figure 5.2.5 Pore volume proportions of pores with different pore widths of Benzene HCPs

The micropore volume proportions of Benzene 1-1, 1-2, 1-4, 1-5 and 1-6 HCP are 55.9%, 36.4%, 44.0%, 51.1% and 54.4%, and the micropore volumes of them are 0.40, 0.59, 0.40, 0.43 and 0.46 cm^3/g respectively. The volume proportions of pores with pore width 2-10 nm in Benzene 1-1, 1-2, 1-4, 1-5 and 1-6 HCP are 29.9%, 29.7%, 31.1%, 33.0% and 34.7%, and the pore volumes of them are 0.21, 0.48, 0.28, 0.28 and 0.29 cm^3/g respectively. For the pores with pore width larger than 10 nm, the pore volume proportions of Benzene 1-1, 1-2, 1-4, 1-5 and 1-6 HCP are 14.2%, 33.9%, 24.9%, 15.9% and 10.9%, the pore volumes of the pores with pore width larger than 10 nm are 0.10, 0.55, 0.23, 0.13 and 0.09 cm^3/g, respectively. The volume proportion of micropores, pores with diameter 2-10 nm and pores with diameter larger than 10 nm of Benzene 1-3 HCP are 41.2%, 34.1% and 24.7%, the pore volumes of these pores are 0.68, 0.56 and 0.41 cm^3/g, respectively. It can be seen that although Benzene 1-3 HCP does not have the highest BET surface area and the highest total pore volume, it has the highest micropore volume and the highest pore volume of the pores with diameter 2-10 nm, followed by Benzene 1-2 HCP. For the variation of the micropore volume proportion, the Benzene HCPs showed a downward tendency followed by an upward tendency.

From Benzene 1-1 HCP to Benzene 1-2 HCP, the micropore volume proportion decreased from 55.9% to 36.4%. From Benzene 1-2 HCP to Benzene 1-6 HCP, the micropore volume proportion increased from 36.4% to 54.4%. For the variation of the pore volume proportion of the pores with diameter 2-10 nm, the Benzene HCPs showed an increasing trend with fluctuations. From Benzene 1-1 HCP to Benzene 1-6 HCP, the pore volume proportion of the pores with diameter 2-10 nm increased from 29.9% to 34.7%. For pores with diameters larger than 10 nm, the variation trend of the pore volume proportion showed a downward tendency due to the increased volume proportion of the pores with pore diameters less than 10 nm.

5.2.2.5 Cyclic Voltammetry

The electrochemical properties of Benzene HCPs were evaluated by a typical three-electrode system with 1 M Na_2SO_4 aqueous solution as electrolyte. The active material on nickel foam, a platinum electrode and an Ag/AgCl (3 M KCl, 0.207 V vs. standard hydrogen electrode at 25 °C) electrode were used as working electrode, counter electrode and reference electrode, respectively. The CV tests were conducted with different scan rates 2, 10, 25, 50, 75, 100 and 200 mV/s in the voltage range of -0.2 V-0.8 V.

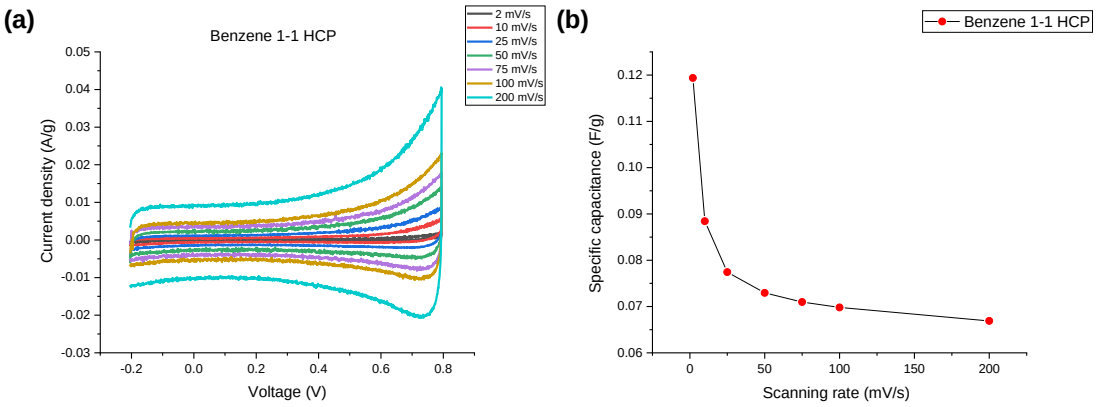

Figure 5.2.6 (a) CV curves at different scanning rates, and (b) Specific capacitance obtained at different scanning rates of Benzene 1-1 HCP

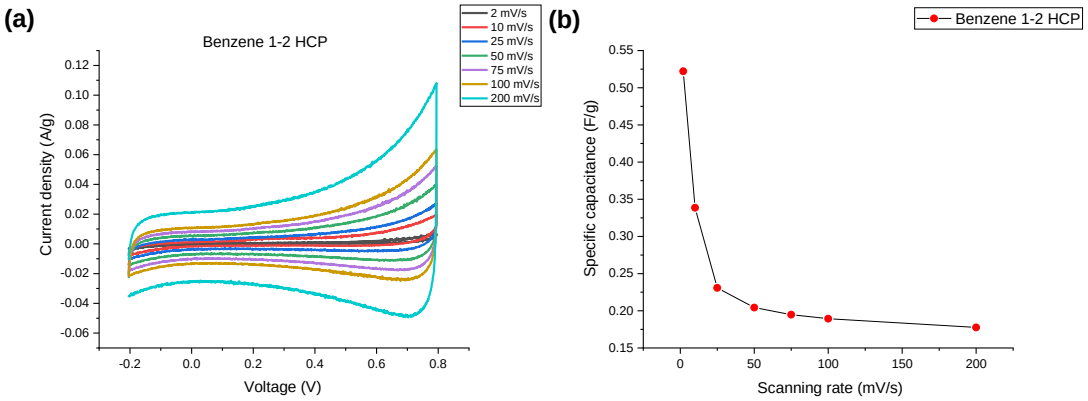

Figure 5.2.7 (a) CV curves at different scanning rates, and (b) Specific capacitance obtained at different scanning rates of Benzene 1-2 HCP

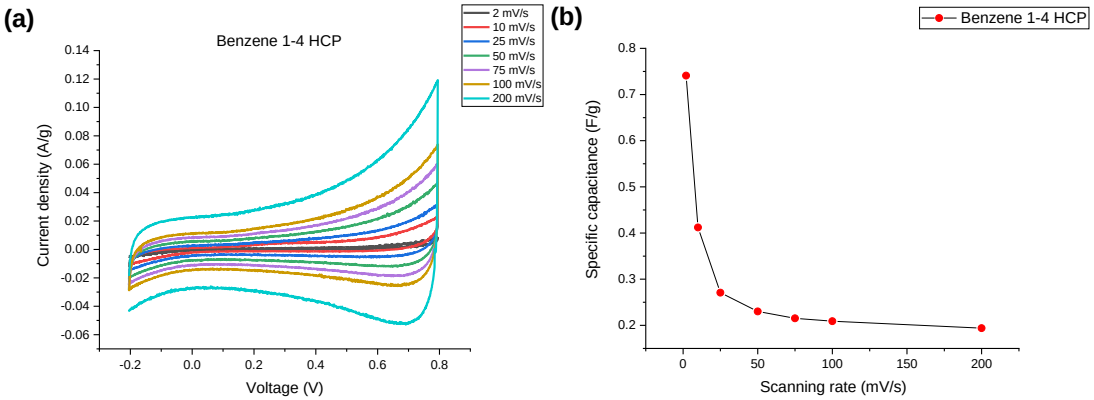

Figure 5.2.8 (a) CV curves at different scanning rates, and (b) Specific capacitance obtained at different scanning rates of Benzene 1-4 HCP

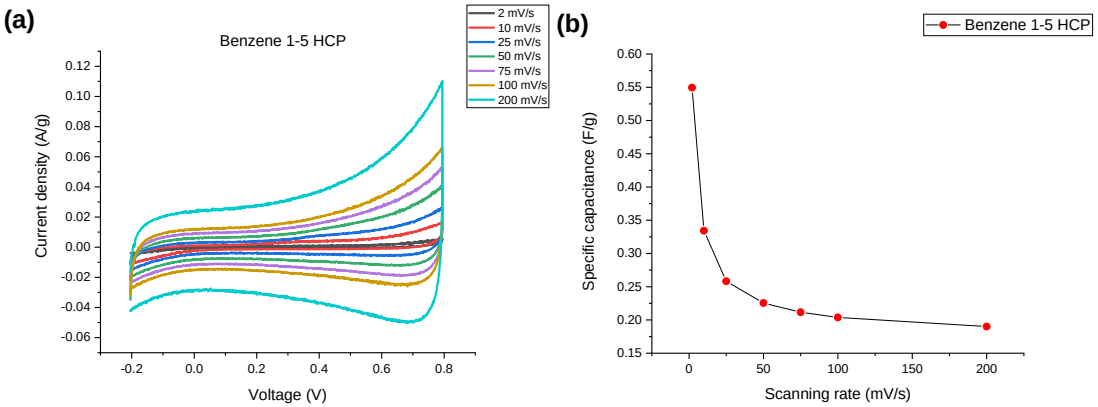

Figure 5.2.9 (a) CV curves at different scanning rates, and (b) Specific capacitance obtained at different scanning rates of Benzene 1-5 HCP

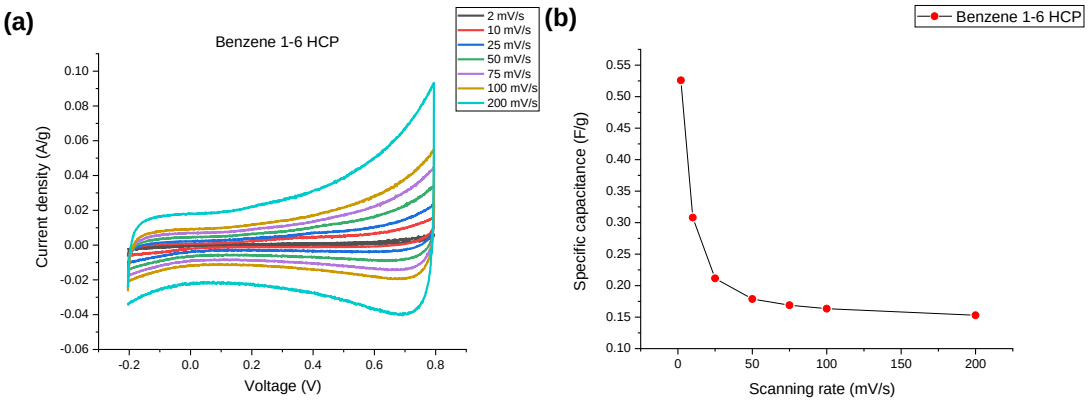

Figure 5.2.10 (a) CV curves at different scanning rates, and (b) Specific capacitance obtained at different scanning rates of Benzene 1-6 HCP

	Specific capacitance obtained at different scanning rates (F/g)							
Scanning rates (mV/s) / Material	2	10	25	50	75	100	200	Retention of capacitance at 200 mV/s
Benzene 1-1 HCP	0.12	0.09	0.08	0.07	0.07	0.07	0.07	56.1%
Benzene 1-2 HCP	0.52	0.34	0.23	0.20	0.19	0.19	0.18	34.0%
Benzene 1-3 HCP	13.9	1.5	0.7	0.4	0.4	0.4	0.4	2.9%
Benzene 1-4 HCP	0.74	0.41	0.27	0.23	0.21	0.21	0.19	26.2%
Benzene 1-5 HCP	0.55	0.33	0.26	0.23	0.21	0.20	0.19	34.6%
Benzene 1-6 HCP	0.53	0.31	0.21	0.18	0.17	0.16	0.15	29.0%

Table 5.2.4 Specific capacitance of benzene HCPs obtained at different scanning rates

From the CV results of Benzene HCPs, it can be found these samples have quite low specific capacitance. The specific capacitance of Benzene 1-1, 1-2, 1-4, 1-5 and 1-6 HCP obtained from 2 mV/s is 0.12, 0.52, 0.74, 0.55 and 0.53 F/g, respectively. The capacitance retention rate from 2 mV/s to 200 mV/s of Benzene 1-1, 1-2, 1-4, 1-5 and 1-6 HCP is 56.1%, 34.0%, 26.2%, 34.6% and 29%, respectively. It can be found the Benzene HCPs have much better rate performance than other HCPs in these chapter, as the capacitance retention rate from 2 mV/s to 200 mV/s of most of the HCPs is slightly

higher than 1%. The Benzene 1-1 HCP has the lowest BET surface area 931.4 m^2/g and the lowest total pore volume 0.71 cm^3/g, the specific capacitance of Benzene 1-1 HCP is the lowest among all Benzene HCPs as well. The Benzene 1-4 HCP has the highest BET surface area and total pore volume, and it has the highest specific capacitance. Although Benzene 1-4 HCP has a higher specific capacitance than Benzene 1-1 HCP, they have quite similar micropore volume. The Benzene 1-5 and 1-6 HCP have similar BET surface area and pore volume, the specific capacitances of these two samples are similar as well. The Benzene 1-2 HCP has the second highest BET surface and pore volume, the micropore volume and the pore volume of the pores with diameter 2-10 nm are higher than those of Benzene 1-5 and 1-6 HCPs, while its specific capacitance is close to that of Benzene 1-5 and 1-6 HCP. For Benzene 1-3 HCP, the specific capacitance at 2 mV/s is 13.9 F/g, higher than that of other Benzene HCPs. It can be found that the Benzene 1-3 HCP does not have the highest BET surface and total pore volume, but it has the highest micropore volume and the highest pore volume of the pores with diameter 2-10 nm. Although the Benzene HCPs have high BET surface area, the specific capacitances of them are quite low. The impedance results show that Benzene HCPs also have poor conductivity, but they have better rate performance than other HCPs. The CV curves of Benzene HCPs could reveal the reasons for the phenomena that seem unreasonable. For CV curves of Benzene HCPs at 200 mV/s, the significant growth from 0.4 V to 0.8 V in the charging process can be observed, and the curve drops dramatically at the beginning of the discharge process. This suggests that the electrolyte ions cannot diffuse into these samples effectively because of the pore structure, so they accumulated on the surface of these samples. With the increasing voltage, the unstable accumulation was gradually enhanced. Therefore, these unsteadily accumulated ions were released instantly at the beginning of the discharge process. Because the electrolyte ions cannot diffuse into the materials, the high porosity of Benzene HCPs cannot be utilized efficiently, thus the capacitance of the Benzene HCPs are quite low.

It can be found from the CV curves that the response current is quite small, suggesting

the poor conductivity of the Benzene HCPs. Except for the shape deviation caused by the accumulation of the electrolyte ions on the outer surface, these CV curves show a quasi-rectangular shape, suggesting these samples show behaviours like parallel plate capacitors which can be charged/discharged rapidly. As the electrolyte ions accumulated on the outer surface of the electrodes, the accumulation and the releasing processes of the ions are relatively faster, thus the rate performance of Benzene HCPs is better than that of other HCPs. To confirm this, the relationship between response current and scanning rate was used for analyzing the energy storage kinetics of these samples. If the response current is linear with scanning rate, the kinetic of the capacity is dominated by the fast surface-controlled process, whereas the linear relationship between response current and scanning root square root demonstrates the kinetic of the capacity is dominated by the slow diffusion-controlled process.[34,35] The response current vs scanning rate plots of Benzene HCPs are listed below.

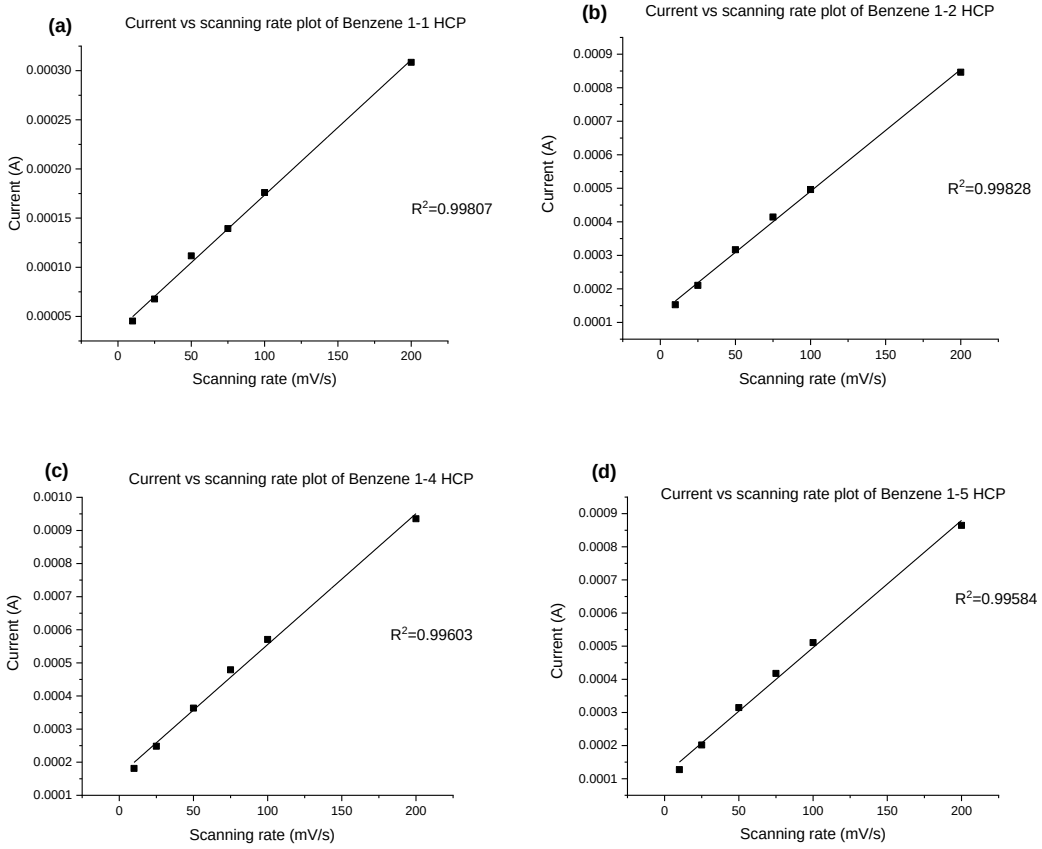

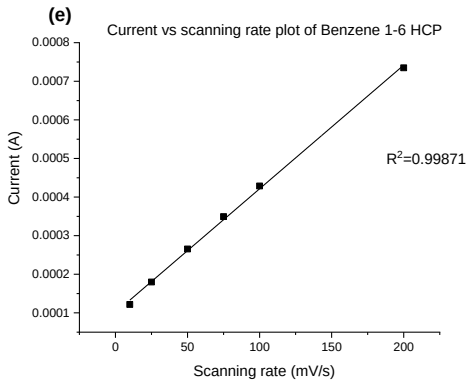

Figure 5.2.11 The response current vs scanning rate plot of Benzene HCPs. (a). - (e). current vs scanning rate plot of Benzene 1-1, 1-2, 1-4, 1-5, 1-6 HCP.

From the figure above, it can be seen the coefficient of determination R^2 of the response current vs scanning rate plot of Benzene 1-1, 1-2, 1-4, 1-5 and 1-6 HCP is 0.99807, 0.99828, 0.99603, 0.99584 and 0.99871, respectively. This shows the good linear relationship between the response current and scanning rate, suggesting the capacitances of the Benzene HCPs are mainly realized by the fast surface-controlled process. So, the rate performance of these samples are higher. This result corresponds to the analysis above. The higher rate performance and lower specific capacitance suggest the porosity of Benzene HCPs cannot be proper utilized, that is to say, it is difficult for the electrolyte ions to diffuse into the Benzene HCPs thus they accumulate on the outer surface. For carbonized Benzene HCP (synthesized from 1 eq. of benzene and 2 eq. of FDA, carbonized under 800°C in N_2 atmosphere for 2 h, BET surface area 539 m^2/g, three-electrode system, 1 M H_2SO_4 aqueous solution), the specific capacitance is 33 F/g at the scanning rate of 10 mV/s.[36] So, it can be found that Benzene HCPs are not particularly suited for the application of supercapacitors, but they may have better performance in other applications.

5.2.2.6 Electrochemical impedance spectroscopy (EIS)

To further investigate the electrochemical performance of Benzene HCPs, electrochemical impedance spectroscopy (EIS) was carried out with amplitude of 10 mV and frequency range 100 k Hz to 0.01 Hz. The Nyquist and Bode plots of Benzene

HCPs are shown in the figures 5.2.12 to 5.2.16.

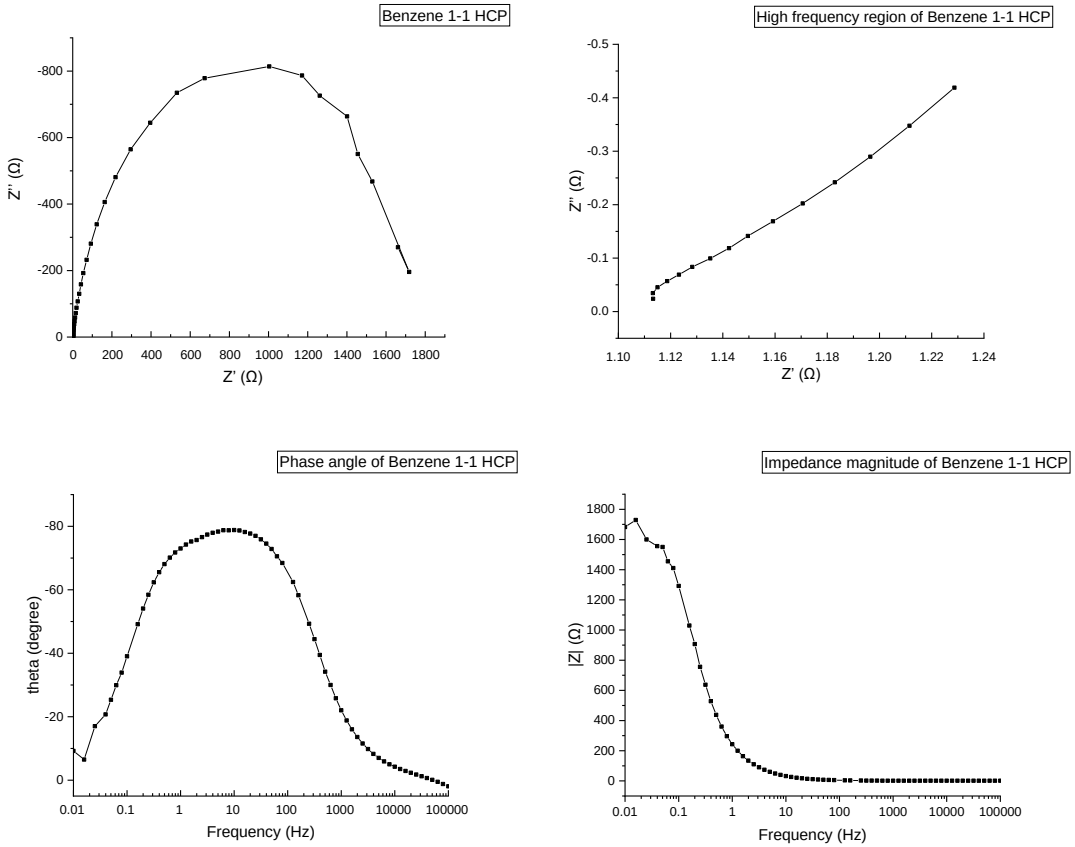

Figure 5.2.12 Nyquist plot and Bode plot of Benzene 1-1 HCP

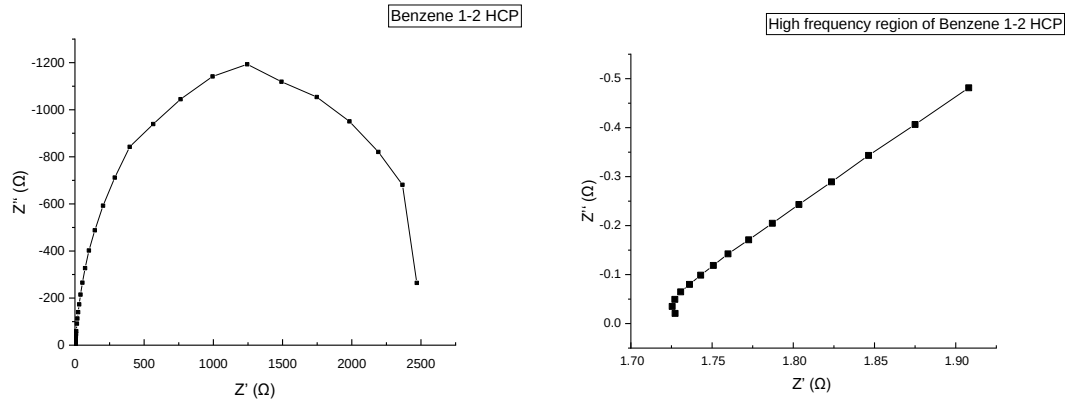

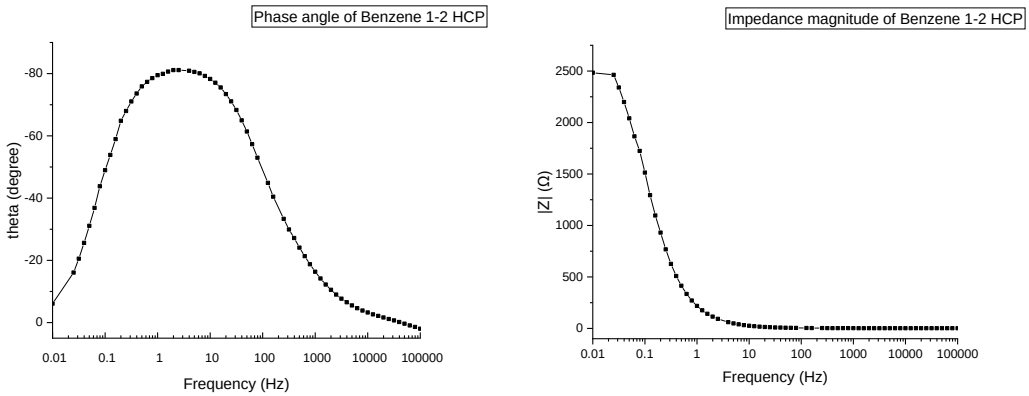

Figure 5.2.13 Nyquist plot and Bode plot of Benzene 1-2 HCP

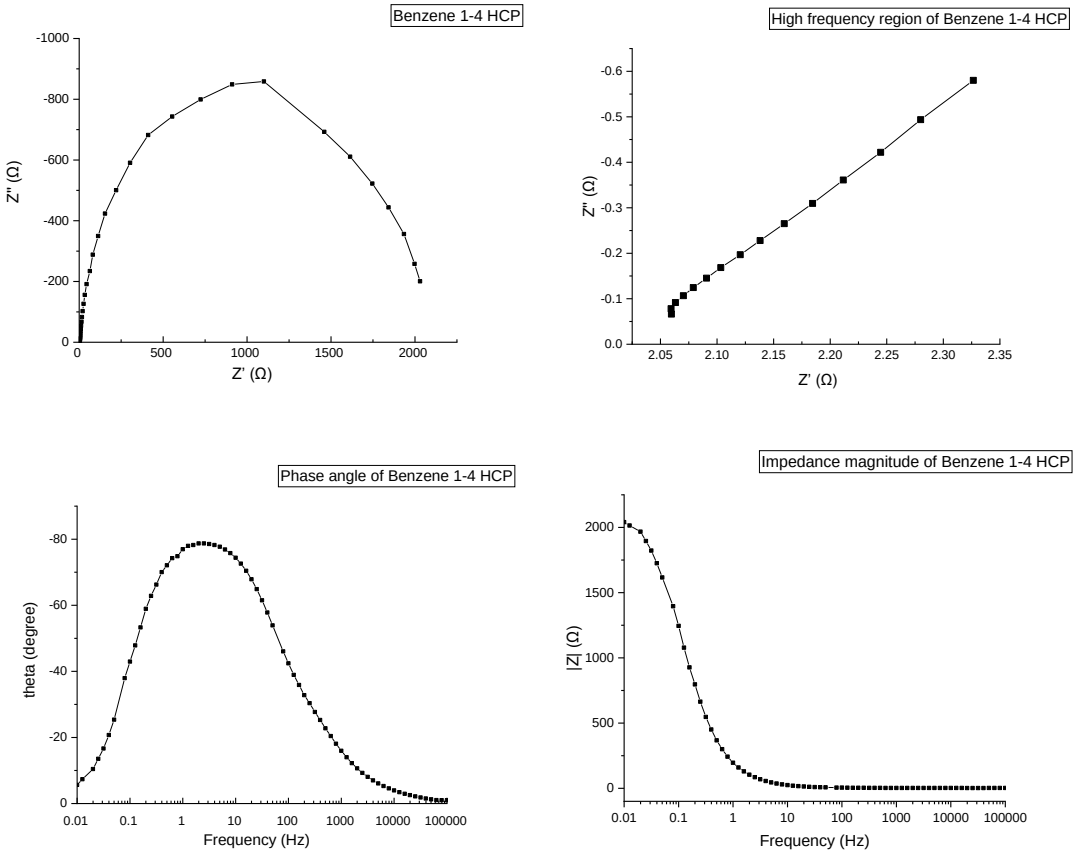

Figure 5.2.14 Nyquist plot and Bode plot of Benzene 1-4 HCP

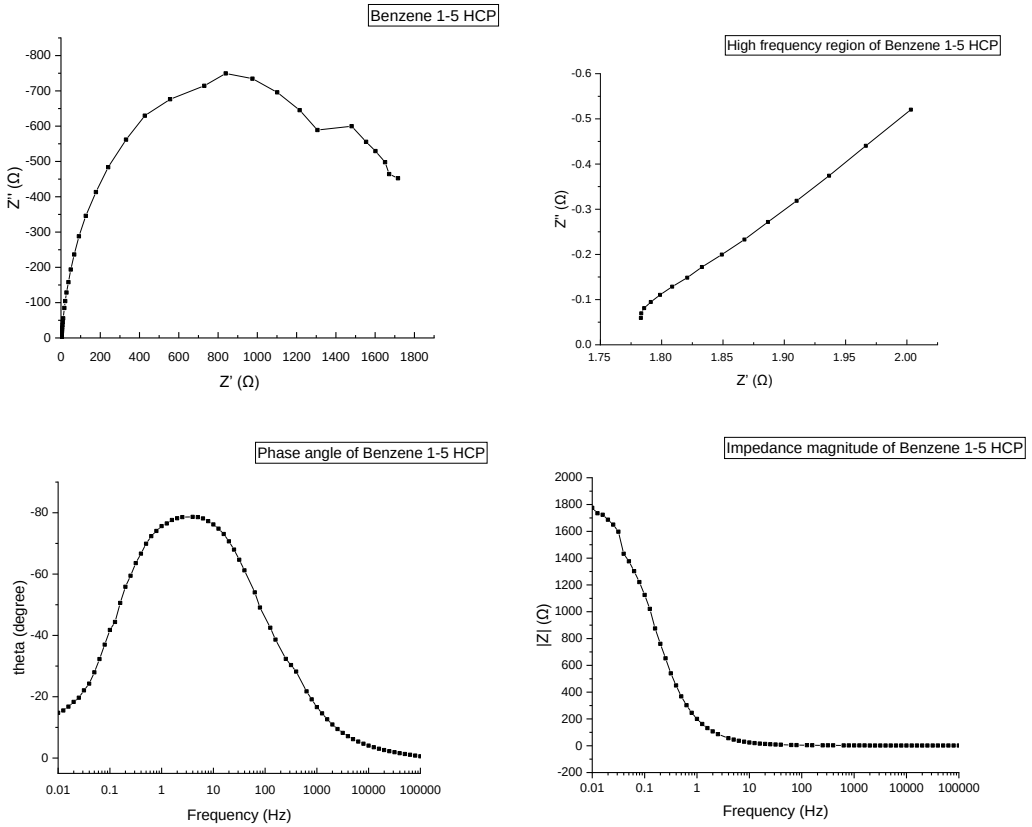

Figure 5.2.15 Nyquist plot and Bode plot of Benzene 1-5 HCP

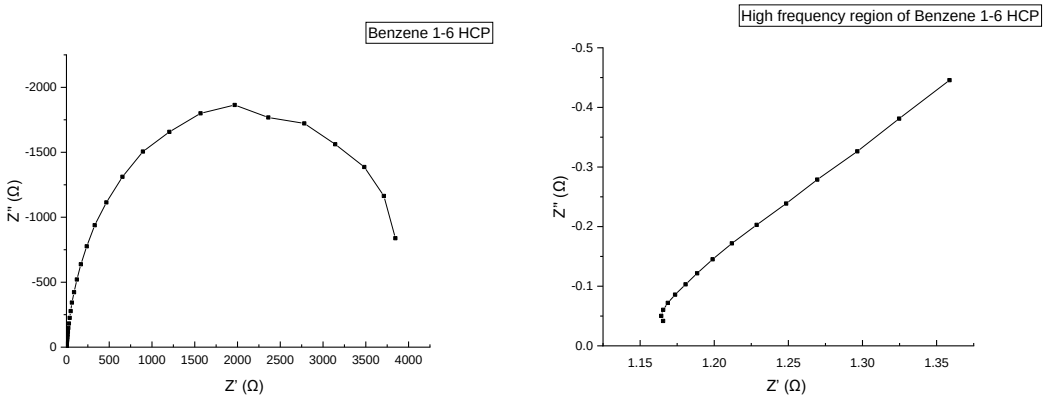

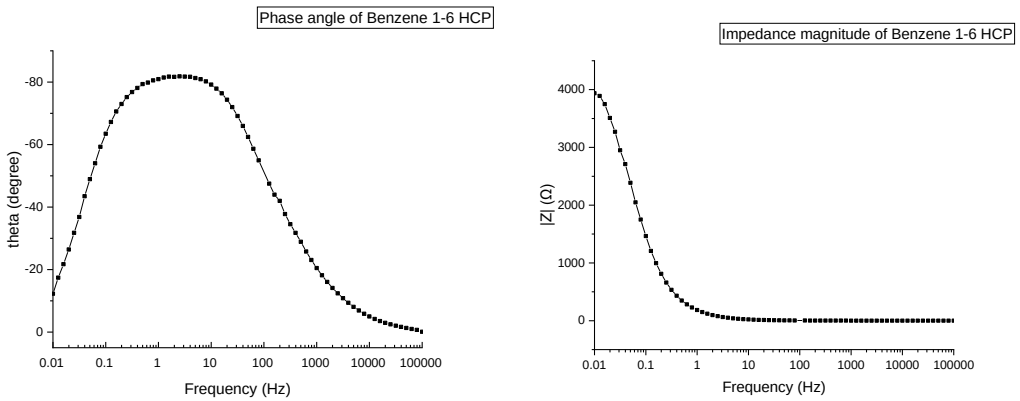

Figure 5.2.16 Nyquist plot and Bode plot of Benzene 1-6 HCP

	Whether the semicircle can be observed at high frequencies?	Whether the Nyquist plot is vertical or near vertical to Z" axis at low frequencies?	The phase angle value of the curve apex	Phase angle at 0.01 Hz	Impedance magnitude at 0.01 Hz (Ω)
Benzene 1-1 HCP	No	No	-79°	-10°	1683
Benzene 1-2 HCP	No	No	-81°	-7°	2483
Benzene 1-4 HCP	No	No	-79°	-5°	2040
Benzene 1-5 HCP	No	No	-79°	-17°	1775
Benzene 1-6 HCP	No	No	-82°	-16°	3936

Table 5.2.5 The results from Nyquist and Bode plot of benzene HCPs

For the Nyquist plots of Benzene HCPs, it can be seen that there was no sharp rise paralleling to Z" axis which indicates the supercapacitor was fully charged. That is to say, the Benzene HCPs do not behave like supercapacitors. The highest points of the phase angle curves of Benzene HCPs are close to -80°. For a resistor, the phase angle is always 0°, whereas for an ideal supercapacitor, the highest point of the phase angle curve is -90°. The more close to -90°, the more close to capacitor behavior. Although -

90° is quite hard to be reached, the phase angle of a common supercapacitor should not change at low frequencies. It can be observed that the phase angle curves of Benzene HCPs decreased sharply after reaching the highest phase angle, suggesting Benzene HCPs did not behave like a supercapacitor. While the phase angle did not decrease to 0°, this means the Benzene HCPs showed some capacitance at low frequencies. The impedance magnitudes of Benzene HCPs at 0.01 Hz are quite high. Based on the shape of the Nyquist plots of Benzene HCPs and the formula of impedance magnitude calculation, it can be found that the internal resistance of Benzene HCPs accounts for a large proportion in the impedance magnitudes obtained at low frequencies. The absence of the semi-circle in the high frequency region can be attributed to the ohmic contact between the current collector and the active materials.[37]

In order to see the poor conductivity of Benzene HCPs more intuitively, the results from fitting are shown in the figure 5.2.17 and the table 5.2.6. The equivalent circuit model used for the fitting of Benzene HCPs is Randles circuit model which is commonly used for supercapacitors.

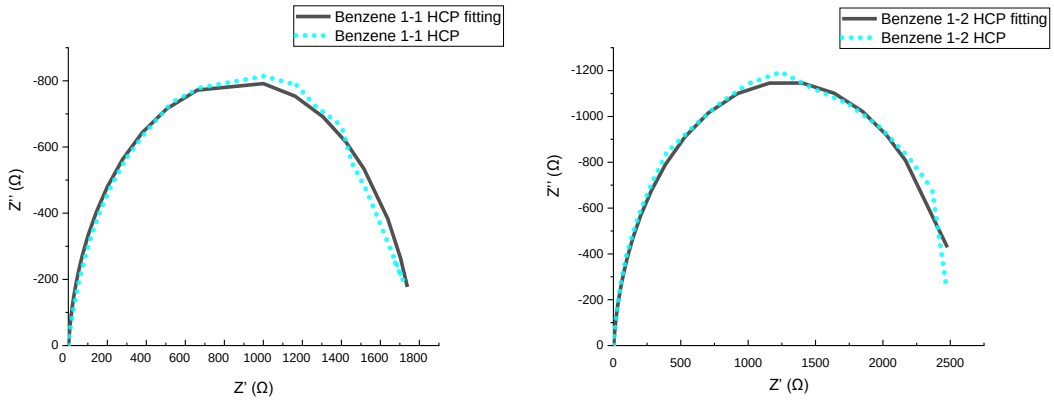

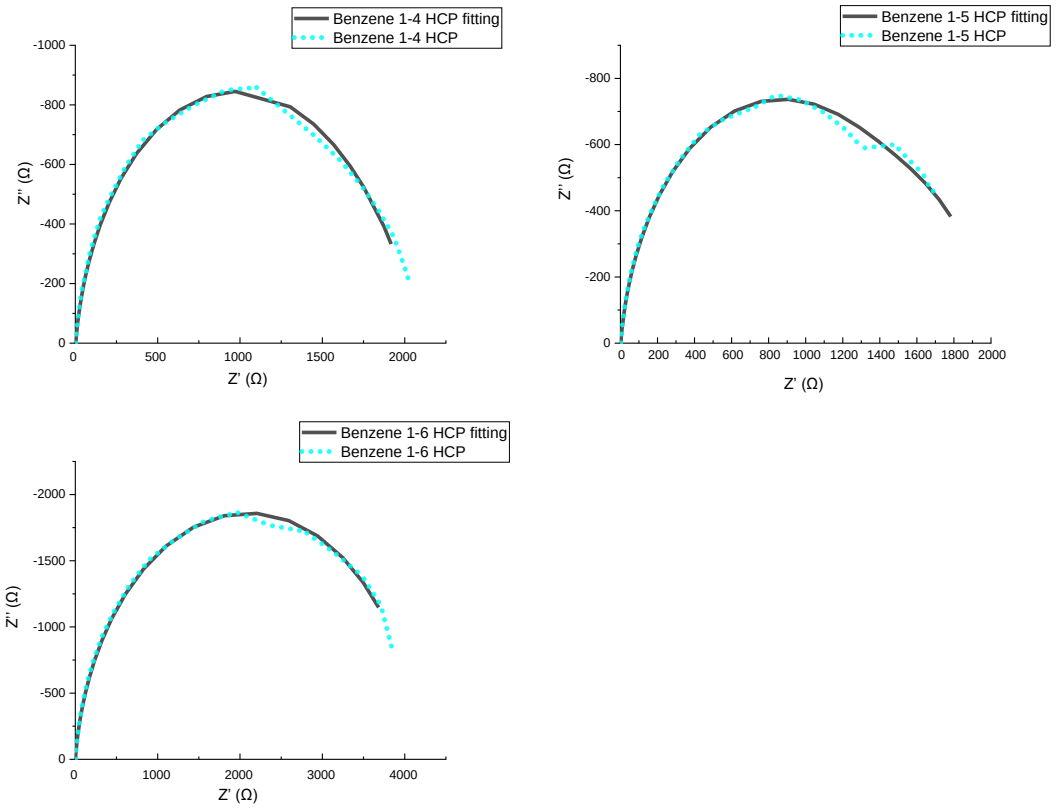

Figure 5.2.17 The impedance fitting curves of Benzene HCPs

From the fitting curves of Benzene HCPs, it can be found that the fitting results matched well with the experimental curves in the high and intermediate frequency region. In the low frequency region, the deviations in the fitting results in the low frequency region can be found due to no proper model can be used for the fitting of the diffusion behaviours in the disordered hierarchical porous structures of Benzene HCPs with poor conductivity.

	R1 (Ω)	CPE1-T (F)	CPE1-P	R2 (Ω)	Ws1-R (Ω)	Ws1-T (s)	Ws1-P
Benzene 1-1 HCP	1.142	0.00075547	0.94012	1752.2	23.3	17.9	0.5
Benzene 1-2 HCP	1.872	0.00082929	0.93527	2530.7	94.7	35.1	0.5
Benzene 1-4 HCP	2.301	0.00096042	0.91131	1914.4	128.9	24.2	0.5
Benzene 1-5 HCP	1.933	0.00098207	0.91445	1602.8	368.9	24.1	0.5
Benzene 1-6 HCP	1.308	0.00100070	0.92887	4091.9	96.8	9.7	0.5

Table 5.2.6 The impedance fitting results of Benzene HCPs

Although the fitting results are not perfect, the poor conductivity of the Benzene HCPs can be seen from the R2 values. The variation in R2 values demonstrate the different

amount of crosslinkers used for Benzene HCP synthesis also influence the conductivity of these samples.

To further study the electrochemical performance of Benzene HCPs under alternating current, the complex capacitances of Benzene HCPs are performed. The complex capacitance C(ω) is defined by equation 5.2.2.6.1. The real part and imaginary of the complex capacitance C'(ω) and C" (ω) is defined by equation 5.2.2.6.2 and 5.2.2.6.3, respectively.

$$C(\omega) = C'(\omega) - jC''(\omega) \qquad 5.2.2.6.1$$

$$C'(\omega) = \frac{-Z''(\omega)}{\omega|Z|^2} \qquad 5.2.2.6.2$$

$$C''(\omega) = \frac{Z'(\omega)}{\omega|Z|^2} \qquad 5.2.2.6.3$$

The complex capacitance curves of Benzene HCPs are shown in the figure 5.2.18.

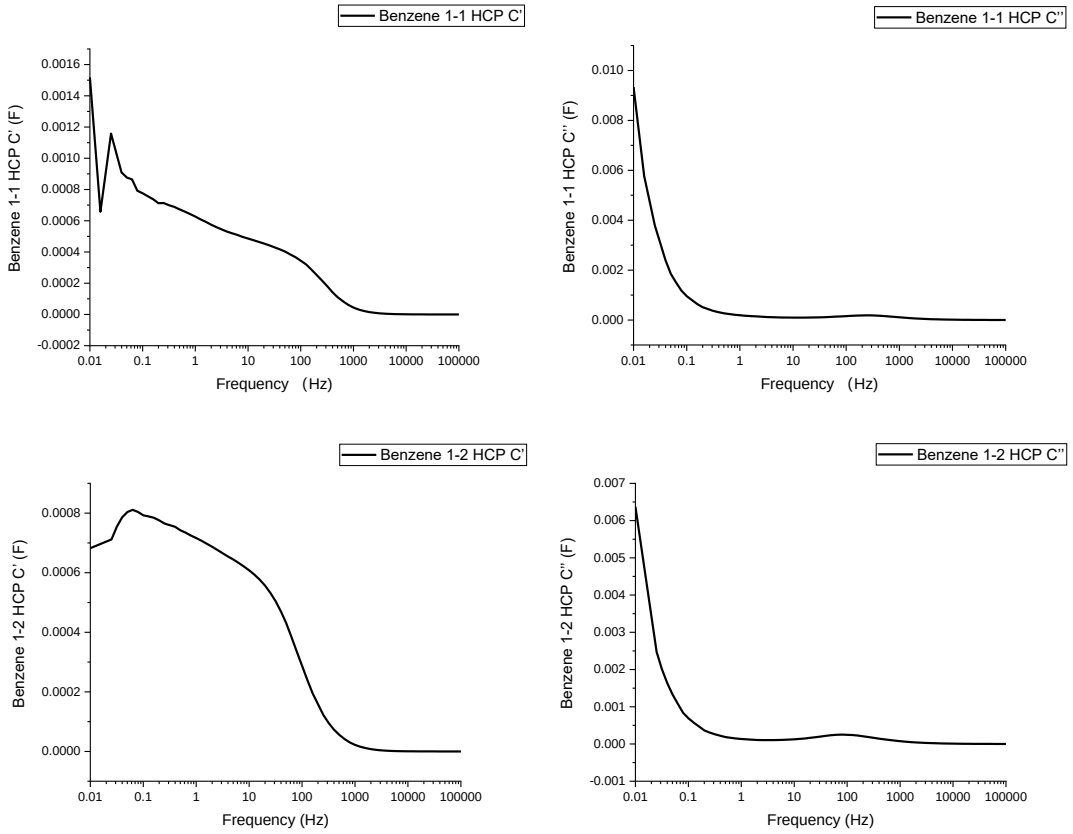

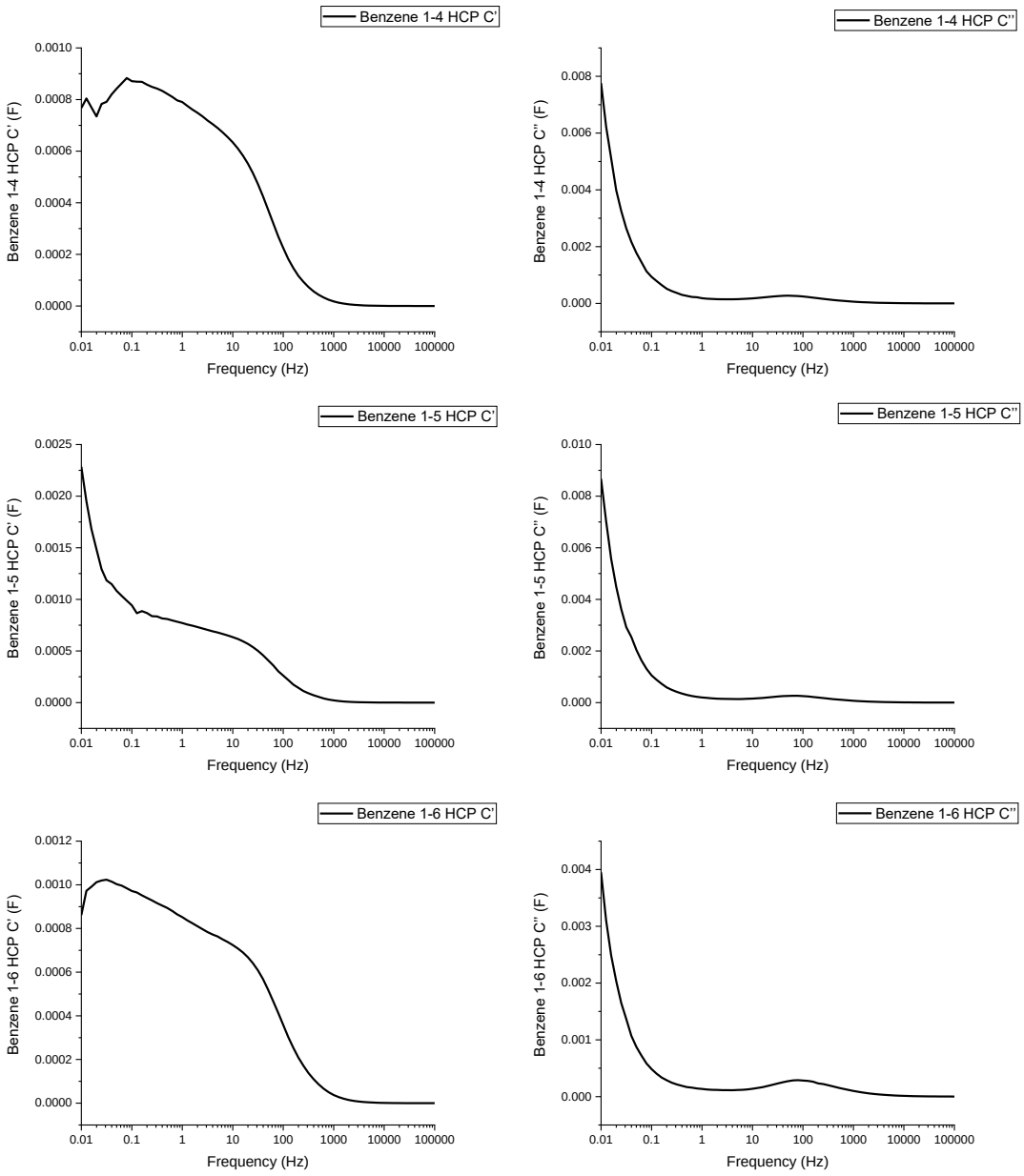

Figure 5.2.18. The complex capacitance of Benzene HCPs

The real part of the complex capacitance C' shows the capacitance variation with the decreasing frequency. For a common supercapacitor, the C' behaves like a resistor in the high frequency region. With the decreasing frequency, C' rises sharply and then gradually becomes less dependent with frequency. The increasing trend of C' will almost disappear at low frequencies as the maximum capacitance of the electrode is almost reached in the low frequency region. For Benzene HCPs, the fluctuations can be seen in the low frequency region of C' curves.

Therefore, from the complex capacitance results, it can be found that the poor

conductivity of Benzene HCPs resulted in the capacitances at low frequencies of these HCPs are unstable, i.e., the accessibility rate of the porous structures of Benzene HCPs are not stable due to the high internal resistances. This corresponds to the specific capacitances of Benzene HCPs obtained from CV tests are independent with the BET surface areas and pore volumes of them. Moreover, it can be seen that the capacitance at very low frequencies in the real part of the complex capacitance is much lower than that obtained from CV results, as the HCPs can only produce quite small response to the low voltage that employed in the impedance test because of the high internal resistance.

The imaginary part of the complex capacitance C" correspond to energy dissipation. For a common supercapacitor, it has no resistance to alternating current in the high frequency region, so the C" is 0 at high frequencies. With the decreasing frequency, the C" increases and attains the peak at the frequency f_0. The frequency f_0 corresponding to the maximum C" can be used to define the relaxation time τ_0, i.e., the time of the capacitor to reach the half of its low-frequency capacitance. The shorter this time, the better rate performance.

$$\tau_0 = \frac{1}{f_0} \qquad 5.2.2.6.4$$

This frequency corresponds to -45° in the phase angle curve which is the inflection point of the curve. At this frequency, the ohmic resistance of the resistor and the capacitive reactance of the capacitor are equal, that is to say, the capacitive behaviour will gradually be the dominant when frequency goes down and the energy dissipation will decrease as well. More specifically, a supercapacitor does not have sufficient time to react with the alternating current at high frequencies, i.e., the diffusion of the electrolyte ions cannot occur due to the rapidly changing of the current direction. With the decreasing frequency, the diffusion of the electrolyte ions progressively occurred thus the capacitance gradually increases, the resistance to the diffusion (e.g., frequency, pore structure of the electrode material, etc.) gradually increased as well. When the resistance to the diffusion reached the maximum, it corresponds to The frequency f_0

and phase angle -45°. To overcome the resistance will cause energy loss, therefore the energy loss reaches the maximum at frequency f_0. After the frequency f_0, the supercapacitor has more sufficient time to react with the alternating currents due to the much slower current direction changing, thus the energy loss decreased. Therefore, the frequency f_0 and phase angle -45° can be seen as the cut-off point of two states of motion of the ions at high and low frequencies.

For Benzene HCPs, it can be seen that the C" remain at 0 in the high frequency region indicating the resistor behaviour. With the decreasing frequency, a weak peak corresponding to the phase angle -45° appeared, while the C" curves shows a sharp rise in the low frequency region, indicating the increased energy loss. This corresponds to the decreasing occurred in phase angle curves at low frequencies, i.e., the tendency of behaving like a pure resistor due to the ultrahigh internal resistance originated from the non-conjugated methylene bridges of HCPs. As the C" of the Benzene HCPs reached the maximum at 0.01 Hz, according to equation 5.2.2.6.4, the relaxation time τ_0 of the Benzene HCPs is 100 s, suggesting the rate performance is not good due to the poor conductivity.

5.3 Biphenyl HCPs

5.3.1 Synthesis of Biphenyl HCPs

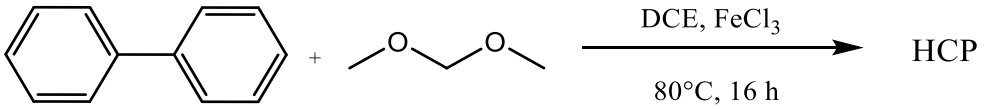

The synthesis of Biphenyl HCPs was performed as follows. Biphenyl (5 mmol, 1eq.) and ferric chloride (15-50 mmol, 3-10 eq.) were added into a dried two-neck flask with a magnetic stirrer and a condenser. DCE (25 mL) was charged into the flask by a syringe with stirring for 5 minutes to disperse the materials. Then, formaldehyde dimethyl acetal (FDA) (15-50 mmol, 3-10 eq.) was injected into the flask by a syringe and the temperature was increased to 80 ℃. The reaction was left for over 20 hours. The reaction was conducted in atmospheric air. The HCP product was cooled and collected by vacuum filtration and washed with water, methanol, acetone. Then the product was transferred to a Soxhlet extractor and washed with methanol overnight. The product was dried under vacuum at 80 ℃ overnight.

Biphenyl 1-3 HCP: biphenyl (5 mmol, 0.771 g, 1eq.), FDA (15 mmol, 1.34 mL, 3 eq.), ferric chloride (15 mmol, 2.45 g, 3eq.). Yield: 1.01 g, 106.3%. Formula: $C_{14}H_{10}$. Calculated value of elemental analysis C: 94.34% H: 5.66%. Found value of elemental analysis C: 84.73% H: 5.14%

Biphenyl 1-6 HCP: biphenyl (5 mmol, 0.771 g, 1eq.), FDA (30 mmol, 2.65 mL, 6 eq.), ferric chloride (30 mmol, 4.87 g, 6 eq.). Yield: 1.02 g, 95.5%. Formula: $C_{16}H_{10}$. Calculated value of elemental analysis C: 95.02% H: 4.98%. Found value of elemental analysis C: 83.04% H: 5.04%

Biphenyl 1-8 HCP: biphenyl (5 mmol, 0.771 g, 1eq.), FDA (40 mmol, 3.54 mL, 8 eq.), ferric chloride (40 mmol, 6.49 g, 8 eq.). Yield: 1.10 g, 102.9%. Formula: $C_{16}H_{10}$. Calculated value of elemental analysis C: 95.02% H: 4.98%. Found value of elemental analysis C: 76.94% H: 4.90%

Biphenyl 1-10 HCP: biphenyl (5 mmol, 0.771 g, 1eq.), FDA (50 mmol, 4.42 mL, 10 eq.), ferric chloride (50 mmol, 8.11 g, 10 eq.). Yield: 1.10 g, 102.4%. Formula: $C_{16}H_{10}$.

Calculated value of elemental analysis C: 95.02% H: 4.98%. Found value of elemental analysis C: 78.37% H: 4.76%

5.3.2 Results and discussion

5.3.2.1 Synthesis

Biphenyl HCPs were synthesized by Friedel-Crafts alkylation reaction with biphenyl used as monomer, formaldehyde dimethyl acetal (FDA) used as an external crosslinker and anhydrous $FeCl_3$ used as a Lewis acid catalyst, in air atmosphere and at 80 ℃. In order to explore influence of different monomer to crosslinker ratio to the properties of the biphenyl hyper-crosslinked polymer, Biphenyl HCPs were synthesized with ratio of biphenyl to FDA 1-3, 1-6, 1-8, 1-10. In this chapter, the Biphenyl HCPs named with Biphenyl 1-3, Biphenyl 1-6, Biphenyl 1-8, and Biphenyl 1-10 correspond to the sample synthesized with ratios of biphenyl to FDA 1-3, 1-6, 1-8, 1-10, respectively. The Biphenyl HCP synthesized in Chapter 3 with a ratio of biphenyl to FDA 1-5, thus it is marked as Biphenyl 1-5. The yields and elemental analysis results of the Biphenyl HCPs are shown in the table 5.3.1.

	Yield		Calculated value		Found value	
			C %	H %	C %	H %
Biphenyl 1-3 HCP	106.3%	1.01 g	94.34	5.66	84.73	5.14
Biphenyl 1-5 HCP	102.1%	1.09 g	95.02	4.98	79.81	4.71
Biphenyl 1-6 HCP	95.5%	1.02 g	95.02	4.98	83.04	5.04
Biphenyl 1-8 HCP	102.9%	1.10 g	95.02	4.98	76.94	4.90
Biphenyl 1-10 HCP	102.4%	1.10 g	95.02	4.98	78.37	4.76

Table 5.3.1 Yield and elemental analysis results of Biphenyl HCPs

In the table 5.3.1, it can be found that the Biphenyl 1-3 HCP has the highest yield of 106.3 %, and the Biphenyl 1-6 HCP has the lowest yield 95.5%. Other Biphenyl HCPs have yields higher than 100%. As discussed previously, the yield higher than 100% is

due to the existence of incompletely reacted crosslinkers -O-CH_3 caused by steric hindrance of the formed rigid HCP networks, while the relative lower yield of the Biphenyl 1-6 HCP is due to some monomers and crosslinker form too small particles to be collected because of the intense steric impediment. The gap between the calculated values and the found values of the elemental analysis is also attributed to the incompletely reacted crosslinker residues.

5.3.2.2 FTIR and ^{13}C Solid State NMR spectroscopy

The molecular structures of Biphenyl HCPs were analyzed and confirmed by using Fourier transform infrared (FTIR) and ^{13}C solid state NMR.

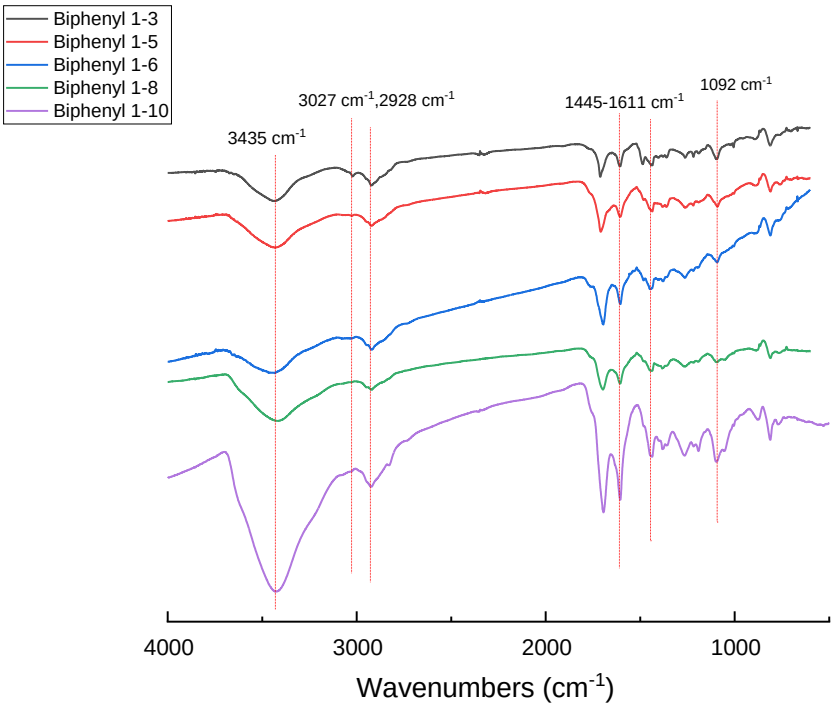

Figure 5.3.1 FTIR spectra of Biphenyl HCPs

For Biphenyl HCPs, the FTIR spectra are consistent with the expected structure. The peaks at 3027 cm^{-1} and 2928 cm^{-1} are assigned to C-H stretching in aromatic rings and methylene bridges, respectively.[23] The peaks at 1445-1611 cm^{-1} correspond to the vibration of aromatic ring skeleton.[38] The peak at 1092 cm^{-1} is assigned to C-O stretching in crosslinker residue.[21] The peak at 3435 cm^{-1} can be attributed to the O-H

stretching in physisorbed water which was in KBr disc and the porous structure.[39,40] In the FTIR spectrum of Biphenyl 1-3 HCP, the peak at 1487 cm^{-1} can be attributed to para-substituted benzene ring.[26] With the increasing ratio of FDA to biphenyl, this peak gradually disappeared demonstrating there were more substitutions in aromatic rings. Moreover, the intensity of the peak assigned to C-H stretching in aromatic rings at 3027 cm^{-1} decreased with the increasing ratio of FDA to biphenyl monomer suggesting more hydrogen in aromatic ring were substituted. This trend was in consistency with previous literatures.[21,41]

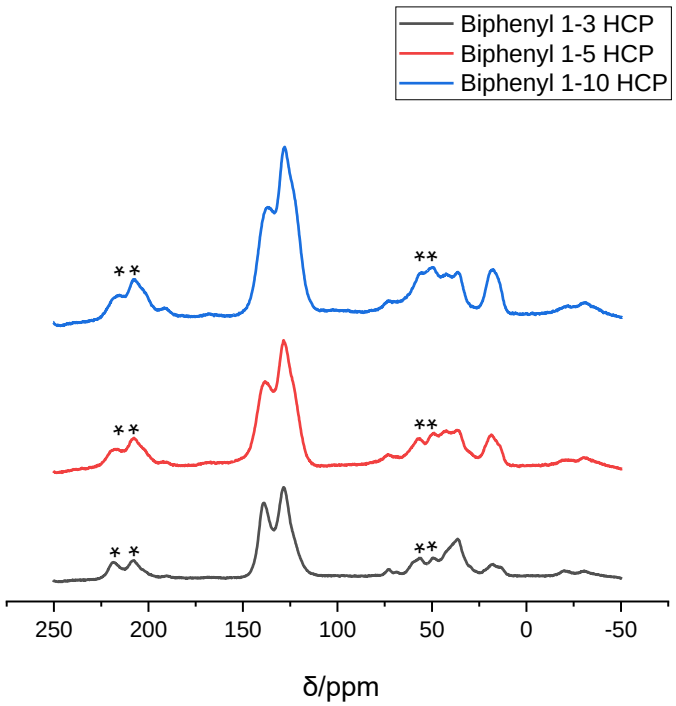

Figure 5.3.2 ^{13}C solid state NMR spectra of Biphenyl HCPs (the asterisks denote spinning side bands)

In the ^{13}C NMR spectra of Biphenyl HCPs, the peaks at 137 ppm and 128 ppm can be assigned to the substituted aromatic carbon and the non-substituted aromatic carbon, respectively.[42] The peak at 36 ppm is attributed to the carbon in methylene bridges.[43] The peak at 73 ppm and 18 ppm can be ascribed to carbon in the methylene group binding to oxygen atom of crosslinker residue and the methyl carbon at the end of crosslinker residue.[22] It can be found that with the ratio of FDA to monomer increasing, the peak at 42 ppm which is due to the different substitution position of methylene

bridges[44] appeared, indicating more substitution in aromatic rings. It can be also seen the relative intensity of the peak at 137 ppm which corresponds to the substituted aromatic carbon decreased with the increasing ratio of FDA to biphenyl, suggesting more hydrogen in aromatic rings were substituted. The results obtained from solid-state NMR spectra are consistent with results from the FTIR spectra to confirm the formation of the methylene bridge, the aromatic moieties in the molecular network, the crosslinker residue, and the structural variation with different ratio of FDA to biphenyl of Biphenyl HCPs.

5.3.2.3 TGA

The thermal stability of Biphenyl HCPs was characterized by using thermalgravimetric analysis (TGA). The TGA was conducted under a N_2 atmosphere and the samples were heated from 25 °C to 800 with a heating rate 10 °C/min.

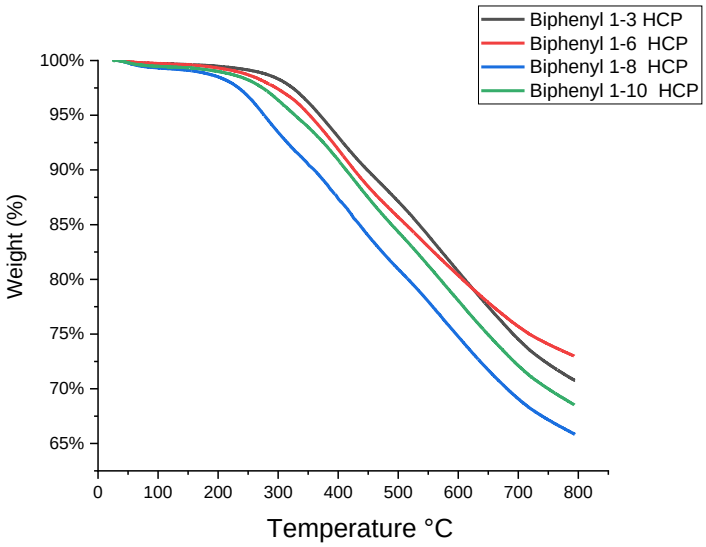

Figure 5.3.3 TGA curves of Biphenyl HCPs

The Biphenyl HCPs showed good thermal stability. The weight residue of the Biphenyl HCPs is higher than 90% at 350 °C. The onset temperature of the Biphenyl 1-8 HCP is obviously lower than that of other sample, the overall variation trend of the onset temperature of the Biphenyl HCPs is decreasing with the increasing ratio of FDA to

biphenyl. The decrease in onset temperature can be attributed to higher content of incompletely reacted crosslinker residues. At 800 °C, the weight residue of Biphenyl 1-3, 1-6, 1-8 and 1-10 HCP is 71%, 73%, 66% and 69%, respectively.

5.3.2.4 N_2 Sorption

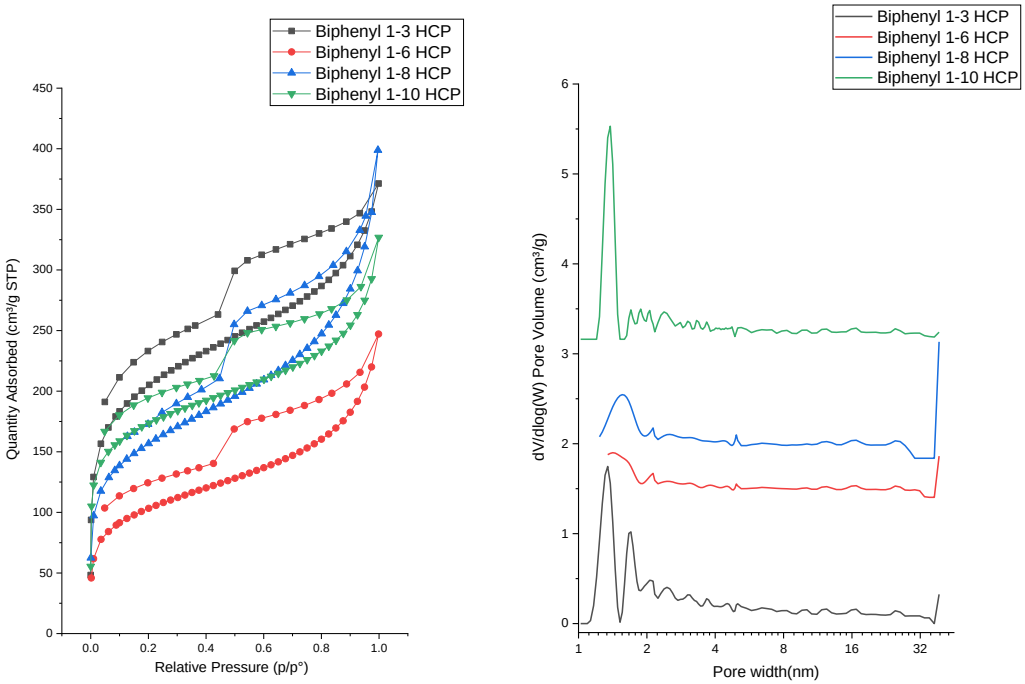

Figure 5.3.4 Isotherm and pore size distribution of Biphenyl HCPs

The porosity of Biphenyl HCPs ware characterized by N_2 adsorption/desorption analysis at 77 K. In accordance with IUPAC definition, all Biphenyl HCPs showed the combined Type II and Type IV isotherms which consist of a sharp rise at low relative pressure (P/P_0 <0.01) indicating the existence of microporous structure, the hysteresis loop in the relative pressure range of 0.43-1.0 suggesting the existence of mesopores, and the gradual rise in the relative pressure range of 0.9-1.0 demonstrating the existence of macropores. It can be seen that Biphenyl 1-6 and 1-8 HCP have less adsorption in the low relative pressure region (P/P_0<0.01) than other samples suggesting less micropores in these two samples, and this can be seen more directly in pore size

distribution of Biphenyl HCPs. In the pore size distribution of Biphenyl HCPs, it can be found the main peaks of these samples located at the range of 1-2 nm suggesting microporosity is the dominant structure in these samples. For Biphenyl 1-3 HCP, there are two strong peaks in the range of 1-2 nm. For Biphenyl 1-6 and 1-8 HCP, it can be seen that the intensity of peak at 1-2 nm was weakened indicating the less micropore volume in these two samples. Compared with Biphenyl 1-6 and 1-8 HCP, the peak in the range of 1-2 nm of Biphenyl 1-10 HCP is stronger, suggesting more micropore in Biphenyl 1-10 HCP. The single point adsorption total pore volumes of Biphenyl HCPs obtained at p/p_0=0.99 and the BET surface areas of them are shown in the table 5.3.2.

	BET surface area (m^2/g)	Single point adsorption total pore volume at p/p_0=0.99 (cm^3/g)
Biphenyl 1-3 HCP	752.1	0.57
Biphenyl 1-5 HCP	639.1	0.65
Biphenyl 1-6 HCP	376.5	0.38
Biphenyl 1-8 HCP	570.0	0.62
Biphenyl 1-10 HCP	640.5	0.51

Table 5.3.2 BET surface area and pore volume of Biphenyl HCPs

In the table 5.3.2, it can be seen the BET surface areas of Biphenyl 1-3, 1-6, 1-8 and 1-10 HCP are 752.1, 376.5, 570.0 and 640.5 m^2/g, respectively. The single point adsorption total pore volumes of these samples are 0.57, 0.38, 0.62 and 0.51 cm^3/g, respectively. The BET surface area and total pore volume of the Biphenyl 1-5 HCP are 639.1 m^2/g and 0.65 cm^3/g, respectively. The increasing ratio of FDA to biphenyl caused a decrease in BET surface area which was followed by subsequent increase. The Biphenyl 1-3 HCP has the highest BET surface among all Biphenyl HCPs, 752.1 m^2/g. With the ratio of FDA to biphenyl increased to 5-1 and 6-1, the BET surface area decreased to 639.1 and 376.5 m^2/g, respectively. With the further increasing ratio of FDA to biphenyl, the BET surface area of Biphenyl 1-8 and 1-10 HCP increased to 570.0 and 640.5 m^2/g, respectively. The Biphenyl 1-5 HCP showed the highest total pore volume, 0.65 cm^3/g, followed by the total pore volume of the Biphenyl 1-8 HCP,

0.62 cm^3/g. Though the Biphenyl 1-10 HCP has a similar BET surface with the Biphenyl 1-5 HCP, but it showed a lower total pore volume. The Biphenyl 1-6 HCP has the lowest total pore volume among Biphenyl HCPs, 0.38 cm^3/g. The Biphenyl HCP has the highest BET surface area, but it has a lower total pore volume than the Biphenyl 1-8 HCP, 0.57 cm^3/g. The biphenyl HCP synthesized with a biphenyl to FDA ratio 1-6 by Li et al. has a BET surface area of 815 m^2/g,[16] higher than that of the Biphenyl 1-6 HCP. The biphenyl HCP synthesized with a biphenyl to FDA ratio 1-3 by Varyambath et al. has a BET surface of 1000 m^2/g,[45] higher than that of the Biphenyl 1-3 HCP.

To further investigate the pore volume composition of Biphenyl HCPs, the pore volumes of the pores with different pore widths are shown in the table 5.3.3 and pore volume proportions of Biphenyl HCPs are performed in the figure 5.3.5. The pore volumes of the pores with pore widths less than 2 nm are obtained at relative pressure p/p_0=0.2 and the pore volumes of the pores with pore widths less than 10 nm are obtained at p/p_0=0.8.

Material	Pore volume of the pores with pore width less than 2 nm (cm^3/g)	Pore volume of the pores with pore width 2-10 nm (cm^3/g)	Pore volume of the pores with pore width larger than 10 nm (cm^3/g)
Biphenyl 1-3 HCP	0.31	0.13	0.13
Biphenyl 1-5 HCP	0.27	0.09	0.29
Biphenyl 1-6 HCP	0.16	0.09	0.13
Biphenyl 1-8 HCP	0.24	0.14	0.24
Biphenyl 1-10 HCP	0.27	0.09	0.15

Table 5.3.3 The pore volumes of the pores with different pore widths of Biphenyl HCPs

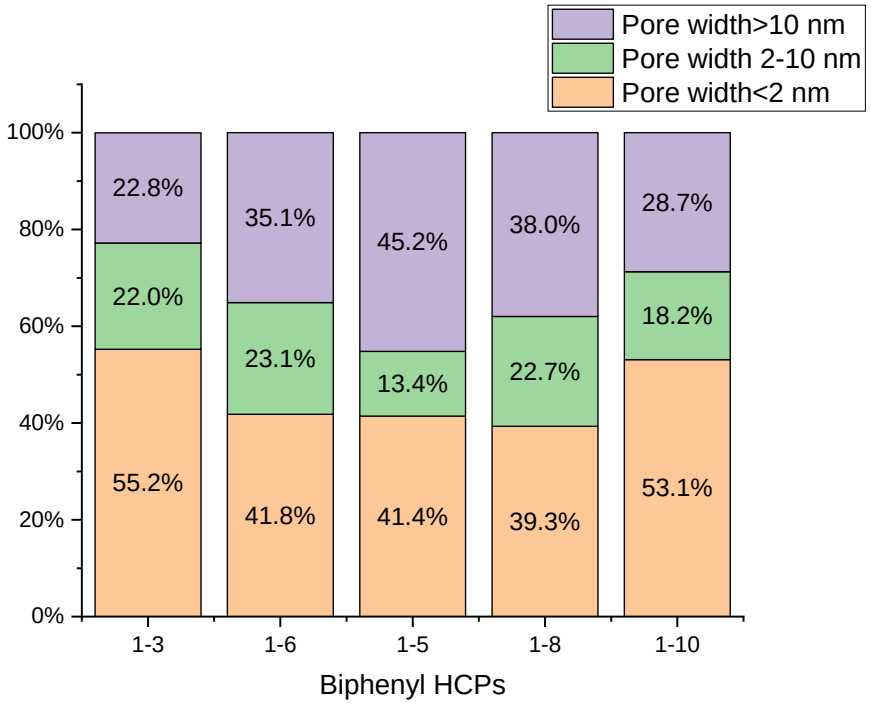

Figure 5.3.5 Pore volume proportions of pores with different pore widths of Biphenyl HCPs

From the pore volume proportions of Biphenyl HCPs, it can be seen that the proportions of micropore volume are the highest proportion in the total pore volumes of Biphenyl HCPs. The micropore volume proportions of Biphenyl 1-3, 1-6, 1-8 and 1-10 HCP are 55.2%, 41.8%, 39.3% and 53.1%, and the micropore volumes of them are 0.31, 0.16, 0.24 and 0.27 cm^3/g respectively. The overall variation trend in micropore volume proportions of total pore volumes of Biphenyl HCPs with the increasing ratio of FDA to biphenyl is same with the variation trend in the BET surface areas of Biphenyl HCPs, i.e., decrease first then increase. The volume proportions of pores with pore width 2-10 nm in Biphenyl 1-3, 1-6, 1-8 and 1-10 are 22.0%, 23.1%, 22.7% and 18.2%, and the pore volumes of the pores with pore width 2-10 nm of them are 0.13, 0.09, 0.14 and 0.09 cm^3/g, respectively. For the pores with pore width larger than 10 nm, the pore volume proportions in Biphenyl 1-3, 1-6, 1-8 and 1-10 HCP are 22.8%, 35.1%, 38.0%, and 28.7%, the pore volumes of them are 0.13, 0.13, 0.24 and 0.15 cm^3/g, respectively. For the Biphenyl 1-5 HCP, the volume proportions of micropores, pores with diameter 2-10 nm, and pores with diameter larger than 10 nm are 41.4%, 13.4% and 45.2%, the pore volumes of them are 0.27, 0.09 and 0.29 cm^3/g, respectively. Therefore, the

Biphenyl 1-3 HCP has the highest micropore volume proportion among Biphenyl HCPs.

5.3.2.5 Cyclic Voltammetry

The electrochemical properties of Biphenyl HCPs were evaluated by a typical three-electrode system with 1 M Na_2SO_4 aqueous solution as electrolyte. The active material on nickel foam, a platinum electrode and an Ag/AgCl electrode (3 M KCl, 0.207 V vs. standard hydrogen electrode at 25 °C) were used as working electrode, counter electrode and reference electrode, respectively. The CV tests were conducted with different scan rates 2, 10, 25, 50, 75, 100 and 200 mV/s in the voltage range of -0.2 V-0.8 V.

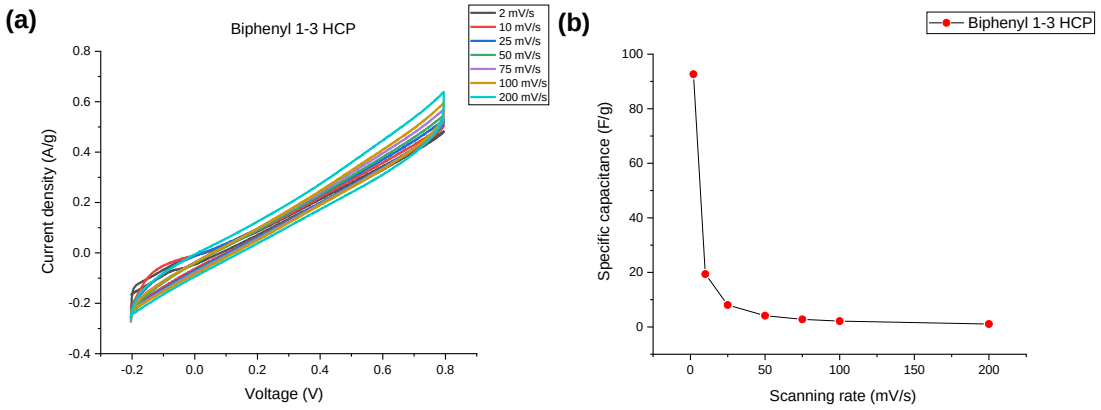

Figure 5.3.6 (a) CV curves at different scanning rates, and (b) Specific capacitance obtained at different scanning rates of Biphenyl 1-3 HCP

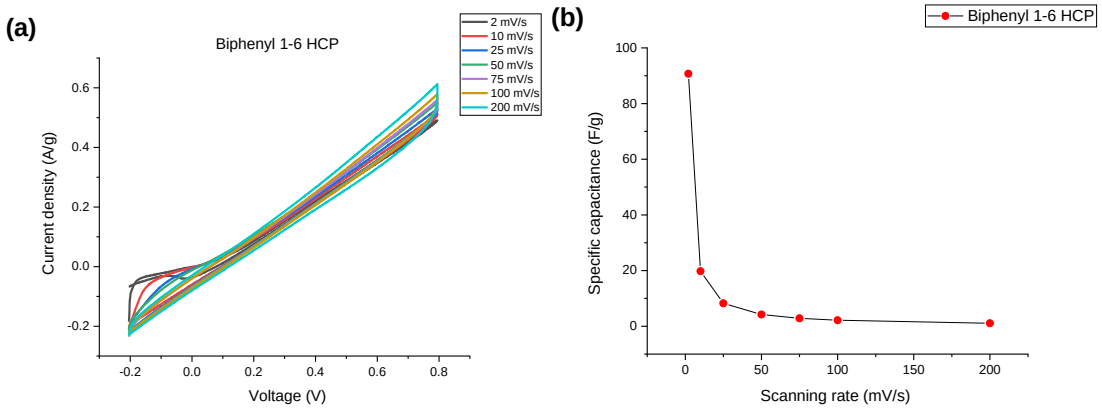

Figure 5.3.7 (a) CV curves at different scanning rates, and (b) Specific capacitance obtained at different scanning rates of Biphenyl 1-6 HCP

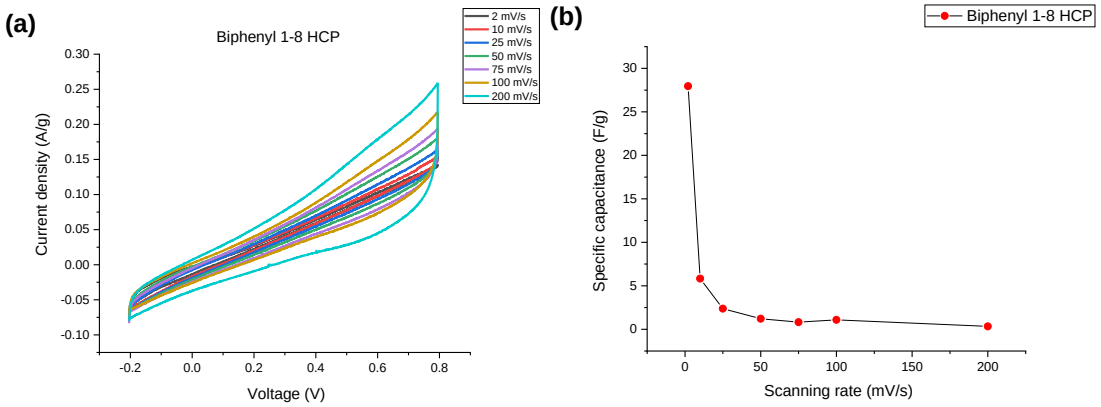

Figure 5.3.8 (a) CV curves at different scanning rates, and (b) Specific capacitance obtained at different scanning rates of Biphenyl 1-8 HCP

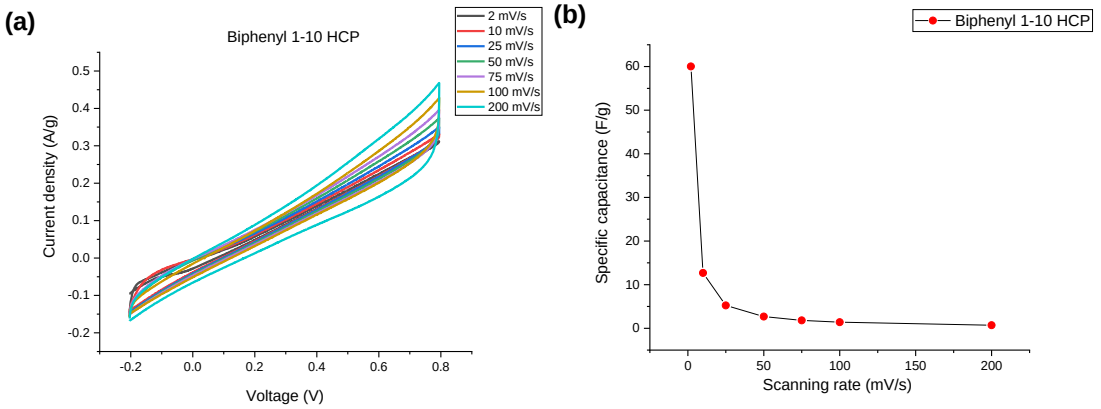

Figure 5.3.9 (a) CV curves at different scanning rates, and (b) Specific capacitance obtained at different scanning rates of Biphenyl 1-10 HCP

	Specific capacitance obtained at different scanning rates (F/g)							
Scanning rates (mV/s) / Material	2	10	25	50	75	100	200	Retention of capacitance at 200 mV/s
Biphenyl 1-3 HCP	92.7	19.4	8.1	4.1	2.8	2.1	1.1	1.2%
Biphenyl 1-5 HCP	30.0	6.2	2.5	1.3	0.9	0.7	0.3	1.0%
Biphenyl 1-6 HCP	90.7	19.8	8.2	4.2	2.8	1.1	1.1	1.2%
Biphenyl 1-8 HCP	27.9	5.8	2.4	1.2	0.8	1.1	0.3	1.2%
Biphenyl 1-10 HCP	60.0	12.7	5.2	2.7	1.8	1.4	0.7	1.2%

Table 5.3.4 Specific capacitance of biphenyl HCPs obtained at different scanning rates

The specific capacitance of Biphenyl 1-3, 1-6, 1-8 and 1-10 HCP obtained at 2 mV/s is 92.7, 90.7, 27.9 and 60.0 F/g, respectively. The capacitance retention from 2 mV/s to 200 mV/s of Biphenyl HCPs is 1.2%, 1.2%, 1.2% and 1.2%, respectively, indicating the poor rate performance. The Biphenyl 1-3 HCP has similar specific capacitance with the Biphenyl 1-6 HCP, while the Biphenyl 1-3 HCP has higher BET surface area (752.1 m^2/g) and total pore volume (0.57 cm^3/g) than those of the Biphenyl 1-6 HCP (376.5 m^2/g, 0.38 cm^3/g). The Biphenyl 1-3 HCP also has higher micropore volume (0.31 cm^3/g) and higher pore volume of the pores with diameter 2-10 nm (0.13 cm^3/g) than those of Biphenyl 1-6 HCP (0.16 cm^3/g and 0.09 cm^3/g, respectively). From the pore volume proportions of Biphenyl HCPs, it can be seen that the Biphenyl 1-3 HCP and Biphenyl 1-6 HCP has different pore volume compositions. The Biphenyl 1-8 HCP has the lowest specific capacitance, but the BET surface area (570.0 m^2/g) and the total pore volume (0.63 cm^3/g) of Biphenyl 1-8 HCP are higher than those of the Biphenyl 1-6 HCP. The micropore volume (0.24 cm^3/g) and the pore volume of the pores with diameter 2-10 nm (0.14 cm^3/g) of Biphenyl 1-8 HCP are higher than those of Biphenyl 1-6 HCP as well. In terms of the pore volume proportions of Biphenyl HCPs, it can be seen that the Biphenyl 1-8 HCP has similar pore volume compositions with the Biphenyl 1-6 HCP. The Biphenyl 1-5 HCP has the specific capacitance 30 F/g at 2 mV/s, lower than that of the Biphenyl 1-10 HCP. The BET surface area of the Biphenyl 1-5 HCP (639.1 m^2/g) is close to that of the Biphenyl 1-10 HCP (640.5 m^2/g), the total pore volume of the Biphenyl 1-5 HCP (0.65 cm^3/g) is higher than that of the Biphenyl 1-10 HCP (0.51 cm^3/g). It can be also seen that The Biphenyl 1-5 HCP has quite similar micropore volume and the pore volume of the pores with 2-10 (0.27 cm^3/g and 0.09 cm^3/g, respectively) with the Biphenyl 1-10 HCP. Although the influences to the capacitances of Biphenyl HCPs generated by different porosity originating from the different amount of crosslinkers used in the synthesis of Biphenyl HCPs can be seen, the variation in the capacitances of the Biphenyl HCPs is independent with the variations in the porosity of the Biphenyl HCPs. Because of the differences in the adsorption in gas phase and liquid phase, the results obtained from the N_2

adsorption/desorption cannot fully explain what happened in the adsorption occurred in the liquid phase. Moreover, the unstable utilization rate of the porous structures caused by the poor conductivity of Biphenyl HCPs and the disordered porous structure of the HCPs could have unpredictable impacts on the capacitances of them.

The relationship between the response current and scanning rate could provide the insight into the energy storage kinetics of Biphenyl HCPs, the results are shown in the figure 5.3.10.

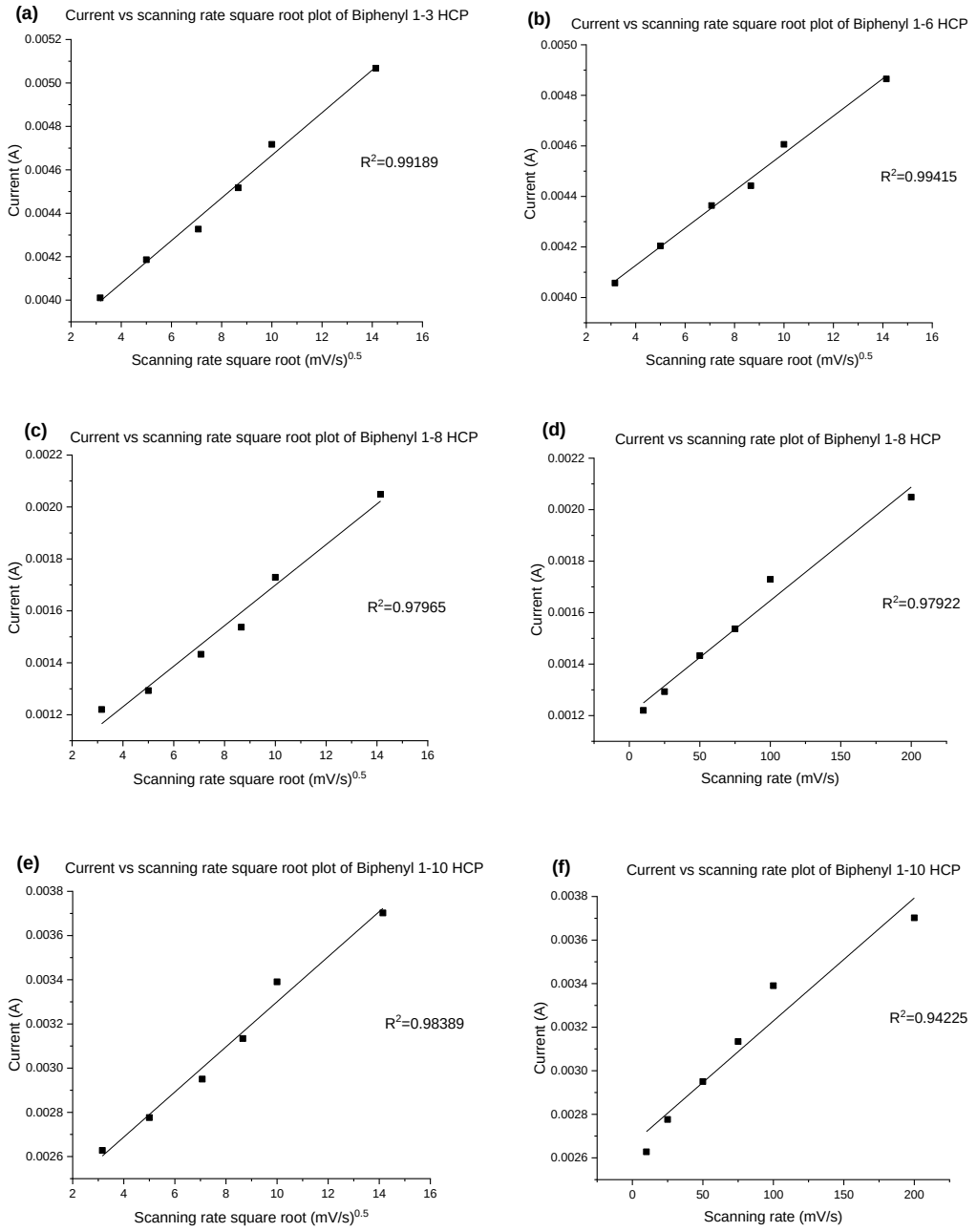

Figure 5.3.10 The relationship between response current and scanning rate of Biphenyl HCPs.

(a). and (b). current vs scanning rate square root plot of Biphenyl 1-3 and 1-6 HCP. (c). current vs scanning rate square root plot and (d). current vs scanning rate plot of Biphenyl 1-8 HCP. (e). current vs scanning rate square root plot and (f). current vs scanning rate plot of Biphenyl 1-10 HCP.

From the figure 5.3.10, it can be seen the coefficient of determination R^2 of the response current vs scanning rate square root plot of Biphenyl 1-3 and 1-6 HCP is 0.99189 and 0.99415, respectively. The good linear relationship between response current and scanning rate square indicates the capacitances of the Biphenyl 1-3 HCP and Biphenyl 1-6 HCP are dominated by slow diffusion-controlled process. As the CV curve of Biphenyl 1-8 HCP at 200 mV/s showed the uneven distribution of electrolyte ions in the charge/discharge process, the linear relationship between response current and scanning rate square and the relationship between response current and scanning rate are compared. It can be seen that the R^2 of the response current vs scanning rate square root plot of Biphenyl 1-8 HCP is 0.97965 whereas the R^2 of the response current vs scanning rate plot is 0.97922. As these two coefficients of determination are quite close, the capacity kinetic of Biphenyl 1-8 HCP is a mixed kinetic involves both surface-controlled process and diffusion-controlled process. Because of the underutilized porosity of the Biphenyl 1-8 HCP (accumulation of the electrolyte ions on the outer surface of the electrode), it can be found that the Biphenyl 1-8 HCP has lower specific capacitance than other samples in this group. For the response current vs scanning rate square root plot of Biphenyl 1-10 HCP, the R^2 is 0.98389, lower than that of Biphenyl 1-3 and 1-6 HCP. So, the relationship between response current vs scanning rate of Biphenyl 1-10 HCP is also presented. It can be seen that the R^2 of response current vs scanning rate plot of Biphenyl 1-10 HCP is 0.94225, thus it can be assured that the capacity kinetic of Biphenyl 1-10 HCP is mainly dominated by the diffusion-controlled process. As the slow diffusion-controlled process is the main capacity kinetic of the Biphenyl HCPs, the rate performance of these samples are quite low. Even if Biphenyl 1-8 HCP has a mixed kinetic, the results from the Benzene HCPs show the surface-controlled process could only contribute tiny amount of capacitance because of the poor

conductivity.

5.3.2.6 Electrochemical impedance spectroscopy (EIS)

To further investigate the electrochemical performance of Biphenyl HCPs, electrochemical impedance spectroscopy (EIS) was carried out with amplitude of 10 mV and frequency range 100 k Hz to 0.01 Hz. The Nyquist and Bode plots of Biphenyl HCPs are shown in the figures 5.3.11 to 5.3.14.

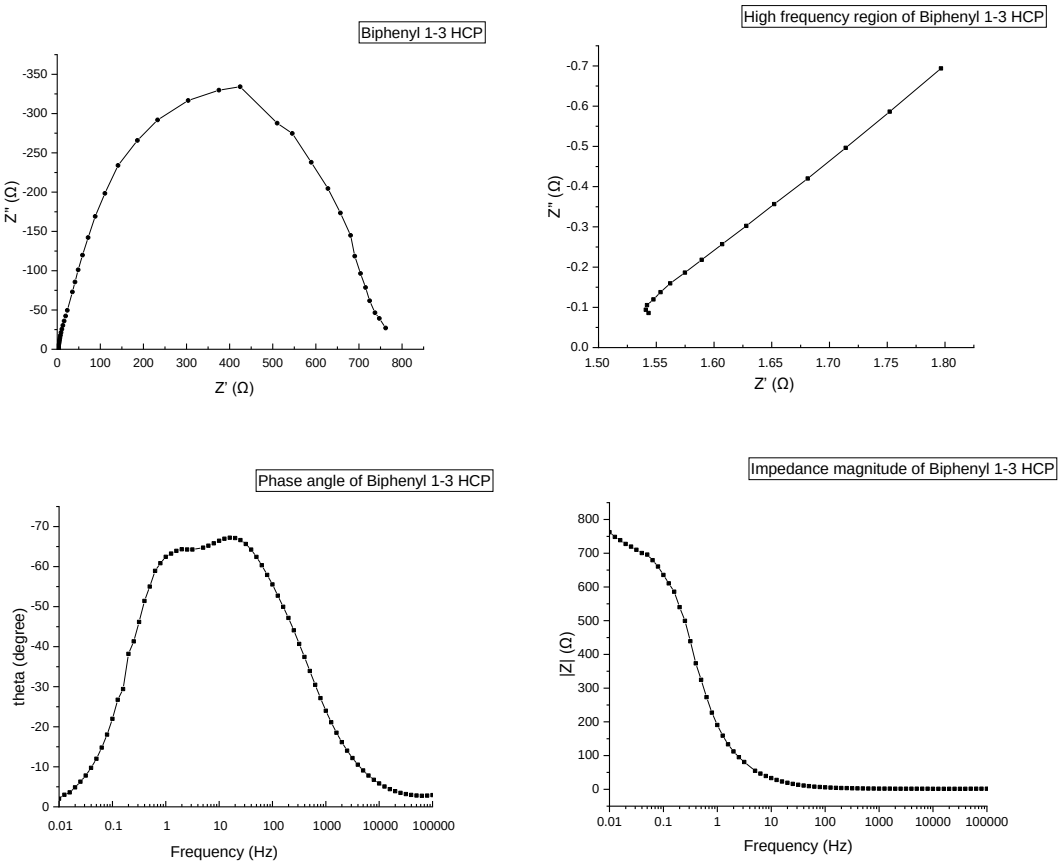

Figure 5.3.11 Nyquist plot and Bode plot of Biphenyl 1-3 HCP

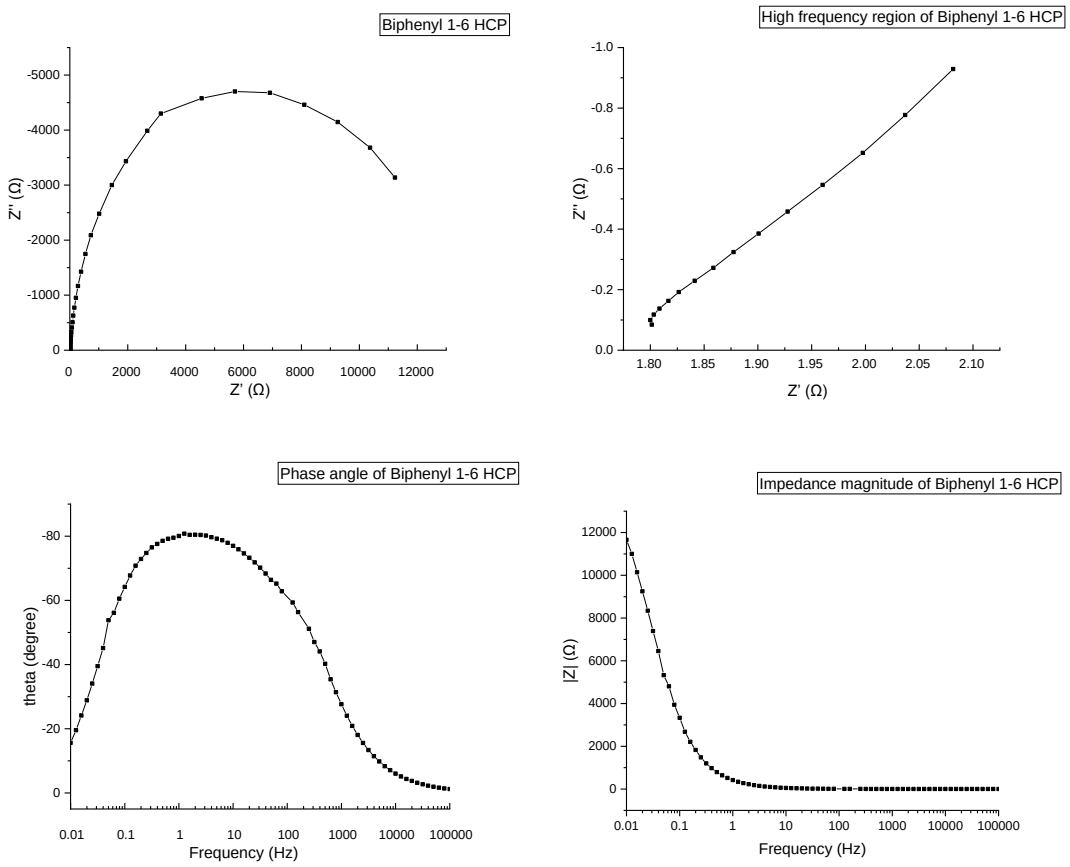

Figure 5.3.12 Nyquist plot and Bode plot of Biphenyl 1-6 HCP

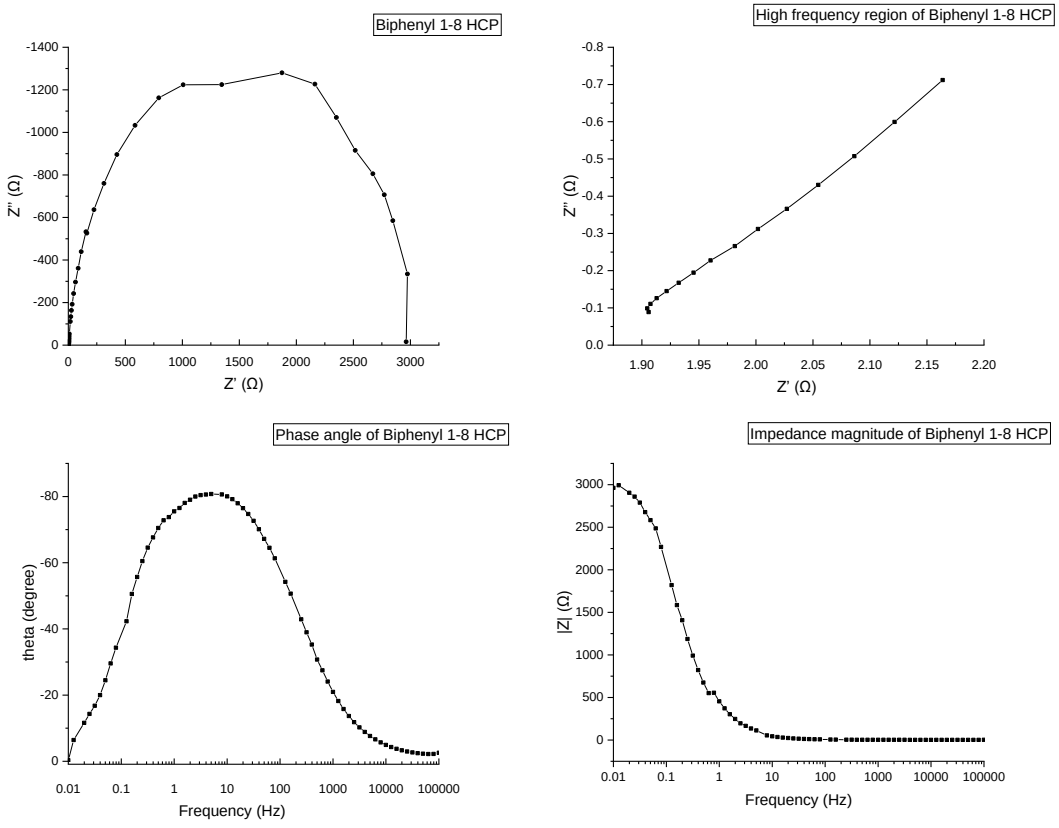

Figure 5.3.13 Nyquist plot and Bode plot of Biphenyl 1-8 HCP

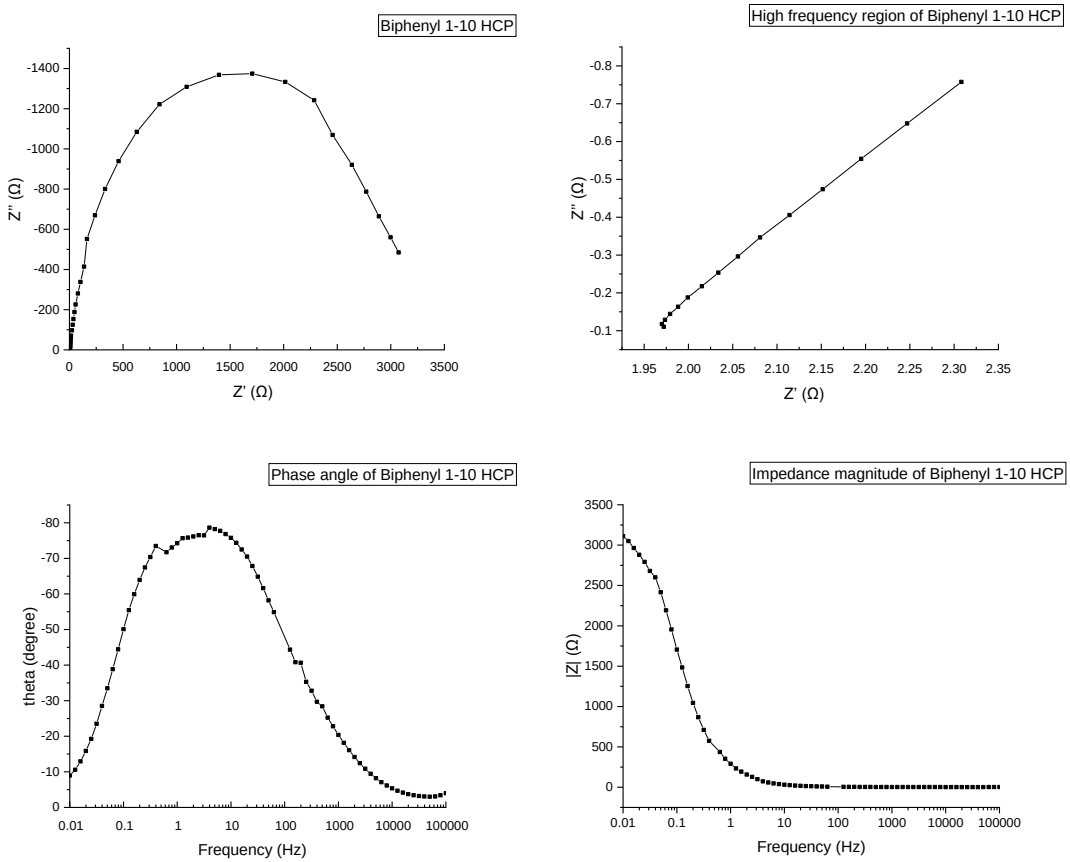

Figure 5.3.14 Nyquist plot and Bode plot of Biphenyl 1-10 HCP

	Whether the semicircle can be observed at high frequencies?	Whether the Nyquist plot is vertical or near vertical to Z'' axis at low frequencies?	The phase angle value of the curve apex	Phase angle at 0.01 Hz	Impedance magnitude at 0.01 Hz (Ω)
Biphenyl 1-3 HCP	No	No	-67°	-2°	762
Biphenyl 1-6 HCP	No	No	-80°	-18°	11004
Biphenyl 1-8 HCP	No	No	-81°	-1°	2963
Biphenyl 1-10 HCP	No	No	-78°	-10°	3111

Table 5.3.5 The results from Nyquist and Bode plot of biphenyl HCPs

For Biphenyl HCPs, the absence of the 'tail' paralleling to Z" axis in the intermediate and low frequency region in Nyquist plots indicates the Biphenyl HCPs did not behave like a supercapacitor. The highest points of the phase angle curves of Biphenyl HCPs varies from -67° to -81° suggesting the Biphenyl HCPs show some deviations from pure capacitor behaviour as well. The phase angle curve decreased to the angle close to 0° after reaching the maximum with the decreasing frequency demonstrates the Biphenyl HCPs tend to behave like a pure ohmic resistor because of the poor conductivity, while the phase angle did not increase to 0° illustrating the Biphenyl HCPs show some capacitance at low frequencies. The impedance magnitudes of Biphenyl HCPs are quite high, based on the quasi-semicircle shape of the impedance curves, it can be seen that the impedance of the Biphenyl HCPs is mainly contributed by the high internal resistances of the Biphenyl HCPs. The absence of the semi-circle in the high frequency region can be attributed to the ohmic contact between the current collector and the active materials.

In order to show the poor conductivity of Biphenyl HCPs more directly, the fitting results are exhibited in the figure 5.3.15 and table 5.3.6. The equivalent circuit model used for the fitting of Biphenyl HCPs is Randles circuit model which is commonly used for supercapacitors.

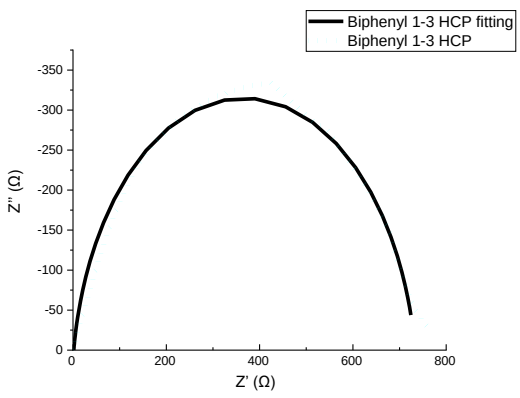

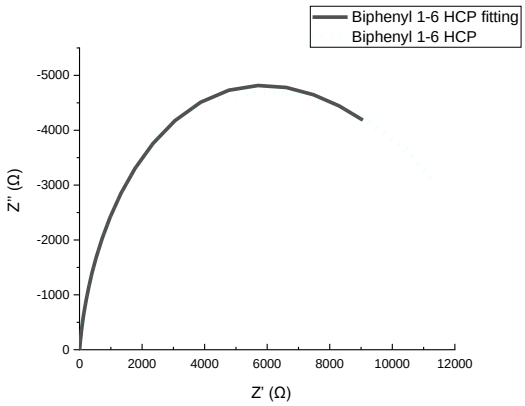

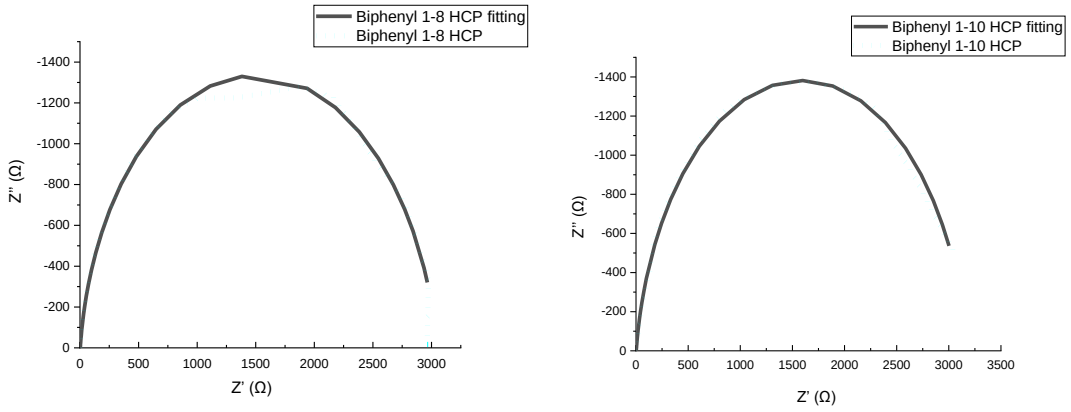

Figure 5.3.15 The impedance fitting curves of Biphenyl HCPs

In the fitting curves of Biphenyl HCPs, the deviations in the fitting result can be found in the low frequency region because the diffusion in the disordered porous structure of Biphenyl HCPs with poor conductivity is hard to be precisely predicted.

	R1 (Ω)	CPE1-T (F)	CPE1-P	R2 (Ω)	Ws1-R (Ω)	Ws1-T (s)	Ws1-P
Biphenyl 1-3 HCP	1.594	0.0010313	0.90734	726.7	5.2	3.5	0.5
Biphenyl 1-6 HCP	1.914	0.00044137	0.91058	10387.3	2237.4	47.3	0.5
Biphenyl 1-8 HCP	2.074	0.00045077	0.92658	2982.1	57.0	14.2	0.5
Biphenyl 1-10 HCP	2.273	0.0007277	0.91259	3168.4	5.9	7.4	0.5

Table 5.3.6 The impedance fitting results of Biphenyl HCPs

In the fitting results of Biphenyl HCPs, the large internal resistance can be seen from R2. The variation in the values of R2 suggests the influence from the different amount of crosslinkers used for Biphenyl HCP synthesis.

To gain further insight into the electrochemical performance of Biphenyl HCPs, the complex capacitance of Biphenyl HCP is performed. The definition of complex capacitance and the definitions of its components were given by equation 5.2.2.6.1, 5.2.2.6.2 and 5.2.2.6.3. The complex capacitance curves of Biphenyl HCP are shown in the figure 5.3.16.

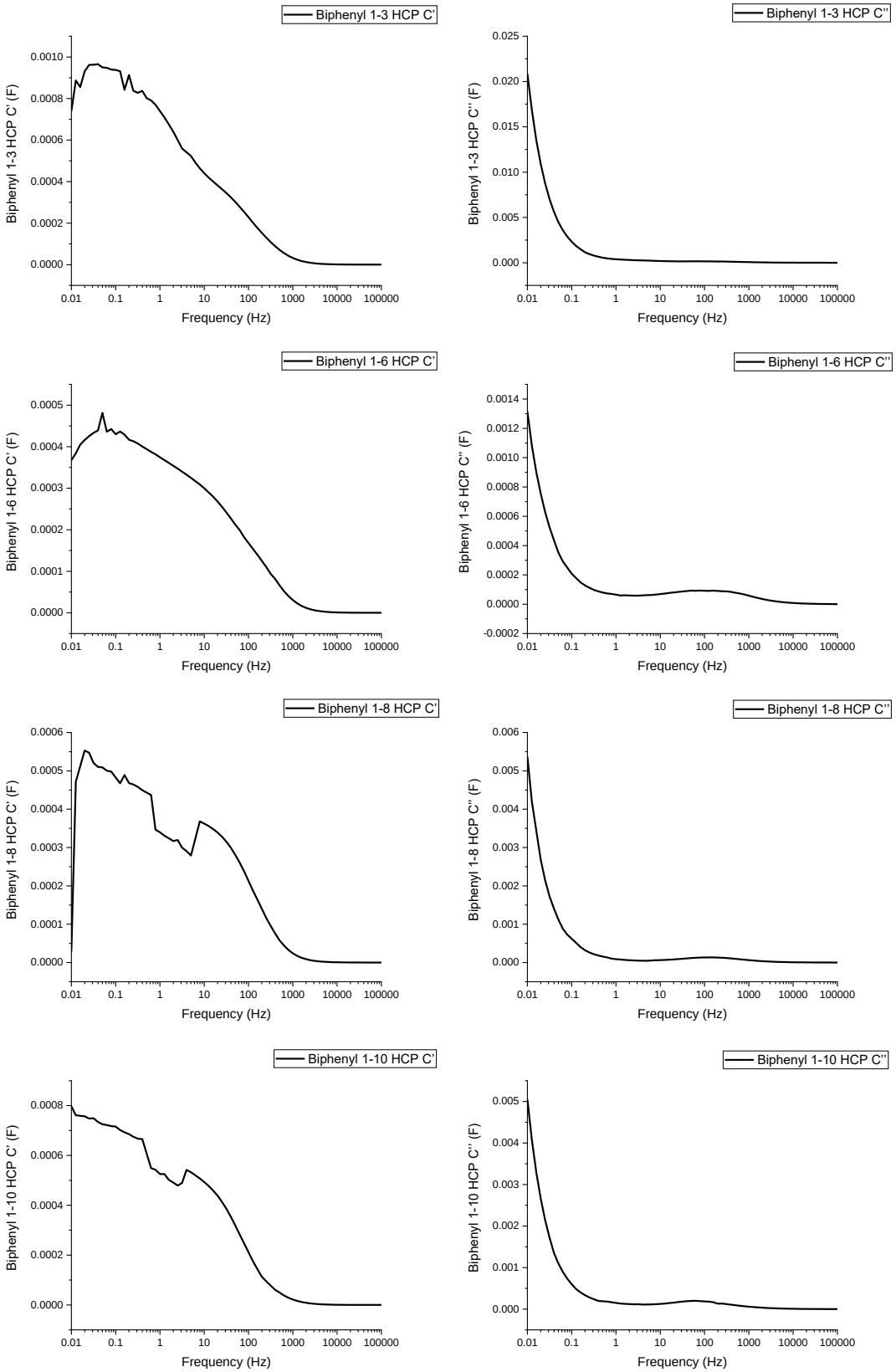

Figure 5.3.16 The complex capacitance of Biphenyl HCPs

The real part of the complex capacitance C' shows the capacitance variation with the decreasing frequency. It can be seen that the variation trend of C' of the Biphenyl HCPs

is same with a common supercapacitor in the high and intermediate frequency region, while significant fluctuations can be seen in the C' curve of Biphenyl HCPs at low frequencies, indicating the unstable accessibility rate of the pore structures caused by the poor conductivity of Biphenyl HCPs, and this corresponds to the specific capacitances obtained from CV test are independent with the porosity of Biphenyl HCPs. The capacitance at very low frequencies in the real part of the complex capacitance is much lower than that obtained from CV results, suggesting the HCPs with high internal resistance can only produce small response to the low voltage that employed in the impedance test.

The imaginary part of the complex C" corresponds to energy dissipation. With the decreasing frequency, the peak corresponding to phase angle -45° appeared then the C" curves began to rise and reached the maximum at 0.01 Hz, demonstrating the increased energy dissipation in the low frequency region caused by poor conductivity of Biphenyl HCPs. This corresponds to the decreasing in the phase angle curves after reaching the maximum phase angle. The frequency at which the C" reaches the maximum can be used to define the relaxation time to assess the rate performance of the materials. The definition of the relaxation time was given by 5.2.2.6.4. The relaxation time τ_0 of the Biphenyl HCPs is 100 s, suggesting the rate performance of Biphenyl HCPs is not good due to the poor conductivity. This result agrees with the results from the CV tests.

5.4 Terphenyl HCPs

5.4.1 Synthesis of p-Terphenyl HCPs

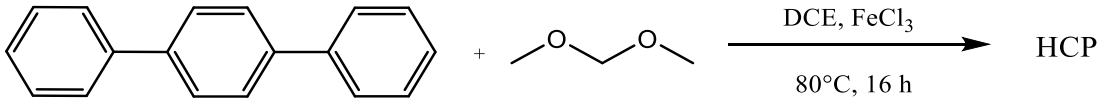

The synthesis of p-Terphenyl HCPs was performed as follows. p-Terphenyl (5 mmol, 1 eq.) and ferric chloride (15-70 mmol, 3-14 eq.) were added into a dried two-neck flask with a magnetic stirrer and a condenser. DCE (25 mL) was charged into the flask by a syringe with stirring for 5 minutes to disperse the materials. Then, formaldehyde dimethyl acetal (FDA) (15-70 mmol, 3-14 eq.) was injected into the flask by a syringe and the temperature was increased to 80 ℃. The reaction was left for over 20 hours. The reaction was conducted in atmospheric air. The HCP product was cooled and collected by vacuum filtration and washed with water, methanol, acetone. Then the product was transferred to a Soxhlet extractor and washed with methanol overnight. The product was dried under vacuum at 80 ℃ overnight.

Terphenyl 1-3 HCP: p-terphenyl (5 mmol, 1.152 g, 1 eq.), FDA (15 mmol, 1.34 mL, 3 eq.), ferric chloride (15 mmol, 2.45 g, 3 eq.). Yield: 1.44 g, 107.7%. Formula: $C_{19}H_{14}$. Calculated value of elemental analysis C: 94.18% H: 5.82%. Found value of elemental analysis C: 84.39% H: 5.11%

Terphenyl 1-6 HCP: p-terphenyl (5 mmol, 1.152 g, 1 eq.), FDA (30 mmol, 2.65 mL, 6 eq.), ferric chloride (30 mmol, 4.87 g, 6 eq.). Yield: 1.53 g, 101.1%. Formula: $C_{22}H_{14}$. Calculated value of elemental analysis C: 94.93% H: 5.07%. Found value of elemental analysis C: 83.06% H:.5.46%

Terphenyl 1-9 HCP: p-terphenyl (5 mmol, 1.152 g, 1 eq.), FDA (45 mmol, 3.98 mL, 9 eq.), ferric chloride (45 mmol, 7.30 g, 9 eq.). Yield: 1.52 g, 96.5%. Formula: $C_{23}H_{14}$. Calculated value of elemental analysis C: 95.14% H: 4.86%. Found value of elemental analysis C: 80.01% H: 5.16%

Terphenyl 1-12 HCP: p-terphenyl (5 mmol, 1.152 g, 1 eq.), FDA (60 mmol, 5.31 mL, 12 eq.), ferric chloride (60 mmol, 9.73 g, 12 eq.). Yield: 1.57 g, 100.0%. Formula:

$C_{23}H_{14}$. Calculated value of elemental analysis C: 95.14% H: 4.86%. Found value of elemental analysis C: 78.59% H: 4.82%

Terphenyl 1-14 HCP: p-terphenyl (5 mmol, 1.152 g, 1 eq.), FDA (70 mmol, 6.20 mL, 14 eq.), ferric chloride (70 mmol, 11.36 g, 14 eq.). Yield: 1.57 g, 99.8%. Formula: $C_{23}H_{14}$. Calculated value of elemental analysis C: 95.14% H: 4.86%. Found value of elemental analysis C: 79.06% H: 4.79%

5.4.2 Results and discussion

5.4.2.1 Synthesis

Terphenyl HCPs were synthesized by Friedel-Crafts alkylation reaction with p-terphenyl used as monomer, formaldehyde dimethyl acetal (FDA) used as an external crosslinker and anhydrous $FeCl_3$ used as a Lewis acid catalyst, in air atmosphere and at 80 °C. To investigate the influence of different monomer to crosslinker ratios influence to the properties of the Terphenyl HCPs, they were synthesized with ratio of terphenyl to FDA 1-3, 1-6, 1-9, 1-12, 1-14 and Terphenyl HCP in Chapter 3 was synthesized with ratio monomer to crosslinker 1-7. Terphenyl HCPs were named after the ratios of monomer to crosslinker, from Terphenyl 1-3 to Terphenyl 1-14. The yield and elemental analysis results of the Terphenyl HCPs are listed in the table 5.4.1.

	Yield %		Calculated value		Found value	
			C %	H %	C %	H %
Terphenyl 1-3 HCP	107.7%	1.44 g	94.18	5.82	84.39	5.11
Terphenyl 1-6 HCP	101.1%	1.53 g	94.93	5.07	83.06	5.46
Terphenyl 1-7 HCP	100.9%	1.59 g	95.14	4.86	77.41	4.96
Terphenyl 1-9 HCP	96.5%	1.52 g	95.14	4.86	80.01	5.16
Terphenyl 1-12 HCP	100.0%	1.57 g	95.14	4.86	78.59	4.82
Terphenyl 1-14 HCP	99.8%	1.57 g	95.14	4.86	79.06	4.79

Table 5.4.1 Yield and elemental analysis results of Terphenyl HCPs

The Terphenyl 1-3 HCP has the highest yield, 107.7% while Terphenyl 1-9 HCP and Terphenyl 1-14 HCP have yields lower than 100%, other samples all have a yield higher than 100%. The yields higher than 100% can be ascribed to the existence of incompletely reacted crosslinker residue, -O-CH_3. Lower yields of Terphenyl 1-9 HCP and Terphenyl 1-14 HCP can be ascribed to the losses of HCP products with small-sized particles which cannot grow larger due to steric hindrance. The incompletely reacted crosslinker residues also cause that the calculated values of the elemental analysis are higher than the experimental values.

5.4.2.2 FTIR and ^{13}C Solid State NMR spectroscopy

The molecular structures of Terphenyl HCPs were analyzed and confirmed by using Fourier transform infrared (FTIR) and ^{13}C solid state NMR.

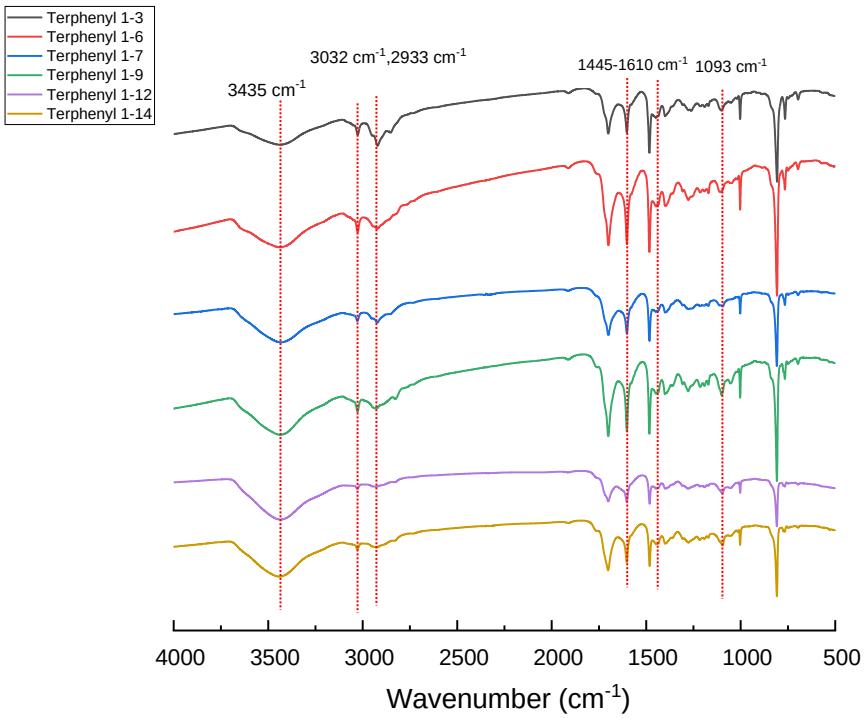

Figure 5.4.1 FTIR spectra of Terphenyl HCPs

For the FTIR spectra of Terphenyl HCPs, the peaks at 3032 and 2933 cm^{-1} can be ascribed to aromatic C-H stretching and methylene bridge C-H stretching, respectively.[46,47] The peaks in the range of 1445-1610 cm^{-1} correspond to the aromatic

ring skeleton vibration.[16] The peak at 1093 cm^{-1} which is due to the C-O stretching in crosslinker residue[21] confirms the existence of incompletely reacted crosslinker. The peak at 3435 cm^{-1} can be assigned to O-H stretching in physisorbed water in KBr disc and porous structure of Terphenyl HCP samples.[48] The intensity of the peak at 1483 cm^{-1} which can be attributed to para-substituted benzene ring[26] did not decrease with the increasing FDA to monomer ratio like other samples in this chapter, this may be because the terphenyl monomer involves para-substituted structure and the para-substitution is prone to occur due to the enhanced steric hindrance from the twisted terphenyl monomer structure.

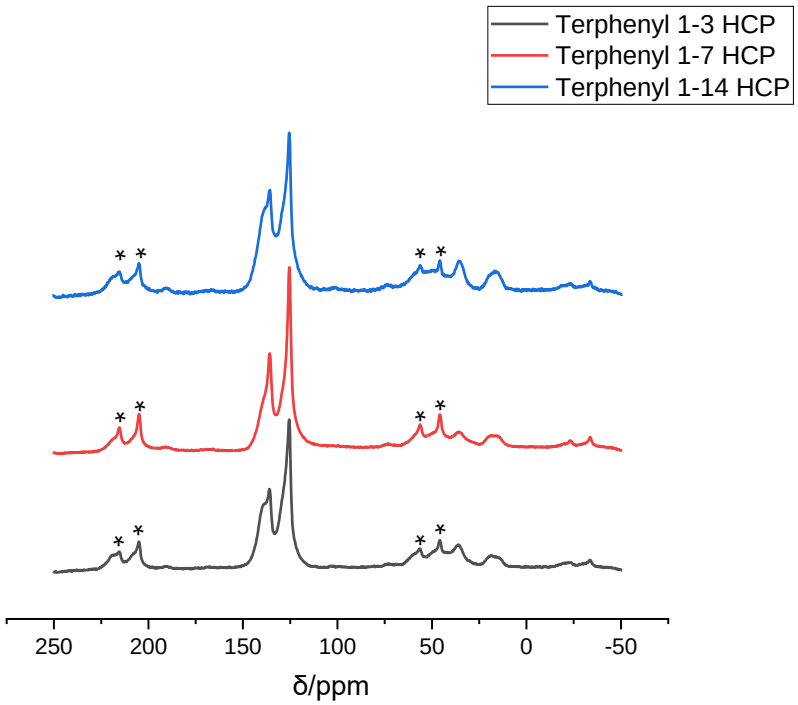

Figure 5.4.2 ^{13}C solid state NMR spectra of Terphenyl HCPs (the asterisks denote spinning side bands)

For NMR spectra of Terphenyl HCPs, the peak at 136 ppm and 126 ppm can be ascribed to substituted and non-substituted aromatic carbon, and the peak at 36 ppm can be assigned to carbon in methylene bridges.[49] The peak at 73 ppm and 17 ppm correspond to carbon in the methylene group binding to oxygen atom of crosslinker residue and the methyl carbon at the end of crosslinker residue, respectively.[22] The peak shoulder at 139 ppm is attributed to the aromatic carbon connected with another benzene ring.[50] Compared with the solid-state NMR spectra of other samples, it can be seen that relative

intensity of the peaks at 136 and 126 ppm which are attributed to substituted and non-substituted aromatic carbon did not change too much with the increasing ratio of FDA to monomer, indicating there were more unsubstituted hydrogen in Terphenyl HCPs at higher ratio of FDA to monomer. This result corresponds to the results from FTIR spectra.

5.4.2.3 TGA

The thermal stability of Terphenyl HCPs was characterized by using thermalgravimetric analysis (TGA). The TGA was conducted under a N_2 atmosphere and the samples were heated from 25 °C to 800 with a heating rate 10 °C/min.

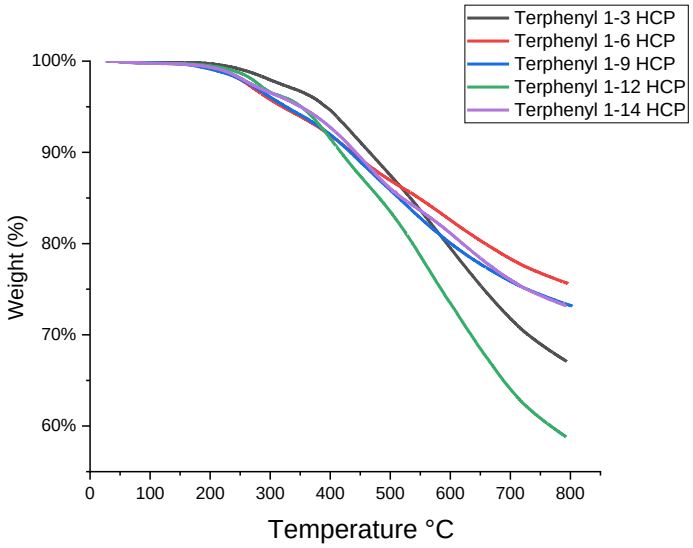

Figure 5.4.3 TGA curves of Terphenyl HCPs

The Terphenyl HCPs showed good thermal stability. The weight residue of the Terphenyl HCPs is higher than 90% at 400 °C. It can be seen that the onset temperature of the Terphenyl 1-3 HCPs is higher than other samples. At 800 °C, the weight residue of Terphenyl 1-3, 1-6, 1-9, 1-12 and 1-14 HCP is 67%, 76%, 73%, 59% and 73%, respectively.

5.4.2.4 N_2 Sorption

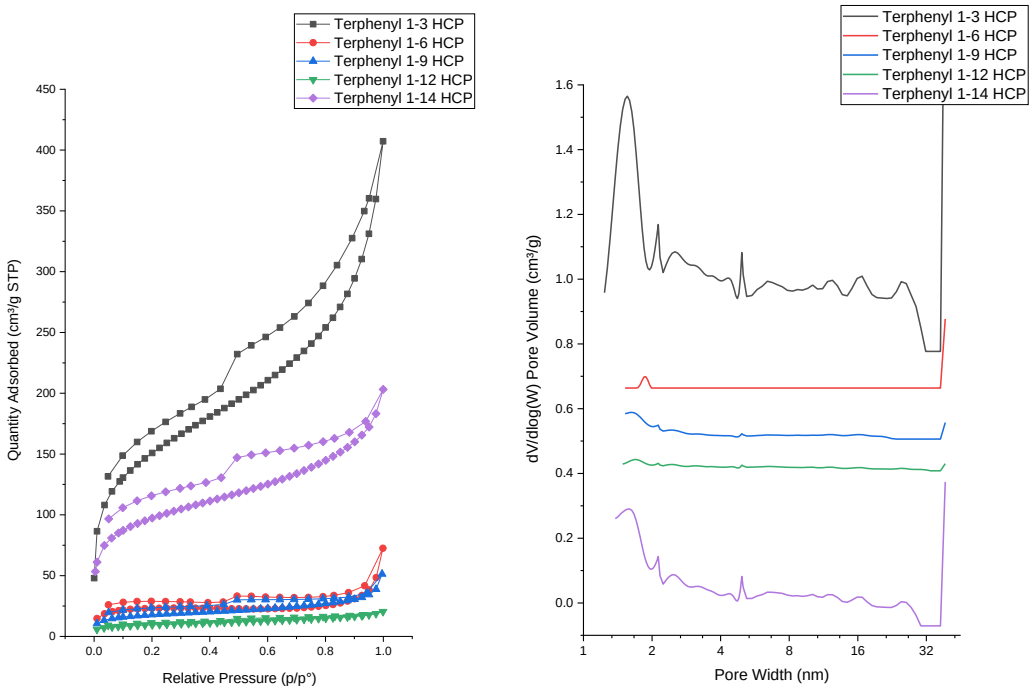

Figure 5.4.4 Isotherm and pore size distribution of Terphenyl HCPs

The porous structures of Terphenyl HCPs were characterized by N_2 adsorption/desorption analysis at 77 K. In the figure 5.4.4, it can be seen that the Terphenyl 1-3 HCP and Terphenyl 1-14 HCP showed the combined Type II and Type IV isotherms according to definition of IUPAC. The sharp rise at low relative pressure ($P/P_0<0.01$) suggests the microporous structures in the samples. The hysteresis loop in the relative pressure range of 0.43-1.0 indicates the existence of mesoporous structures in the samples. The rise in relative pressure range of 0.9-1.0 demonstrates the macropores in the samples. Due to the low N_2 adsorption of Terphenyl 1-6, 1-9, and 1-12 HCP, the isotherm curves of these samples are shown in the figure 5.4.5 separately.

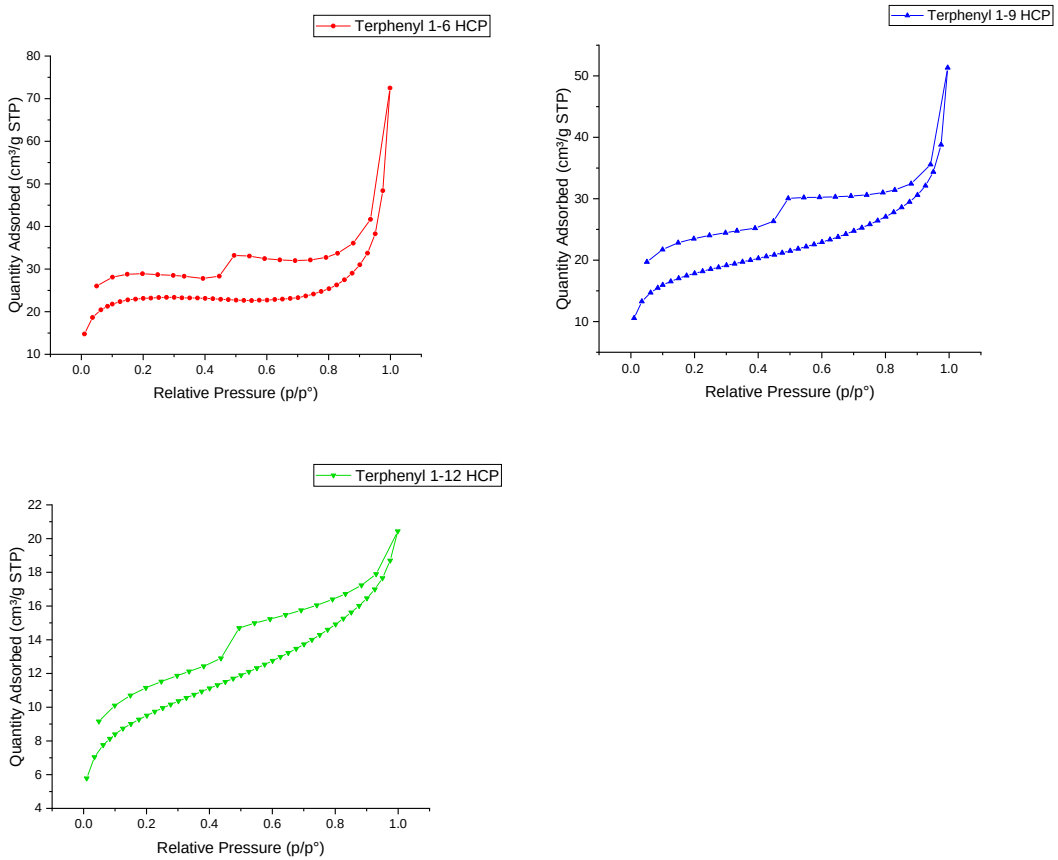

Figure 5.4.5 The isotherms of Terphenyl 1-6, 1-9, and 1-12 HCP

In the figure 5.4.5, the rise in the relative pressure range of $P/P_0<0.01$, the hysteresis loop in the relative pressure range of 0.43-1.0 and the rise in 0.9-1.0 can be also found in the isotherm curves of Terphenyl 1-6, 1-9, and 1-12 HCP, suggesting the existence of micropores, mesopores and macropores in these three samples.

In terms of pore size distribution of Terphenyl HCPs, it can be found that the peaks of the Terphenyl 1-3 HCP are in the similar positions with those of the Terphenyl 1-14 HCP, but the peaks of Terphenyl 1-14 HCP have lower intensity. The main peaks of these two samples are located within 1-2 nm, and the weaker peaks can be observed in the range of 2-32 nm. For the pore size distribution curves of Terphenyl 1-6, 1-9 and 1-12 HCP, some quite weak peaks can be seen within 1-2 nm, corresponding to the low amount of N_2 adsorption of these samples shown in their isotherms.

The single point adsorption total pore volumes of Terphenyl HCPs obtained at $p/p_0=0.99$ and the BET surface areas of them are shown in the table 5.4.2.

	BET surface area (m^2/g)	Single point adsorption total pore volume at p/p_0=0.99 (cm^3/g)
Terphenyl 1-3 HCP	548.5	0.63
Terphenyl 1-6 HCP	89.5	0.09
Terphenyl 1-7 HCP	127.1	0.16
Terphenyl 1-9 HCP	66.5	0.08
Terphenyl 1-12 HCP	34.5	0.03
Terphenyl 1-14 HCP	355.2	0.31

Table 5.4.2 BET surface area and single point adsorption total pore volume of Terphenyl HCPs

The BET surface areas of Terphenyl 1-3 HCP, Terphenyl 1-6 HCP, Terphenyl 1-9 HCP, Terphenyl 1-12 HCP, Terphenyl 1-14 HCP are 548.5, 89.5, 66.5, 34.5 and 355.2 m^2/g, and the single point adsorption total pore volumes of these samples are 0.63, 0.09, 0.08, 0.03 and 0.31 cm^3/g. It can be found that the BET surface areas and pore volumes of these five Terphenyl HCPs kept decreasing with increasing ratio of FDA to terphenyl. When the ratio of FDA to terphenyl increased to 14-1, the BET surface area and single point adsorption total pore volume increased sharply. Interestingly, the BET surface area and pore volume of Terphenyl 1-7 HCP are 127.1 m^2/g 0.16 cm^3/g, respectively. If Terphenyl 1-7 HCP was taken into consideration, the variation in BET surface areas and the variation in pore volumes of the Terphenyl HCPs showed a W-type fluctuation.

To further investigate the porous structures of Terphenyl HCPs, the pore volumes of the pores with different pore widths are shown in the table 5.4.3 and pore volume proportions of Terphenyl HCPs are performed in the figure 5.4.6. The pore volumes of the pores with pore widths less than 2 nm are obtained at relative pressure p/p_0=0.2 and the pore volumes of the pores with pore widths less than 10 nm are obtained at p/p_0=0.8.

Material	Pore volume of the pores with pore width less than 2 nm (cm^3/g)	Pore volume of the pores with pore width 2-10 nm (cm^3/g)	Pore volume of the pores with pore width larger than 10 nm (cm^3/g)
Terphenyl 1-3 HCP	0.234	0.159	0.237
Terphenyl 1-6 HCP	0.033	0.013	0.045
Terphenyl 1-7 HCP	0.054	0.037	0.069
Terphenyl 1-9 HCP	0.028	0.014	0.038
Terphenyl 1-12 HCP	0.014	0.008	0.008
Terphenyl 1-14 HCP	0.148	0.073	0.089

Table 5.4.3 The pore volumes of the pores with different pore widths of Terphenyl HCPs

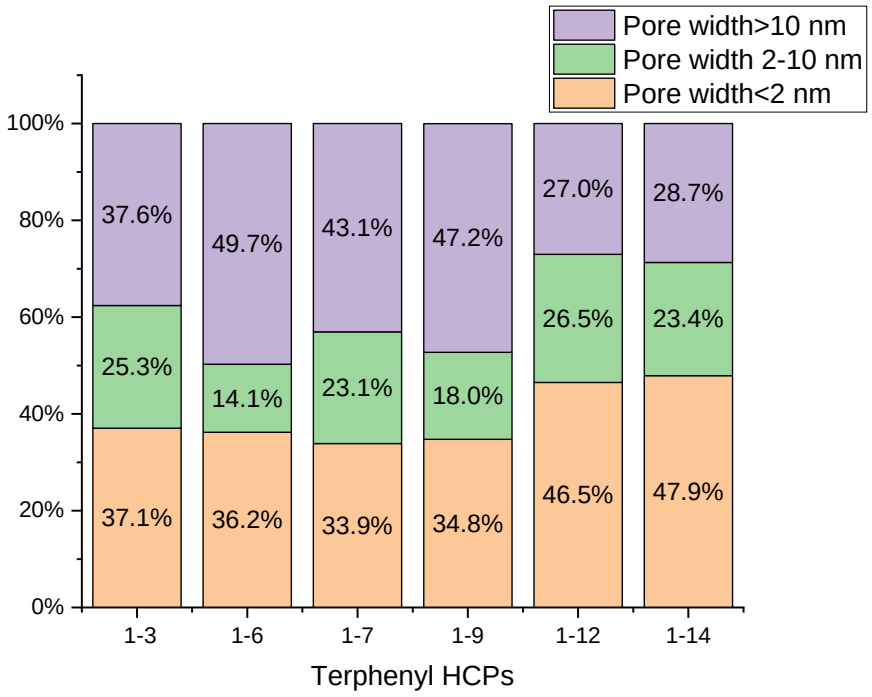

Figure 5.4.6 Pore volume proportions of pores with different pore widths of Terphenyl HCPs

In the pore volume proportion of Terphenyl HCPs, it can be found that the change in the composition of the pore volume of different Terphenyl HCPs was independent with the variation of BET surface area and single point adsorption total pore volume. The micropore volume proportions of Terphenyl 1-3, 1-6, 1-9, 1-12 and 1-14 HCP are 37.1%,

36.2%, 34.8%, 46.5% and 47.9%, and the micropore volumes of them are 0.234, 0.033, 0.028, 0.014 and 0.148 cm^3/g respectively. The volume proportions of pores with pore width 2-10 nm in Terphenyl 1-3, 1-6, 1-9, 1-12 and 1-14 HCP are 25.3%, 14.1%, 18.0%, 26.5% and 23.4%, and the pore volumes of them are 0.159, 0.013, 0.014, 0.008 and 0.073 cm^3/g respectively. For the pores with pore width larger than 10 nm, the pore volume proportions in Terphenyl 1-3, 1-6, 1-9, 1-12 and 1-14 HCP are 37.6%, 49.7%, 47.2%, 27.0% and 28.7%, the pore volumes of the pores with pore width larger than 10 nm are 0.237, 0.045, 0.038, 0.008 and 0.089 cm^3/g, respectively. The Terphenyl 1-3 HCP has the highest micropore volume followed by the Terphenyl 1-14 HCP. The Terphenyl 1-3 HCP has similar pore size distribution with the Terphenyl 1-14 HCP, while it can be seen that they have different pore volume proportions. These two samples have similar volume proportions of the pores with width 2-10 nm, while the Terphenyl 1-14 HCP has higher volume proportion of the micropores while the proportion of the pores with diameter larger than 10 nm is higher in the Terphenyl 1-3 HCP. For the Terphenyl 1-7 HCP, the volume proportions of micropores, pores with diameter 2-10 nm, and pores with diameter larger than 10 nm are 33.8%, 23.1% and 43.1%, the pore volumes of them are 0.054, 0.037 and 0.069 cm^3/g, respectively. Although the Terphenyl 1-7 HCP have an increase in BET surface area, total pore volume compared with the Terphenyl 1-6 and 1-12 HCP, the Terphenyl 1-7 HCP showed a quite similar pore volume composition with them. It is interesting to see the Terphenyl 1-12 and 1-14 HCP have similar pore volume compositions but the Terphenyl 1-14 HCP has around ten times higher BET surface area and pore volume than the Terphenyl 1-14 HCP.

5.4.2.5 Cyclic Voltammetry

The electrochemical properties of Terphenyl HCPs were evaluated by a typical three-electrode system with 1 M Na_2SO_4 aqueous solution as electrolyte. The active material on nickel foam, a platinum electrode and an Ag/AgCl electrode (3 M KCl, 0.207 V vs.

standard hydrogen electrode at 25 °C) were used as working electrode, counter electrode and reference electrode, respectively. The CV tests were conducted with different scan rates 2, 10, 25, 50, 75, 100 and 200 mV/s in the voltage range of -0.2 V-0.8 V.

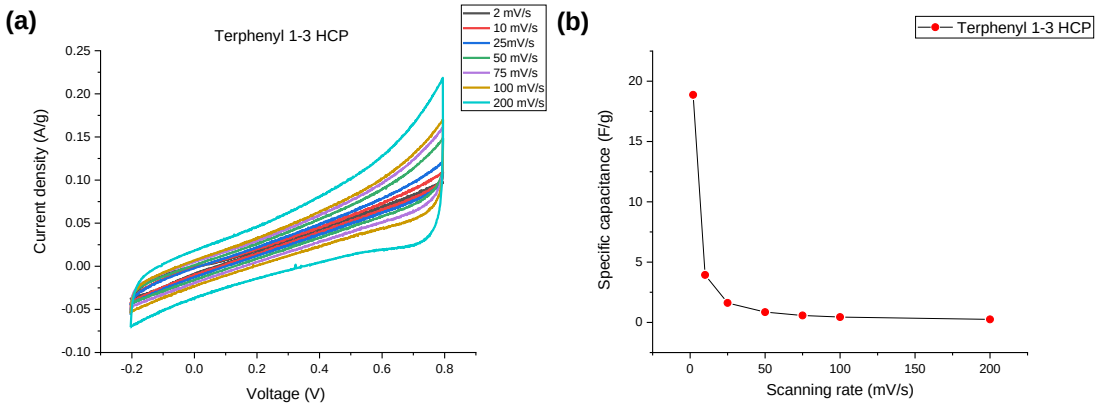

Figure 5.4.7 (a) CV curves at different scanning rates, and (b) Specific capacitance obtained at different scanning rates of Terphenyl 1-3 HCP

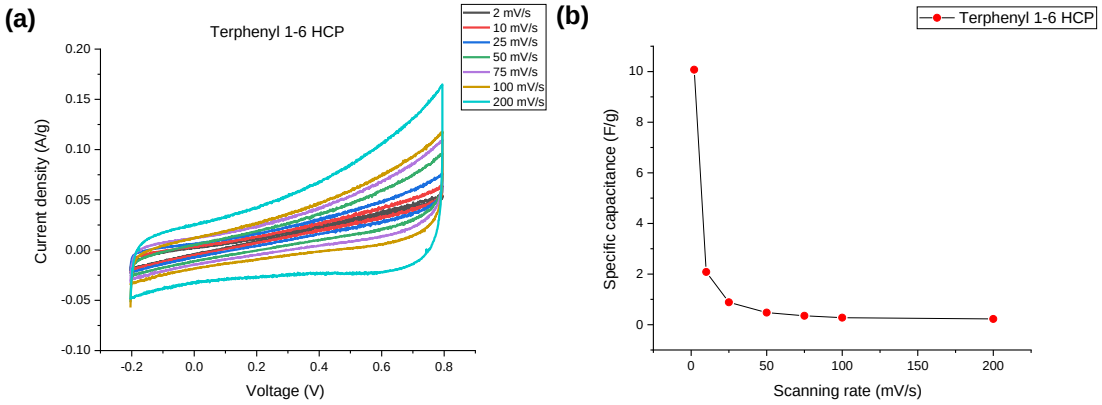

Figure 5.4.8 (a) CV curves at different scanning rates, and (b) Specific capacitance obtained at different scanning rates of Terphenyl 1-6 HCP

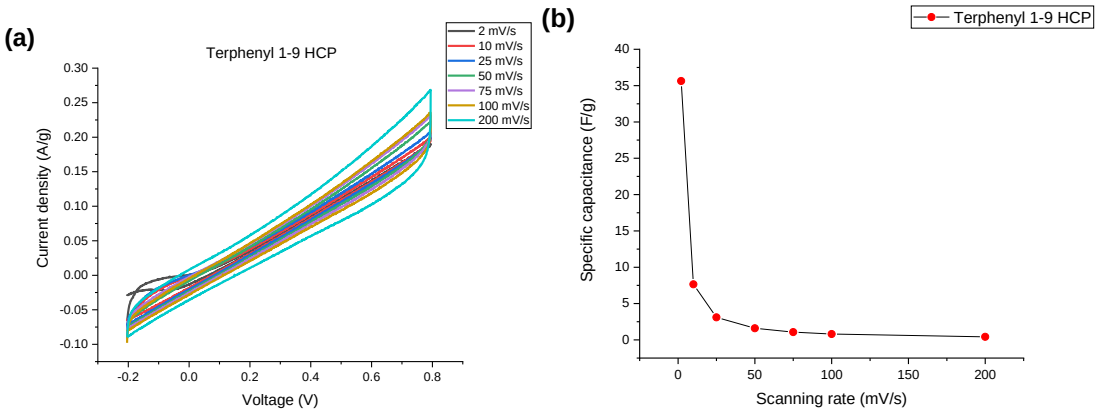

Figure 5.4.9 (a) CV curves at different scanning rates, and (b) Specific capacitance obtained at different scanning rates of Terphenyl 1-9 HCP

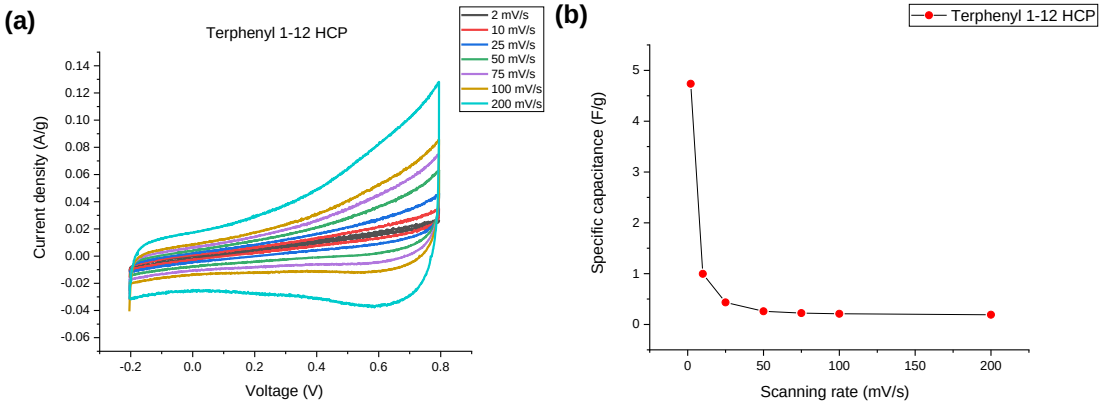

Figure 5.4.10 (a) CV curves at different scanning rates, and (b) Specific capacitance obtained at different scanning rates of Terphenyl 1-12 HCP

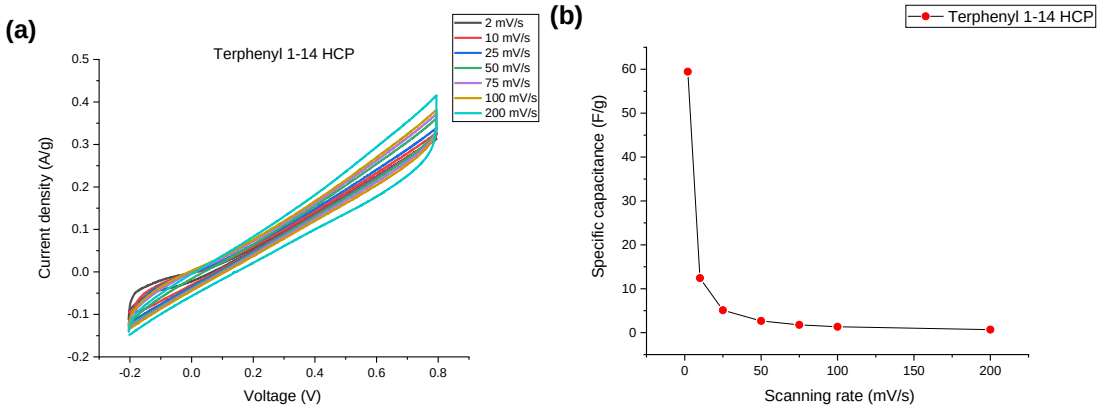

Figure 5.4.11 (a) CV curves at different scanning rates, and (b) Specific capacitance obtained at different scanning rates of Terphenyl 1-14 HCP

	Specific capacitance obtained at different scanning rates (F/g)							
Scanning rates (mV/s) / Material	2	10	25	50	75	100	200	Retention of capacitance at 200 mV/s
Terphenyl 1-3 HCP	18.9	3.9	1.6	0.9	0.6	0.4	0.3	1.6%
Terphenyl 1-6 HCP	10.1	2.1	0.9	0.5	0.4	0.3	0.2	2.0%
Terphenyl 1-7 HCP	2.2	0.5	0.2	0.2	0.2	0.2	0.2	9.1%
Terphenyl 1-9 HCP	35.6	7.6	3.1	1.6	1.1	0.8	0.4	1.1%
Terphenyl 1-12 HCP	4.7	1.0	0.4	0.3	0.2	0.2	0.2	4.3%
Terphenyl 1-14 HCP	59.4	12.4	5.1	2.7	1.8	1.3	0.7	1.2%

Table 5.4.4 Specific capacitance of terphenyl HCPs obtained at different scanning rates

The specific capacitance at 2 mV/s of Terphenyl 1-3, 1-6, 1-9, 1-12 and 1-14 HCP is 18.9, 10.1, 35.6, 4.7, 59.4 F/g, respectively, and the capacitance retention from 2 mV/s to 200 mV/s of them is 1.6%, 2.0%, 1.1%, 4.3% and 1.2%, respectively. Overall, the Terphenyl HCPs showed relatively lower capacitances compared with others. In these five samples, Terphenyl 1-12 HCP has the lowest specific capacitance, it also has the lowest BET surface area (34.5 m^2/g), total pore volume (0.03 cm^3/g), micropore volume (0.014 cm^3/g) and the pore volume of the pores with diameter 2-10 nm (0.008 cm^3/g). The Terphenyl 1-3 HCP has the highest BET surface area (548.5 m^2/g), total pore volume (0.63 cm^3/g), micropore volume (0.234 cm^3/g) and the pore volume of the pores with diameter 2-10 nm (0.159 cm^3/g), while the specific capacitance of the Terphenyl 1-3 HCP is lower than the Terphenyl 1-9 HCP with much lower BET surface area (66.5 m^2/g), total pore volume (0.08 cm^3/g), micropore volume (0.028 cm^3/g) and the pore volume of the pores with diameter 2-10 nm (0.014 cm^3/g). The Terphenyl 1-14 HCP has the highest capacitance, the BET surface area (355.2 m^2/g), total pore volume (0.31 cm^3/g), micropore volume (0.148 cm^3/g) and the pore volume of the pores with diameter 2-10 nm (0.073 cm^3/g) of the Terphenyl 1-14 HCP is the second highest among

all the Terphenyl HCPs (including Terphenyl 1-7 HCP). It can be seen from the pore volume proportions of Terphenyl HCPs that the Terphenyl 1-14 HCP has similar pore volume compositions with the Terphenyl 1-12 HCP, but Terphenyl 1-14 HCP has much higher capacitance than that of the Terphenyl 1-12 HCP. The BET surface area (89.5 m^2/g), total pore volume (0.09 cm^3/g), and the micropore volume (0.033 cm^3/g) of Terphenyl 1-6 HCP are higher than those of the Terphenyl 1-9 HCP, and it also has similar pore volume of the pores with diameter 2-10 nm (0.013 cm^3/g) with the Terphenyl 1-9 HCP. The Terphenyl 1-9 HCP has higher specific capacitance than the Terphenyl 1-6 HCP. If Terphenyl 1-7 HCP is taken into consideration, it has the lowest specific capacitance (2.2 F/g) among all the Terphenyl HCPs, but the BET surface (127.1 m^2/g), total pore volume (0.16 cm^3/g), micropore volume (0.054 cm^3/g) and the pore volume of the pores with diameter 2-10 nm (0.037 cm^3/g) of the Terphenyl 1-7 HCP are higher than those of the Terphenyl 1-9 HCP. Therefore, it can be seen that the capacitances of the Terphenyl HCPs are influenced by the different porosities of these samples, however, the variation in the capacitances of the Terphenyl HCPs is independent with the variations in the porosity of them can be observed as well.

The relationship between the response current and scanning rate is employed to provide the insight into the energy storage kinetics of Terphenyl HCPs, the results are shown in the figure 5.4.12.

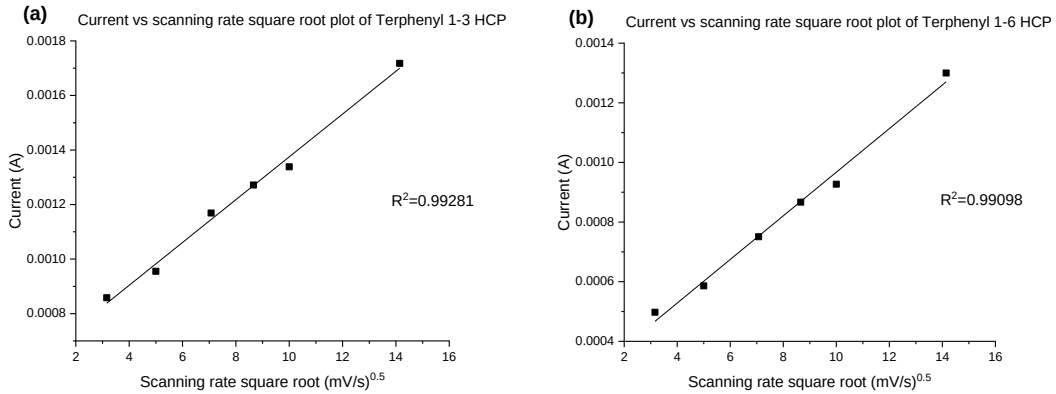

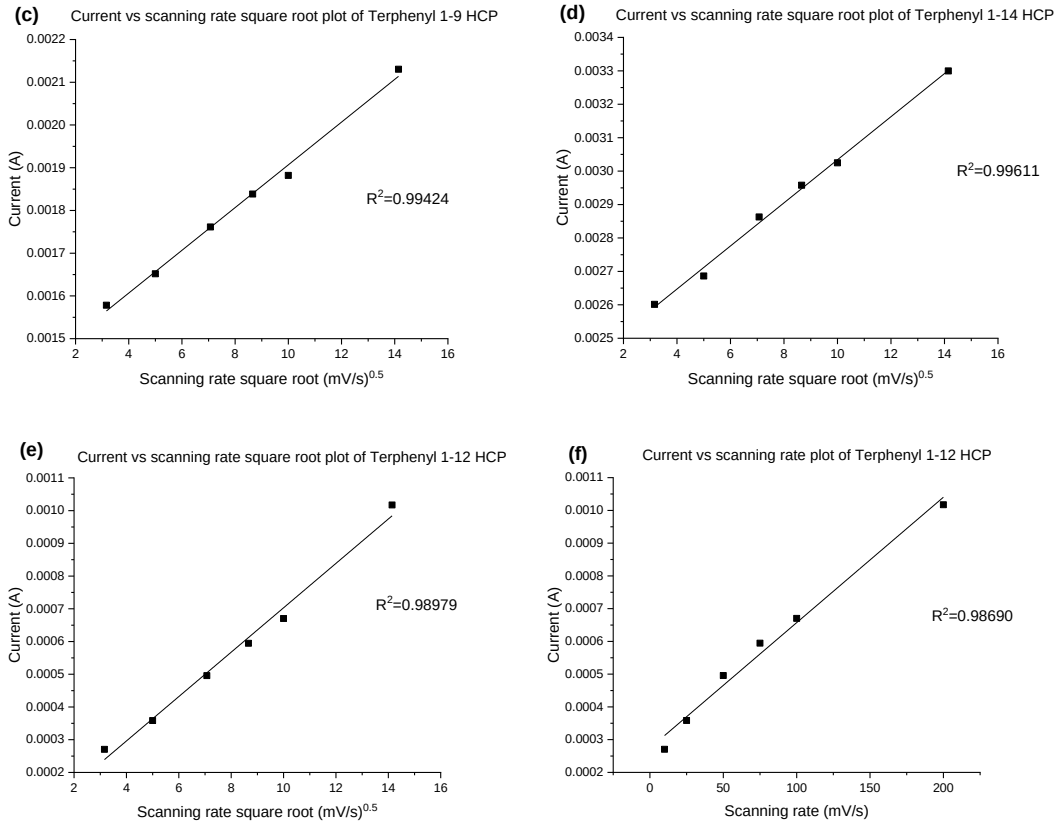

Figure 5.4.12 The relationship between response current and scanning rate of Terphenyl HCPs. (a). – (d). current vs scanning rate square root plot of Terphenyl 1-3, 1-6, 1-9 and 1-14 HCP. (e). current vs scanning rate square root plot and (f). current vs scanning rate plot of Terphenyl 1-12 HCP.

From the figure 5.4.12, it can be seen the coefficient of determination R^2 of the response current vs scanning rate square root plot of Terphenyl 1-3, 1-6, 1-9 and 1-14 HCP is 0.99281, 0.99098, 0.99424 and 0.99611, respectively, indicating the good linear relationship between the response current and scanning rate square root. Therefore, the capacity kinetics of these samples are dominated by the diffusion-controlled process. For the CV curve at 200 mV/s of the Terphenyl 1-3 HCP and Terphenyl 1-6 HCP, the uneven distribution of the electrolyte ions can be found, the R^2 of these two samples are lower that of Terphenyl 1-9 and 1-14 HCP, the specific capacitances of these two samples are lower than that of Terphenyl 1-9 and 1-14 HCP as well. The CV curve at 200 mV/s of Terphenyl 1-6 HCP showed a more quasi-rectangular than that of Terphenyl 1-3 HCP, it can be seen that the Terphenyl 1-6 HCP has lower R^2 than Terphenyl 1-3 HCP, it also has lower specific capacitance than Terphenyl 1-3 HCP.

Therefore, it can be found that the inappropriate pore structures will result in the underutilization of the porosity and the uneven distribution of the electrolyte ions, thus the lower capacitance. For Terphenyl 1-12 HCP, the R^2 of the response current vs scanning rate square root plot is 0.98979, lower than that of other samples in this group. So, the R^2 of the response current vs scanning rate of Terphenyl 1-12 HCP is used for comparing to confirm the capacity kinetic of Terphenyl 1-12 HCP. It can be seen the R^2 of the response current vs scanning rate of Terphenyl 1-12 HCP is 0.98690. As these two coefficients of determination from different plots are close, the Terphenyl 1-12 HCP has a mixed energy storage kinetic that involves both diffusion-controlled process and surface-controlled process. The Terphenyl 1-12 HCP has the lowest specific capacitance among all the samples in this group, because of the underutilized porosity which can be found from the CV curves. The poor conductivity of Terphenyl HCPs determines the capacity kinetic of Terphenyl HCPs is diffusion-controlled process, thus the low capacitance retention rate of these samples. Although the Terphenyl 1-12 HCP showed a mixed kinetic of capacity and higher capacitance retention rate, the low specific capacitance of the Terphenyl 1-12 HCP shows the fast surface-controlled process could only provide small amounts of capacitances.

5.4.2.6 Electrochemical impedance spectroscopy (EIS)

To further investigate the electrochemical performance of Terphenyl HCPs, electrochemical impedance spectroscopy (EIS) was carried out with amplitude of 10 mV and frequency range 100 k Hz to 0.01 Hz. The Nyquist and Bode plots of Terphenyl HCPs are shown in the figures 5.4.13 to 5.4.17.

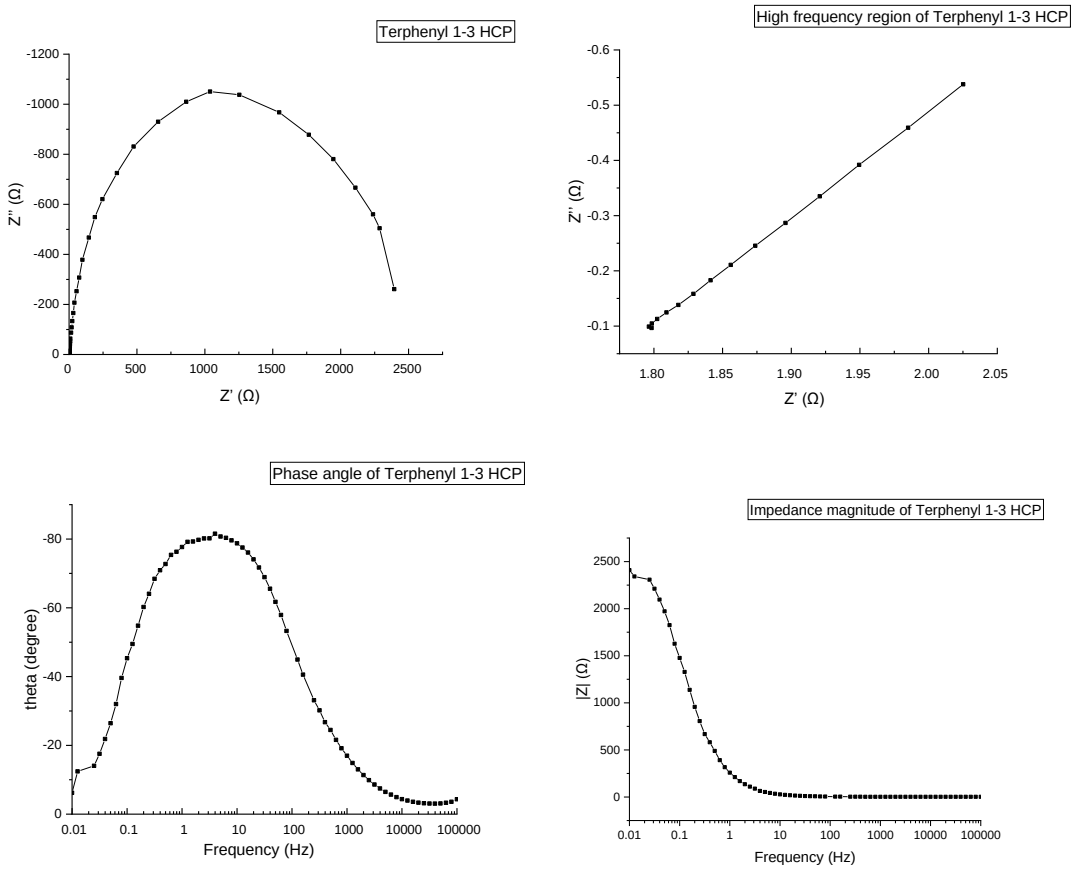

Figure 5.4.13 Nyquist plot and Bode plot of Terphenyl 1-3 HCP

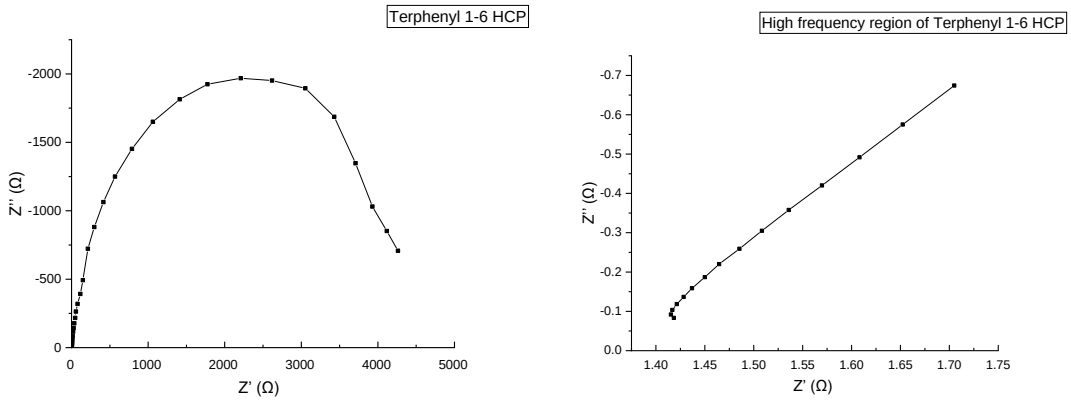

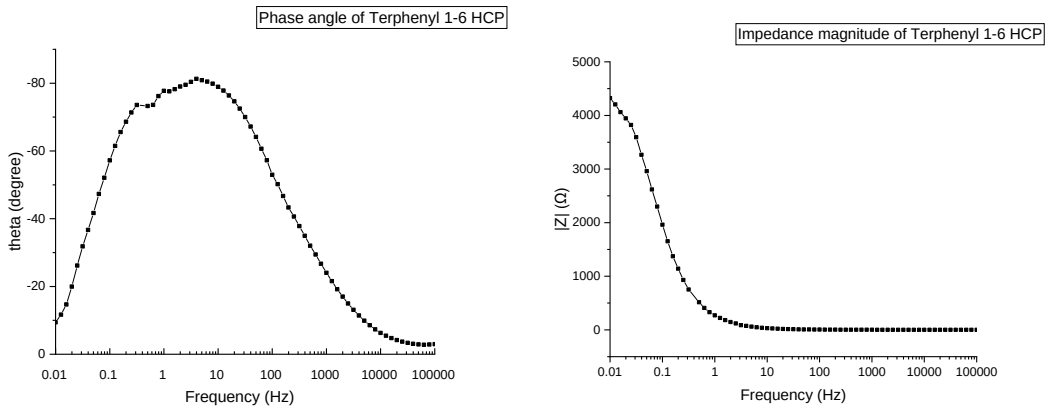

Figure 5.4.14 Nyquist plot and Bode plot of Terphenyl 1-6 HCP

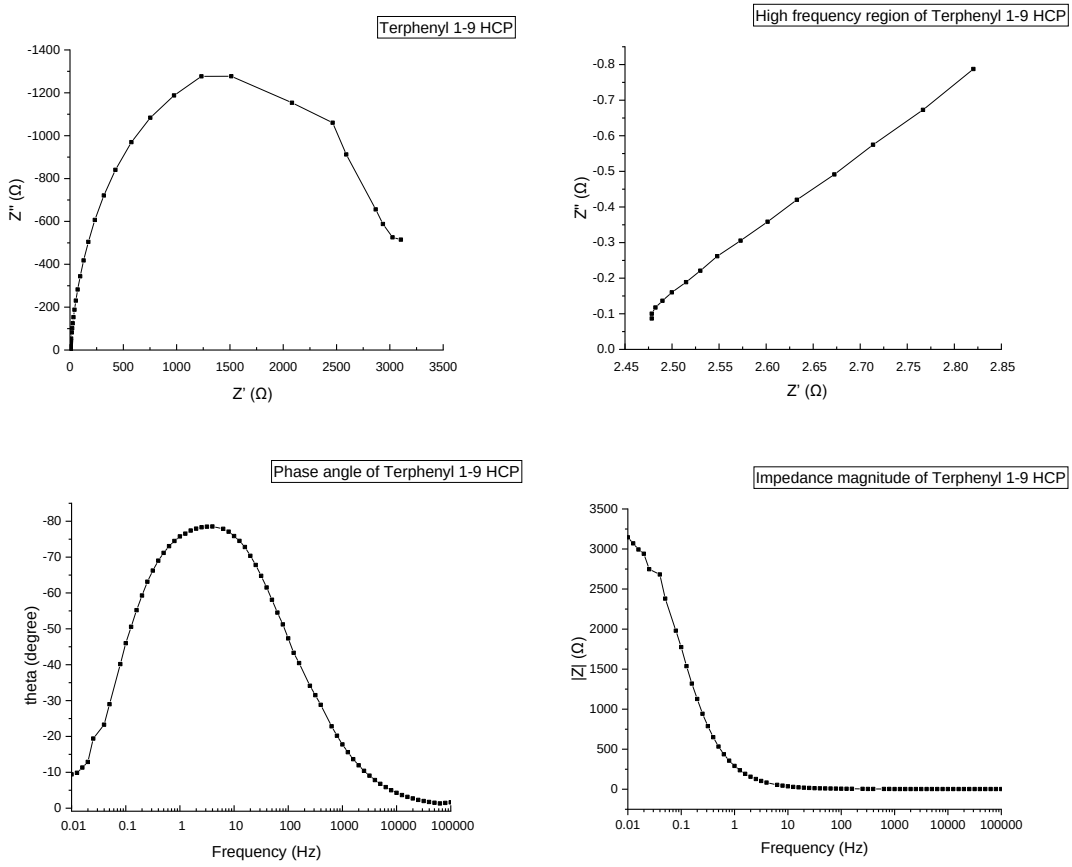

Figure 5.4.15 Nyquist plot and Bode plot of Terphenyl 1-9 HCP

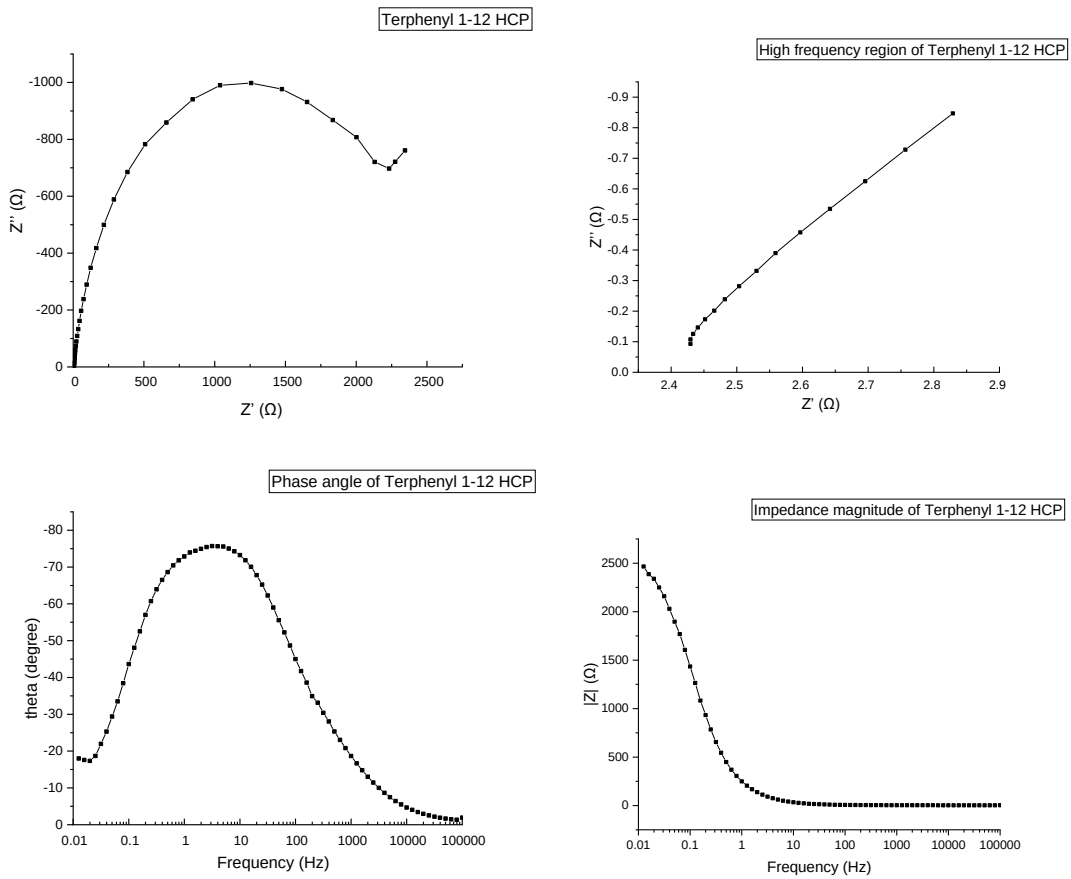

Figure 5.4.16 Nyquist plot and Bode plot of Terphenyl 1-12 HCP

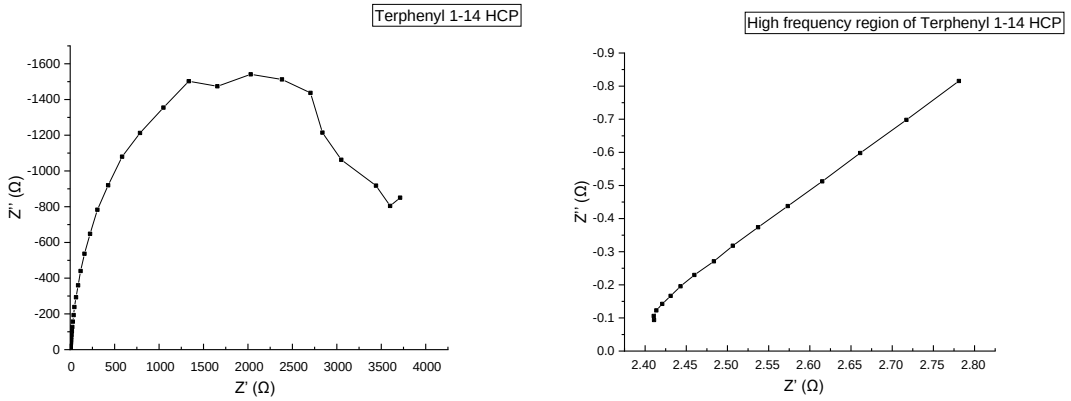

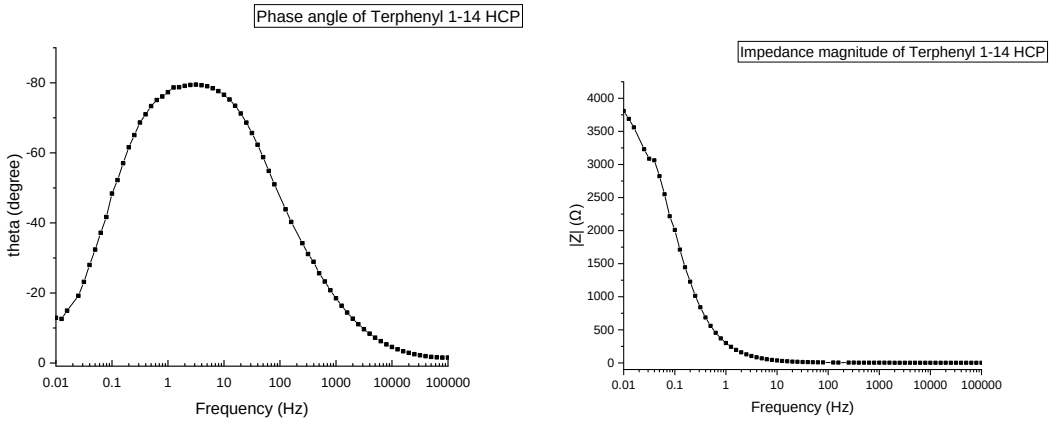

Figure 5.4.17 Nyquist plot and Bode plot of Terphenyl 1-14 HCP

	Whether the semicircle can be observed at high frequencies?	Whether the Nyquist plot is vertical or near vertical to Z" axis at low frequencies?	The phase angle value of the curve apex	Phase angle at 0.01 Hz	Impedance magnitude at 0.01 Hz (Ω)
Terphenyl 1-3 HCP	No	No	-81°	-5°	2409
Terphenyl 1-6 HCP	No	No	-81°	-10°	4320
Terphenyl 1-9 HCP	No	No	-78°	-10°	3145
Terphenyl 1-12 HCP	No	No	-76°	-18°	2465
Terphenyl 1-14 HCP	No	No	-79°	-16°	3808

Table 5.4.5 The results from Nyquist and Bode plot of terphenyl HCPs

In the Nyquist plot of Terphenyl HCPs, the absence of the sharp rising 'tail' in the intermediate and low frequency region that parallels to the Z" axis indicated he Terphenyl HCPs did not show supercapacitor behaviour. The highest angle of Terphenyl HCPs varies from -81° to -76°, showing the gap between Terphenyl HCP electrodes and a pure capacitor. The phase angle curves of Terphenyl HCPs showed a downward tendency after reaching the highest point, suggesting the Terphenyl HCPs tended to behave like resistors with the decreasing frequency because of the poor conductivity of

Terphenyl HCPs. The phase angles of Terphenyl HCPs at 0.01 Hz were not 0°, indicating they showed some capacitance at low frequencies. The impedance magnitude value of the Terphenyl HCPs at 0.01 Hz are large. It can be found that the ohmic resistance occupies a quite large proportion in the impedance of Terphenyl HCPs at low frequencies due to their phase angles are close to 0° at 0.01 Hz. The absence of the semi-circle in the high frequency region is due to the ohmic contact between the current collector and the active materials.

To exhibit the poor conductivity of Terphenyl HCPs more intuitively, the fitting results are shown in the figure 5.4.18 and table 5.4.6. The Randles circuit model is employed as the equivalent circuit for the impedance fitting.

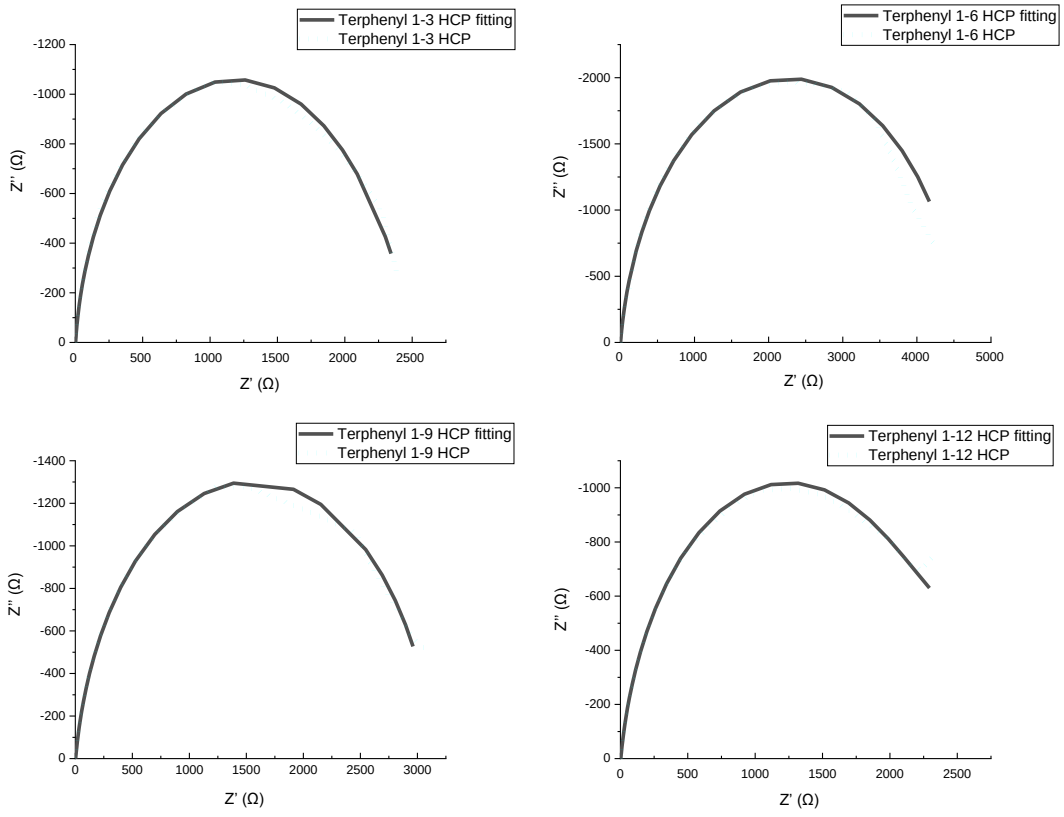

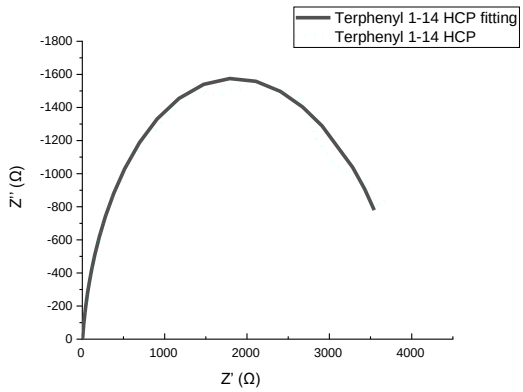

Figure 5.4.18 The impedance fitting curves of Terphenyl HCPs

The deviations in the fitting curves of Terphenyl HCPs can be found in the low frequency region as the diffusion in the disordered porous structure of Terphenyl HCPs with poor conductivity is hard to be precisely predicted.

	R1 (Ω)	CPE1-T (F)	CPE1-P	R2 (Ω)	Ws1-R (Ω)	Ws1-T (s)	Ws1-P
Terphenyl 1-3 HCP	1.972	0.00074344	0.92852	2347.3	113.1	26.1	0.5
Terphenyl 1-6 HCP	1.604	0.00071434	0.91096	4572.4	39.3	23.4	0.5
Terphenyl 1-9 HCP	2.701	0.00067153	0.89865	2996.8	148.7	10.9	0.5
Terphenyl 1-12 HCP	2.689	0.00081916	0.88466	2362.2	436.8	47.2	0.5
Terphenyl 1-14 HCP	2.674	0.00063505	0.91353	3505.9	373.2	22.1	0.5

Table 5.4.6 The impedance fitting results of Terphenyl HCPs

The R2 values in the table suggest the high internal resistance of the Terphenyl HCPs. The variation of in R2 values indicates the impacts generated by different amount of crosslinkers used in the synthesis of Terphenyl HCPs.

To gain further insight into the electrochemical performance of Terphenyl HCPs with AC is applied, the complex capacitance of Terphenyl HCP is performed. The definition of complex capacitance and the definitions of its components were given by equation 5.2.2.6.1, 5.2.2.6.2 and 5.2.2.6.3. The complex capacitance curves of Terphenyl HCP are listed in the figure 5.4.19.

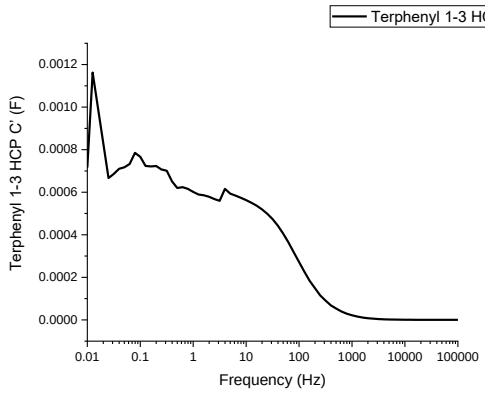
Terphenyl 1-3 HCP C'
Terphenyl 1-3 HCP C' (F)
Frequency (Hz)

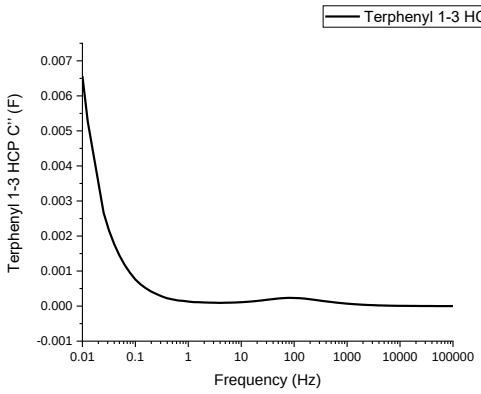
Terphenyl 1-3 HCP C''
Terphenyl 1-3 HCP C'' (F)
Frequency (Hz)

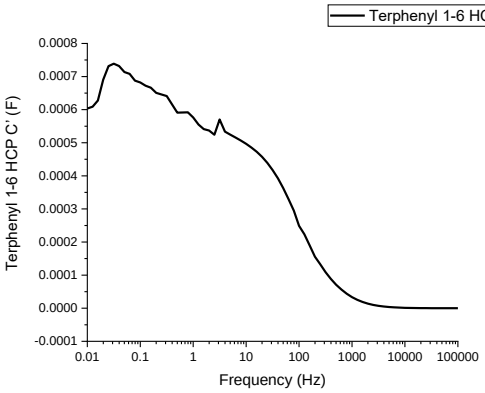
Terphenyl 1-6 HCP C'
Terphenyl 1-6 HCP C' (F)
Frequency (Hz)

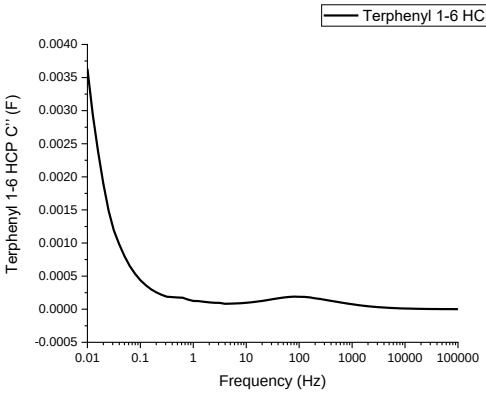
Terphenyl 1-6 HCP C''
Terphenyl 1-6 HCP C'' (F)
Frequency (Hz)

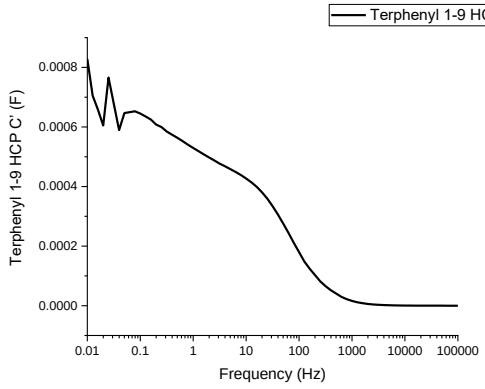
Terphenyl 1-9 HCP C'
Terphenyl 1-9 HCP C' (F)
Frequency (Hz)

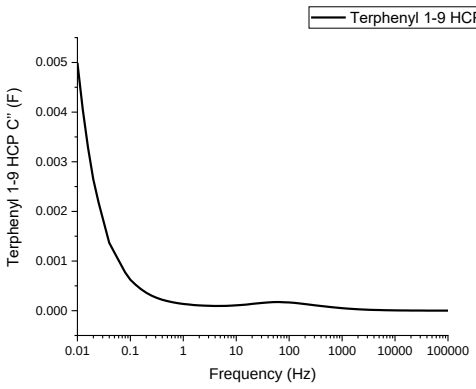
Terphenyl 1-9 HCP C''
Terphenyl 1-9 HCP C'' (F)
Frequency (Hz)

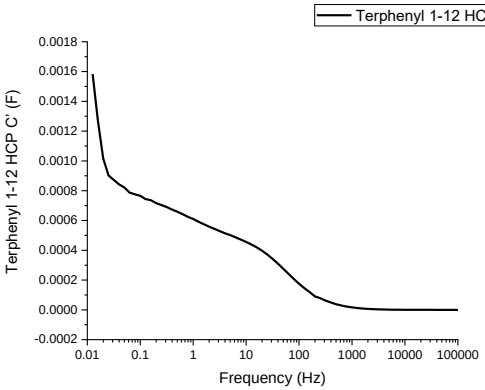
Terphenyl 1-12 HCP C'
Terphenyl 1-12 HCP C' (F)
Frequency (Hz)

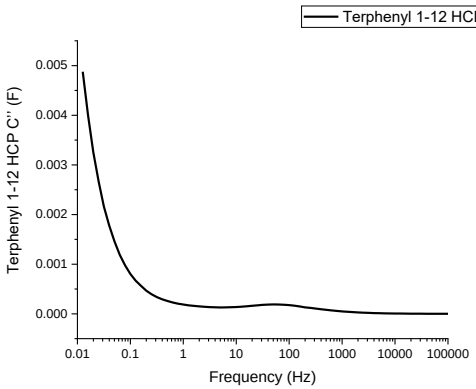
Terphenyl 1-12 HCP C''
Terphenyl 1-12 HCP C'' (F)
Frequency (Hz)

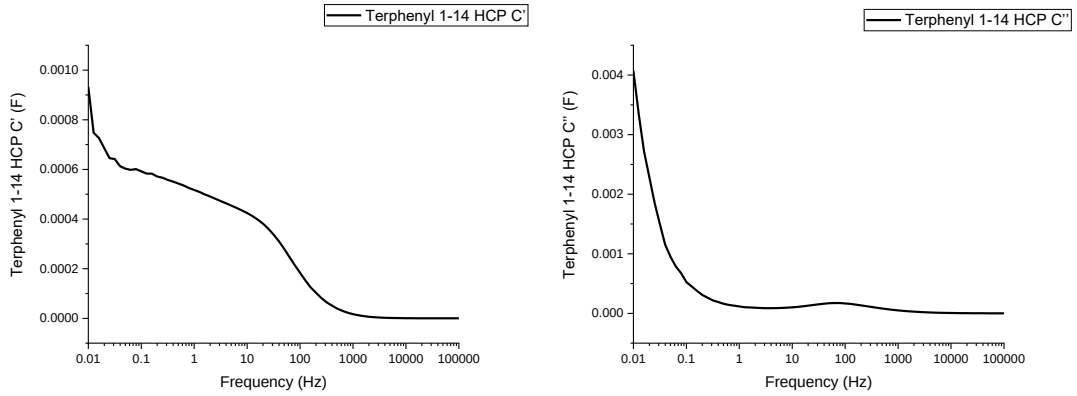

Figure 5.4.19 The complex capacitance of Terphenyl HCPs

The real part of the complex capacitance C' shows the capacitance variation with the decreasing frequency. It can be seen that the C' curves of the Terphenyl HCPs showed the same variation trend with a common supercapacitor in the high and intermediate frequency region, while significant fluctuations can be seen at low frequencies, suggesting the unstable accessibility rate of Terphenyl HCPs caused by the poor conductivity. This corresponds to the specific capacitances obtained from CV tests are independent with the BET surface areas and pore volumes of Terphenyl HCPs. The low capacitance at low frequencies suggests the Terphenyl HCPs with high internal resistance can only produce very small response to the low voltage. The imaginary part of the complex C" corresponds to energy dissipation. With the decreasing frequency, the weak peak corresponding to phase angle -45° appeared then the C" curves began to rise and reached the maximum at 0.01 Hz, demonstrating the increased energy dissipation in the low frequency region caused by poor conductivity of Terphenyl HCPs. This corresponds to the decreasing in the phase angle curves at low frequencies. The frequency at which the C" reaches the maximum can be used to define the relaxation time to assess the rate performance of the materials. The definition of the relaxation time was given by 5.2.2.6.4. The relaxation time τ_0 of the Terphenyl HCPs is 100 s, suggesting the poor rate performance of Terphenyl HCPs. This corresponds to the results from the CV tests. As discussed in previous parts, the capacitance at very low frequencies in the real part of the complex capacitance is much lower than that obtained from CV results is due to the high internal resistance of uncarbonized HCPs as well.

5.5 Triphenylmethane (TPM) HCPs

5.5.1 Synthesis of TPM HCPs

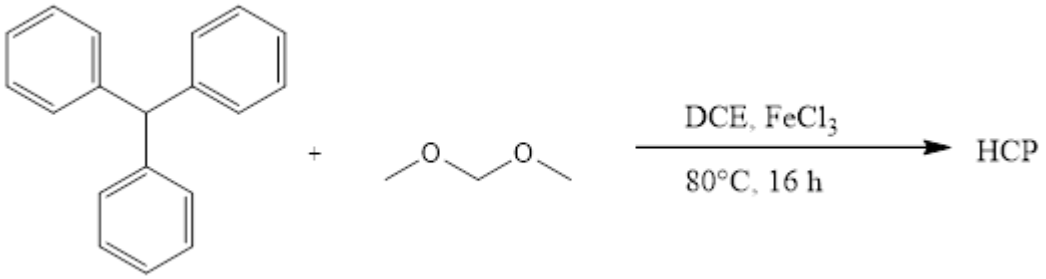

The synthesis of triphenylmethane (TPM) HCPs was performed as follows. Triphenylmethane (5 mmol, 1 eq.) and ferric chloride (15-75 mmol, 3-15 eq.) were added into a dried two-neck flask by syringes with a magnetic stirrer and a condenser. DCE (25 mL) was charged into the flask by a syringe with stirring for 5 minutes to disperse the materials. Then, formaldehyde dimethyl acetal (FDA) (15-75 mmol, 3-15 eq.) was injected into the flask by a syringe and the temperature was increased to 80 ℃. The reaction was left for over 20 hours. The reaction was conducted in atmospheric air. The HCP product was cooled and collected by vacuum filtration and washed with water, methanol, acetone. Then the product was transferred to a Soxhlet extractor and washed with methanol overnight. The product was dried under vacuum at 80 ℃ overnight.

TPM 1-3 HCP: triphenylmethane (5 mmol, 1.22 g, 1 eq.), FDA (15 mmol, 1.34 mL, 3 eq.), ferric chloride (15 mmol, 2.45 g, 3 eq.). Yield: 1.38 g, 98.7%. Formula: $C_{22}H_{16}$. Calculated value of elemental analysis C: 94.25% H: 5.75%. Found value of elemental analysis C: 84.16% H: 5.45%.

TPM 1-6 HCP: triphenylmethane (5 mmol, 1.22 g, 1 eq.), FDA (30 mmol, 2.65 mL, 6 eq.), ferric chloride (30 mmol, 4.87 g, 6 eq.). Yield: 1.58 g, 100.2%. Formula: $C_{25}H_{16}$. Calculated value of elemental analysis C: 94.90% H: 5.10%. Found value of elemental analysis C: 81.97% H: 5.23%

TPM 1-9 HCP: triphenylmethane (5 mmol, 1.22 g, 1 eq.), FDA (45 mmol, 3.98 mL, 9 eq.), ferric chloride (45 mmol, 7.30 g, 9 eq.). Yield: 1.72 g, 102.9%. Formula: $C_{26.5}H_{16}$.

Calculated value of elemental analysis C: 95.21% H: 4.79%. Found value of elemental analysis C: 78.83% H: 5.00%

TPM 1-12 HCP: triphenylmethane (5 mmol, 1.22 g, 1 eq.), FDA (60 mmol, 5.31 mL, 12 eq.), ferric chloride (60 mmol, 9.73 g, 12 eq.). Yield: 1.69 g, 101.3%. Formula: $C_{26.5}H_{16}$. Calculated value of elemental analysis C: 95.21% H: 4.79%. Found value of elemental analysis C: 78.41% H: 4.95%

TPM 1-15 HCP: triphenylmethane (5 mmol, 1.22 g, 1 eq.), FDA (75 mmol, 6.64 mL, 15 eq.), ferric chloride (75 mmol, 12.20 g, 15 eq.). Yield: 1.69 g, 100.8%. Formula: $C_{26.5}H_{16}$. Calculated value of elemental analysis C: 95.21% H: 4.79%. Found value of elemental analysis C: 75.51% H: 4.75%

5.5.2 Results and discussion

5.5.2.1 Synthesis

TPM HCPs were synthesized by Friedel-Crafts alkylation reaction with triphenylmethane used as monomer, formaldehyde dimethyl acetal (FDA) used as an external crosslinker and anhydrous $FeCl_3$ used as a Lewis acid catalyst, in air atmosphere and at 80 ℃. To explore the influence of different ratios of monomer to crosslinker, TPM HCPs were synthesized with different ratios of triphenylmethane to FDA 1-3, 1-6, 1-9, 1-12, and 1-15. TPM HCP discussed in Chapter 3 was synthesized with a monomer to crosslinker ratio of 1-7.5. These TPM HCP sample are named after the ratios of monomer to crosslinker used for synthesis, from TPM 1-3 HCP to TPM 1-15 HCP. The yield and elemental analysis results of TPM HCPs are performed in the table 5.5.1.

	Yield %		Calculated value		Found value	
			C %	H %	C %	H %
TPM 1-3 HCP	98.7%	1.38 g	94.25	5.75	84.16	5.45
TPM 1-6 HCP	100.2%	1.58 g	94.90	5.10	81.97	5.23

TPM 1-7.5 HCP	104.3%	1.74 g	95.21	4.79	76.37	5.54
TPM 1-9 HCP	102.9%	1.72 g	95.21	4.79	78.83	5.00
TPM 1-12 HCP	101.3%	1.69 g	95.21	4.79	78.41	4.95
TPM 1-15 HCP	100.8%	1.69 g	95.21	4.79	75.51	4.75

Table 5.5.1 Yield and elemental analysis results of TPM HCPs

In the table 5.5.1, it can be found that TPM 1-3 HCP has the lowest yield, 98.7%. For other TPM HCPs, they all have a yield higher than 100%. The yields higher than 100% are owing to the existence of the incompletely reacted crosslinker residues, -O-CH_3. HCP products with small particles that cannot be collected by filtration are formed under intense steric impediment. The lower yield of the TPM 1-3 HCP can be attributed to the losses of the HCP products with small particles in the collecting and washing process. The calculated values of elemental analysis of TPM HCPs are higher than the experimental values can be ascribed to the incompletely reacted crosslinker residues as well.

5.5.2.2 FTIR and ^{13}C Solid State NMR spectroscopy

The molecular structures of TPM HCPs were analyzed and confirmed by using Fourier transform infrared (FTIR) and ^{13}C solid state NMR.

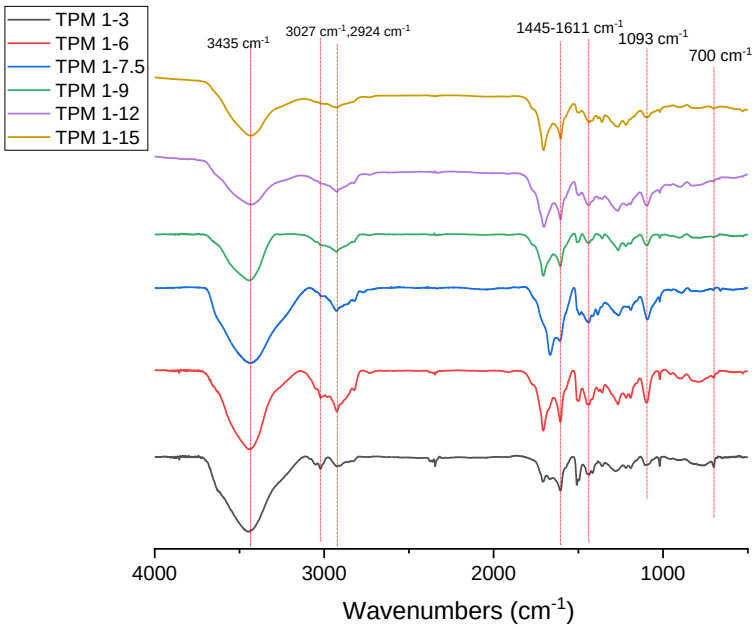

Figure 5.5.1 FTIR spectra of TPM HCPs

For FTIR spectra of TPM HCPs, the peak at 3027 cm^{-1} and 2924 cm^{-1} correspond to C-H stretching in aromatic rings and methylene bridges, respectively.[51] The peaks in 1445-1611 cm^{-1} are attributed to the aromatic ring skeleton vibration.[52] The peak at 1093 cm^{-1} is due to C-O stretching in incompletely reacted crosslinkers.[21] The peak at 700 cm^{-1} is related with mono-substituted aromatic ring.[27] The peak at 3435 cm^{-1} is assigned to O-H stretching in physisorbed water in the KBr disc and porous structure of TPM HCP samples.[53] With the increasing ratio of FDA to TPM, the peak at 3027 cm^{-1} gradually disappeared demonstrating more hydrogen atoms in aromatic rings were substituted when the ratio was higher. The intensity of peak at 1501 cm^{-1} which can be attributed to para-substituted aromatic ring[26] and the intensity of the peak at 700 cm^{-1} which is ascribed to mono-substituted aromatic ring also decreased with the increasing ratio of FDA to TPM suggesting there were more substitution occurred in aromatic rings.

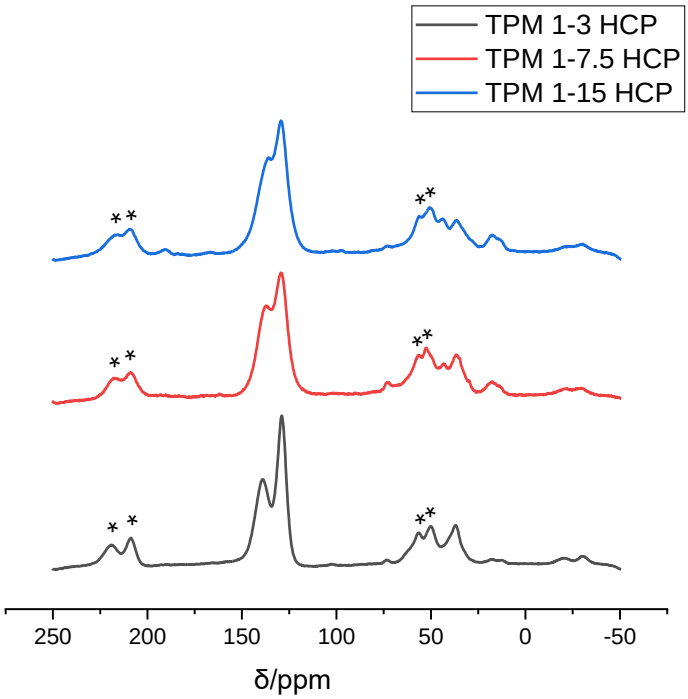

Figure 5.5.2 ^{13}C solid state NMR spectra of TPM HCPs (the asterisks denote spinning side bands)

In the ^{13}C NMR spectra of TPM HCPs, the peak at 138 ppm, 129 ppm, and 36 ppm correspond to the substituted aromatic carbon, the non-substituted aromatic carbon, and the carbon in methylene bridges, respectively.[54] The peak at 73 ppm corresponds to the carbon in the methylene group binding to oxygen atom of crosslinker residue and the peak at 17 ppm is assigned to methyl carbon at the end of crosslinker residue crosslinker residue.[22] With the increasing ratio of FDA to TPM, it can be found that the relative intensity of the peak at 138 ppm corresponding to the substituted aromatic carbon increased indicating more hydrogen atom were substituted in aromatic rings which is in consistency with FTIR results. The peak at 43 ppm which is ascribed to different substitution positions of methylene bridges[44] appeared with increasing ratio of FDA to TPM confirms more substitution occurred in aromatic rings when the ratio of crosslinker to monomer went higher.

5.5.2.3 TGA

The thermal stability of TPM HCPs was characterized by using thermalgravimetric analysis (TGA). The TGA was conducted under a N_2 atmosphere and the samples were heated from 25 °C to 800 with a heating rate 10 °C/min.

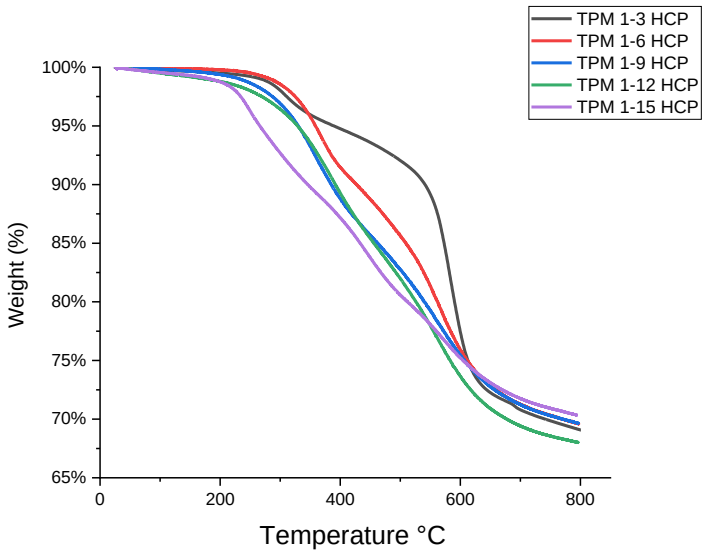

Figure 5.5.3 TGA curves of TPM HCPs

In the figure 5.5.3, the TPM HCPs showed good thermal stability. The weight residue of the TPM HCPs is higher than 90% at 350 °C. The onset temperature of the TPM 1-15 HCPs is obviously lower than other samples, the TPM 1-9 and 1-12 HCP showed a lower onset temperature than the TPM 1-3 and 1-6 HCP. So, the onset temperature of the TPM HCPs gradually decreased with the increasing ratio of FDA to TPM. The decrease in onset temperature can be attributed to higher content of incompletely reacted crosslinker residues. At 800 ℃, the weight residue of TPM 1-3, 1-6, 1-9, 1-12 and 1-15 HCP is 69%, 70%, 70%, 68% and 71%, respectively.

5.5.2.4 N_2 Sorption

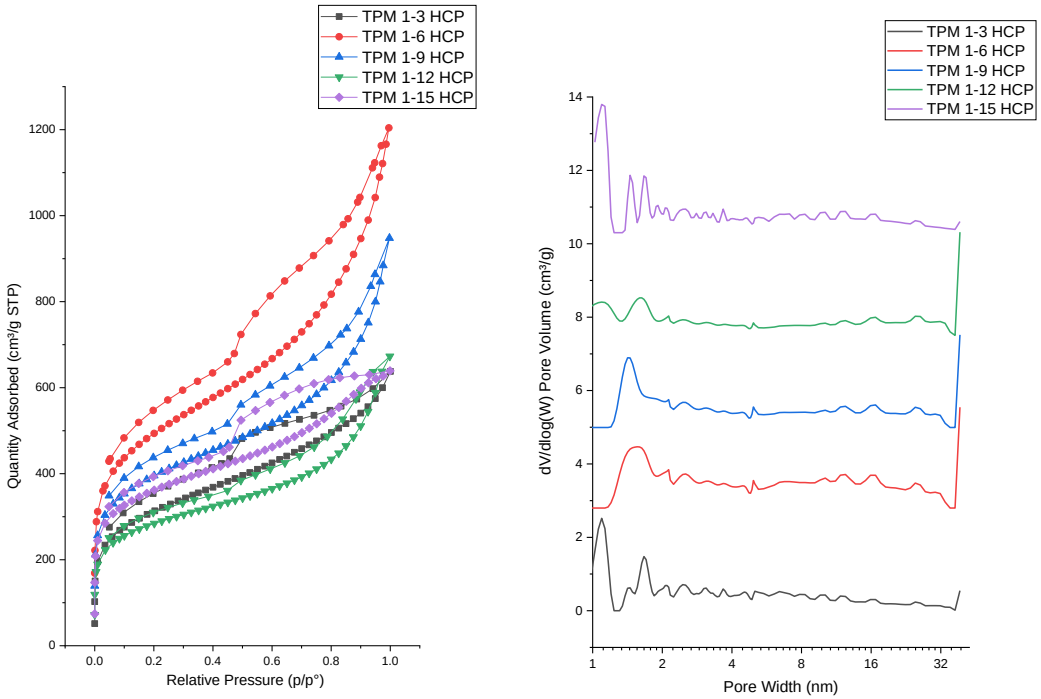

Figure 5.5.4 Isotherm and pore size distribution of TPM HCPs

The porous structures of TPM HCPs were characterized by N_2 adsorption/desorption analysis at 77 K. In the figure 5.5.4, it can be found that the TPM HCPs showed the combined Type II and Type IV isotherms according to definition of IUPAC. The sharp rise can be seen in low relative pressure range of $P/P_0<0.001$ indicating the existence of microporous structure. The hysteresis loop in the relative pressure 0.45-1.0 suggesting the mesoporous structure in these samples. The rise of the isotherm curves in the relative pressure range of 0.9-1.0 demonstrating the macropores in the TPM HCP samples. In the pore size distribution of TPM HCPs, the main peaks of these samples are located in the range of 1-2 nm, illustrating the extensive microporous structures of TPM HCPs.

The single point adsorption total pore volumes of TPM HCPs obtained at $p/p_0=0.99$ and the BET surface areas of them are shown in the table 5.5.2.

	BET surface area (m^2/g)	Single point adsorption total pore volume at p/p_0=0.99 (cm^3/g)
TPM 1-3 HCP	1134.3	0.98
TPM 1-6 HCP	1783.5	1.86
TPM 1-7.5 HCP	1219.1	0.81
TPM 1-9 HCP	1443.9	1.47
TPM 1-12 HCP	1039.4	1.04
TPM 1-15 HCP	1325.8	0.99

Table 5.5.2 BET surface area and single point adsorption total pore volume of TPM HCPs

The BET surface areas of TPM 1-3 HCP, TPM 1-6 HCP, TPM 1-9 HCP, TPM 1-12 HCP, and TPM 1-15 HCP are found to be 1134.3, 1783.5, 1443.9, 1039.4 and 1325.8 m^2/g, respectively. The single point adsorption total pore volumes of the samples are 0.98, 1.86, 1.47, 1.04 and 0.99 cm^3/g, respectively. The BET surface area and single point adsorption total pore volume of TPM 1-7.5 HCP are 1219.1 m^2/g and 0.81 cm^3/g, respectively. It can be seen that all TPM HCPs have a high BET surface area, the TPM 1-6 HCP has the highest BET surface of 1783.5 m^2/g and the TPM 1-12 HCP has the lowest BET surface area, 1039.4 m^2/g. The TPM 1-6 HCP also has the highest total pore volume as well, 1.86 cm^3/g, followed by the TPM 1-9 HCP with a total pore volume of 1.47 cm^3/g. Most of the other samples have a total pore volume close to 1 cm^3/g. To further investigate the porous structures of the TPM HCPs, the pore volumes of the pores with different pore widths are shown in the table 5.5.3 and pore volume proportions of TPM HCPs are displayed in the figure 5.5.5. The pore volumes of the pores with pore widths less than 2 nm are obtained at relative pressure p/p_0=0.2 and the pore volumes of the pores with pore widths less than 10 nm are obtained at p/p_0=0.8.

Material	Pore volume of the pores with pore width less than 2 nm (cm^3/g)	Pore volume of the pores with pore width 2-10 nm (cm^3/g)	Pore volume of the pores with pore width larger than 10 nm (cm^3/g)
TPM 1-3 HCP	0.49	0.28	0.21
TPM 1-6 HCP	0.76	0.50	0.60
TPM 1-7.5 HCP	0.52	0.23	0.06
TPM 1-9 HCP	0.61	0.35	0.51
TPM 1-12 HCP	0.44	0.23	0.37
TPM 1-15 HCP	0.56	0.28	0.15

Table 5.5.3 The pore volumes of the pores with different pore widths of TPM HCPs

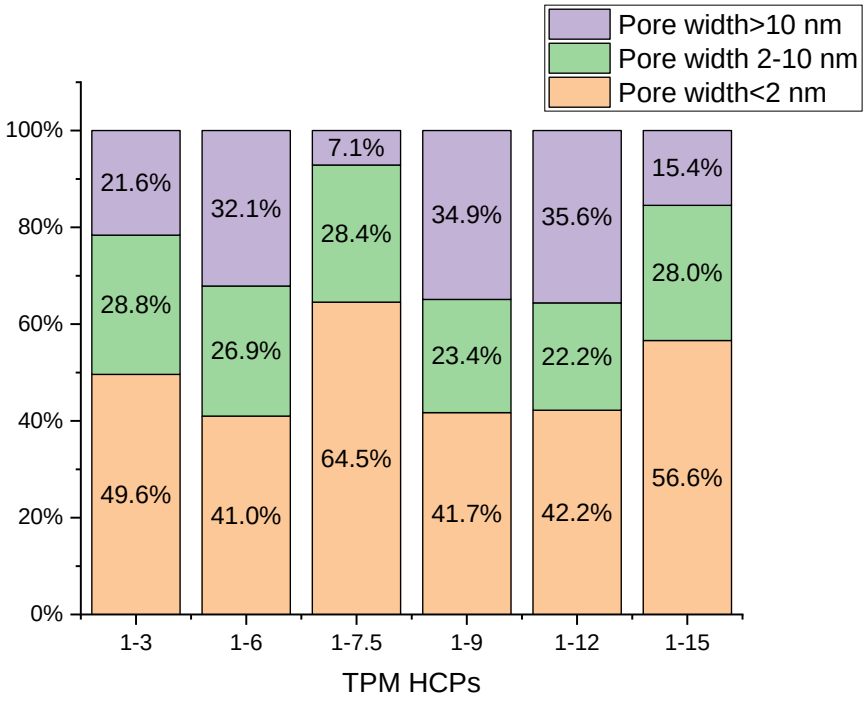

Figure 5.5.5 Pore volume proportions of pores with different pore widths of TPM HCPs

The micropore volume proportions of TPM 1-3, 1-6, 1-9, 1-12 and 1-15 HCP are 49.6%, 41.0%, 41.7%, 42.2% and 56.6%, and the micropore volumes of them are 0.49, 0.76, 0.61, 0.44 and 0.56 cm^3/g, respectively. The volume proportions of pores with pore width 2-10 nm in TPM 1-3, 1-6, 1-9, 1-12 and 1-15 HCP are 28.8%, 26.9%, 23.4%,

22.2% and 28.0%, and the pore volumes of them are 0.28, 0.50, 0.35, 0.23 and 0.28 cm^3/g respectively. For the pores with pore width larger than 10 nm, the pore volume proportions in TPM 1-3, 1-6, 1-9, 1-12 and 1-15 HCP are 21.6%, 32.1%, 34.9%, 35.6% and 15.4%, the pore volumes of the pores with pore width larger than 10 nm are 0.21, 0.60, 0.51, 0.37 and 0.15 cm^3/g, respectively. TPM 1-6 HCP has the highest micropore volume and the pore volume of pores with diameter 2-10 nm among all the TPM HCP samples. From the pore volume proportions of TPM HCPs, it can be seen the volume proportion of micropores in each sample is no lower than 40%. The volume proportions of the pores with pore diameter 2-10 nm of the TPM HCPs show slight fluctuation, the proportion fluctuates between 22.2% to 28.8%. The TPM 1-6, 1-9, and 1-12 HCP have higher volume proportion of the pores with diameter larger than 10 nm, 32.1%, 34.9%, and 35.6% respectively. The volume proportion of micropores, pores with diameter 2-10 nm and pores with diameter larger than 10 nm of TPM 1-7.5 HCP are 64.5%, 28.4% and 7.1%, the pore volumes of these pores are 0.52, 0.23 and 0.06 cm^3/g, respectively. Therefore, the TPM 1-7.5 HCP has the highest micropore pore volume proportion, and the volume proportion of the pores with pore widths less than 10 nm in the TPM 1-7.5 HCP is as high as 92.9%. In addition, although TPM 1-9 and 1-12 HCP have different BET surface area and total pore volume, they have similar pore volume composition.

5.5.2.5 Cyclic Voltammetry

The electrochemical properties of TPM HCPs were evaluated by a typical three-electrode system with 1 M Na_2SO_4 aqueous solution as electrolyte. The active material on nickel foam, a platinum electrode and an Ag/AgCl electrode (3 M KCl, 0.207 V vs. standard hydrogen electrode at 25 °C) were used as working electrode, counter electrode and reference electrode, respectively. The CV tests were conducted with different scan rates 2, 10, 25, 50, 75, 100 and 200 mV/s in the voltage range of -0.2 V-0.8 V.

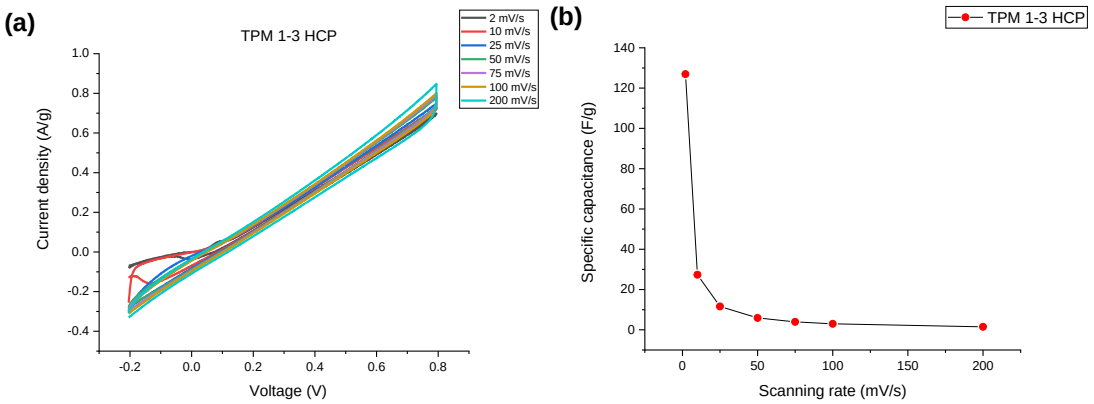

Figure 5.5.6 (a) CV curves at different scanning rates, and (b) Specific capacitance obtained at different scanning rates of TPM 1-3 HCP

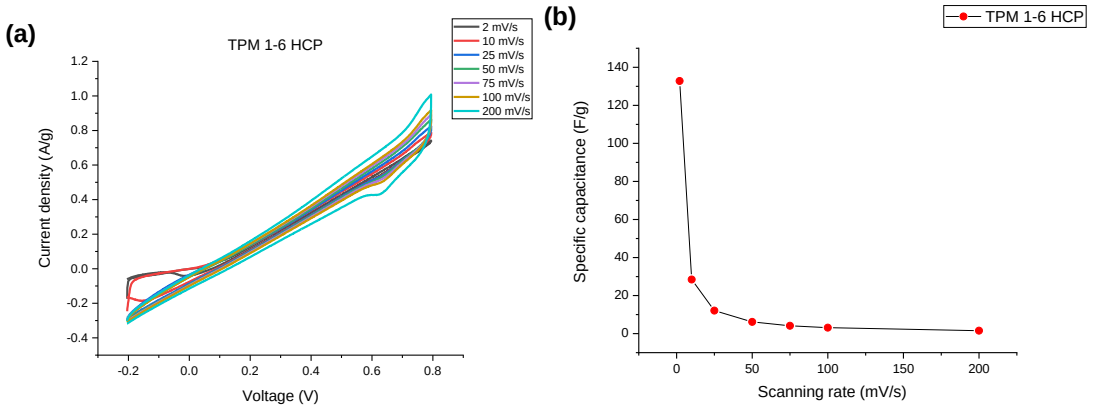

Figure 5.5.7 (a) CV curves at different scanning rates, and (b) Specific capacitance obtained at different scanning rates of TPM 1-6 HCP

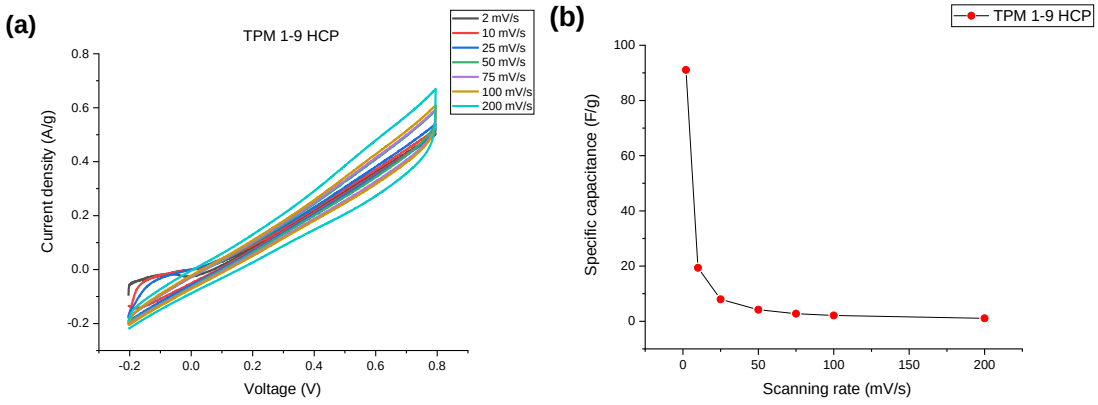

Figure 5.5.8 (a) CV curves at different scanning rates, and (b) Specific capacitance obtained at different scanning rates of TPM 1-9 HCP

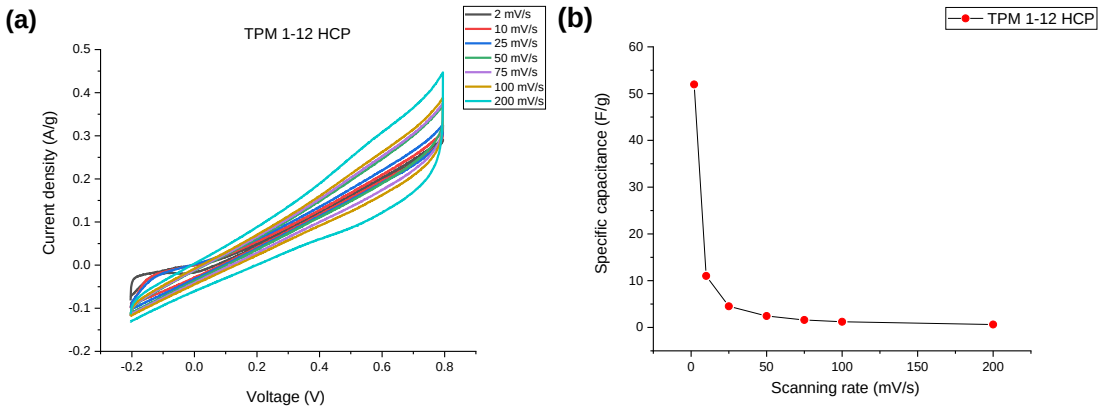

Figure 5.5.9 (a) CV curves at different scanning rates, and (b) Specific capacitance obtained at different scanning rates of TPM 1-12 HCP

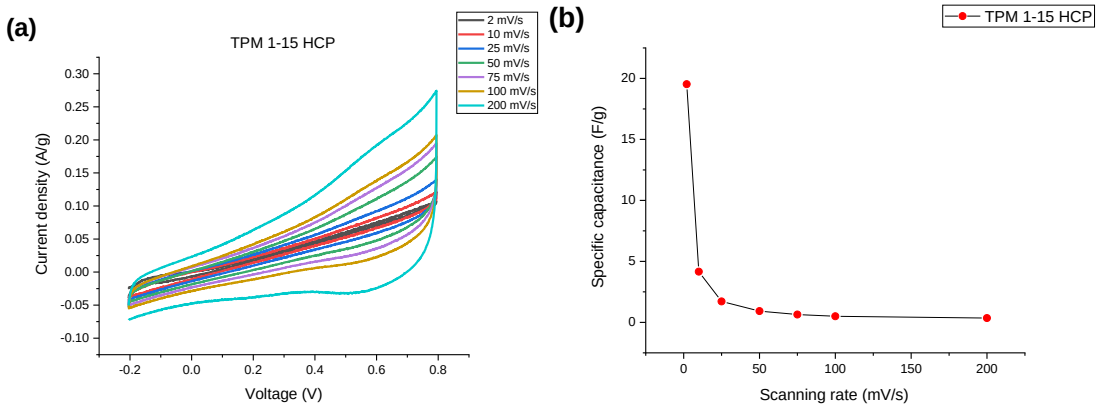

Figure 5.5.10 (a) CV curves at different scanning rates, and (b) Specific capacitance obtained at different scanning rates of TPM 1-15 HCP

	Specific capacitance obtained at different scanning rates (F/g)							
Scanning rates (mV/s) / Material	2	10	25	50	75	100	200	Retention of capacitance at 200 mV/s
TPM 1-3 HCP	126.9	27.3	11.6	5.9	4.0	3.0	1.5	1.2%
TPM 1-6 HCP	132.8	28.5	12.1	6.1	4.1	3.1	1.6	1.2%
TPM 1-7.5 HCP	92.7	19.6	8.0	4.2	2.8	2.1	1.1	1.2%
TPM 1-9 HCP	91.1	19.4	8.0	4.2	2.8	2.1	1.1	1.2%
TPM 1-12 HCP	52.0	11.0	4.5	2.5	1.6	1.2	0.6	1.2%

TPM 1-15 HCP	19.5	4.2	1.7	0.9	0.6	0.5	0.4	2.0%

Table 5.5.4 Specific capacitance of TPM HCPs obtained at different scanning rates

The specific capacitance at 2 mV/s of TPM 1-3, 1-6, 1-9, 1-12 and 1-15 HCP is 126.9, 132.8, 91.1, 52.0 and 19.5 F/g, and the capacitance retention from 2 mV/s to 200 mV/s of them is 1.2%, 1.2%, 1.2%, 1.2% and 2.0%, respectively. Overall, the TPM HCPs show higher specific capacitances than others. The TPM 1-6 HCP has the highest specific capacitance among all the TPM HCPs (including TPM 1-7.5 HCP), it also has the highest BET surface area (1783.5 m^2/g), total pore volume (1.86 cm^3/g), micropore volume (0.76 cm^3/g) and the pore volume of the pores with diameter 2-10 nm (0.50 cm^3/g) among all the TPM HCPs. The TPM 1-3 HCP has higher specific capacitance than the TPM 1-9 HCP, while the BET surface area (1443.9 m^2/g), total pore volume (1.47 cm^3/g), micropore volume (0.61 cm^3/g) and the pore volume of the pores with diameter 2-10 nm (0.35 cm^3/g) of the TPM 1-9 HCP are higher than those of the TPM 1-3 HCP (1134.3 m^2/g, 0.98 cm^3/g, 0.49 cm^3/g and 0.28 cm^3/g, respectively). The TPM 1-12 HCP showed a lower specific capacitance than the TPM 1-9 HCP, and the BET surface area (1039.4 m^2/g), total pore volume (1.04 cm^3/g), micropore volume (0.44 cm^3/g) and the pore volume of the pores with diameter 2-10 nm (0.23 cm^3/g) of the TPM 1-12 HCP are lower than those of the TPM 1-9 HCP as well. From the TPM 1-12 HCP to TPM 1-15 HCP, the specific capacitance decreased, and the TPM 1-15 HCP has the lowest capacitance among all the TPM HCPs (including TPM 1-7.5 HCP). The BET surface area of the TPM 1-15 HCP (1325.8 m^2/g) is higher than that of the TPM 1-12 HCP, but the total pore volume of the TPM 1-15 HCP (0.99 cm^3/g) is lower than that of the TPM 1-12 HCP. The TPM 1-15 HCP also has higher micropore volume (0.56 cm^3/g) and the pore volume of the pores with diameter 2-10 nm (0.28 cm^3/g) than the TPM 1-12 HCP. The specific capacitance at 2 mV/s of the TPM 1-7.5 HCP is 92.7 F/g much higher than that of the TPM 1-15 HCP, while it can be found that the and the BET surface area (1219.1 m^2/g), total pore volume (0.81 cm^3/g), micropore volume (0.52 cm^3/g) and the pore volume of the pores with diameter 2-10 nm (0.23 cm^3/g) of the

TPM 1-7.5 HCP are lower than those of the TPM 1-15 HCP. As the TPM 1-7.5 HCP has the similar specific capacitance with the TPM 1-9 HCP, but it can be seen that the BET surface area, total pore volume, micropore volume and the pore volume of the pores with diameter 2-10 nm of the TPM 1-7.5 HCP are lower than those of the TPM 1-9 HCP. From the pore volume proportions of the TPM HCPs, it can be found that the pore volume compositions of the TPM 1-9 HCP is different from that of the TPM 1-7.5 HCP. The TPM HCPs synthesized from different ratio of FDA to monomer have different pore structures, as well as different capacitances. However, the variation in the capacitances of the TPM HCPs is independent with the variations in the porosity of them can be found.

The relationship between the response current and scanning rate is employed to provide the insight into the energy storage kinetics of TPM HCPs, the results are shown in the figure 5.5.11.

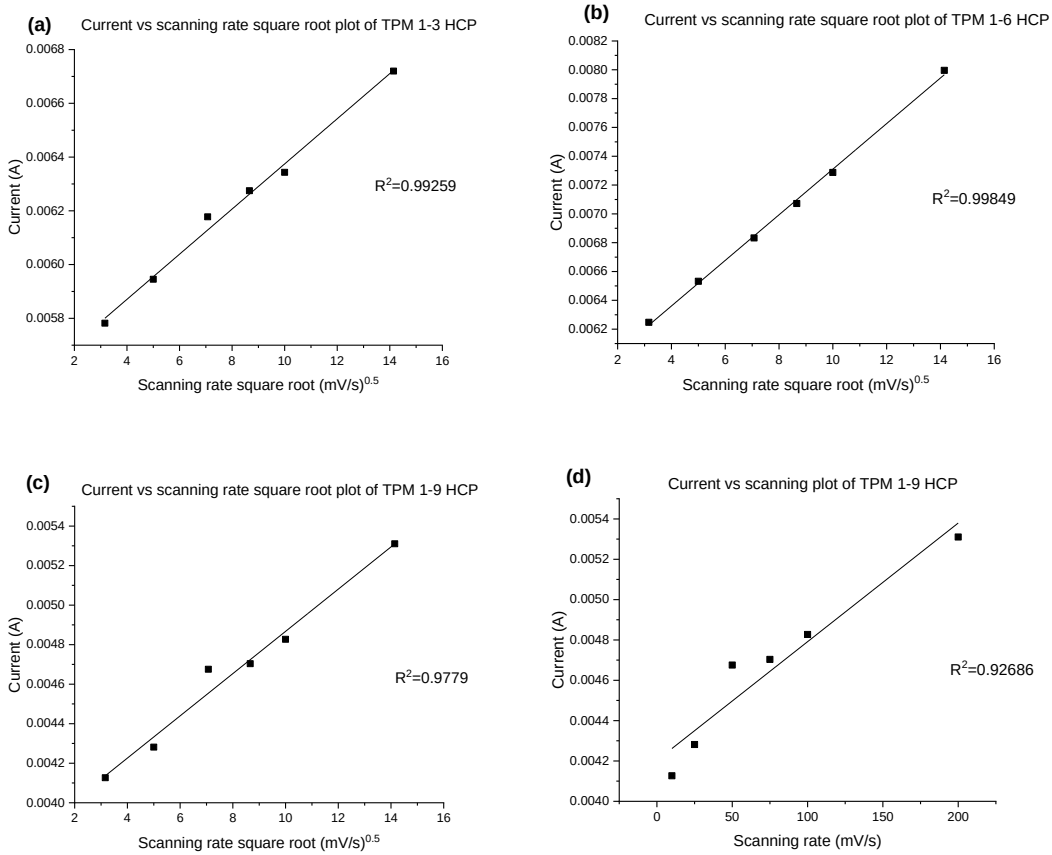

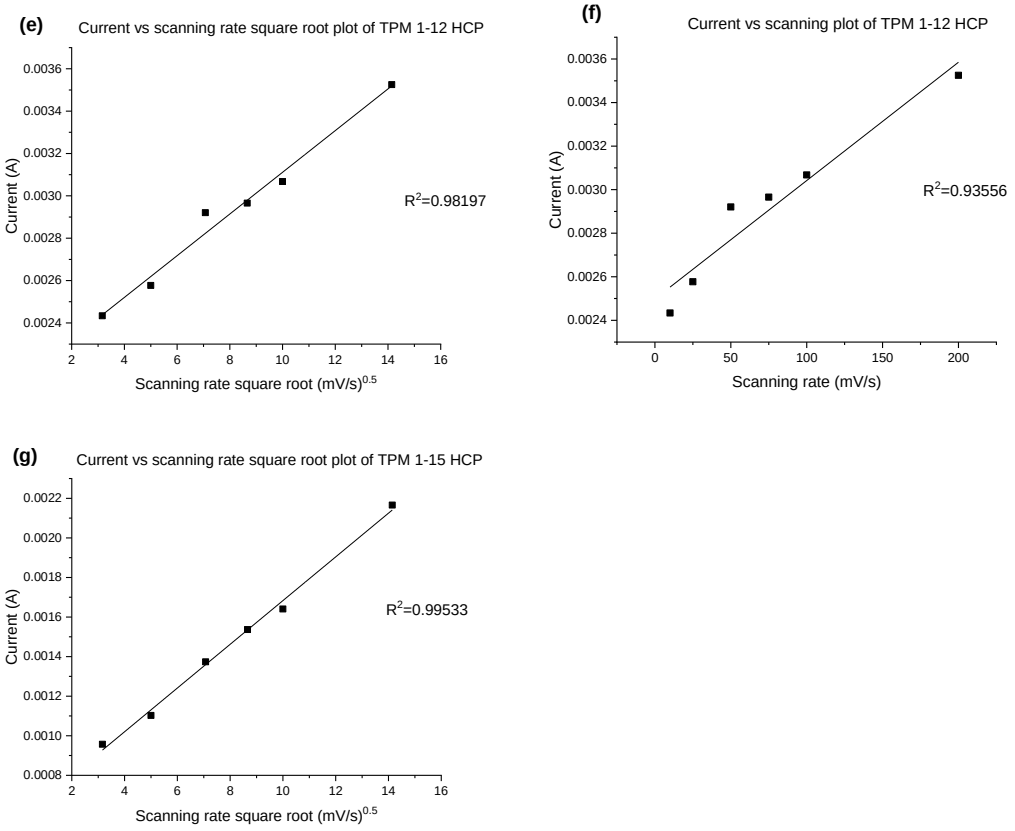

Figure 5.5.11 The relationship between response current and scanning rate of TPM HCPs. (a). and (b). current vs scanning rate square root plot of TPM 1-3 and 1-6 HCP. (c). current vs scanning rate square root plot and (d). current vs scanning rate plot of TPM 1-9 HCP. (e). current vs scanning rate square root plot and (f). current vs scanning rate plot of TPM 1-12 HCP. (g) current vs scanning rate square root plot of TPM 1-15 HCP.

From the figure 5.5.11, it can be seen the coefficient of determination R^2 of the response current vs scanning rate square root plot of TPM 1-3, 1-6 and 1-15 HCP is 0.99259, 0.99849 and 0.99533 respectively, indicating the good linear relationship between the response current and scanning rate square root. Therefore, the capacity kinetics of these samples are dominated by the diffusion-controlled process. Because coefficient of determination of the response current vs scanning rate square root plot of TPM 1-9 HCP and TPM 1-12 HCP is 0.97790 and 0.98179, respectively, lower than that of others, the response current vs scanning rate plot of these two samples are presented for comparing. It can be seen that the R^2 of the response current vs scanning rate plot of TPM 1-9 HCP and TPM 1-12 HCP is 0.92686 and 0.93556, respectively, suggesting the linear

relationship between response current and scanning rate of TPM 1-9 and 1-12 HCP is not good. Moreover, only one point shows obvious deviation from the linear fitting results, therefore, the capacity kinetics of these samples are dominated by the diffusion-controlled process as well, corresponding to the low capacitance retention rate of these samples.

5.5.2.6 Electrochemical impedance spectroscopy (EIS)

To further investigate the electrochemical performance of TPM HCPs, electrochemical impedance spectroscopy (EIS) was carried out with amplitude of 10 mV and frequency range 100 k Hz to 0.01 Hz. The Nyquist and Bode plots of TPM HCPs are shown in the figures 5.5.12 to 5.5.16.

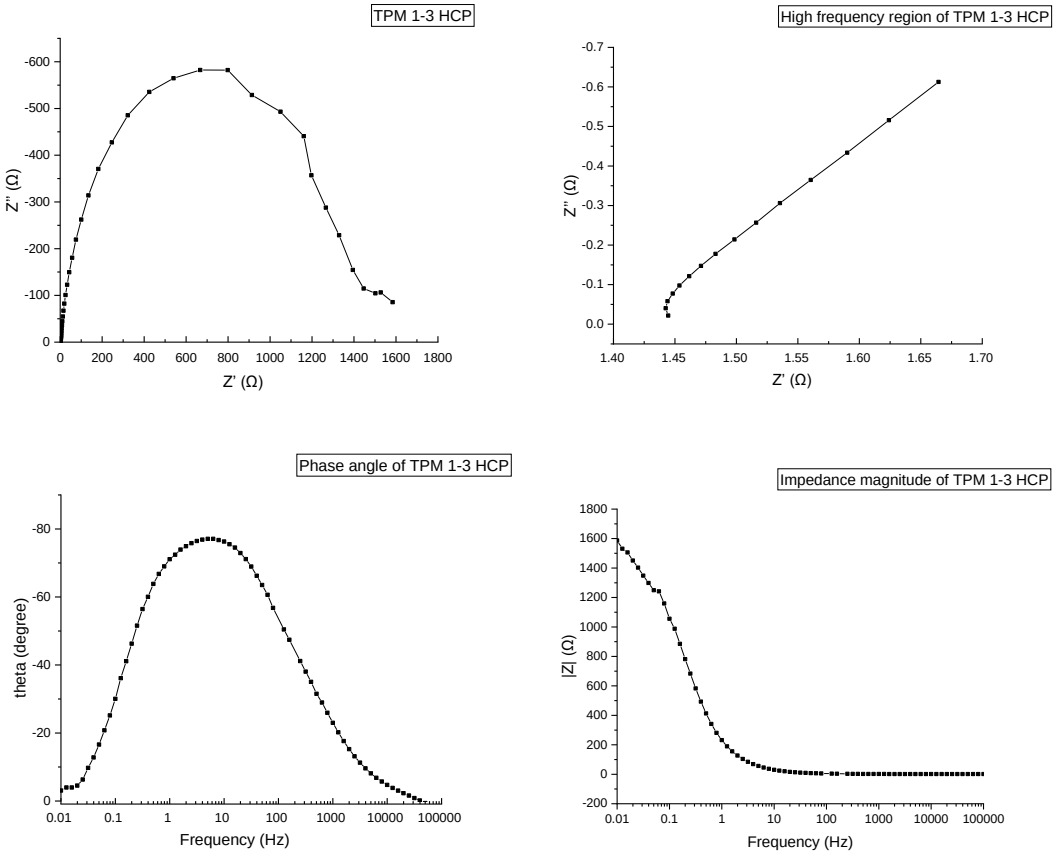

Figure 5.5.12 Nyquist plot and Bode plot of TPM 1-3 HCP

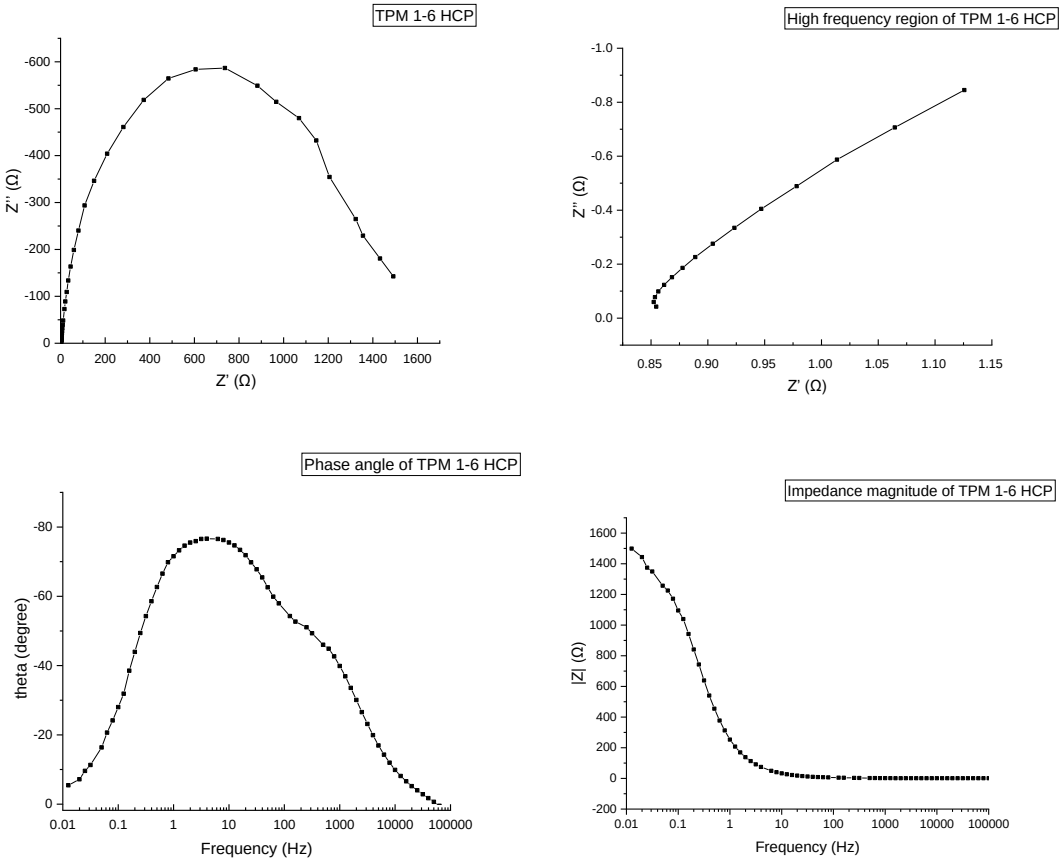

Figure 5.5.13 Nyquist plot and Bode plot of TPM 1-6 HCP

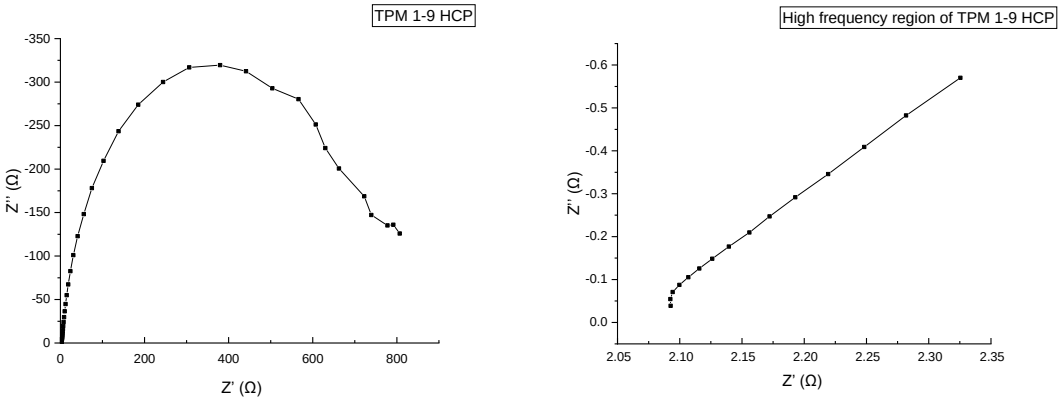

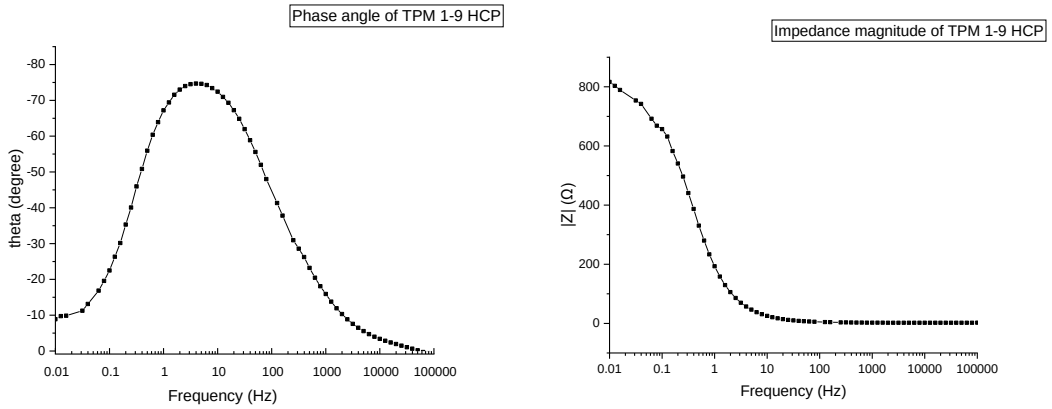

Figure 5.5.14 Nyquist plot and Bode plot of TPM 1-9 HCP

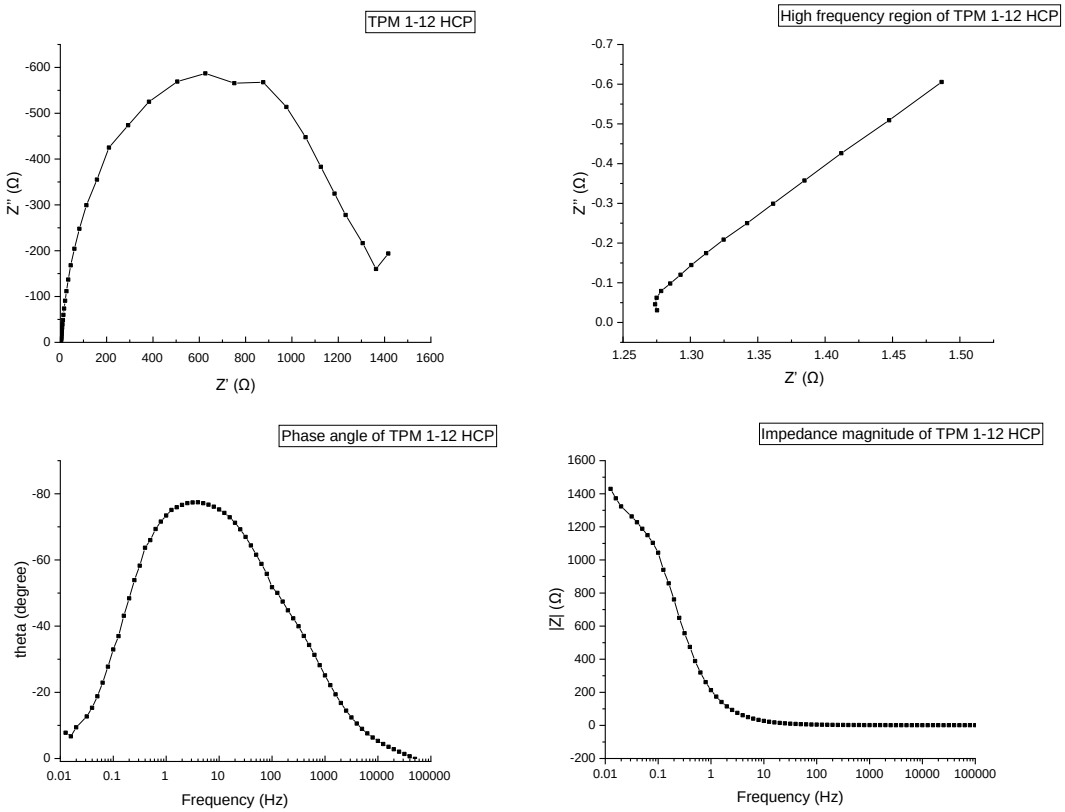

Figure 5.5.15 Nyquist plot and Bode plot of TPM 1-12 HCP

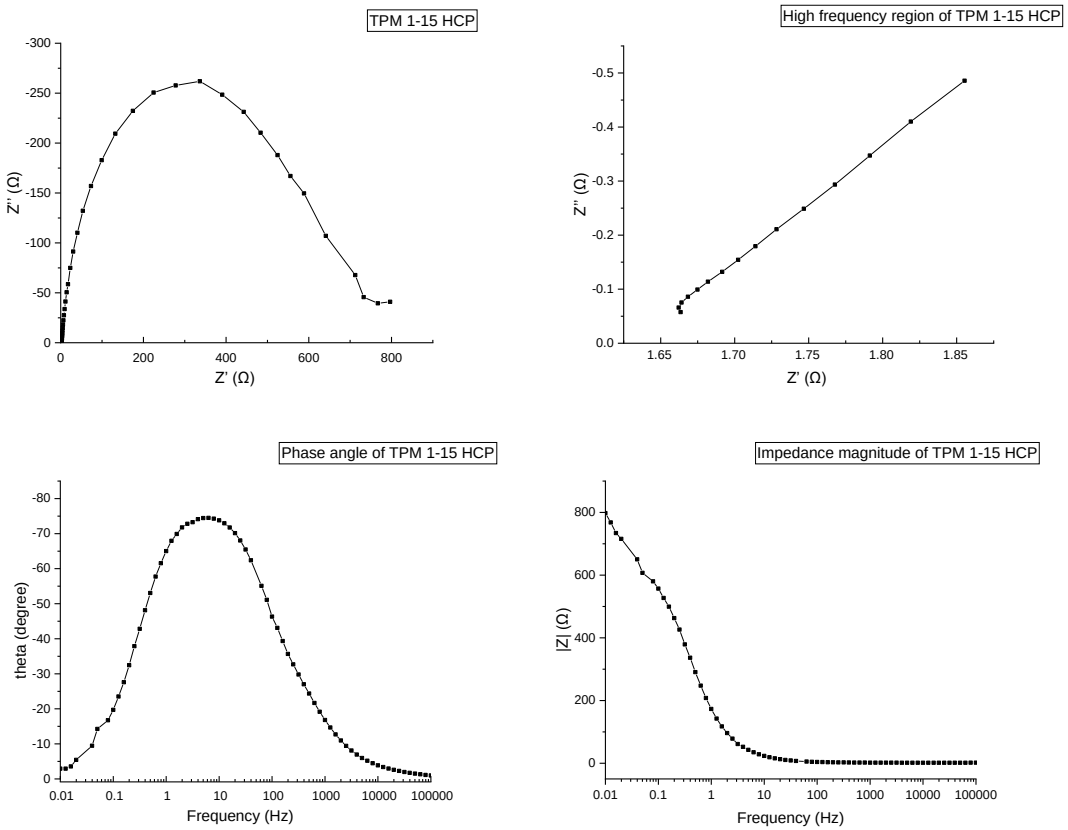

Figure 5.5.16 Nyquist plot and Bode plot of TPM 1-15 HCP

	Whether the semicircle can be observed at high frequencies?	Whether the Nyquist plot is vertical or near vertical to Z" axis at low frequencies?	The phase angle value of the curve apex	Phase angle at 0.01 Hz	Impedance magnitude at 0.01 Hz (Ω)
TPM 1-3 HCP	No	No	-77°	-2°	1586
TPM 1-6 HCP	No	No	-76°	-5°	1499
TPM 1-9 HCP	No	No	-75°	-10°	817
TPM 1-12 HCP	No	No	-77°	-10°	1429
TPM 1-15 HCP	No	No	-74°	-10°	797

Table 5.5.5 The results from Nyquist and Bode plot of TPM HCPs

The absence of the sharp rising ‘tail’ in the intermediate and low frequency region that parallels to the Z” axis can be found in the Nyquist plot of TPM HCPs illustrating the TPM HCPs do not show supercapacitor behaviour. The highest points of the phase angle curves of TPM HCPs vary from -77° to -74°, showing the TPM HCP did not show the behaviour like a pure capacitor. With the decreasing frequency, the phase angle curves of TPM HCPs decreased to the phase angle close to 0° from the highest point suggesting the TPM HCPs tend to behave like resistors at low frequencies owing to their poor conductivity. It can be seen that the phase angles of TPM HCPs at 0.01 Hz did not decrease to 0°, indicating the TPM HCPs still showed some capacitance at low frequencies. The large impedance magnitude value of the TPM HCPs can be found at 0.01 Hz. It can be found that the ohmic resistance occupies a quite large proportion in the impedance based on the shape of Nyquist plot of TPB HCPs and the calculation formula of impedance magnitude, or based on their quasi resistor-behaviour at low frequencies which can be seen from the phase angle curves. The absence of the semi-circle in the high frequency region can be attributed to the ohmic contact between the current collector and the active materials.

In order to show the poor conductivity of TPM HCPs more directly, the fitting results are shown in the figure 5.5.17 and table 5.5.6. The Randles circuit model is used as the equivalent circuit for the impedance fitting.

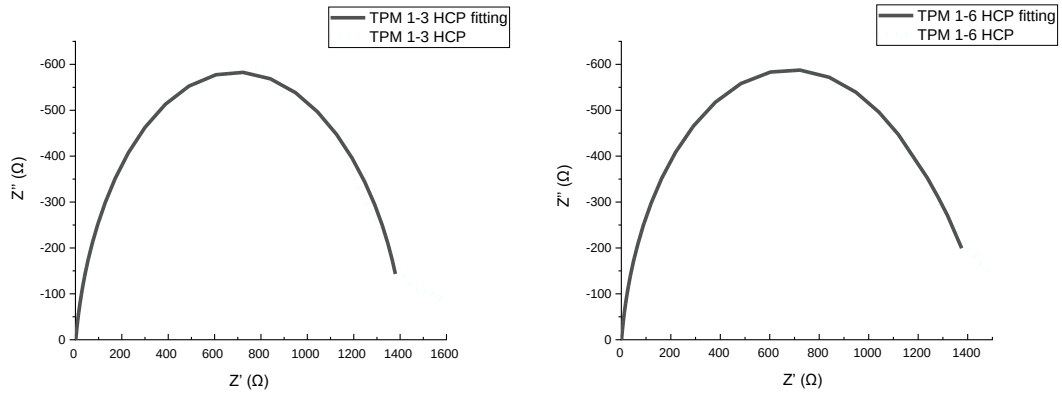

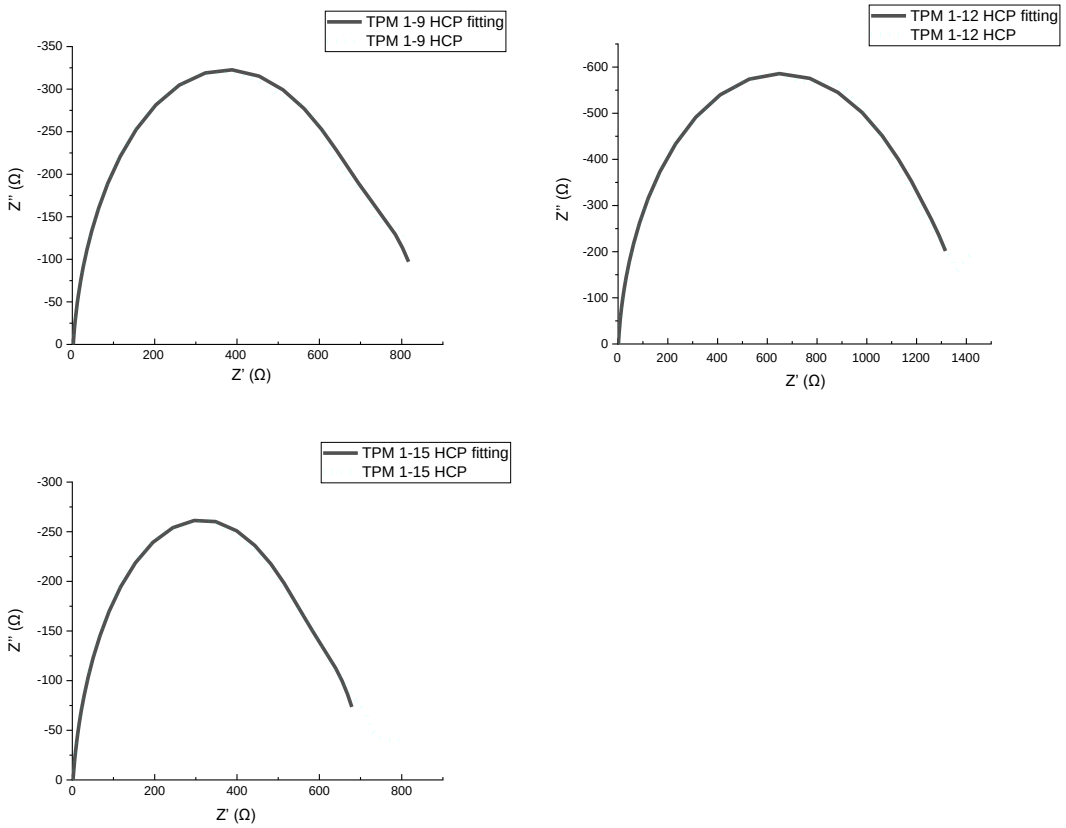

Figure 5.5.17 The impedance fitting curves of TPM HCPs

In the fitting curves of TPM HCPs, the deviations can be found in the low frequency region as the poor conductivity and the disordered porous structure of TPM HCPs made the diffusion is hard to be precisely predicted.

	R1 (Ω)	CPE1-T (F)	CPE1-P	R2 (Ω)	Ws1-R (Ω)	Ws1-T (s)	Ws1-P
TPM 1-3 HCP	1.549	0.00083486	0.89517	1357.3	61.2	9.2	0.5
TPM 1-6 HCP	0.894	0.00083429	0.90804	1337.4	114.8	19.1	0.5
TPM 1-9 HCP	2.245	0.0010133	0.91697	713.1	139.2	19.3	0.5
TPM 1-12 HCP	1.372	0.00094601	0.93852	1267.3	127.1	21.9	0.5
TPM 1-15 HCP	1.784	0.0011084	0.89807	597.1	107.3	17.1	0.5

Table 5.5.6 The impedance fitting results of TPM HCPs

From the table 5.5.6, it can be found that the high values of R2, suggesting the high internal resistance of TPM HCPs. The variation in the R2 values of TPM HCPs

demonstrates the impacts of different amount of crosslinkers used in the synthesis of TPM HCPs.

To gain further insight into the electrochemical performance of TPM HCPs with alternating current is applied, the complex capacitance of TPM HCP is performed. The definition of complex capacitance and the definitions of its components were given by equation 5.2.2.6.1, 5.2.2.6.2 and 5.2.2.6.3. The complex capacitance curves of TPM HCP are shown in the figure 5.5.18.

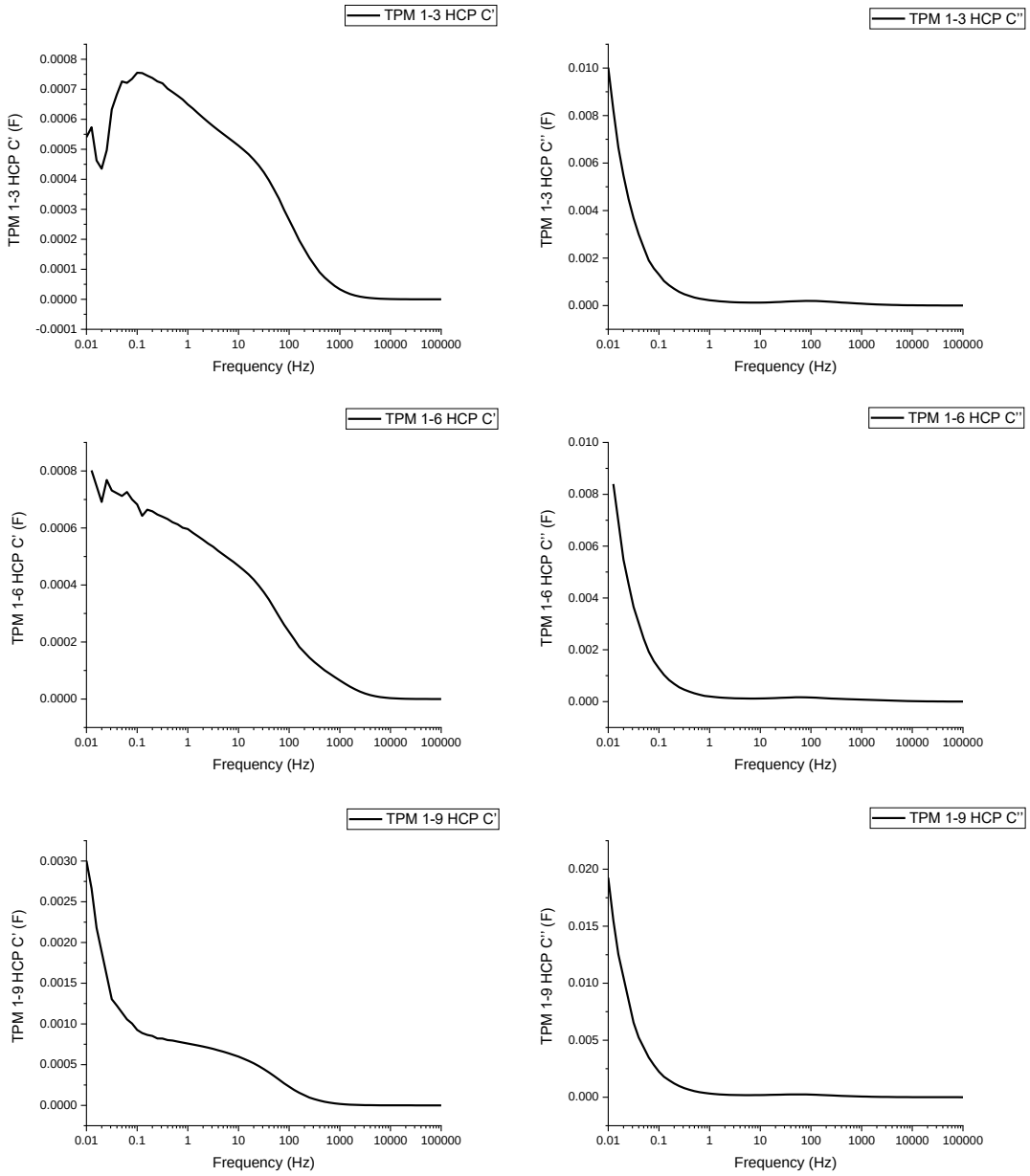

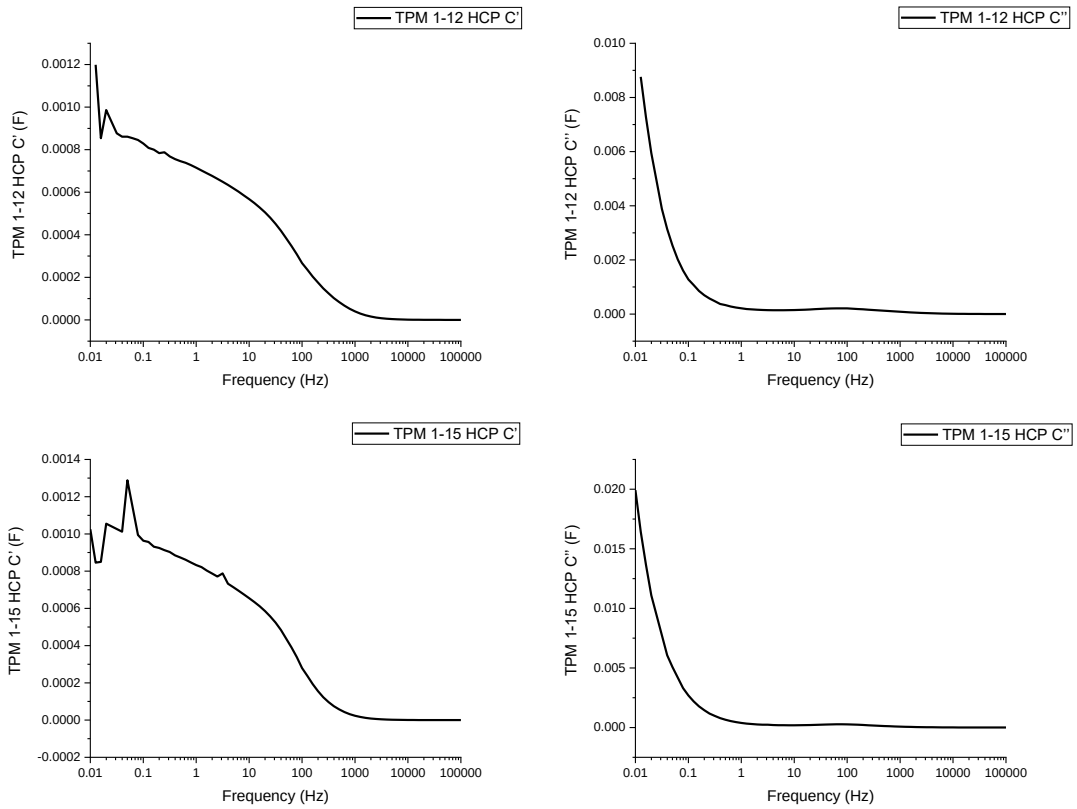

Figure 5.5.18 The complex capacitance of TPM HCPs

The real part of the complex capacitance C' shows the capacitance variation with the decreasing frequency. It can be seen that the C' curves of the TPM HCPs showed the same variation trend with a common supercapacitor in the high and intermediate frequency region, while some significant fluctuations can be seen at low frequencies, suggesting the unstable utilization rate of the porous structures of TPM HCP caused by the poor conductivity. This corresponds to the independent relationship between the specific capacitances obtained from CV results and the porosity of TPM HCPs. As discussed in previous parts, the very poor capacitance at very low frequencies in the real part of the complex capacitance is also due to the high internal resistance of uncarbonized HCPs.

The imaginary part of the complex C'' corresponds to energy dissipation. With the decreasing frequency, the weak peak corresponding to phase angle -45° appeared then the C'' curves began to increase sharply and reached the maximum at 0.01 Hz, demonstrating the increased energy dissipation in the low frequency region caused by poor conductivity of TPM HCPs. This corresponds to the decreasing in the phase angle

curves at low frequencies. The frequency at which the C" reaches the maximum can be used to define the relaxation time to evaluate the rate performance of the materials. The definition of the relaxation time was given by 5.2.2.6.4. The relaxation time τ_0 of the TPM HCPs is 100 s, suggesting the poor rate performance of TPM HCPs. This corresponds to the results from the CV tests.

5.6 Triphenylbenzene (TPB) HCPs

5.6.1 Synthesis of TPB HCPs

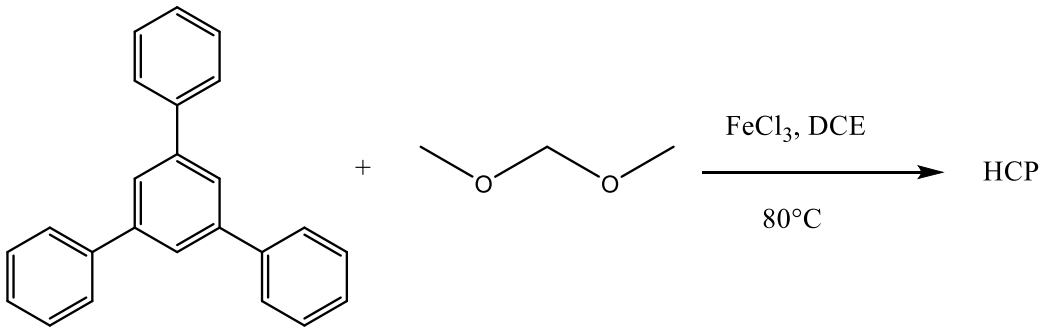

The synthesis of triphenylbenzene (TPB) HCP was performed as follows. 1,3,5-triphenylbenzene (5 mmol, 1 eq.) and ferric chloride (15-75 mmol, 3-15 eq.) were added into a dried two-neck flask with a magnetic stirrer and a condenser. DCE (25 mL) was charged by a syringe into the flask with stirring for 5 minutes to disperse the materials. Then, formaldehyde dimethyl acetal (FDA) (15-75 mmol, 3-15 eq.) was injected into the flask by a syringe and the temperature was increased to 80 ℃. The reaction was left for over 20 hours. The reaction was conducted in atmospheric air. The HCP product was cooled and collected by vacuum filtration and washed with water, methanol, acetone. Then the product was transferred to a Soxhlet extractor and washed with methanol overnight. The product was dried under vacuum at 80 ℃ overnight.

TPB 1-3 HCP: 1,3,5-triphenylbenzene (5 mmol, 1.53 g, 1 eq.), FDA (15 mmol, 1.34 mL, 3 eq.), ferric chloride (15 mmol, 2.45 g, 3 eq.). Yield: 1.79 g, 104.6%. Formula: $C_{24}H_{18}$. Calculated value of elemental analysis C: 94.08% H: 5.92%. Found value of elemental analysis C: 88.25% H: 4.98%

TPB 1-6 HCP: 1,3,5-triphenylbenzene (5 mmol, 1.53 g, 1 eq.), FDA (30 mmol, 2.65 mL, 6 eq.), ferric chloride (30 mmol, 4.87 g, 6 eq.). Yield: 1.99 g, 105.3%. Formula: $C_{27}H_{18}$. Calculated value of elemental analysis C: 94.70% H: 5.30%. Found value of elemental analysis C: 82.48% H: 4.54%

TPB 1-9 HCP: 1,3,5-triphenylbenzene (5 mmol, 1.53 g, 1 eq.), FDA (45 mmol, 3.98 mL, 9 eq.), ferric chloride (45 mmol, 7.30 g, 9 eq.). Yield: 1.91 g, 96.4%. Formula:

$C_{28.5}H_{18}$. Calculated value of elemental analysis C: 95.00% H: 5.00%. Found value of elemental analysis C: 82.48% H: 4.33%.

TPB 1-12 HCP: 1,3,5-triphenylbenzene (5 mmol, 1.53 g, 1 eq.), FDA (60 mmol, 5.31 mL, 12 eq.), ferric chloride (60 mmol, 9.73 g, 12 eq.). Yield: 2.00 g, 100.9%. Formula: $C_{28.5}H_{18}$. Calculated value of elemental analysis C: 95.00% H: 5.00%. Found value of elemental analysis C: 82.44% H: 4.43%

TPB 1-15 HCP: 1,3,5-triphenylbenzene (5 mmol, 1.53 g, 1 eq.), FDA (75 mmol, 6.64 mL, 15 eq.), ferric chloride (75 mmol, 12.20 g, 15 eq.). Yield: 1.97 g, 99.4%. Formula: $C_{28.5}H_{18}$. Calculated value of elemental analysis C: C: 95.00% H: 5.00%. Found value of elemental analysis C: 82.14% H: 4.20%

5.6.2 Results and discussion

5.6.2.1 Synthesis

The TPB HCPs were synthesized by Friedel-Crafts alkylation reaction with 1,3,5-triphenylbenzene used as monomer, formaldehyde dimethyl acetal (FDA) used as an external crosslinker and anhydrous $FeCl_3$ used as a Lewis acid catalyst, in air atmosphere and at 80 ℃. To investigate influence of different reactant ratios to the properties of the TPB HCPs, they were synthesized with ratios of TPB to FDA 1-3, 1-6, 1-9, 1-12 and 1-15. TPB HCP in Chapter 3 was synthesized with the ratio of TPB to FDA 1-7.5. The names of TPB HCPs are given according to monomer to crosslinker ratios, from TPB 1-3 HCP to TPB 1-15 HCP. The yields and elemental analysis results of TPB HCPs are performed in the table 5.6.1.

	Yield		Calculated value		Found value	
			C %	H %	C %	H %
TPB 1-3 HCP	104.6%	1.79 g	94.08	5.92	88.25	4.98
TPB 1-6 HCP	105.3%	1.99 g	94.70	5.30	82.48	4.54
TPB 1-7.5 HCP	101.7%	2.02 g	95.00	5.00	83.60	4.58
TPB 1-9 HCP	96.4%	1.91 g	95.00	5.00	82.48	4.33

TPB 1-12 HCP	100.9%	2.00 g	95.00	5.00	82.44	4.43
TPB 1-15 HCP	99.4%	1.97 g	95.00	5.00	82.14	4.20

Table 5.6.1 Yield and elemental analysis results of TPB HCPs

In the table 5.6.1, except for the TPB 1-9 HCP and TPB 1-15 HCP, all the TPB HCPs have a yield higher than 100%, owing to the existence of the incompletely reacted crosslinker residues, -O-CH_3. Due to some monomers and crosslinkers cannot construct large particles that can be collected by filtration under high steric hindrance, the losses of these small particles in the collecting and washing process cause the lower yield of the TPB 1-9 HCP and TPB 1-15 HCP. The differences between the calculated values and the found values of the elemental analysis are ascribed to incompletely reacted crosslinker residues in TPB HCP networks.

5.6.2.2 FTIR and ^{13}C Solid State NMR spectroscopy

The molecular structures of TPB HCPs were analyzed and confirmed by using Fourier transform infrared (FTIR) and ^{13}C solid state NMR.

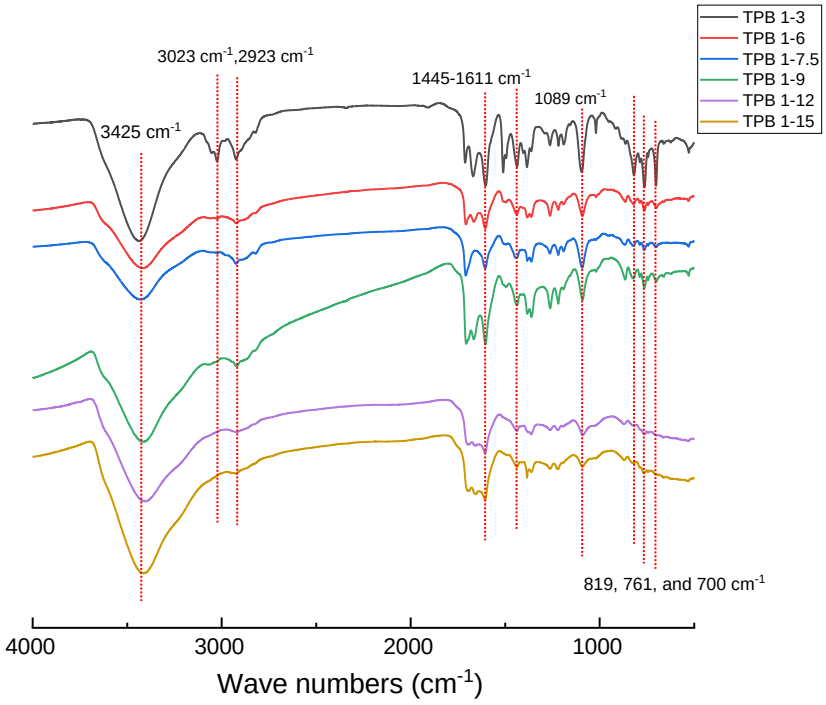

Figure 5.6.1 FTIR spectra of TPB HCPs

In the FTIR spectra of TPB HCPs, the peak at 3023 cm^{-1} and 2923 cm^{-1} can be assigned to C-H stretching in aromatic rings and methylene bridges, respectively.[55] The peaks in the range of 1445-1611 cm^{-1} can be attributed to the aromatic ring skeleton vibration.[16] The peak at 1089 cm^{-1} which is ascribed to C-O stretching could confirm the existence of incompletely reacted crosslinkers in the TPB HCP samples.[21] The peak at 3425 cm^{-1} which is assigned to O-H stretching[56] confirmed physisorbed water in the KBr disc and the porous structure of TPB HCP samples.[39] The peak at 1501 cm^{-1} together with the peak at 819 cm^{-1} corresponds to para-substituted aromatic ring.[26] The peaks at 761 cm^{-1} and 700 cm^{-1} are related with mono-substituted aromatic ring.[27]

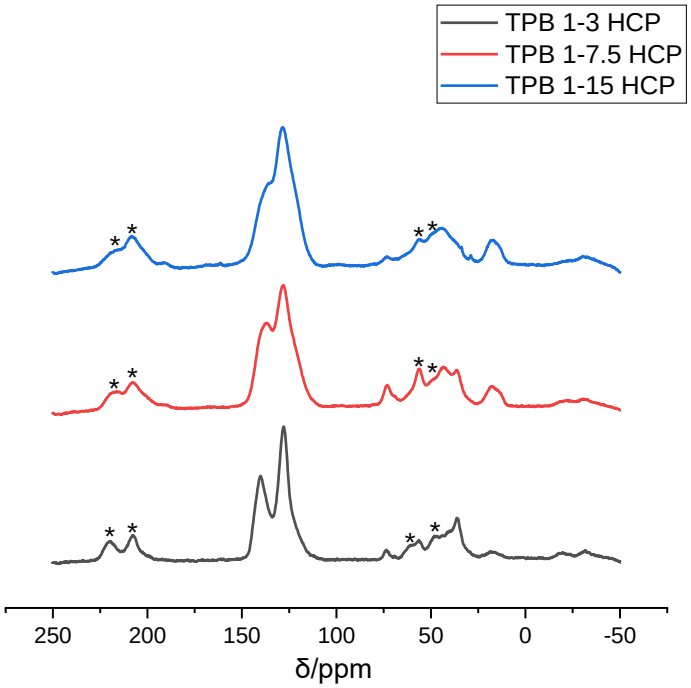

Figure 5.6.2 ^{13}C solid state NMR spectra of TPB HCPs (the asterisks denote spinning side bands)

In the ^{13}C NMR spectra of TPB HCPs, the peaks at 137 ppm and 128 ppm can be assigned to the substituted aromatic carbon and the non-substituted aromatic carbon, respectively.[57] The peak at 36 ppm corresponds to the carbon atom in methylene bridges.[58] The peak at 73 ppm and 17 ppm correspond to the carbon in the methylene group binding to oxygen atom of crosslinker residue and the methyl carbon at the end of crosslinker residue, respectively.[22] When the ratio of FDA to TPB went higher, the peak at 43 ppm which is due to carbon in methylene bridges that in different substitution

positions[44] appeared. At the ratio of FDA to TPB 15-1, a new peak at 29 ppm appeared which is also due to the different substitution positions of the methylene bridges.[59] It can be found that the gaps between the peaks at 137 ppm and 128 ppm gradually disappear with the increasing ratio of FDA to TPB, this trend is in consistency with the previous literature.[21]

5.6.2.3 TGA

The thermal stability of TPB HCPs was characterized by using thermalgravimetric analysis (TGA). The TGA was conducted under a N_2 atmosphere and the samples were heated from 25 °C to 800 with a heating rate 10 °C/min.

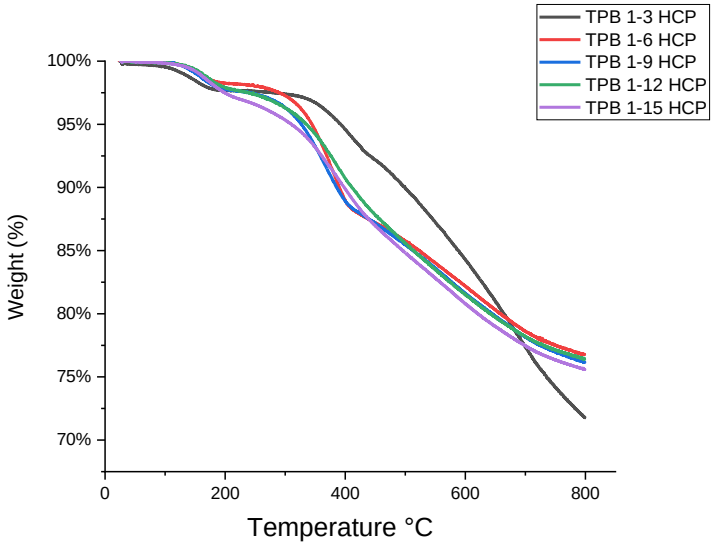

Fig 5.6.3 TGA curves of TPB HCPs

In the figure 5.6.3, the TPB HCPs showed good thermal stability. The weight residue of the TPB HCPs is higher than 90% at 350 °C. The onset temperature of the TPB 1-3 HCPs is slightly lower than other samples. At 800 °C, the weight residue of TPB 1-3 is 72%, and the weight residue of other samples is around 76%

5.6.2.4 N_2 Sorption

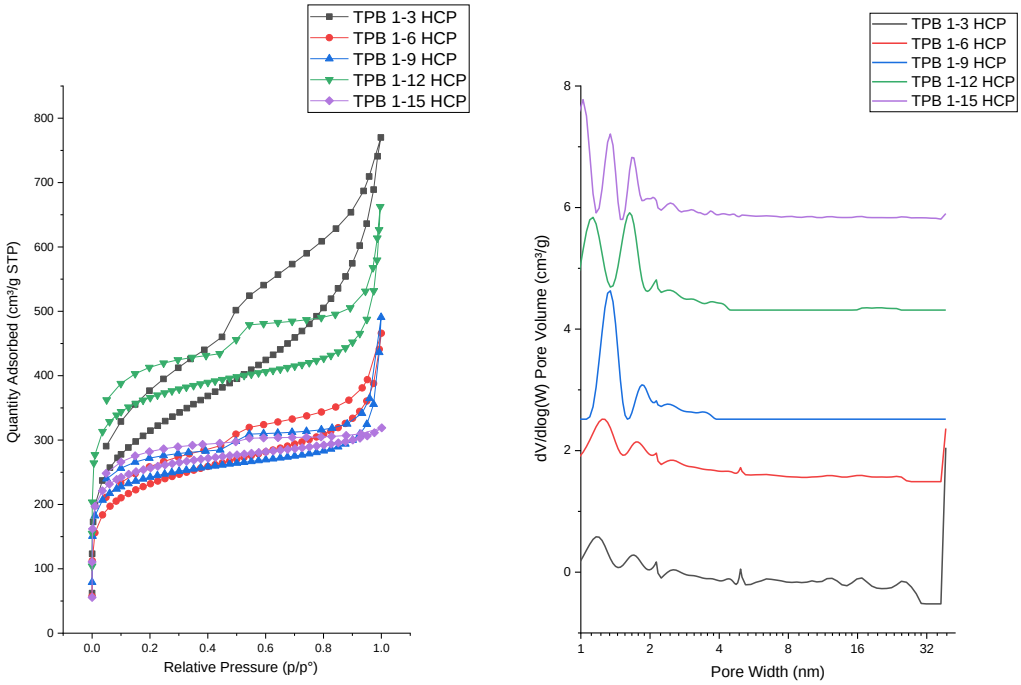

Figure 5.6.4 Isotherm and pore size distribution of TPB HCPs

The porous structures of TPB HCPs were characterized by N_2 adsorption/desorption analysis at 77 K. It can be found that the TPB HCPs showed the combined Type II and Type IV isotherms according to IUPAC definition. The sharp rise in the low relative pressure range of $P/P_0<0.01$ indicating the microporous structures in TPB HCPs. The hysteresis loop in the relative pressure range of 0.44-1.0 suggesting the existence of mesopores. The rise in the relative pressure range of 0.9-1.0 demonstrating the macropores in these samples. For the TPB 1-15 HCP, the hysteresis loop is not obvious, illustrating the less mesopores in the TPB 1-15 HCP. For the pore size distribution of TPB HCPs, it can be seen that the main peaks of these samples are located in the range of 1-2 nm, indicating the microporous structures are predominant in TPB HCPs. TPB 1-3 HCP and TPB 1-6 HCP have similar pore size distribution. When compare with TPB 1-9 HCP, the peaks in the range of 1-2 nm of TPB 1-12 HCP split into two peaks while the peaks in the range of 1-2 nm of TPB 1-15 HCP split into three peaks. The single point adsorption total pore volumes of TPB HCPs obtained at $p/p_0=0.99$ and the

BET surface areas of them are shown in the table 5.6.2.

	BET surface area (m^2/g)	Single point adsorption total pore volume at p/p_0=0.99 (cm^3/g)
TPB 1-3 HCP	1139.7	1.19
TPB 1-6 HCP	855.8	0.68
TPB 1-7.5 HCP	1255.6	0.98
TPB 1-9 HCP	908.3	0.76
TPB 1-12 HCP	1372.4	1.02
TPB 1-15 HCP	966.1	0.49

Table 5.6.2 BET surface area and single point adsorption total pore volume of TPB HCPs

The BET surface areas of TPB 1-3 HCP, TPB 1-6 HCP, TPB 1-9 HCP, TPB 1-12 HCP and TPB 1-15 HCP are 1139.7, 855.8, 908.3, 1372.4 and 966.1 m^2/g, respectively. The single point adsorption total pore volumes of them are 1.19, 0.68. 0.76, 1.02 and 0.49 cm^3/g, respectively. The BET surface area and total pore volume of TPB 1-7.5 HCP are 1255.6 m^2/g and 0.98 cm^3/g, respectively. With the increasing amount of crosslinkers, the BET surface areas of TPB HCPs varied from the 855.8 m^2/g to the 1372.4 m^2/g. The TPB 1-12 HCP has the highest BET surface area, 1372.4 m^2/g, and the TPB 1-6 HCP has the lowest BET surface area, 855.8 m^2/g. For the variation trend of total pore volume of TPB HCPs, although the fluctuation can be seen with the increasing ratio of FDA to TPB, the overall trend is decreasing, the TPB 1-3 HCP has the highest total pore volume of 1.19 cm^3/g while the TPB 1-15 HCP has the lowest total pore volume, 0.49 cm^3/g. The 1,3,5-triphenylbenzene HCP synthesized with a monomer to crosslinker ratio 1-6 by Li et al.[16] has a BET surface area of 1059 m^2/g, higher than that of the TPB 1-6 HCP.

To further investigate the differences in the porosity of TPB HCPs, the pore volumes of the pores with different pore widths are shown in the table 5.6.3 and pore volume proportions of TPM HCPs are displayed in the figure 5.6.5. The pore volumes of the pores with pore widths less than 2 nm are obtained at relative pressure p/p_0=0.2 and the

pore volumes of the pores with pore widths less than 10 nm are obtained at p/p_0=0.8.

Material	Pore volume of the pores with pore width less than 2 nm (cm^3/g)	Pore volume of the pores with pore width 2-10 nm (cm^3/g)	Pore volume of the pores with pore width larger than 10 nm (cm^3/g)
TPB 1-3 HCP	0.49	0.29	0.41
TPB1-6 HCP	0.36	0.12	0.20
TPB 1-7.5 HCP	0.53	0.20	0.25
TPB 1-9 HCP	0.38	0.06	0.32
TPB 1-12 HCP	0.56	0.10	0.36
TPB 1-15 HCP	0.40	0.05	0.04

Table 5.6.3 The pore volumes of the pores with different pore widths of TPB HCPs

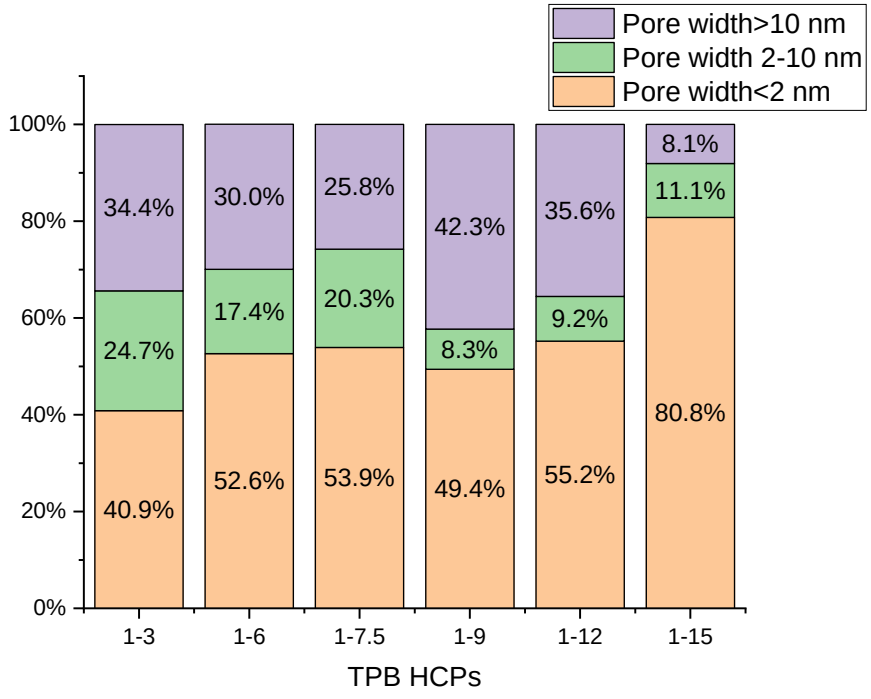

Figure 5.6.5 Pore volume proportions of pores with different pore widths of TPB HCPs

The micropore volume proportions of TPB 1-3, 1-6, 1-9, 1-12 and 1-15 HCP are 40.9%, 52.6%, 49.4%, 55.2% and 80.8%, and the micropore volumes of them are 0.49, 0.36,

0.38, 0.56 and 0.40 cm^3/g, respectively. The volume proportions of pores with pore width 2-10 nm in TPM 1-3, 1-6, 1-9, 1-12 and 1-15 HCP are 24.7%, 17.4%, 8.3%, 9.2% and 11.1%, and the pore volumes of them are 0.29, 0.12, 0.06, 0.10 and 0.05 cm^3/g respectively. For the pores with pore width larger than 10 nm, the pore volume proportions in TPM 1-3, 1-6, 1-9, 1-12 and 1-15 HCP are 34.4%, 30.0%, 42.3%, 35.6% and 8.1%, the pore volumes of the pores with pore width larger than 10 nm are 0.41, 0.20, 0.32, 0.36 and 0.04 cm^3/g, respectively. The volume proportion of micropores, pores with diameter 2-10 nm and pores with diameter larger than 10 nm of TPB 1-7.5 HCP are 53.9%, 20.3% and 25.8%, the pore volume of these pores are 0.53, 0.20 and 0.25 cm^3/g, respectively. From the pore volume proportions of TPB HCPs, it can be found that the overall variation trend of the volume proportion of micropores is going up with the increasing ratio of crosslinker to monomer, with some fluctuations can be found. From TPB 1-3 HCP to TPB 1-15 HCP, the micropore volume proportion increased from 40.9% to 80.8%. The variation of the volume proportion of the mesopores with diameter 2-10 nm showed a downward tendency with some fluctuation. From TPB 1-3 HCP to TPB 1-15 HCP, the volume proportion of the mesopores with diameter 2-10 nm decreased from 24.7% to 11.1%. In the TPB 1-15 HCP, the pore volume proportion of the pores with diameters less than 10 nm is as high as 91.9%.

5.6.2.5 Cyclic Voltammetry

The electrochemical properties of TPB HCPs were evaluated by a typical three-electrode system with 1 M Na_2SO_4 aqueous solution as electrolyte. The active material on nickel foam, a platinum electrode and an Ag/AgCl electrode (3 M KCl, 0.207 V vs. standard hydrogen electrode at 25 °C) were used as working electrode, counter electrode and reference electrode, respectively. The CV tests were conducted with different scan rates 2, 10, 25, 50, 75, 100 and 200 mV/s in the voltage range of -0.2 V-0.8 V.

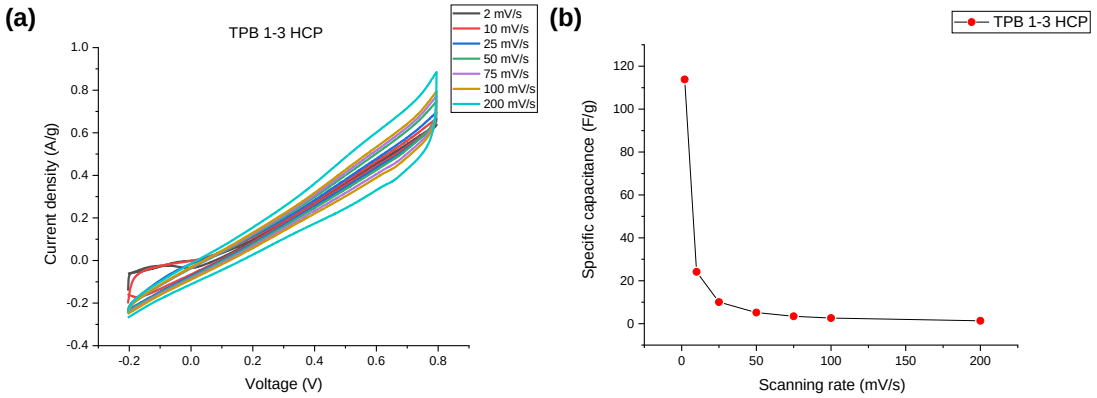

Figure 5.6.6 (a) CV curves at different scanning rates, and (b) Specific capacitance obtained at different scanning rates of TPB 1-3 HCP

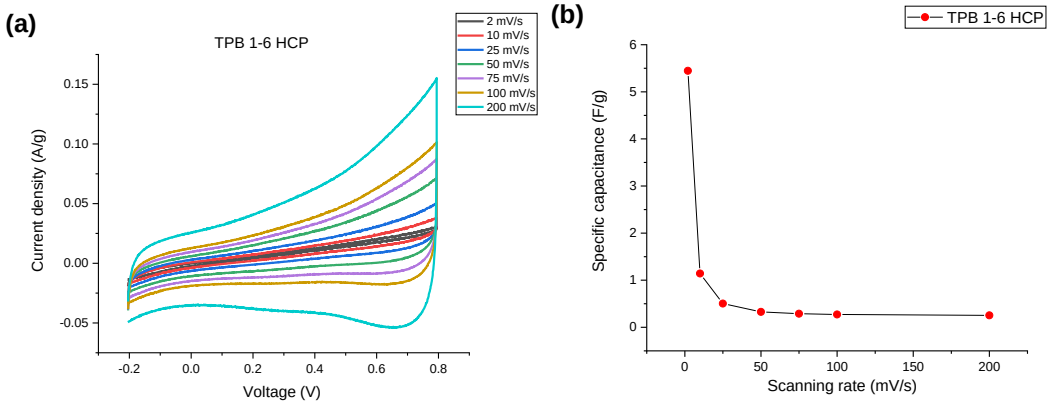

Figure 5.6.7 (a) CV curves at different scanning rates, and (b) Specific capacitance obtained at different scanning rates of TPB 1-6 HCP

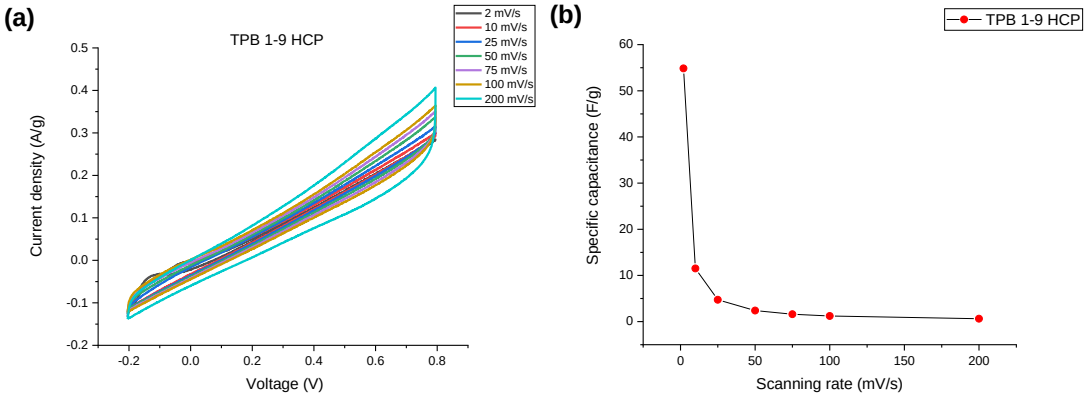

Figure 5.6.8 (a) CV curves at different scanning rates, and (b) Specific capacitance obtained at different scanning rates of TPB 1-9 HCP

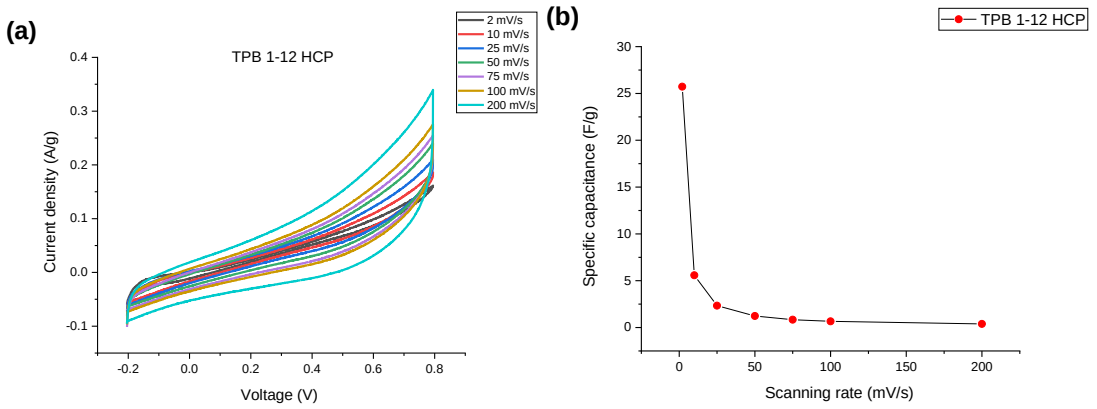

Figure 5.6.9 (a) CV curves at different scanning rates, and (b) Specific capacitance obtained at different scanning rates of TPB 1-12 HCP

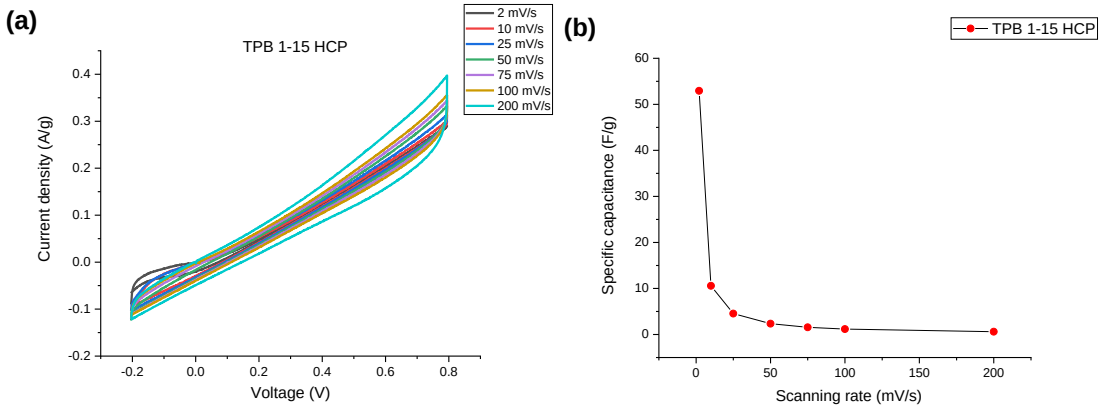

Figure 5.6.10 (a) CV curves at different scanning rates, and (b) Specific capacitance obtained at different scanning rates of TPB 1-15 HCP

	Specific capacitance obtained at different scanning rates (F/g)							
Scanning rates (mV/s) / Material	2	10	25	50	75	100	200	Retention of capacitance at 200 mV/s
TPB 1-3 HCP	113.8	24.1	10.0	5.2	3.4	2.6	1.3	1.1%
TPB 1-6 HCP	5.4	1.1	0.5	0.3	0.3	0.3	0.3	4.6%
TPB 1-7.5 HCP	20.1	4.4	1.9	1.1	0.7	0.6	0.3	1.5%
TPB 1-9 HCP	54.9	11.5	4.7	2.4	1.6	1.2	0.6	1.1%
TPB 1-12 HCP	25.7	5.6	2.3	1.2	0.8	0.7	0.4	1.6%

TPB 1-15 HCP	52.9	10.6	4.5	2.3	1.6	1.2	0.6	1.1%

Table 5.6.4 Specific capacitance of TPB HCPs obtained at different scanning rates

The specific capacitance at 2 mV/s of TPB 1-3, 1-6, 1-9, 1-12 and 1-15 HCP is 113.8, 5.4, 54.9, 25.7 and 52.9 F/g, and the capacitance retention from 2 mV/s to 200 mV/s of them is 1.1%, 4.6%, 1.1%, 1.6% and 1.1%, respectively. The TPB 1-3 HCP has the highest specific capacitance among all the TPB HCPs (including TPB 1-7.5). The BET surface area of the TPB 1-3 HCP (1139.7 m^2/g) is lower than that of the TPB 1-12 HCP (1372.4 m^2/g), but the TPB 1-3 HCP has higher total pore volume (1.19 cm^3/g) than that of the TPB 1-12 HCP (1.02 cm^3/g). The TPB 1-12 HCP has higher micropore volume (0.56 cm^3/g) than the TPB 1-3 HCP (0.49 cm^3/g), while the pore volume of the pores with diameter 2-10 nm of TPB 1-3 HCP (0.29 cm^3/g) is higher than that of the TPB 1-12 HCP (0.10 cm^3/g). The TPB 1-6 HCP has the lowest specific capacitance among all the TPB HCPs, the BET surface area of the TPB 1-6 HCP (855.8 m^2/g) is the lowest of all the TPB HCPs, while the total pore volume of it (0.68 cm^3/g) is not the lowest one. The TPB 1-6 HCP has the lowest micropore volume (0.36 cm^3/g), while the pore volume of the pores with diameter 2-10 nm of TPB 1-6 HCP (0.12 cm^3/g) is the third highest among all the TPB HCPs (including TPB 1-7.5 HCP). It can be found that the TPB 1-9 HCP has the similar capacitance with the TPB 1-15 HCP. The TPB 1-15 HCP has higher BET surface area (966.1 m^2/g) than that of the TPB 1-9 HCP (908.3 m^2/g), while the total pore volume of the TPB 1-9 HCP (0.76 cm^3/g) is higher than that of the TPB 1-15 HCP (0.49 cm^3/g). The micropore volume and the pore volume of the pores with diameter 2-10 nm of the TPB 1-9 HCP is 0.38 and 0.06 cm^3/g, while those of the TPB 1-15 HCP is 0.40 and 0.05 cm^3/g, respectively. Although TPB 1-9 and 1-15 HCP have the similar micropore volume and the pore volume of the pores with diameter 2-10 nm, it can be seen from the pore volume proportion of the TPB HCPs that the TPB 1-15 HCP has quite high volume proportion of the micropores. The specific capacitance of the TPB 1-7.5 HCP at 2 mV/s is 20.1 F/g, lower than that of the TPB 1-12 HCP. The TPB 1-7.5 HCP has lower BET surface area (1255.6 m^2/g), total pore volume (0.98 cm^3/g) and micropore volume (0.53 cm^3/g) than those of TPB 1-12 HCP, while the TPB

1-7.5 HCP has higher pore volume of the pores with diameter 2-10 nm (0.20 cm^3/g) than that of the TPB 1-12 HCP. The variation in the capacitance of TPB HCPs is independence with the variation in the porosity of these samples can be found from the results above, as the porous structures of the HCPs cannot be fully used when they are charged because of the high internal resistance of uncarbonized HCPs.

The relationship between the response current and scanning rate is used for the insight into the capacity kinetics of TPB HCPs, the results are shown in the figure 5.6.11.

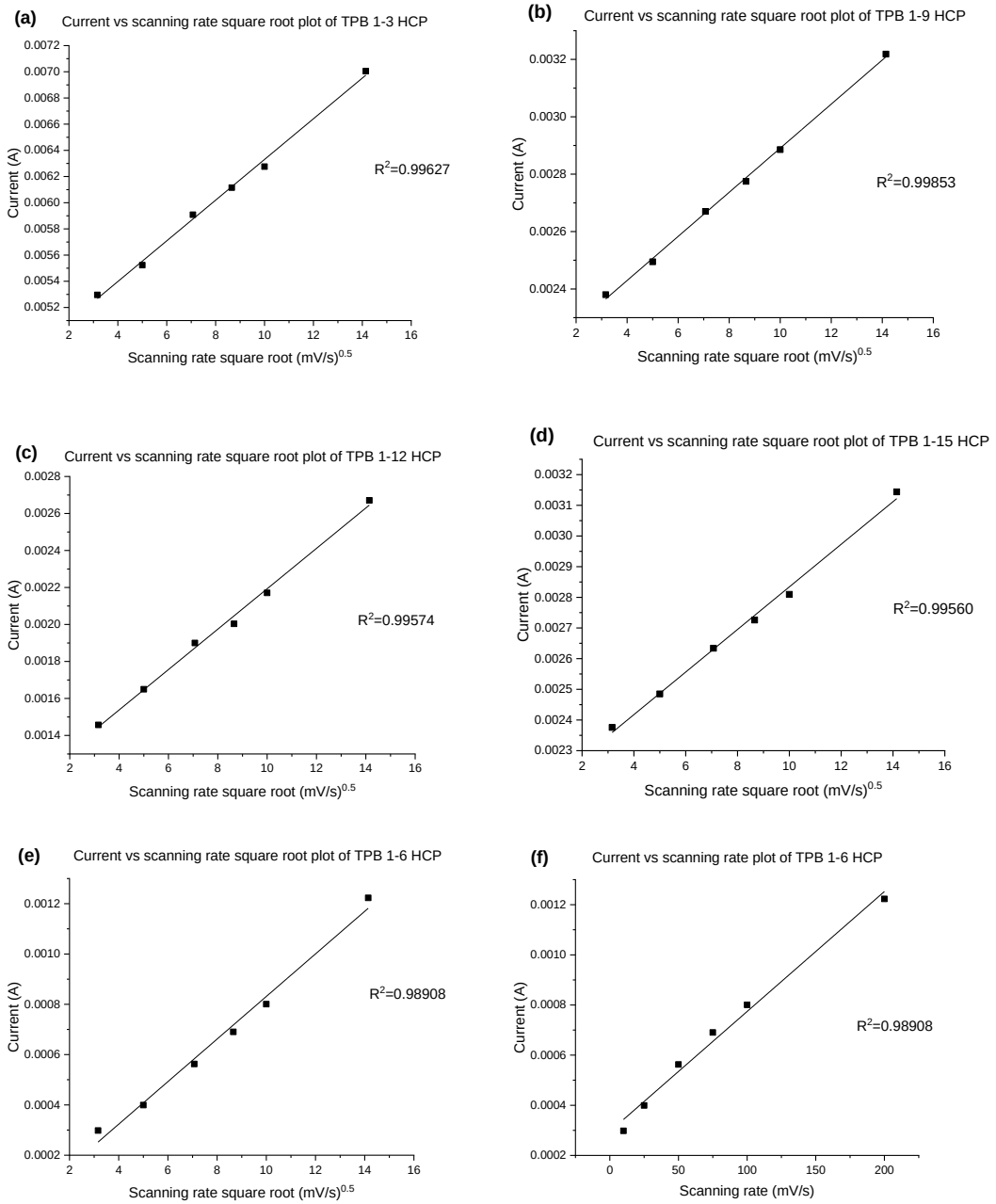

Figure 5.6.11 The relationship between response current and scanning rate of TPB HCPs. (a). – (d). current vs scanning rate square root plot of TPB 1-3, 1-9, 1-12, 1-15 HCP. (e). current vs scanning rate square root plot and (f). current vs scanning rate plot of TPB 1-6 HCP.

From the figure 5.6.11, it can be seen the coefficient of determination R^2 of the response current vs scanning rate square root plot of TPB 1-3, 1-9, 1-12 and 1-15 HCP is 0.99627, 0.99853, 0.99574 and 0.99560, respectively, indicating the good linear relationship between the response current and scanning rate square root. Therefore, the capacity kinetics of these samples are dominated by the diffusion-controlled process. Because of the obvious uneven distribution of the electrolyte ions found from the CV curve of TPB 1-6 HCP at 200 mV/s, the R^2 in both of the response current vs scanning rate plot and response current vs scanning rate square root plot are compared together to confirm the capacity kinetic of the TPB 1-6 HCP. It can be seen that the response current vs scanning rate plot and response current vs scanning rate square root plot have the same value of R^2, 0.98908, suggesting the mixed capacity kinetic of the TPB 1-6 HCP. The poor conductivity determines the capacity kinetic of the TPB HCPs is slow diffusion-controlled process, thus the rate performance of TPB HCPs is quite low. Though the TPB 1-6 HCP have a mixed capacity kinetic, the low capacitance of it confirms the fast surface-controlled process could not provide too much capacitance, the underutilized porosity of the TPB 1-6 HCP results in the low specific capacitance of this sample.

5.6.2.6 Electrochemical impedance spectroscopy (EIS)

To further investigate the electrochemical performance of TPB HCPs, electrochemical impedance spectroscopy (EIS) was carried out with amplitude of 10 mV and frequency range 100 k Hz to 0.01 Hz. The Nyquist and Bode plots of TPB HCPs are listed in the figures 5.6.12 to 5.6.16.

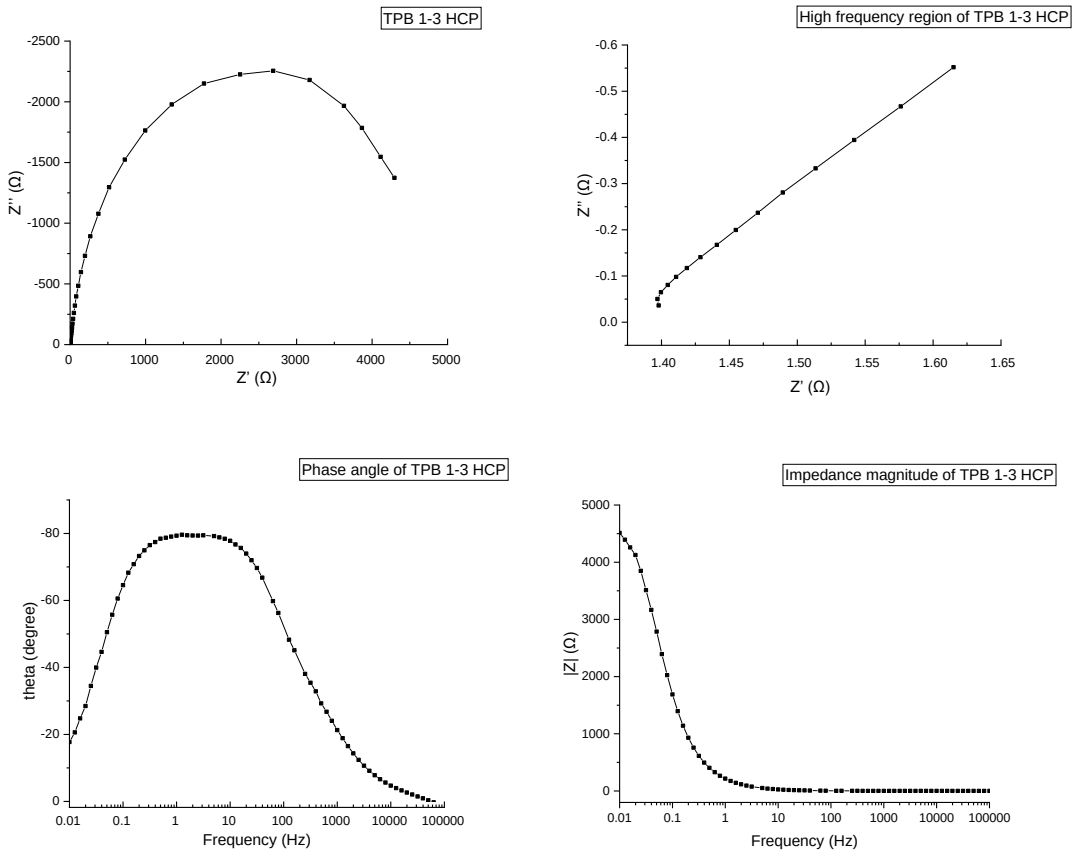

Figure 5.6.12 Nyquist plot and Bode plot of TPB 1-3 HCP

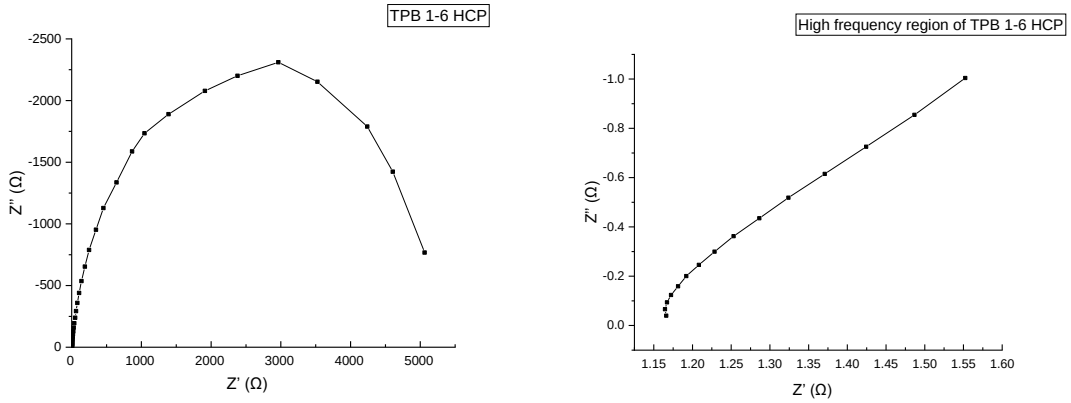

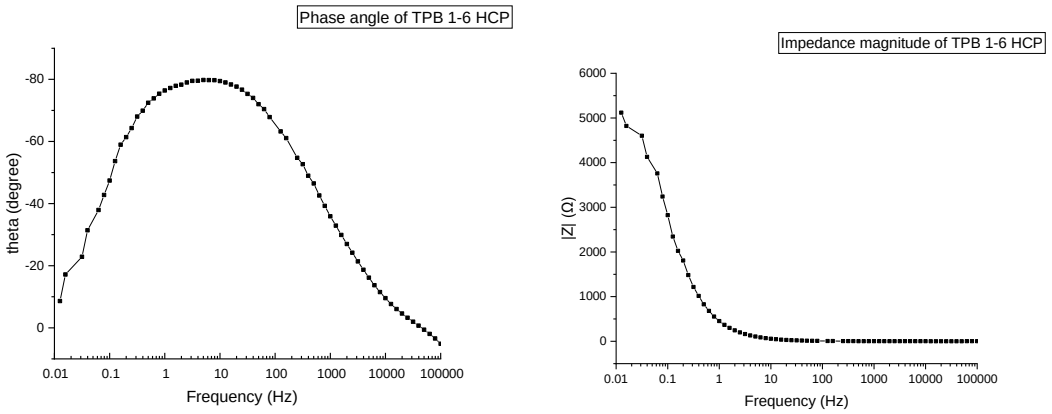

Figure 5.6.13 Nyquist plot and Bode plot of TPB 1-6 HCP

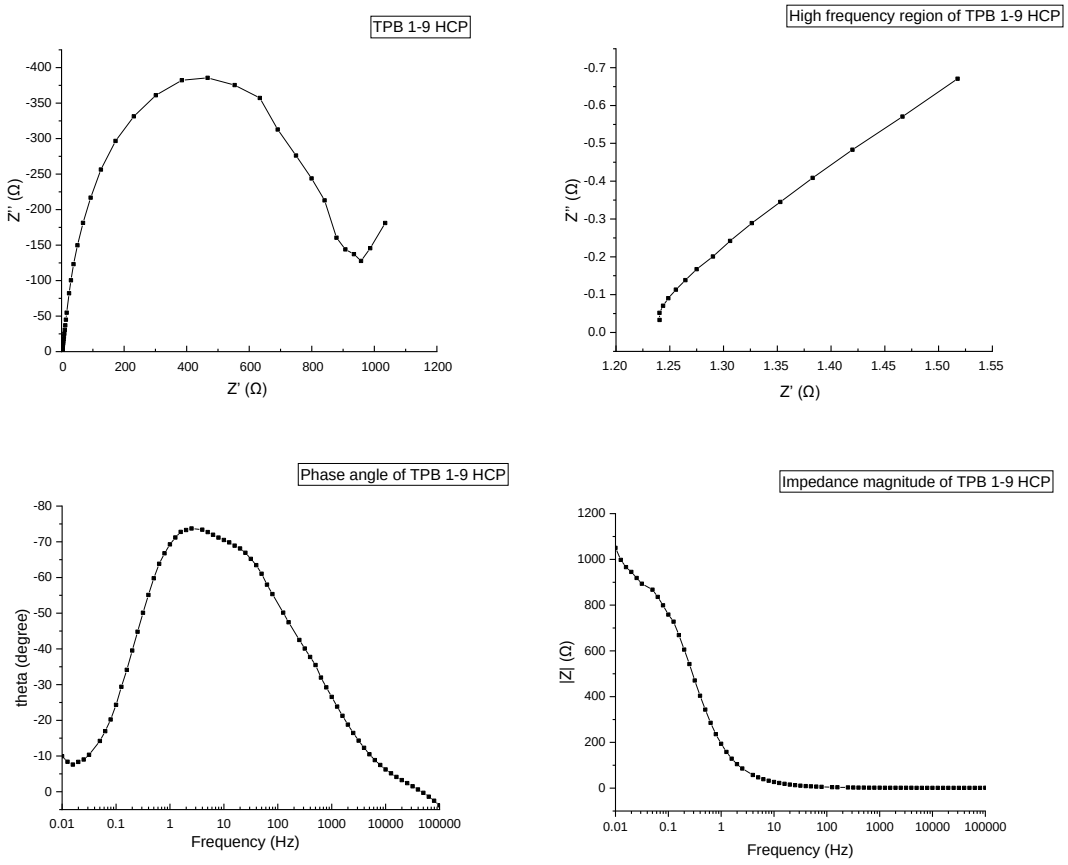

Figure 5.6.14 Nyquist plot and Bode plot of TPB 1-9 HCP

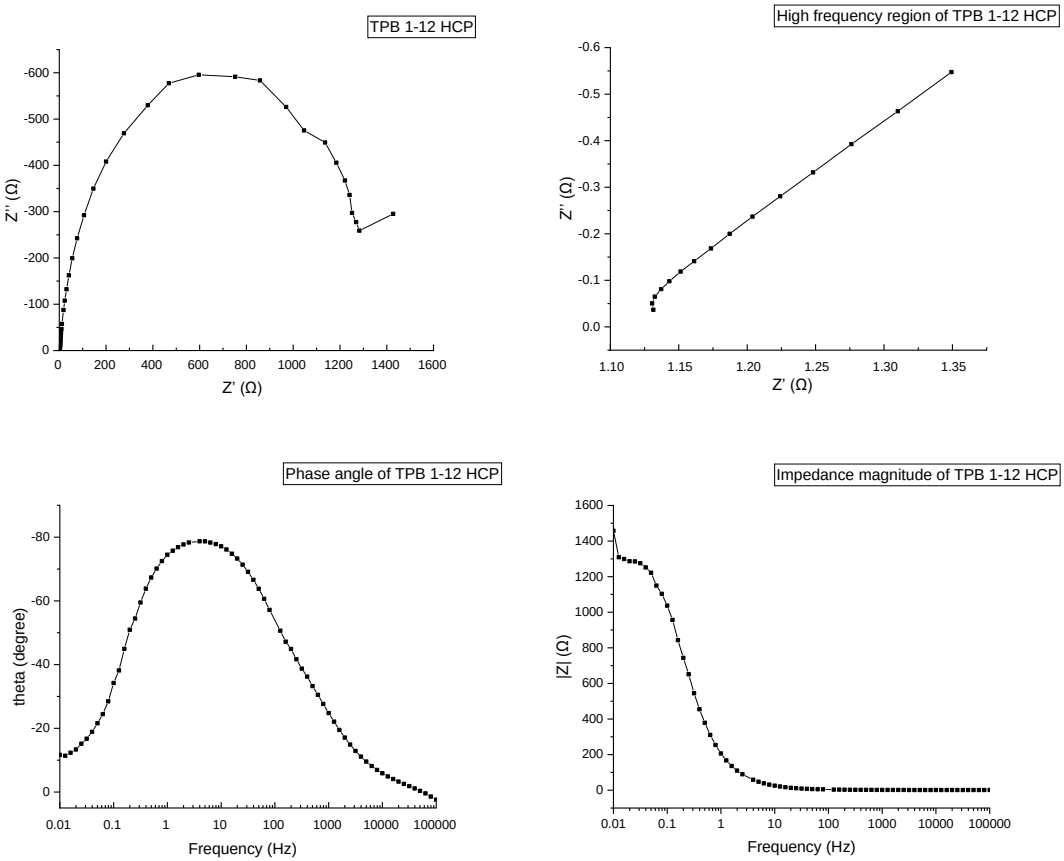

Figure 5.6.15 Nyquist plot and Bode plot of TPB 1-12 HCP

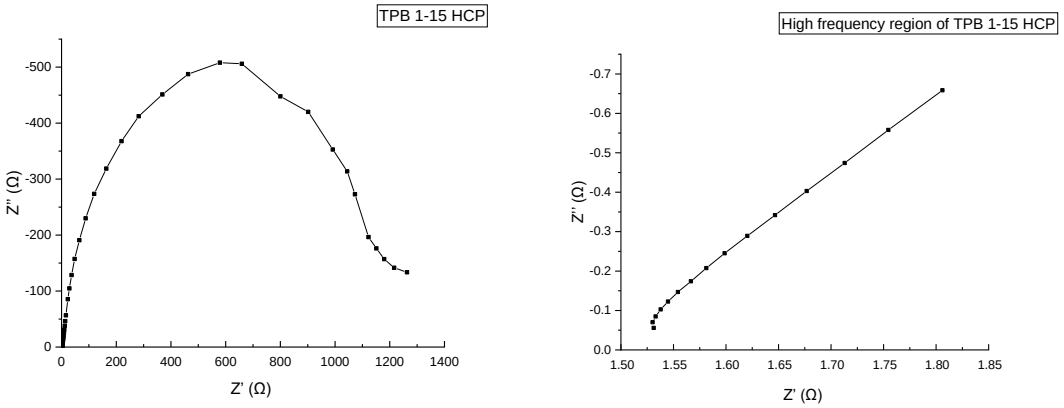

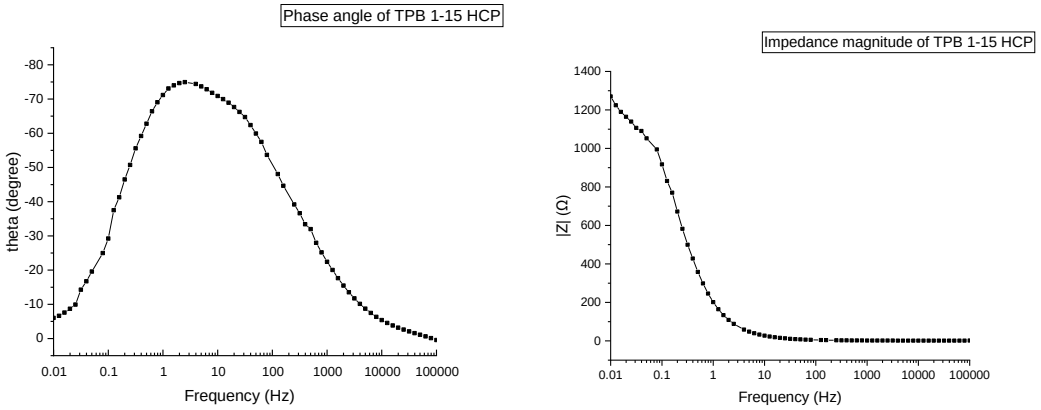

Figure 5.6.16 Nyquist plot and Bode plot of TPB 1-15 HCP

	Whether the semicircle can be observed at high frequencies?	Whether the Nyquist plot is vertical or near vertical to Z" axis at low frequencies?	The phase angle value of the curve apex	Phase angle at 0.01 Hz	Impedance magnitude at 0.01 Hz (Ω)
TPB 1-3 HCP	No	No	-80°	-19°	4511
TPB 1-6 HCP	No	No	-80°	-10°	5119
TPB 1-9 HCP	No	No	-74°	-10°	1050
TPB 1-12 HCP	No	No	-79°	-10°	1458
TPB 1-15 HCP	No	No	-75°	-5°	1270

Table 5.6.5 The results from Nyquist and Bode plot of TPB HCPs

The Nyquist plot of TPB HCPs showed the absence of the sharp rising 'tail' in the intermediate and low frequency region that parallels to the Z" axis illustrating the TPB HCPs did not show supercapacitor behaviour. The highest point of the phase angle curves of TPB HCPs vary from -80° to -74°, demonstrating the TPB HCP cannot behave like pure capacitors. The phase angle curves of TPB HCPs went downward to the phase angle close to 0° from the highest point with the decreasing frequency, suggesting the

quasi resistor-behaviour of the TPB HCPs. The phase angles of TPB HCPs at 0.01 Hz did not decrease to 0°, indicating the TPB HCPs still showed some capacitance at low frequencies. The large impedance magnitude values of the TPB HCPs can be found at 0.01 Hz. It can be found that the ohmic resistance occupies a quite large proportion in the impedance based on the shape of Nyquist plot of TPB HCPs and the calculation formula of impedance magnitude. The absence of the semi-circle in the high frequency region can be attributed to the ohmic contact between the current collector and the active materials.

To present the poor conductivity of TPB HCPs more directly, the fitting results are shown in the figure 5.6.17 and table 5.6.6. The Randles circuit model is used as the equivalent circuit for the impedance fitting.

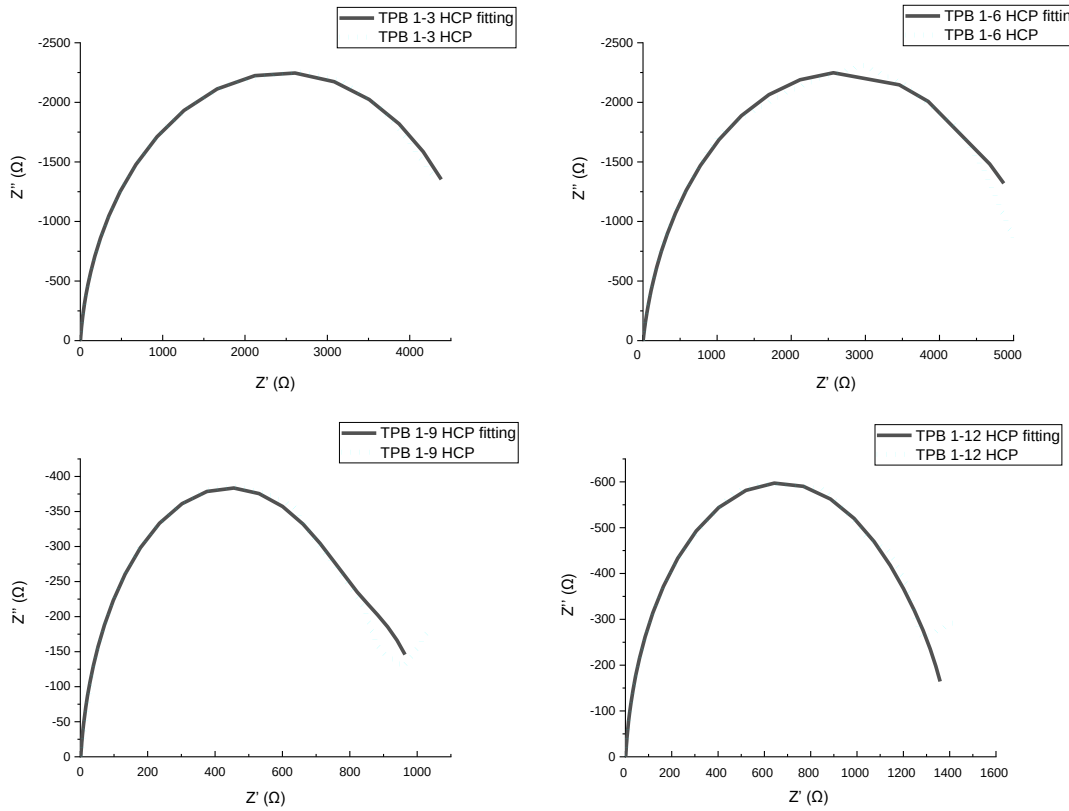

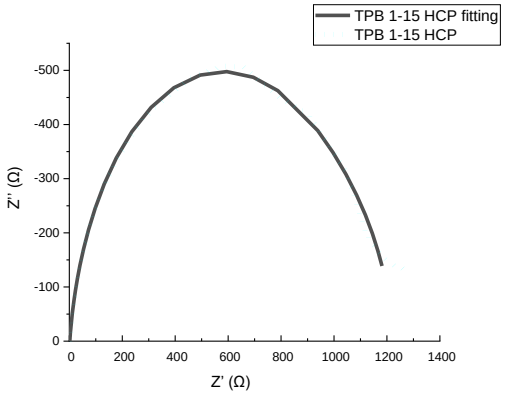

Figure 5.6.17 The impedance fitting curves of TPB HCPs

In the fitting curves of TPB HCPs, the deviations can be found in the low frequency region as the poor conductivity and the disordered porous structure of TPB HCPs made the diffusion is hard to be precisely predicted.

	R1 (Ω)	CPE1-T (F)	CPE1-P	R2 (Ω)	Ws1-R (Ω)	Ws1-T (s)	Ws1-P
TPB 1-3 HCP	1.531	0.00087056	0.94015	4921.2	23.1	4.2	0.5
TPB 1-6 HCP	1.262	0.00044034	0.89197	5239.3	582.2	64.2	0.5
TPB 1-9 HCP	1.334	0.00106060	0.92327	832.9	197.3	28.8	0.5
TPB 1-12 HCP	1.244	0.00095766	0.93682	1297.1	107.1	16.7	0.5
TPB 1-15 HCP	1.648	0.00101730	0.91012	1124.4	97.0	14.1	0.5

Table 5.6.6 The impedance fitting results of TPB HCPs

The high R2 values in the table 5.6.4 suggest the high internal resistance of TPB HCPs. The variation in the R2 values of TPB HCPs indicate the influence of different amount of crosslinkers used in the synthesis of TPB HCPs.

To gain further insight into the electrochemical performance of TPB HCPs with alternating current is applied, the complex capacitance of TPB HCP is performed. The definition of complex capacitance and the definitions of its components were given by equation 5.2.2.6.1, 5.2.2.6.2 and 5.2.2.6.3. The complex capacitance curves of TPB HCP are shown in the figure 5.6.18.

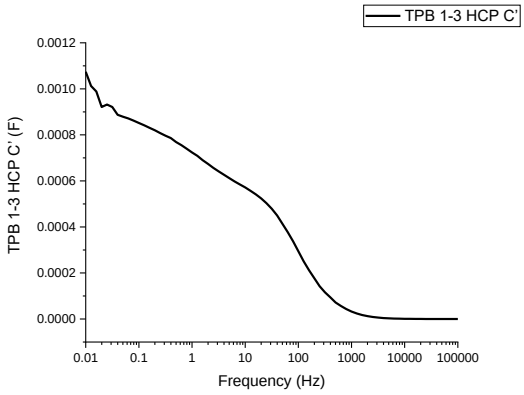
TPB 1-3 HCP C'
TPB 1-3 HCP C' (F)
Frequency (Hz)

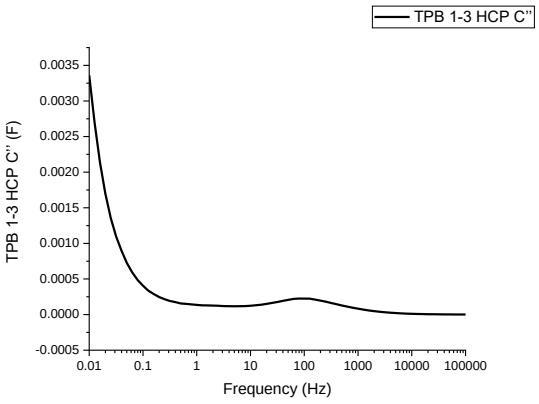
TPB 1-3 HCP C''
TPB 1-3 HCP C'' (F)
Frequency (Hz)

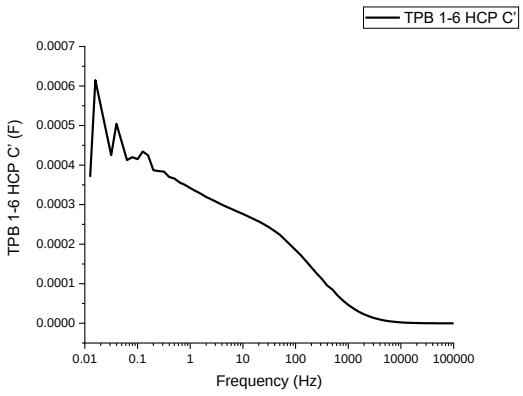
TPB 1-6 HCP C'
TPB 1-6 HCP C' (F)
Frequency (Hz)

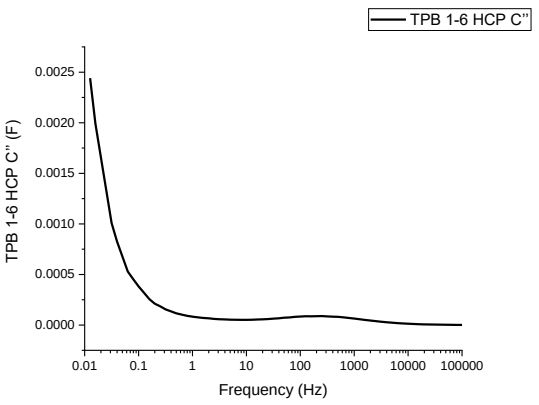
TPB 1-6 HCP C''
TPB 1-6 HCP C'' (F)
Frequency (Hz)

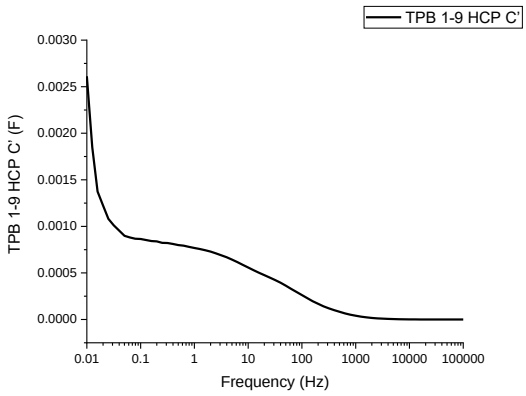
TPB 1-9 HCP C'
TPB 1-9 HCP C' (F)
Frequency (Hz)

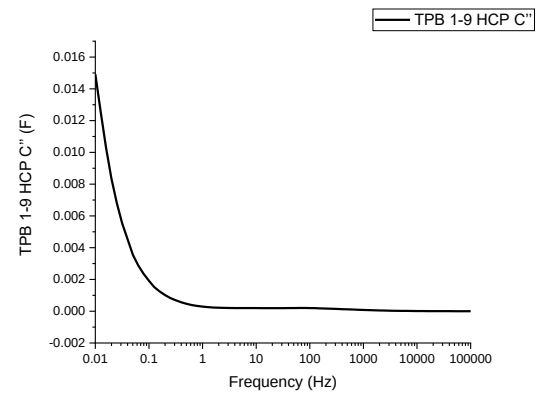
TPB 1-9 HCP C''
TPB 1-9 HCP C'' (F)
Frequency (Hz)

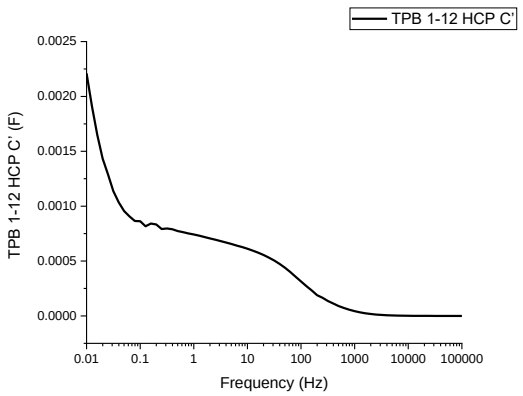
TPB 1-12 HCP C'
TPB 1-12 HCP C' (F)
Frequency (Hz)

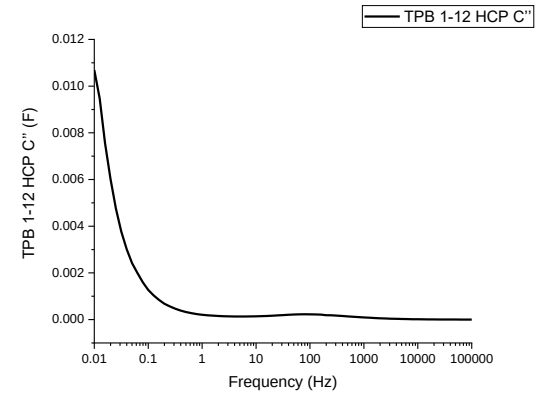
TPB 1-12 HCP C''
TPB 1-12 HCP C'' (F)
Frequency (Hz)

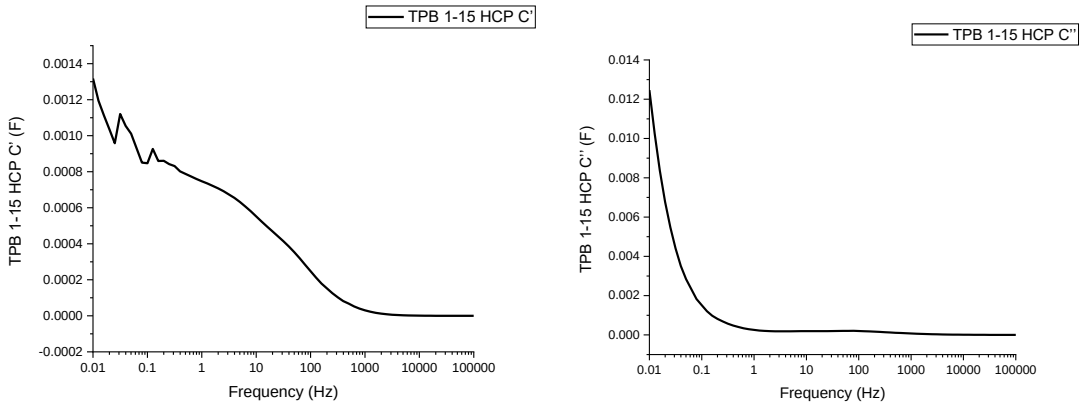

Figure 5.6.18 The complex capacitance of TPB HCPs

The real part of the complex capacitance C' shows the capacitance variation with the decreasing frequency. It can be seen that the C' curves of the TPB HCPs showed the same variation trend with a common supercapacitor in the high and intermediate frequency region, while significant fluctuations can be seen at low frequencies, suggesting the unstable accessibility rate of the porous structures of TPB HCPs caused by the poor conductivity, this corresponds to the specific capacitances of TPB HCPs obtained from CV tests are independent with the BET surface and pore volumes of TPB HCPs. As discussed in previous parts, the poor capacitance at very low frequencies in the C' of the complex capacitance is caused by the high internal resistance of uncarbonized HCPs as well.

The imaginary part of the complex C'' corresponds to energy dissipation. With the decreasing frequency, the weak peak corresponding to phase angle -45° appeared then the C'' curves began to increase sharply and reached the maximum at 0.01 Hz, demonstrating the increased energy dissipation in the low frequency region caused by poor conductivity of TPB HCPs. This corresponds to the decreasing in the phase angle curves at low frequencies. The frequency at which the C'' reaches the maximum can be used to define the relaxation time to evaluate the rate performance of the materials. The definition of the relaxation time was given by 5.2.2.6.4. The relaxation time τ_0 of the TPB HCPs is 100 s, suggesting the poor rate performance of TPB HCPs. This corresponds to the results from the CV tests.

In this chapter, specific capacitances of the HCPs vary with monomer to crosslinker ratios used for synthesis, the TPM 1-6 HCP has the highest specific capacitance in this chapter, 132.8 F/g. Compared with the TPM 1-7.5 HCP synthesized in chapter 3 with a specific capacitance of 92.7 F/g, the TPM 1-6 HCP shows higher specific capacitance, indicating using monomer to crosslinker ratios for structure controlling of HCPs is effective. However, the supercapacitive performance of the TPM HCP is incomparable with that of the POPs with a fully conjugated molecular network, e.g., β-ketoenamine-linked conjugated microporous polymer (KECMP-1) with specific capacitances of 252 F/g at 1 A/g and 126 F/g at 100 A/g,[60] conjugated microporous polymer synthesized from Buchwald–Hartwig coupling (PAQTA) which has specific capacitances of 576 F/g at 1 A/g and 410 F/g at 10 A/g,[61] nanoporous nitrogen-enriched triazine containing polymer (NENP-1) with specific capacitances of 1064 F/g at a scanning rate of 5 mV/s and 497 F/g at a scanning rate of 100 mV/s.[62] Although Triazine containing porous organic polymer ($POP_{M–TFP}$) shows lower supercapacitive performance with specific capacitances of 178 F/g at 0.5 A/g and 77 F/g at 8 A/g, [63] the rate performance of $POP_{M–TFP}$ is much higher than that of the TPM 1-6 HCP with poor conductivity originated from the unconjugated methylene bridges.

5.7 Summary and conclusion

5.7.1 Summary

After the analysis to the HCPs synthesized from benzene, biphenyl, terphenyl, triphenylmethane and triphenylbenzene with different ratios of monomer to crosslinker, it can be seen that the HCPs synthesized from one monomer with different pore structures and specific capacitances can be obtained by using different ratios of monomer to crosslinker. Through the horizontal comparison of different groups of HCPs synthesized from different monomers, it can be found that the different structures of monomers also have an effect on the porosities and specific capacitances. The BET surface area and specific capacitance of the HCPs discussed in chapter 5 are shown in the table 5.7.1.

	BET surface area (m^2/g)	Specific capacitance at 2 mV/s (F/g)
Benzene 1-1 HCP	931.4	0.12
Benzene 1-2 HCP	1381.9	0.52
Benzene 1-3 HCP	1040.4	13.9
Benzene 1-4 HCP	1698.4	0.74
Benzene 1-5 HCP	1085.2	0.55
Benzene 1-6 HCP	1072.3	0.53
Biphenyl 1-3 HCP	752.1	92.7
Biphenyl 1-5 HCP	639.1	30.0
Biphenyl 1-6 HCP	376.5	90.7
Biphenyl 1-8 HCP	570.0	27.9
Biphenyl 1-10 HCP	640.5	60.0
Terphenyl 1-3 HCP	548.5	18.9
Terphenyl 1-6 HCP	89.5	10.1
Terphenyl 1-7 HCP	127.1	2.2
Terphenyl 1-9 HCP	66.5	35.6

Terphenyl 1-12 HCP	34.5	4.7
Terphenyl 1-14 HCP	355.2	59.4
TPM 1-3 HCP	1134.3	126.9
TPM 1-6 HCP	1783.5	132.8
TPM 1-7.5 HCP	1219.1	92.7
TPM 1-9 HCP	1443.9	91.1
TPM 1-12 HCP	1039.4	52.0
TPM 1-15 HCP	1325.8	19.5
TPB 1-3 HCP	1139.7	113.8
TPB 1-6 HCP	855.8	5.4
TPB 1-7.5 HCP	1255.6	20.1
TPB 1-9 HCP	908.3	54.9
TPB 1-12 HCP	1372.4	25.7
TPB 1-15 HCP	966.1	52.9

Table 5.7.1 The BET surface area and specific capacitance of HCPs in chapter 5

From the Benzene HCPs to the Biphenyl HCPs, then to the Terphenyl HCPs, the specific surface areas of these samples decrease with the increasing sizes of the monomers. For the group of Benzene HCPs, the Benzene 1-4 HCP has the highest BET surface area, 1698.4 m^2/g whereas the Benzene 1-1 HCP has the lowest BET surface of 931.4 m^2/g. As for the Biphenyl HCP group, the Biphenyl 1-3 HCP has the highest BET surface of 752.1 m^2/g while the Biphenyl 1-6 HCP has the lowest BET surface in this group, 376.5 m^2/g. In the group of the Terphenyl HCPs, the Terphenyl 1-3 HCP has the highest BET surface area, 548.5 m^2/g and the Terphenyl 1-12 HCP has the lowest BET surface area, 34.5 m^2/g. In terms of TPB HCP group, the BET surface areas of them are slightly lower than those of the Benzene HCPs, the TPB 1-12 HCP has the highest BET surface area of 1372.4 m^2/g and the TPB 1-6 HCP has the lowest BET surface area of 855.8 m^2/g. The BET surface areas of the TPM HCPs are overall the highest among all the samples discussed in this chapter. In the group of TPM HCPs, the TPM 1-6 HCP

has the highest BET surface area, 1783.5 m^2/g, and the TPM 1-12 HCP has the lowest BET surface area 1039.4 m^2/g.

The monomers with different structures also have influence upon the specific capacitance of the HCPs. In the Benzene HCP group, the Benzene 1-3 HCP has the highest specific capacitance, 13.9 F/g while the Benzene 1-1 HCP has the lowest specific capacitance, 0.12 F/g. For the group of the Biphenyl HCPs, the Biphenyl 1-3 HCP has the highest specific capacitance, 92.7 F/g and the Biphenyl 1-8 HCP has the lowest specific capacitance, 27.9 F/g. As for the Terphenyl HCP group, the Terphenyl 1-14 HCP has the highest specific capacitance, 59.4 F/g while the Terphenyl 1-7 HCP has the lowest specific capacitance, 2.2 F/g. For the group of the TPB HCPs, the TPB 1-3 HCP has the highest specific capacitance, 113.8 F/g, whereas the TPB 1-6 HCP has the lowest specific capacitance, 5.4 F/g. As for the TPM HCP group, the TPM 1-6 HCP has the highest specific capacitance among all the samples discussed in this chapter, 132.8 F/g, and the TPM 1-15 HCP has the lowest specific capacitance in this group, 19.5 F/g. Although the lowest specific capacitance in the TPM HCP group is 19.5 F/g, the specific capacitances of TPM 1-3 HCP, TPM 1-7.5 HCP and the TPM 1-9 HCP are 126.9, 92.7 and 91.1 F/g, respectively, demonstrating the TPM HCPs have overall higher specific capacitances than other group of samples in this chapter.

In the previous analyses, it can be found the variation of the specific capacitances is usually independent with the variation of the porosities, the main reason for this is the porous structures of the HCPs cannot be fully used when they are charged due to the high internal resistance of HCPs. The differences in the specific capacitances of different HCPs obtained at a low scanning rate 2 mV/s demonstrate these HCP materials have different utilization rates under the poor conductivity. The higher capacitances of some HCPs indicate the pore structures are conducive to the diffusion of electrolyte ions. To obtain an HCP material with highly porous structure that is beneficial to electrolyte ion diffusion by using knitting method, the selection of monomers is important. The 1,3,5-triphenylmethane is a good candidate as TPM HCPs have both high BET surface area and relatively high specific capacitance. The TPB HCPs

synthesized with different ratios of monomer to crosslinker show the specific capacitances vary from 5.4 F/g to 113.8 F/g, demonstrating adjusting ratios of monomer to crosslinker is also an effective method for HCP structure controlling. Therefore, it can be inferred that using proper monomers and appropriate ratio of monomer to crosslinker can be used for the performance optimization of different applications of HCP materials synthesized by using the knitting method.

5.7.2 Conclusion

With using different monomer to crosslinker ratios for HCPs synthesized from different monomers, the porous structures and specific capacitances of these HCPs are various. The TPM 1-6 HCP has the highest BET surface area of 1783.5 m^2/g and the highest specific capacitance among all the samples discussed in this chapter, 132.8 F/g. For the TPM 1-7.5 HCP synthesized in Chapter 3, the BET surface area and specific capacitance are 1219.1 m^2/g and 92.7 F/g, respectively. The increases in the performance of porosities and specific capacitances of the TPM HCPs indicate using different monomer to crosslinker ratios is an effective method for structure controlling of HCPs. Most of the HCPs synthesized in this chapter show low rate performance and the capacity kinetic of them is diffusion-controlled process. For Benzene HCPs, the capacity kinetic of them is surface-controlled process, corresponding to their relative higher rate performance, but the capacitances of them are much lower. This indicates the accessibility of the porous structures of the Benzene HCPs are much lower than that of other samples.

In EIS results, the Nyquist plots and phase angle curves of the HCPs indicated they do not show supercapacitor behaviours. The impedance magnitudes of these HCP samples show high internal resistances of them. In the complex capacitances, the pore structures of the HCPs cannot be fully used due to their high internal resistances is confirmed by the fluctuations in the low frequency region of the C’ curves and the poor rate performance of the HCPs can be also seen in the C” curves. The very poor capacitance

at very low frequencies in the real part of the complex capacitance is also due to the high internal resistance of uncarbonized HCPs.

For the HCPs synthesized with different monomer to crosslinker ratios, thermal treatments are necessary as well due to the high internal resistances. Although using different monomers for HCP synthesis is also an effective method for structure controlling of HCPs, the method of using different monomer to crosslinker ratios could provide more possibilities for obtaining HCPs with various pore structures. The HCPs with different pore structures are promising candidates of activated carbon precursors. The highly various pore structures of HCPs are the advantage when compared with the biomass precursors for activated carbons, as the inherent structures of the biomass precursors are not tunable or fully tunable. It can be also inferred that using proper monomers and an appropriate ratio of monomer to crosslinker can be used for the performance optimization of different applications of HCP materials synthesized by using the knitting method.

Reference

1 W. Raza, F. Ali, N. Raza, Y. Luo, K. H. Kim, J. Yang, S. Kumar, A. Mehmood and E. E. Kwon, *Nano Energy*, 2018, **52**, 441–473.

2 M. Passalacqua, D. Lanzarotto, M. Repetto and M. Marchesoni, *Energies*, 2017, **10**, 1–14.

3 X. Luo, Y. Chen and Y. Mo, *New Carbon Mater.*, 2021, **36**, 49–68.

4 H. Zhong, F. Xu, Z. Li, R. Fu and D. Wu, *Nanoscale*, 2013, **5**, 4678–4682.

5 F. Xu, Z. Tang, S. Huang, L. Chen, Y. Liang, W. Mai, H. Zhong, R. Fu and D. Wu, *Nat. Commun.*, , DOI:10.1038/ncomms8221.

6 J. Chmiola, G. Yushin, Y. Gogotsi, C. Portet, P. Simon and P. L. Taberna, *Science (80-.).*, 2006, **313**, 1760–1763.

7 K. Xia, Q. Gao, J. Jiang and J. Hu, *Carbon N. Y.*, 2008, **46**, 1718–1726.

8 H. J. Liu, J. Wang, C. X. Wang and Y. Y. Xia, *Adv. Energy Mater.*, 2011, **1**, 1101–1108.

9 E. Frackowiak, *Phys. Chem. Chem. Phys.*, 2007, **9**, 1774–1785.

10 H. Jiang, J. Ma and C. Li, *Adv. Mater.*, 2012, **24**, 4197–4202.

11 H. Nishihara and T. Kyotani, *Adv. Mater.*, 2012, **24**, 4473–4498.

12 H. Nishihara, H. Itoi, T. Kogure, P. X. Hou, H. Touhara, F. Okino and T. Kyotani, *Chem. - A Eur. J.*, 2009, **15**, 5355–5363.

13 H. Itoi, H. Nishihara, T. Kogure and T. Kyotani, *J. Am. Chem. Soc.*, 2011, **133**, 1165–1167.

14 Y. Korenblit, M. Rose, E. Kockrick, L. Borchardt, A. Kvit, S. Kaskel and G. Yushin, *ACS Nano*, 2010, **4**,

1337–1344.
15 S. Lei, Y. Lu, X. Zhang, P. Gao, X. Cui and Y. Yang, *Chem. Commun.*, 2019, **55**, 2305–2308.
16 B. Li, R. Gong, W. Wang, X. Huang, W. Zhang, H. Li, C. Hu and B. Tan, *Macromolecules*, 2011, **44**, 2410–2414.
17 H. Ramezanipour Penchah, A. Ghaemi and H. Ganadzadeh Gilani, *Energy and Fuels*, , DOI:10.1021/acs.energyfuels.9b03136.
18 S. Hou, S. Razzaque and B. Tan, *Polym. Chem.*, 2019, **10**, 1299–1311.
19 G. Ji, Z. Yang, X. Yu, Y. Zhao, F. Zhang and Z. Liu, *ACS Sustain. Chem. Eng.*, 2020, **8**, 16320–16326.
20 L. Tan, B. Li, X. Yang, W. Wang and B. Tan, *Polymer (Guildf).*, 2015, **70**, 336–342.
21 C. Wilson, M. J. Main, N. J. Cooper, M. E. Briggs, A. I. Cooper and D. J. Adams, *Polym. Chem.*, 2017, **8**, 1914–1922.
22 J. H. Zhu, Q. Chen, Z. Y. Sui, L. Pan, J. Yu and B. H. Han, *J. Mater. Chem. A*, 2014, **2**, 16181–16189.
23 G. Wang, B. Dou, J. Wang, W. Wang and Z. Hao, *RSC Adv.*, 2013, **3**, 20523–20531.
24 J. Bai, W. Zhang, X. Ma, L. Chen, L. Liu and C. Zhang, *Microporous Mesoporous Mater.*, 2020, **294**, 109892.
25 L. Pan, Q. Chen, J. H. Zhu, J. G. Yu, Y. J. He and B. H. Han, *Polym. Chem.*, 2015, **6**, 2478–2487.
26 R. V. Law, D. C. Sherrington, C. E. Snape, I. Ando and H. Kurosu, *Macromolecules*, 1996, **29**, 6284–6293.
27 Y. Yang, B. Tan and C. D. Wood, *J. Mater. Chem. A*, 2016, **4**, 15072–15080.
28 R. V. Law, D. C. Sherrington, C. E. Snape, I. Ando and H. Kurosu, *Macromolecules*, 1996, **29**, 6284–6293.
29 S. Seo, W. Chaikittisilp, N. Koike, T. Yokoi and T. Okubo, *Microporous Mesoporous Mater.*, 2019, **278**, 212–218.
30 W. Wang, W. Wang, S. Zhang, Z. Li, C. Wang and Z. Wang, *J. Chromatogr. A*, 2018, **1556**, 47–54.
31 H. Xu, J. Wu, B. Zheng, W. Mai, F. Xu, L. Chen, H. Liu, R. Fu, D. Wu and K. Matyjaszewski, *Chem. Commun.*, 2017, **53**, 5294–5297.
32 P. Puthiaraj and W. S. Ahn, *Ind. Eng. Chem. Res.*, 2016, **55**, 7917–7923.
33 Y. Luo, B. Li, W. Wang, K. Wu and B. Tan, *Adv. Mater.*, 2012, **24**, 5703–5707.
34 W. Lv, M. Guo, M. H. Liang, F. M. Jin, L. Cui, L. Zhi and Q. H. Yang, *J. Mater. Chem.*, 2010, **20**, 6668–6673.
35 V. Augustyn, P. Simon and B. Dunn, *Energy Environ. Sci.*, 2014, **7**, 1597–1614.
36 J. S. M. Lee, M. E. Briggs, C. C. Hu and A. I. Cooper, *Nano Energy*, 2018, **46**, 277–289.
37 Z. Bo, Z. Wen, H. Kim, G. Lu, K. Yu and J. Chen, *Carbon N. Y.*, 2012, **50**, 4379–4387.
38 X. Fu, Y. Liu, X. Jiang, Q. Wang, Y. Luo and Y. Lyu, *Thermochim. Acta*, 2018, **665**, 111–118.
39 R. Dawson, T. Ratvijitvech, M. Corker, A. Laybourn, Y. Z. Khimyak, A. I. Cooper and D. J. Adams, *Polym. Chem.*, 2012, **3**, 2034–2038.
40 Y. Shigemasa, H. Matsuura, H. Sashiwa and H. Saimoto, *Int. J. Biol. Macromol.*, 1996, **18**, 237–242.
41 H. Ramezanipour Penchah, A. Ghaemi and H. Ganadzadeh Gilani, *Energy and Fuels*, , DOI:10.1021/acs.energyfuels.9b03136.
42 Y. Luo, S. Zhang, Y. Ma, W. Wang and B. Tan, *Polym. Chem.*, 2013, **4**, 1126–1131.
43 S. Krishnan and C. V. Suneesh, *Mater. Today Commun.*, 2021, **27**, 102251.
44 R. Rego, P. J. Adriaensens, R. A. Carleer and J. M. Gelan, *Polymer (Guildf).*, 2004, **45**, 33–38.
45 A. Varyambath, W. L. Song, S. Singh, J. S. Kim and I. Kim, *Microporous Mesoporous Mater.*, 2021, **312**, 110800.

46 H. Wei, F. Wang, H. Sun, Z. Zhu, C. Xiao, W. Liang, B. Yang, L. Chen and A. Li, *J. Mater. Chem. A*, 2018, **6**, 8633–8642.

47 Y. Liu, X. Chen, X. Jia, X. Fan, B. Zhang, A. Zhang and Q. Zhang, *Ind. Eng. Chem. Res.*, 2018, **57**, 17259–17265.

48 B. Purevsuren, Y. Davaajav and D. Batkhishig, *Mong. J. Chem.*, 2016, **16**, 5–12.

49 L. Ding, H. Gao, F. Xie, W. Li, H. Bai and L. Li, *Macromolecules*, 2017, **50**, 956–962.

50 J. A. Mikroyannidis, *Polymer (Guildf).*, 1999, **40**, 3107–3117.

51 D. Chen, S. Gu, Y. Fu, Y. Zhu, C. Liu, G. Li, G. Yu and C. Pan, *Polym. Chem.*, 2016, **7**, 3416–3422.

52 R. Lu, C. Xu, Q. Wang, Y. Wang, Y. Zhang, D. Gao, J. Bi and G. Fan, *Int. J. Hydrogen Energy*, 2018, **43**, 18253–18260.

53 P. R. Solomon and R. M. Carangelo, *Fuel*, 1982, **61**, 663–669.

54 S. Xu, K. Song, T. Li and B. Tan, *J. Mater. Chem. A*, 2015, **3**, 1272–1278.

55 J. He, G. Zhao, P. Mu, H. Wei, Y. Su, H. Sun, Z. Zhu, W. Liang and A. Li, *Sol. Energy Mater. Sol. Cells*, , DOI:10.1016/j.solmat.2019.110111.

56 M. Keiluweit, P. S. Nico, M. Johnson and M. Kleber, *Environ. Sci. Technol.*, 2010, **44**, 1247–1253.

57 Y. Cheng, S. Razzaque, Z. Zhan and B. Tan, *Chem. Eng. J.*, 2021, **426**, 130731.

58 G. Liu, Y. Wang, C. Shen, Z. Ju and D. Yuan, *J. Mater. Chem. A*, 2015, **3**, 3051–3058.

59 T. Yoshida and Y. Maekawa, *Fuel Process. Technol.*, 1987, **15**, 385–395.

60 S. Chai, N. Hu, Y. Han, X. Zhang, Z. Yang, L. Wei, L. Wang and H. Wei, *RSC Adv.*, 2016, **6**, 49425–49428.

61 Y. Liao, H. Wang, M. Zhu and A. Thomas, *Adv. Mater.*, 2018, **30**, 1–10.

62 M. Chaudhary, A. K. Nayak, R. Muhammad, D. Pradhan and P. Mohanty, *ACS Sustain. Chem. Eng.*, 2018, **6**, 5895–5902.

63 L. Xu, R. Liu, F. Wang, S. Yan, X. Shi and J. Yang, 2019, 1586–1590.

Chapter 6 Conclusion

In this work, Hypercrosslinked polymers are synthesized with Friedel-Crafts reaction, the molecular structures of these HCPs are characterized by ^{13}C solid state NMR and FTIR, the porous structures of them are measured by N_2 adsorption/desorption, and the high thermal stabilities of these HCP originated from the covalent linkages in molecular networks are shown in the TGA results.

In chapter 3, benzene, biphenyl, p-terphenyl, diphenylmethane, fluorene, triphenylmethane and 1,3,5-triphenylbenzene, the monomers with different sizes and geometries are used for HCP synthesis, and the HCPs synthesized from different monomers show different pore structures. The Terphenyl HCP has the lowest BET surface area of 127.1 m^2/g and the TPB HCP shows the highest BET surface of 1255.6 m^2/g. The specific capacitances of the HCPs with different pore structures vary from 2.2 F/g (Terphenyl HCP) to 96.0 F/g (Fluorene HCP).

In chapter 4, the monomers containing heteroatoms with different configurations are used for HCP synthesis. Most of the heteroatom containing HCPs have a lower BET surface area than that of the corresponding non-doped HCPs, while the TPMT HCP shows a higher BET surface area of 1520.5 m^2/g than that of the TPM HCP, 1219.1 m^2/g. The Diphenyl ether HCP and Dibenzofuran HCP have higher specific capacitances than other heteroatom containing HCPs, 123.3 F/g and 100.1 F/g, respectively. The specific capacitances of the Diphenyl ether HCP and Dibenzofuran HCP are higher than those of the Diphenylmethane HCP and Fluorene HCP, indicating the specific capacitances of the HCPs could be enhanced by oxygen contents with some specific configurations. The diphenyl sulfide and dibenzothiophene are not suitable for Friedel-Crafts alkylation reaction, due to the sulfur atoms in the diphenyl sulfide and dibenzothiophene decrease the electron density in the conjugation systems of these two monomers, thus the electrophilic aromatic substitution is hard to occur.

In chapter 5, the HCPs are synthesized with different monomer to crosslinker ratios. With using different monomer to crosslinker ratios for HCPs synthesized from different

monomers, the HCPs show various porous structures and specific capacitances. The TPM HCP synthesized with a monomer to crosslinker ratio of 1-6 has the highest BET surface area and highest specific capacitance in this work, 1783.5 m^2/g and 132.8 F/g, higher than the BET surface area and specific capacitance of the TPM HCP synthesized in chapter 3 with a monomer to crosslinker ratio of 1-7.5, 1219.1 m^2/g and 92.7 F/g, respectively. Terphenyl HCPs have BET surface areas varying from 34.5 m^2/g to 548.5 m^2/g and TPB HCPs show specific capacitances ranging from 5.4 F/g to 113.8 F/g, demonstrating the method of using different monomer to crosslinker ratios for HCP synthesis is effective on structure controlling of HCPs.

Samples in chapter 3	BET surface area (m^2/g)	Specific capacitance at 2 mV/s (F/g)
Benzene HCP	1040.4	13.9
Biphenyl HCP	639.1	30.0
Terphenyl HCP	127.1	2.2
TPM HCP	1219.1	92.7
TPB HCP	1255.6	20.1
Diphenylmethane HCP	1240.8	21.4
Fluorene HCP	1003.9	96.0
Samples in chapter 4	BET surface area (m^2/g)	Specific capacitance at 2 mV/s (F/g)
Carbazole HCP	523.4	14.0
Dibenzofuran HCP	945.9	100.1
Diphenyl ether HCP	1049.2	123.3
TPMA HCP	412.6	78.7
TPMT HCP	1520.5	82.8
TPMO HCP	574.3	67.1
Dibenzothiophene HCP	1.6	1.6
Diphenylamine HCP	2.8	12.4

Samples in chapter 5	BET surface area (m^2/g)	Specific capacitance at 2 mV/s (F/g)
Benzene 1-1 HCP	931.4	0.12
Benzene 1-2 HCP	1381.9	0.52
Benzene 1-4 HCP	1698.4	0.74
Benzene 1-5 HCP	1085.2	0.55
Benzene 1-6 HCP	1072.3	0.53
Biphenyl 1-3 HCP	752.1	92.7
Biphenyl 1-6 HCP	376.5	90.7
Biphenyl 1-8 HCP	570.0	27.9
Biphenyl 1-10 HCP	640.5	60.0
Terphenyl 1-3 HCP	548.5	18.9
Terphenyl 1-6 HCP	89.5	10.1
Terphenyl 1-9 HCP	66.5	35.6
Terphenyl 1-12 HCP	34.5	4.7
Terphenyl 1-14 HCP	355.2	59.4
TPM 1-3 HCP	1134.3	126.9
TPM 1-6 HCP	1783.5	132.8
TPM 1-9 HCP	1443.9	91.1
TPM 1-12 HCP	1039.4	52.0
TPM 1-15 HCP	1325.8	19.5
TPB 1-3 HCP	1139.7	113.8
TPB 1-6 HCP	855.8	5.4
TPB 1-9 HCP	908.3	54.9
TPB 1-12 HCP	1372.4	25.7
TPB 1-15 HCP	966.1	52.9

Table 6.1 The BET surface area and specific capacitance of HCPs in this thesis

For all the HCPs synthesized in this work, have shown poor rate performance due to the high internal resistances originated from the unconjugated methylene bridges.

Usually, the energy storage mechanism of the materials is analyzed by power law, i.e., if *b* value is 0.5, the charge storage mechanism is controlled by diffusion-controlled process; if *b* value is 1, the mechanism is controlled by surface-controlled process. Due to the high internal resistances of uncarbonized HCPs, the power law is not suitable. Therefore, the energy storage mechanism is analyzed by using Randles−Sevcik equation which was introduced in 2.3.1.

Compared with the POPs with a fully conjugated molecular structure that are reported in previous literatures, the specific capacitances of the HCPs in this work are much lower as the porous structures of them cannot be fully utilized. Because of the methylene bridge linkage in the HCP molecule network, as well as steric hindrance caused by the rigidity of the aromatic rings, it is quite hard to address the high internal resistance of HCPs by other methods, like post-synthetic modifications. Therefore, further thermal treatments are necessary for the HCPs to get rid of the poor conductivity, thus better supercapacitive performance can be achieved.

Chapter 7 Future work

As the HCPs synthesized in this work have high internal resistances because of their unconjugated methylene linkages, the high porosity of them cannot be fully used, thermal treatments for these HCPs are necessary before they are used as supercapacitor electrode materials. Earlier this year, Varyambath et al. synthesized biphenyl HCPs with biphenyl to FDA ratios of 1-1, 1-2, 1-3 and 1-4.[1] After carbonization in a N_2 atmosphere with KOH as an activation agent at 800 ℃ for 2 h, the carbonized biphenyl HCPs were obtained. The porous carbon derived from the biphenyl HCP synthesized with the monomer to crosslinker ratio 1-4 has the highest specific capacitance, 421 F/g at the current density of 1 A/g in a 3 M KOH aqueous solution. After 10000 charge/discharge cycles at 12 A/g, the capacitance rate retention of this carbonized sample is 98.3%, indicating the good cycle stability of it. This work shows that HCP materials with thermal treatments have good potential for achieving better supercapacitive performance.

For my work, chemical activation will be employed due to it requires lower temperature and it could provide better activation results.[2,3] KOH is a widely used activation agent for producing POPs derived carbons, while the influences of different activation agents should be considered, for instance, ONC-T1-850,[4] a POP derived carbon with superior supercapacitive performance, was activated by K_2CO_3. There are also some other activation agents such as zinc chloride, phosphoric acid, sodium hydroxide, and so on, so the effects of different activation agents are worth investigating. For more comprehensive understanding of the influences of activation temperature to the HCP derived carbons, a wide range of temperature should be used, for instance, 500 ℃ to 1200 ℃.

The aims of the carbonization of the HCPs involve investigating the influences of the different pore structures of the precursors to the pore structures of HCP derived carbons and investigating whether the heteroatom-doped porous carbons derived from heteroatom containing HCPs could have enhanced supercapacitive performance and

what configuration of the heteroatoms in HCP precursors could result in higher heteroatom contents HCP in derived carbons. Therefore, the HCPs synthesized with different ratios of monomer to crosslinker can be used as precursors for carbonization with different activation agents and under different temperature, and the HCP-derived carbons can be obtained. Then, the relationship between the pore structures of HCP precursors and the supercapacitive performance of the HCP derived carbons can be found. The investigation into heteroatom containing HCP derived carbons can be performed in the same way.

In term of the synthesis of the HCPs, there are other methods for structure controlling of HCPs. In chapter 4, diphenylamine is found that it cannot form a porous HCP network, but actually it can be used for the synthesis of a porous hypercrosslinked copolymer, i.e., diphenylamine can be mixed with a monomer that could form a porous HCP network to synthesize a hypercrosslinked copolymer, such as benzene or triphenylmethane. Because aniline cannot form a porous structure with the knitting method for HCP synthesis either, this method was used for the synthesis of the porous aniline-benzene hypercrosslinked copolymer.[5] Therefore, the synthesis of hypercrosslinked copolymers can be a method for controlling the structures and functionalities of HCPs with more possibilities, for instance, a hypercrosslinked copolymer can be synthesized from more than two monomers, the molar ratio of each individual monomer could have an impact on the final product as well. Moreover, using different ratios of monomer to crosslinker for the synthesis of hypercrosslinked copolymers could provide more possibilities for obtaining HCP precursors with various porous structures.

Reference

1 A. Varyambath, W. L. Song, S. Singh, J. S. Kim and I. Kim, *Microporous Mesoporous Mater.*, 2021, **312**, 110800.

2 J. Hayashi, A. Kazehaya, K. Muroyama and A. P. Watkinson, *Carbon N. Y.*, 2000, **38**, 1873–1878.

3 J. A. Maciá-Agulló, B. C. Moore, D. Cazorla-Amorós and A. Linares-Solano, *Carbon N. Y.*, 2004, **42**, 1367–1370.

4 D. Yan, Y. Wu, R. Kitaura and K. Awaga, *J. Mater. Chem. A*, 2019, **7**, 26829–26837.

5 R. Dawson, T. Ratvijitvech, M. Corker, A. Laybourn, Y. Z. Khimyak, A. I. Cooper and D. J. Adams, *Polym. Chem.*, 2012, **3**, 2034–2038.